DEVELOPMENT OF A ROBUST ELLIPTIC-BLENDING TURBULENCE MODEL FOR NEAR-WALL, SEPARATED AND BUOYANT FLOWS

A thesis submitted to the University of Manchester
for the degree of Doctor of Philosophy
in the Faculty of Engineering and Physical Sciences

2011

Flavien Billard

School of Mechanical, Aerospace and Civil Engineering

Contents

Word count 30579

List of Tables

List of Figures

The University of Manchester

Flavien Billard
Doctor of Philosophy
Development of a robust elliptic-blending turbulence model for near-wall, separated and buoyant flows
February 7, 2012

The thesis introduces a new version of an elliptic-blending low-Reynolds-number eddy-viscosity Reynolds-averaged Navier Stokes model. It is a model intended to be implemented in an industrial solver. It will be argued that there is still room for such a simple model, though eddy-viscosity models must rely on developments specifically made for higher order formulations. It is the aim of the $\overline{v^2} - f$ model to integrate elements of Reynolds-stress modelling developments into a simpler formulation, but the former paradoxically suffers from numerical stiffness, which kept it out of reach of industry researchers everyday simulations. The $\overline{v^2} - f$ formulation endeavours to reproduce the near-wall asymptotic behaviour of the turbulent quantities, as sounder alternative to empirical damping functions, and the required near-wall balance of small terms represents a numerical challenge.

The present work first provides a comprehensive review of $\overline{v^2} - f$ developments proposed over the past twenty years, and the different remedies for the numerical stiffness linked to the original formulation. The review focuses on ten $\overline{v^2} - f$ variants, proposed between 1991 and 2006, whose behaviour is compared in some fundamental flows: the channel flow for five different Reynolds numbers, the asymptotic case of the logarithmic layer at infinite Reynolds number and the case of a flow with homogeneous sheared turbulence.

Based on the conclusions of the review, the thesis proposes new developments. Firstly, the derivation of a new model, namely the $\varphi - \alpha$ model, is introduced. It relies on the resolution of two non-dimensional variables: φ represents the wall-normal anisotropy and α is a wall-proximity sensor. It is argued that only this formulation can address the numerical problems already mentioned without altering the predictions. Secondly, additional upgrades of the $\varphi - \alpha$ model are proposed to correct the dissipation rate equation. The aim is to improve the model behaviour in some specific regions of a boundary layer, by isolating some viscous terms and by improving the representation of turbulent transport at the edge of a boundary layer. Final developments are combined in a new model, the BL-$\overline{v^2}/k$ model.

The $\varphi - \alpha$ and BL-$\overline{v^2}/k$ models are then validated for a set of two pressure induced separated flows and two buoyant flows, and beneficial effects of the proposed developments on the predictions are demonstrated. The numerical properties of the convergency of the BL-$\overline{v^2}/k$ model are also reported at the end of this work.

Declaration

No portion of the work referred to in this thesis has been submitted in support of an application for another degree or qualification of this or any other university or other institute of learning.

Copyright Statement

i. The author of this thesis (including any appendices and/or schedules to this thesis) owns certain copyright or related rights in it (the "Copyright") and s/he has given The University of Manchester certain rights to use such Copyright, including for administrative purposes.

ii. Copies of this thesis, either in full or in extracts and whether in hard or electronic copy, may be made **only** in accordance with the Copyright, Designs and Patents Act 1988 (as amended) and regulations issued under it or, where appropriate, in accordance with licensing agreements which the University has from time to time. This page must form part of any such copies made.

iii. The ownership of certain Copyright, patents, designs, trade marks and other intellectual property (the "Intellectual Property") and any reproductions of copyright works in the thesis, for example graphs and tables ("Reproductions"), which may be described in this thesis, may not be owned by the author and may be owned by third parties. Such Intellectual Property and Reproductions cannot and must not be made available for use without the prior written permission of the owner(s) of the relevant Intellectual Property and/or Reproductions.

iv. Further information on the conditions under which disclosure, publication and commercialisation of this thesis, the Copyright and any Intellectual Property and/or Reproductions described in it may take place is available in the University IP Policy (see `http://www.campus.manchester.ac.uk/medialibrary/policies/intellectualproperty.pdf`), in any relevant Thesis restriction declarations deposited in the University Library, The University Librarys regulations (see `http://www.manchester.ac.uk/library/aboutus/regulations`) and in The Universitys policy on presentation of Theses.

Acknowledgements

First and foremost I would like to thank my supervisor Professor Dominique Laurence for his patience and constant help. His unique approach to turbulence modelling and original ideas were the cornerstone of the present work. I would like to thank Dr David Monfort and Dr Juan Uribe, who both at different times showed an infinite patience, and helped me so much without excepting anything in return. I also wish to express my sincere gratitude to Dr Alistair Revell with its amazing energy. It is a real pleasure to work with him now. My thanks go also to Dr. Charles Moulinec and the Daresbury Laboratory for their help in using *Code_Saturne* with HPC facilities.

I would like to thank Électricité de France (EDF) for hosting me 6 months during my first year and in particular Dr. Sofiane Benhamadouche, Jérôme Bonnelle and Yvan Fournier.

Thanks to my office mates Amir, Dalila, Neil, Alastair, Iaonnis, Ruggero, Mark, Imama, Caroline, Pourya, Imran, Clare: all have contributed to create a great athmosphere in our department. Finally I would like to thank all the people I met during my PhD. I would like to thank Stefano who has been a wonderful friend both at work and in life. Thanks to Rui, with whom I shared so much in my first years here. My thanks go also to my friends Nicolas Jarrin, Nicolas Chini, Yannick and Yacine, in particular, for the amazing and endless conversations we had on many topics.

I would like to deeply thank my girlfriend Otgontsetseg for her endless patience and understanding.

Finally I would like to thank my parents, my sisters, my brother in law and my niece for always supporting me over the past four years.

Nomenclature

Greek letters

α	Elliptic variable used in the elliptic blending method
β	Thermal expansion coefficient
Δ	Filter width or Laplacian operator
δ	Boundary layer thickness or channel half width
δ_ν	Viscous length-scale in a boundary layer
δ_{ij}	Kronecker symbol
ε	Knudsen number (in the context of Sec. 2.1) or dissipation rate of turbulent kinetic energy
ε_{ij}	Tensor of turbulent dissipation of Reynolds Stresses, Eq. 2.20
κ	Wave number (in the context of Subsec. 2.2.1) or Von Kármán constant
μ	Dynamic viscosity
ν	Kinematic viscosity
ν_t	Turbulent kinematic viscosity
ν_{SGS}	Sub-grid scale viscosity
Ω	Computational domain
Ω_{ij}	Vorticity-rate tensor
ϕ^*	Pressure diffusion term of the turbulent kinetic energy, Eq. 2.35

ϕ_{ij} Tensor of the pressure strain-rate correlation, Eq. 2.22

ϕ^*_{ij} Tensor of the pressure term in the Reynolds Stresses transport equations, Eq. 2.20

ϕ^r_{ij} Rapid part of the pressure strain-rate correlation, Eq. 2.26

ϕ^s_{ij} Slow part of the pressure strain-rate correlation, Eq. 2.26

φ Wall-normal turbulent anisotropy $\varphi = \overline{v^2}/k$

φ_{ij} Modified variable (defined in Eq. 3.23) entering the definition of the elliptic variable f_{ij}

ρ Density

σ_k,σ_ε Turbulent Prandtl number associated to the model for the turbulent diffusion of k or ε

τ Relaxation time scale (as used in the Bhatnagar-Gross-Krook approximation (Bhatnagar et al. (1954)))

Latin letters

A_2 Second invariant of the turbulence anisotropy tensor

a_{ij} Turbulence anisotropy tensor

$\underline{c}$ Velocity vector of a particle

C_f Skin-friction coefficient

C_p Pressure coefficient

D^ν_ε Molecular diffusion of the dissipation rate, Eq. 2.21

D^P_ε Pressure transport of the dissipation rate, Eq. 2.21

D^T_ε Turbulent transport of the dissipation rate, Eq. 2.21

D^ν_{ij} Tensor of molecular diffusion of Reynolds Stresses, Eq. 2.20

D^P_{ij} Tensor of the pressure transport of the Reynolds Stress, Eq. 2.22

D_{ij}^T Tensor of turbulent transport of Reynolds Stresses, Eq. 2.20

f Distribution function (in the context of Sec. 2.1)

f_{eq} Equilibrium distribution function (as used in the Bhatnagar-Gross-Krook approximation (Bhatnagar et al. (1954)))

f_{ij} Elliptic variable used in the elliptic relaxation method

G_k Production of turbulent kinetic energy by buoyancy

G_{ij} Tensor of production by buoyancy

K Scale of turbulent kinetic energy

k_{SGS} Sub-grid scale energy

L Length scale

l_m Mixing length

M Molar mass

$\underline{n}$ Wall-normal unitary vector

P^1 First part of the mixed production of the dissipation rate, Eq. 2.21

P^2 Second part of the mixed production of the dissipation rate, Eq. 2.21

P^3 Gradient production of the dissipation rate, Eq. 2.21

P^4 Turbulent production term of the dissipation rate, Eq. 2.21

P_k Production of turbulent kinetic energy

P_{ij} Tensor of turbulent production of Reynolds Stresses, Eq. 2.20

R Gas constant (in the context of Sec. 2.1)

Re Reynolds number

Re_τ Friction velocity based Reynolds number

S_{ij} Strain-rate tensor

P Instantaneous pressure

T	Instantaneous temperature
t	Time
$\overline{uv}$	Turbulent shear stress
$\underline{U}$	Instantaneous velocity vector
U	Stream-wise component of the instantaneous velocity
U^+	Non-dimensional stream-wise component of the instantaneous velocity
u_τ	Friction velocity
U_i	i^{th} component of the instantaneous velocity vector
$\widetilde{\underline{U}}$	LES averaged velocity vector
$\overline{\underline{U}}$	RANS averaged velocity vector
$\underline{u}'$	Fluctuating velocity vector in the LES sense
$\underline{u}$	Fluctuating velocity vector in the RANS sense
$\overline{v^2}$	Wall-normal Reynolds stress
V	Velocity scale or wall-normal component of the instantaneous velocity
W	Span-wise component of the instantaneous velocity
$\underline{x}$	Position vector
x	Coordinate in the stream-wise direction
x_i	i^{th} component of the position vector
Y	Viscous destruction term of the dissipation rate, Eq. 2.21
y	Wall distance or coordinate in the wall-normal direction
y^+	Non dimensional wall distance
z	Coordinate in the span-wise direction

Acronyms

CFD	Computational fluid dynamics

CPU Central processing unit

DNS Direct numerical simulation

EVM Eddy viscosity model

FVM Finite volume method

GGDH Generalised gradient diffusion hypothesis

LES Large eddy simulation

LRR Launder Reece and Rodi

RANS Reynolds averaged Navier Stokes

RSM Reynolds stress model

SGDH Simple gradient diffusion hypothesis

SGS Subgrid scale

SSG Speziale Sarkar and Gatski

SST Shear stress transport

Chapter 1

Introduction

The constant improvement of the numerical methods and of computer performance leads to Computational Fluid Dynamics (CFD) being increasingly used by companies in the design process, at the expense of experiments, which are in general more costly. An accurate description of the flow is needed in many domains, such as aerodynamics or heat transfer. For instance, the correct prediction of the heat-transfer coefficient helps to improve the design of the power-plant components, which is a key factor in reducing the operation cost, and in guaranteeing the safety of facilities. Unfortunately, in industrial applications, flows are mostly turbulent. Due to the randomness of turbulence flows, simplifications arising both from its numerical discretisation and from models for its physical description can easily lead to a poor prediction of the real characteristics of the flow. Indeed turbulence is characterised by unsteadiness at different scales and structures of different size, which strongly interact with the main features of the flow. The nodes of a computational grid need to be close enough to one another to correctly capture the rapid changes in the computed variables due to turbulence. This requirement is too difficult to fulfil, as it would make the computation highly expensive both in terms of time and memory. In practice, the grid used is coarse, and most of the effort is put into modelling the turbulence which cannot be captured with the discretisation used, and in particular into modelling its interactions with the simulated mean flow.

In an industrial approach of the numerical simulation, the turbulence modelling is a key aspect, and its correct representation is of utmost importance for the engineering process, whether this helps or impairs the normal operation of a man-made device. Therefore, turbulence modelling is a big challenge for the scientific community. Depending on the grid resolution, the turbulence field can be partly or entirely modelled. In the Large Eddy Simulation approach (LES) only the smallest turbulent structures are taken into account in the model. As the turbulence at this scale has a behaviour that is universal (*i.e.* only weakly dependent on the main flow and the geometry), the modelling is simpler. In the Reynolds-averaged Navier Stokes (RANS) modelling approach, all the turbulent content is modelled, and only the time-averaged flow field is resolved. Therefore, its cost is affordable in many more flow cases. Many RANS models have been derived, from the well known two-equation $k-\varepsilon$ model of Jones and Launder and the $k-\omega$ model of Wilcox to more complex non-linear eddy-viscosity models and Reynolds-stress models.

The development of models was mainly driven by industrial needs, and even though a firm stem of theoretical results emerged from the academic world, upon which were built more and more complex models, the most widely used models in everyday engineering practice are those which seem to retain a substantial amount of pragmatism and simplicity. In the paper introducing one of the most popular models, the $k-\omega$ SST model, Menter (1994) explains the "slow progress in engineering turbulence modelling" and the "confusing picture it often presents" by an "over-emphasis of theoretical concepts and a virtual denial of the empirical nature of the subject". The five occurences of the functions *min* or *max* in the $k-\omega$ SST equations (acting as "limiters") can lead to $2^5 = 32$ different modes. This is a feature which could not originate from purely theoretical derivation and is more in line with the "if ... then ... else ..." programmer pragmatism. The $k-\omega$ SST model inherits the near-wall robustness and accuracy of the $k-\omega$ model and the reduced free-stream sensitivity of the $k-\varepsilon$ model, while ensuring a proportionality link between the Reynolds shear stress and the turbulent kinetic energy in a boundary layer. Its combined simplicity

and accuracy in predicting flows developing in an adverse pressure gradient makes it undoubtedly one of the most popular in aerospace applications. The pragmatism confessed by one of the most cited turbulence modellers will be the cornerstone of the present work which will aim at incorporating into a simple formulation some elements of higher order modelling.

1.1 Study objectives

A key aspect of turbulence modelling is the way walls affect the flow. The behaviour of the variables in the near-wall layer and the influence of the wall on the whole flow are very important, as they rule many of the main flow characteristics an engineer is interested in, such as heat transfer, pressure forces, friction and separation. Due to viscous effects, the velocity is zero at the wall, and it sharply increases in a thin layer. Large velocity gradients near the walls produce most of the turbulence; therefore the variables in this region need to be accurately predicted. However many models usually do not correctly take into account near-wall-turbulence features. For instance, turbulent structures are highly anisotropic, but most of the eddy-viscosity models cannot capture this anisotropy. Corrections are usually needed, in addition to the basic models, such as empirical functions used to damp the variables near walls, to force simulations to fit the theoretical behaviour. But these corrections usually suffer from lack of physical justifications, and some of them can hardly be used in a very complex geometry, as they require geometric parameters to be known, such as the distance to the nearest wall.

Another approach has recently been devised to model the effects of the wall in a more universal manner, using the elliptic-relaxation method (Durbin, 1991). The eddy-viscosity $\overline{v^2}-f$ model uses this method to solve for the variables $\overline{v^2}$ and f representing the wall-normal diagonal component of the Reynolds Stress tensor and of the pressure strain-rate term respectively, and enables accurate results to be produced by keeping the computational affordability of the two-equation models. Unfortunately, numerical problems arise when using this model in an industrial solver. Different

strategies have been tried to enhance the robustness of the $\overline{v^2} - f$ model, thus enabling its implementation and use in several popular CFD software packages. Some of the modified versions addressed the numerical problems efficiently, but the quality of the simulation is not as good as that of the original model, whereas some others actually predicted results comparable to the one given by the original formulation, but the numerical robustness was still below the standard of most of the eddy-viscosity models.

This work introduces the developments of a new version of the $\overline{v^2} - f$ model. The objectives are twofold:

- First, a solution to the numerical problems previously mentioned is proposed, by using a new approach, the elliptic blending, to reduce the extent of the trade-off between predictive accuracy of the $\overline{v^2} - f$ model and its computational robustness. A model is sought that strengthens the coupling between the elliptic variable and the wall-normal Reynolds stress, without impairing the numerical stability.

- Second, beyond the mere numerical problems of the $\overline{v^2} - f$ model, it is proposed that there is still room for improvement, as far as the predictive capabilities of the original formulation are concerned. The model, as originally introduced, stems from a very simple near-wall adaptation of the $k - \varepsilon$ model, and more advanced results on this matter, some of them derived no later than in the $70's$, were clearly overlooked. The proposed developments in this work to enrich the model will be made, while keeping the simplicity and pragmatism in mind, as the proposed model will be used in an industrial code.

1.2 Outline of the thesis

The presentation of the work is organised as follows. Chapter 2 introduces the basic concepts of turbulence and its modelling. Chapter 3 first presents a description of

the wall effects on turbulence and then focuses on the study of the plane channel flow, an academic case often studied as part of the development of models. Results of direct numerical simulations are analysed as a source of information for near-wall modelling. The end of this chapter reports the classical modelling strategies to cope with near-wall flows with an emphasis on the elliptic-relaxation approach, and in particular, the $\overline{v^2} - f$ type of models.

Chapter 4 provides a comprehensive survey of virtually all $\overline{v^2} - f$ models proposed over the past 20 years. The different solutions developed to tackle the numerical problems associated to the first version are described. Then, the behaviour of all these versions is assessed in a set of simple laboratory flows: the channel flow at various Reynolds numbers, the logarithmic region at infinite Reynolds number and the case of homogeneous shear turbulence.

Chapter 5 describes the steps of the developments of the new model. The first output is an intermediate model, which will be denoted as $\varphi - \alpha$ whose sole aim is to feature a "code-friendly" $\overline{v^2} - f$ formulation with no effect on the predictive capabilities. From the $\varphi - \alpha$ model, additional improvements are then proposed, mainly in the dissipation-rate equation: they are incorporated into the $\varphi - \alpha$ model in a final version, the BL-$\overline{v^2}/k$ model.

Chapter 6 presents results of the $\varphi - \alpha$ and BL-$\overline{v^2}/k$ models, compared to two other versions of the $\overline{v^2} - f$ model and the $k - \omega$ SST model. The cases considered are two pressure-induced separating flows and two buoyant flows where turbulence is impaired due to buoyant forces.

Finally Chapter 7 reports details about the numerical execution of the simulations whose results were presented in Chap 6, for all cases and all models considered, so as to assess the robustness of each model.

For an updated version of this thesis, please refer to:

`http://cfd.mace.manchester.ac.uk/twiki/bin/view/CfdTm/ResPub281`

Chapter 2

Theoretical background

2.1 The Navier Stokes equations

The fluid or gas is described using a distribution function $f(\underline{x}, \underline{c}, t)$: The quantity $f(\underline{x}, \underline{c}, t)d\underline{c}$ represents for a given time t at a given location $\underline{x}$, the total mass per unit volume of particles whose velocity lies between $\underline{c}$ and $\underline{c} + d\underline{c}$. This description offers a way to correctly define the density ρ and velocity $\underline{U}$ used in the Navier Stokes equations at a mesoscopic scale:

$$\rho(\underline{x}, t) = \int_{\mathbb{R}^3} f(\underline{x}, \underline{c}, t)d\underline{c} \tag{2.1}$$

$$\rho\underline{U}(\underline{x}, t) = \int_{\mathbb{R}^3} \underline{c} f(\underline{x}, \underline{c}, t)d\underline{c} \tag{2.2}$$

With no external forces applied, collisions represent the only source of momentum transfer between particles. The function f is governed by the Boltzmann equation (i index $\in [1, 2, 3]$ for the 3 spatial components):

$$\frac{\partial f}{\partial t} + c_i \frac{\partial f}{\partial x_i} = \left(\frac{\partial f}{\partial t}\right)_{coll} \tag{2.3}$$

where the term $\left(\frac{\partial f}{\partial t}\right)_{coll}$ is the net total mass of particles whose velocity changes to $\underline{c}$ because of collisions.

The collisions are supposed to be elastic, so neither mass nor momentum is created. This leads to conservation laws which are presented in the following. The mass

conservation can be expressed as :

$$\int_{\mathbb{R}^3} \left(\frac{\partial f}{\partial t}\right)_{coll} d\underline{c} = 0 \tag{2.4}$$

Which yields (using Eq. 2.1 and Eq. 2.2) the continuity equation:

$$\frac{\partial \rho}{\partial t} + \frac{\partial \rho U_i}{\partial x_i} = 0 \tag{2.5}$$

The conservation of momentum can be written as:

$$\forall i \in [1,3], \int_{\mathbb{R}^3} c_i \left(\frac{\partial f}{\partial t}\right)_{coll} d\underline{c} = 0 \tag{2.6}$$

which can be recast as:

$$\frac{\partial \rho U_i}{\partial t} + \frac{\partial \left(\rho U_i U_j + P_{ij}\right)}{\partial x_j} = 0 \tag{2.7}$$

where $P_{ij} = \int_{\mathbb{R}^3} (c_i - U_i)(c_j - U_j) f d\underline{c}$

A classical modelling of the collision operator $\left(\frac{\partial f}{\partial t}\right)_{coll}$ is proposed by the approximation of Bhatnagar-Gross-Krook (Bhatnagar et al. (1954)), it is a restoring force pushing f back towards an equilibrium value f^{eq}, with a relaxation time τ corresponding to the average time between two successive collisions of a particle.

$$\left(\frac{\partial f}{\partial t}\right)_{coll} = -\frac{1}{\tau}(f - f^{eq}) \tag{2.8}$$

The equilibrium function is the Maxwell-Bolzmann distribution which is given by (T being the temperature and R the gas constant):

$$f^{eq} = \rho \left(\frac{1}{2\pi RT}\right)^{3/2} \times exp\left[\frac{-\left|\underline{c} - \underline{U}\right|^2}{2RT}\right] \tag{2.9}$$

The closure of the conservation equation 2.7, leading to the pressure and viscosity term, follows the Chapman-Enskog development (see for instance Dubois (2006)), whose sole aim is to introduce scales of time and velocity, and shape an analogy with physical scales of turbulence. The Knudsen number ε represents the mean length-scale of molecular fluctuations[1] non-dimensionalised by the characteristic length-scale

[1] also called *mean free path*

of the macroscopic flow. A Taylor series expansion of f as function of ε about the equilibrium function reads:

$$f = f^{eq} + \varepsilon f^{(1)} + \varepsilon^2 f^{(2)} + \dots \tag{2.10}$$

The 0^{th} order approximation in ε for f (*i.e.* $f = f^{eq}$) yields the following 0^{th} order model for the momentum flux $P_{ij}^{(0)} = \rho \frac{R}{M} T \delta_{ij}$, where M is the molar mass of the gas, which is the expression of the pressure as given by the law of ideal gas. Pressure thus derived can be seen as an isotropic stress due to the molecular fluctuations autocorrelation when the mean free path tends to 0.

Using a first order development in ε for f (i.e. $f = f^{eq} + \varepsilon f^{(1)}$) an expression for the first order approximation of P_{ij}, noted $P_{ij}^{(1)}$ can be derived (the flow is supposed to be incompressible, that is $\frac{\partial U_i}{\partial x_i} = 0$):

$$P_{ij}^{(1)} = P_{ij}^{(0)} - \tau_{ij} \qquad \text{with} \qquad \tau_{ij} = 2\mu S_{ij} \tag{2.11}$$

Where $S_{ij} = \frac{1}{2}\left(\frac{\partial u_i}{\partial x_j} + \frac{\partial u_j}{\partial x_i}\right)$ is the strain-rate tensor and $\mu = \tau \rho T$ is the dynamic viscosity. The viscous stresses appear when particles travel a non-zero average distance before colliding with another particle.

Denoting $P_{ij}^{(0)} = P\delta_{ij}$ one obtains the incompressible Navier Stokes equations:

$$\frac{\partial U_i}{\partial x_i} = 0 \tag{2.12}$$

$$\frac{\partial U_i}{\partial t} + U_j \frac{\partial U_i}{\partial x_j} = -\frac{1}{\rho}\frac{\partial P}{\partial x_i} + \frac{\partial}{\partial x_j} 2\nu S_{ij} \tag{2.13}$$

where $\nu = \frac{\mu}{\rho}$ is the cinematic viscosity.

2.2 Turbulence

Turbulence is directly linked to the non-linearities of the second term of equation 2.13. Osborne Reynolds was one of the first to attempt to understand how turbulence works and where it comes from, as well as how it interacts with the main flow (and efficiently increases the mixing). To this end, he devised the famous experiment of a

dye stream in a pipe flow. Depending on the nature of the fluid (*i.e.* its viscosity), its velocity and the dimension of the pipe, the streamlines can remain parallel to the axis of the pipe, and the dye forms a long streak whose lateral diameter remains nearly constant, in which case, the flow is laminar. Alternatively the streamlines can be brought together, mix and the flow becomes turbulent. The dye then starts to spread everywhere in the tube section. Reynolds established that the nature of the flow (whether it is turbulent or laminar) is characterised by a non-dimensional parameter, now known as the Reynolds number, $Re = \frac{VL}{\nu}$ where V and L are the characteristic velocity and length-scale of the flow respectively and ν is the kinematic viscosity. There is a critical Reynolds number value for which the transition between laminar and turbulence occurs that depends on the conditions of the experiment.

2.2.1 The scales of turbulence

An explanation to the origin and evolution of turbulence can be found in the Navier-Stokes Eq. 2.13: the non-linear convection term representing the interactions of the flow with itself gives rise to a complex evolution of instabilities, provided the Reynolds number is higher than the critical value. Although turbulence may appear chaotic and unpredictable, the study of the evolution of the physical properties, such as velocity and pressure, along time, shows that the quantities fluctuate around a mean value. Moreover, the analysis of a flow field shows that the velocities are correlated in time and space, over a bounded domain and a finite time. The turbulence can then be seen as a sum of structures of finite size and finite lifetime, which are also referred to as eddies. These eddies are not of same size. The size of the largest eddies are determined by the flow geometry. In a wall-bounded channel flow, the size of the biggest structure is of order $0.2L$ where L is the distance between the two walls. Certain rules were advanced almost a century ago in Richardson (1922) and later in Kolmogorov (1941) to describe certain aspects of the scales structure and interactions. The interactions between the turbulent scales of a given size yield smaller structures. Looking at the whole range of scales, this results in a transfer of kinetic energy from

the largest scales to the smallest ones (heat containing eddies). This process is known as the Kolmogorov cascade. While the largest scales are produced by the mean flow distortion, the smallest ones are dissipated and their energy is converted into heat. The dissipation rate of the smallest scales is denoted by ε.

The Kolmogorov hypothesis features a description of turbulence when the Reynolds number is sufficiently large.

- The smallest dissipative scales are only function of ε and ν and are therefore independent on the flow domain geometry. This goes along with another part of the Kolmogorov hypothesis, stating that these smallest scales are isotropic. Any stretching or squeezing of large-scale turbulence by mean flow distortion progressively disappears through the cascading process, as turbulence recovers a universal behaviour. The quantities ε and ν form the Kolmogorov length scale, $\eta = (\nu^3/\varepsilon)^{1/4}$ representing the smallest eddies.

- A range of eddies whose size is separated to largest and smallest scales by orders of magnitude have a universal behaviour only depending on ε. A dimensional analysis based on the two former hypothesis was used by Kolmogorov to derive one of fluid mechanics most verified principle: In this intermediate range, or inertial subrange, the turbulence energy spectrum $E(\kappa)$ can be expressed as $E(\kappa) = f(\varepsilon)\kappa^{-5/3}$. Where $E(\kappa)$ represents the function of distribution of energy over the different wave numbers κ (κ being defined as $\kappa = \frac{2\pi}{l}$ where l is the size of the scale).

2.2.2 The numerical representation of turbulence

Numerical simulation is increasingly used to study complex flows and predict its characteristics, as it becomes more and more affordable compared to experiments. However, due to the wide range of turbulent scales a flow may contain, the spatial and temporal discretisation has to be fine enough in order to capture all the structures. Otherwise, the turbulent information can be ill-predicted and the mean motion computed erroneously, as these two features strongly interact with each other. One

can decide not to simulate each and every scale of the flow, but to model some of them, and accurately reproduce their effects on the simulated flow. Depending on the level of detail desired, different methods have been devised, which will be presented now.

Direct Numerical Simulation (DNS)

This approach consists in solving all the scales contained in the flow, without any modelling. The equations are discretised directly and solved numerically, leading to a complete, assumption-free solution. The only difference remaining between the computed solution and the actual flow represented lays on the errors in the numerical scheme and the assumptions done in deriving the Navier Stokes equations (see Sec. 2.1), as well as uncertainties linked to the boundary conditions prescription. The strong need for numerical accuracy required by such methods leads to the use of higher order schemes, or spectral methods, which are difficult to adapt in complex geometries. Moreover the number of points required severely increases with the Reynolds number[2]. Therefore, this method is still seldom used, but its results on simple geometries, for low Reynolds numbers, constitute an invaluable source of information compared to those given by an experiment, and help develop new turbulence models.

Large Eddy Simulation (LES)

This approach relies on the modelling of the smallest scales, which are supposed to be isotropic, and the modelled turbulence is assumed to be at equilibrium (turbulence production and dissipation are in equilibrium). Hence, a simple model can be used for its representation. This level of resolution enables the use a coarser grid compared to the ones required by DNS. With this method, one can expect to capture turbulent structures whose size is bigger than twice the cell size. However, as not all the turbulence is solved, one has to find a model for the interactions of the unresolved

[2]The number of nodes required for the DNS of decaying isotropic turbulence was shown(Pope, 2008) to scale as $Re_\lambda^{9/2}$, λ being the integral length scale

scales with the resolved ones. By noting $\widetilde{\underline{U}}$ the computed velocity field and $\underline{U}$ the actual velocity field, one can assume there is a spatial filter $G(\underline{r},\underline{x})$ which enables to get $\widetilde{\underline{U}}$ from $\underline{U}$:

$$\widetilde{\underline{U}}(\underline{x},t) = \int_\Omega G(\underline{r},\underline{x})\underline{U}(\underline{x}-\underline{r},t)d\underline{r} \tag{2.14}$$

With $\int_\Omega G(\underline{r},\underline{x})d\underline{r} = 1$ (Ω being the computational domain). The residual velocity is then defined as : $\underline{u'}(\underline{x},t) = \underline{U}(\underline{x},t) - \widetilde{\underline{U}}(\underline{x},t)$. The Navier Stokes equations need to be reformulated, when applying the filter operator, to see where the residual velocity is going to appear, and to find a way to model it. In this formulation, shortcomings are present, mainly on the basis of two properties of the filter, which are not correct most of the time :

- the filter function is supposed to be homogeneous (*i.e.* independent of $\underline{x}$) which allows the filter and the spatial derivatives to commute.
- $\widetilde{\underline{u'}} = 0$, which is true only if the filter has a sharp cutoff in wave-number space[3].

The filtered Navier Stokes equations becomes:

$$\begin{aligned} \frac{\partial \widetilde{U_i}}{\partial x_i} &= 0 \\ \frac{\partial \widetilde{U_i}}{\partial t} + \widetilde{U_j}\frac{\partial \widetilde{U_i}}{\partial x_j} &= -\frac{1}{\rho}\frac{\partial \widetilde{P}}{\partial x_i} + \frac{\partial}{\partial x_j}\left(2\nu\widetilde{S_{ij}} - \widetilde{u_i'u_j'}\right) \end{aligned}$$

Using an analogy between the viscous effects and the effects of the sub-grid turbulence on the computed field, one can introduce a sub-grid-scale viscosity (Smagorinsky, 1963) and model the auto-correlation term as:

$$\widetilde{u_i'u_j'} = -2\nu_{SGS}\widetilde{S_{ij}} + \frac{2}{3}k_{SGS}\delta_{ij} \tag{2.15}$$

where the sub-grid scale viscosity is given by : $\nu_{SGS} = (C_s\Delta)^2\sqrt{2\widetilde{S_{ij}}\,\widetilde{S_{ij}}}$ (Δ being the filter width, typically twice the cubic root of the cell volume), and k_{SGS} is the sub-grid-scale energy. The constant C_s, the Smagorinsky constant, is taken equal to 0.065 in channel flows, and its value falls between 0.14 and 0.18 in decaying isotropic turbulence, depending on the model and the filter used (Sagaut, 2006).

[3]Alternatively one may use Germano's more rigorous generalised central moments framework (Germano, 1992), not detailed here as LES is not our main focus.

2.3 The Reynolds-Averaged Navier Stokes models

All RANS models aim at deriving information about the statistics of the flow considered. The computed velocity and pressure fields do not represent the actual flow at a mesoscopic scale, but rather an ensemble-average (a mean value) of this flow, that can be interpreted in different ways. One can consider the mean value $\overline{U}$, as the mean of the variable over time. $\overline{U}$ can then be defined as :

$$\overline{U}(\underline{x}) = \lim_{T\to\infty} \frac{1}{T} \int_0^T U(\underline{x}, t')dt' \tag{2.16}$$

The above definition of $\overline{U}$ is not applicable to transient flows (as $\overline{U}$ does not depend on the time anymore). If a time-dependent solution is to be expected another definition needs to be sought for $\overline{U}$. For instance, in the case of a periodic flow the operator can be seen as a phase-averaging:

$$\overline{U}(\underline{x}, t) = \lim_{N\to\infty} \frac{1}{N} \sum_{i=0}^{N} U(\underline{x}, t + i\tau) \tag{2.17}$$

Where τ is a characteristic period of the physical phenomenon. This is what yields an unsteady RANS (URANS).

The statistical mean operator $\bar{\cdot}$ applied to the Navier Stokes equations yields the RANS equations:

$$\frac{\partial \overline{U_i}}{\partial x_i} = 0 \tag{2.18}$$

$$\frac{\partial \overline{U_i}}{\partial t} + \overline{U_j}\frac{\partial \overline{U_i}}{\partial x_j} = -\frac{1}{\rho}\frac{\partial \overline{P}}{\partial x_i} + \frac{\partial}{\partial x_j}\left(2\nu\overline{S_{ij}} - \overline{u_i u_j}\right) \tag{2.19}$$

The variable considered in a RANS calculation is not turbulent at all. All of the turbulence is modelled. Therefore, the RANS operator, which is a statistic average, has nothing to do with an LES filter. As the Reynolds-stresses $\overline{u_i u_j}$ are supposed to model the action of all the turbulent structures on the mean flow, this quantity is much larger than the sub-grid scale stress. The time-averaged stresses are often anisotropic and the turbulent state is in non-equilibrium. Simple models (eddy-viscosity models (EVM)) use a relation similar to Eq. 2.15 to model $\overline{u_i u_j}$. The eddy viscosity (counterpart of the sub-grid scale viscosity) is denoted as ν_t and can be

calculated from analytical relations (mixing-length model), or as a combination of one or more solved turbulent quantities. On the other hand, Reynolds-stress models (RSM) stem from the derivation of exact transport equations of the Reynolds Stresses $\overline{u_i u_j}$ which are then resolved. The following gives an overview of RSM and EVM approaches.

2.3.1 Reynolds Stress models

Transport equations ruling the six independent[4] Reynolds stress components can be derived by taking the second order moments of the fluctuating velocity. They can be written:

$$\begin{aligned}\frac{D\overline{u_i u_j}}{Dt} = & \underbrace{-\left(\overline{u_i u_k}\frac{\partial \overline{U_j}}{\partial x_k} + \overline{u_j u_k}\frac{\partial \overline{U_i}}{\partial x_k}\right)}_{P_{ij}} \underbrace{- 2\nu\overline{\frac{\partial u_i}{\partial x_k}\frac{\partial u_j}{\partial x_k}}}_{\varepsilon_{ij}} \underbrace{-\frac{1}{\rho}\overline{u_i\frac{\partial p}{\partial x_j}} - \frac{1}{\rho}\overline{u_j\frac{\partial p}{\partial x_i}}}_{\phi^*_{ij}} \\ & \underbrace{-\frac{\partial \overline{u_i u_j u_k}}{\partial x_k}}_{D^T_{ij}} + \underbrace{\nu\frac{\partial^2 \overline{u_i u_j}}{\partial x_k^2}}_{D^\nu_{ij}}\end{aligned} \tag{2.20}$$

Where P_{ij}, ε_{ij}, ϕ^*_{ij}, D^T_{ij} and D^ν_{ij}, are, respectively, the production of stress, the dissipation rate, the pressure term, the turbulent transport and the molecular diffusion. The terms which are not in a closed form are ε_{ij}, D^T_{ij} and ϕ^*_{ij}.

Transport equations can be derived for the terms ε_{ij} and D^T_{ij} and involve more complex unclosed terms and higher-order moments. A transport equation for $\varepsilon = \frac{1}{2}\varepsilon_{ii}$, equation 2.21, was originally derived in Daly and Harlow (1970) (The terms

[4] due to the commutativity of the operator $\overline{\cdot \times \cdot}$ (*i.e.* $\forall i, j \quad \overline{u_j u_i} = \overline{u_i u_j}$)

notation introduced in Mansour et al. (1988) is adopted here).

$$\begin{aligned}\frac{D\varepsilon}{Dt} &= \underbrace{-2\nu\left(\overline{\frac{\partial u_i}{\partial x_l}\frac{\partial u_k}{\partial x_l}}+\overline{\frac{\partial u_l}{\partial x_i}\frac{\partial u_l}{\partial x_k}}\right)\frac{\partial \overline{U_i}}{\partial x_k}}_{P^1+P^2}\underbrace{-2\nu\overline{u_k\frac{\partial u_i}{\partial x_l}}\frac{\partial^2\overline{U_i}}{\partial x_k\partial x_l}}_{P^3}\\ &\underbrace{-2\nu\overline{\frac{\partial u_i}{\partial x_k}\frac{\partial u_i}{\partial x_l}\frac{\partial u_k}{\partial x_l}}}_{P^4}\underbrace{-2\overline{\left(\nu\frac{\partial^2 u_i}{\partial x_k\partial x_l}\right)^2}}_{Y}\\ &+\underbrace{\frac{\partial}{\partial x_k}\left(-\overline{u_k\varepsilon'}\right)}_{\mathcal{D}^t_\varepsilon}+\underbrace{\frac{\partial}{\partial x_k}\left(-\frac{2\nu}{\rho}\overline{\frac{\partial p}{\partial x_i}\frac{\partial u_k}{\partial x_i}}\right)}_{\mathcal{D}^p_\varepsilon}+\underbrace{\frac{\partial}{\partial x_k}\left(\nu\frac{\partial\varepsilon}{\partial x_k}\right)}_{\mathcal{D}^\nu_\varepsilon}\end{aligned}\tag{2.21}$$

Where the terms P_1+P_2, P_3, P_4, Y, $\mathcal{D}^p_\varepsilon$, $\mathcal{D}^T_\varepsilon$, $\mathcal{D}^\nu_\varepsilon$ are respectively named[5] the mixed production, the gradient production, the turbulent production, the viscous destruction, the pressure transport, the turbulent transport and the molecular diffusion.

The following now presents the modelling adopted for all unclosed terms of equation 2.20.

The pressure-velocity correlations:

The modelling is often based on a decomposition into two terms, one of them being trace-free. The most commonly adopted decomposition reads as follows (other splittings exist).

$$\phi^*_{ij}=\underbrace{-\frac{1}{\rho}\frac{\partial}{\partial x_k}(\overline{u_i p}\delta_{jk}+\overline{u_j p}\delta_{ik})}_{D^p_{ij}}\underbrace{+\frac{1}{\rho}\left[\overline{p\frac{\partial u_i}{\partial x_j}}+\overline{p\frac{\partial u_j}{\partial x_i}}\right]}_{\phi_{ij}}\tag{2.22}$$

The two different terms are often modelled separately as they are of different nature. D^p_{ij} is seen as a divergence, hence it does not create turbulent energy, but transports it between different regions. The term ϕ_{ij} is trace free, hence it is not seen in the evolution of the turbulent kinetic energy $\frac{1}{2}\overline{u_i u_i}$. It is a purely redistributive term, among the different normal components of the Reynolds-stress tensor. In a channel flow, this term represents the only source term of the wall normal and the

[5] we say "named" rather than "representing" because the separation between the different physical processes is far from obvious

span-wise fluctuations evolution, as there is no production. This term tends to spread the energy evenly amongst the components of the Reynolds stress tensor. Modellers are mainly focused on this term, which if often of the same order as the production, when looking at the budgets. The term D_{ij}^{p}, being only significant in the near-wall regions, is usually lumped into the turbulent transport term. In order to model the redistributive part of the pressure term, also referred to as pressure strain-rate correlation, the fluctuating pressure Poisson equation is invoked:

$$\nabla^2 p = -2\rho \frac{\partial \overline{U_i}}{\partial x_j}\frac{\partial u_j}{\partial x_i} - \rho \frac{\partial^2}{\partial x_i \partial x_j}\left(u_i u_j - \overline{u_i u_j}\right) \tag{2.23}$$

The general solution for the fluctuating pressure p can be cast into an integral form. Multiplying this solution by the gradient of the fluctuating velocity one obtains the integral form of the pressure strain-rate correlation:

$$\begin{aligned}
\rho\phi_{ij}(\underline{x}) \;=\; & -\int_{\Omega} \overline{\nabla^2 p(\underline{x}')\left(\frac{\partial u_i}{\partial x_j}(\underline{x}) + \frac{\partial u_j}{\partial x_i}(\underline{x})\right)} \frac{dV(\underline{x}')}{4\pi\|\underline{x}' - \underline{x}\|} \\
& - \int_{\partial\Omega} \overline{p(\underline{x}')\left(\frac{\partial u_i}{\partial x_j}(\underline{x}) + \frac{\partial u_j}{\partial x_i}(\underline{x})\right)} \frac{\partial}{\partial \underline{n}'}\left(\frac{1}{4\pi\|\underline{x}' - \underline{x}\|}\right) dS(\underline{x}') \\
& + \int_{\partial\Omega} \overline{\frac{\partial p}{\partial \underline{n}}(\underline{x}')\left(\frac{\partial u_i}{\partial x_j}(\underline{x}) + \frac{\partial u_j}{\partial x_i}(\underline{x})\right)} \frac{dS(\underline{x}')}{4\pi\|\underline{x}' - \underline{x}\|}
\end{aligned} \tag{2.24}$$

The surface term can be neglected far from solid walls, as $\|\underline{x}' - \underline{x}\|$ becomes large[6]. The volume term can be split into two parts, ϕ_{ij}^{s} and ϕ_{ij}^{r}, called, respectively, slow and rapid part:

$$\phi_{ij}^{s} = \int_{\Omega} \overline{\frac{\partial^2 (u_l u_m - \overline{u_l u_m})}{\partial x_l \partial x_m}(\underline{x}')\left(\frac{\partial u_i}{\partial x_j}(\underline{x}) + \frac{\partial u_j}{\partial x_i}(\underline{x})\right)} \frac{dV(\underline{x}')}{4\pi\|\underline{x}' - \underline{x}\|} \tag{2.25}$$

$$\phi_{ij}^{r} = \int_{\Omega} \frac{\partial U_l}{\partial x_m}(\underline{x}') \overline{\frac{\partial u_m}{\partial x_l}(\underline{x}')\left(\frac{\partial u_i}{\partial x_j}(\underline{x}) + \frac{\partial u_j}{\partial x_i}(\underline{x})\right)} \frac{dV(\underline{x}')}{2\pi\|\underline{x}' - \underline{x}\|} \tag{2.26}$$

The first term is purely turbulent and represents the interactions between the Reynolds components. It is referred to as "slow" term, as it only indirectly changes

[6]The first of the surface terms represents the wall-echo term which is significant at the vicinity of walls and is taken into account in near-wall models. The second term is linked to the Stokes pressure (Kim (1989)).

with a mean-flow shear or strain. The second term, involving the mean-velocity gradient is called rapid part, because it instantaneously reacts to a mean-flow distortion.

The slow part:

This can be modelled by considering an homogeneous field of anisotropic turbulence which is decaying in time. It is natural to suppose that the anisotropy of the field tends to disappear as it decays. On the basis of this notion, Rotta (1951) proposed the simple model:

$$\phi_{ij}^s = -C_1 \frac{1}{T}\left(\overline{u_i u_j} - \frac{2}{3}k\delta_{ij}\right) = -C_1 \varepsilon a_{ij} \tag{2.27}$$

Where $T = \dfrac{k}{\varepsilon}$ is the characteristic time scale of the turbulence, and $a_{ij} = \dfrac{\overline{u_i u_j}}{k} - \dfrac{2}{3}\delta_{ij}$ is the turbulence anisotropy tensor. This model states that the turbulence has a trend to return to an isotropic state with a constant rate. More complex models can be found, where the return to isotropy depends on the invariants of the anisotropy tensor. It has been shown that this slow term is stronger in case of high anisotropy. Its intensity is smaller for low values of $\|a_{ij}\|$. For instance, the model of Speziale et al. (1991) uses: $\phi_{ij}^s = -C_1\varepsilon a_{ij} + C_2\varepsilon(a_{ik}a_{kj} - \frac{1}{3}A_2\delta_{ij})$, where $A_2 = a_{ij}a_{ij}$ is the second invariant of the anisotropy tensor. The constants are $C_1 = 1.7 + 0.9P/\varepsilon$ and $C_1' = 1.05$ in this model.

The rapid part:

The main assumption which is made in modelling this term, is the homogeneity of the mean-velocity gradients across the space, which enables to consider the velocity gradient at point $\underline{x}$ instead of $\underline{x}'$ in 2.26: this is the hypothesis of quasi-homogeneity. In this way, the mean-velocity gradient is taken out of the integral, and only two-point correlations between fluctuating velocity gradients have to be modelled. The most frequently used models stem from the simple IP (Isotropisation of production) model (Naot et al., 1970), where the production tensor is driven back to an isotropic

state.

$$\phi_{ij}^r = -C_2 \left(P_{ij} - \frac{2}{3} P_k \delta_{ij} \right) \tag{2.28}$$

With the production term P_k is defined as $\frac{1}{2} P_{ii}$. In general, the models used are more complex, sometimes non-linear, and involve both the mean strain rate $S_{ij} = \frac{1}{2}(\partial U_i/\partial x_j + \partial U_j/\partial x_i)$ and the mean vorticity $\Omega_{ij} = \frac{1}{2}(\partial U_i/\partial x_j - \partial U_j/\partial x_i)$.

Models for ϕ_{ij}:

Models for the slow and rapid parts introduce the following relation: $\phi_{ij} = f(a_{ij}, S_{ij}, \Omega_{ij})$. A general expression can be derived, introducing terms of higher order. One of the most popular models, which retains only the linear terms for the rapid term, is the one of Speziale et al. (1991) (referred to as the SSG model):

$$\begin{aligned} \phi_{ij} \quad = \quad & -C_1 \varepsilon a_{ij} + C_2 \varepsilon (a_{ik} a_{kj} - \frac{1}{3} A_2) + C_3 k S_{ij} \\ & + C_4 k (a_{ik} S_{jk} + a_{jk} S_{ik} - \frac{2}{3} a_{mn} S_{mn} \delta_{ij}) \\ & + C_5 k (a_{ik} \Omega_{jk} + a_{jk} \Omega ik) \end{aligned} \tag{2.29}$$

The constants of the model are :

C_1	C_2	C_3	C_4	C_5
$1.7 + 0.9\frac{P_k}{\varepsilon}$	1.05	$0.8 - 0.625\sqrt{A_2}$	0.625	0.2

The SSG model for the rapid term is *quasi-linear*, as it introduces non-linearity via the term C_3 which depends on the second invariant of the anisotropy tensor. An earlier yet still popular[7] model is the LRR model of Launder et al. (1975). In this version the slow term is linear and the coefficient C_3 of the rapid term is constant.

The turbulent transport

The behaviour of the term D_{ij}^T was investigated, for instance in Hanjalic and Launder (1972), who derived transport equations for the 10 independent triple correlations. In

[7] It is still available in many CFD codes as a legacy model

practice, the model of Daly and Harlow (1970) is used to approximate the triple correlations. It is referred to as the Generalised Gradient Diffusion Hypothesis (GGDH).

$$D_{ij}^T = -\frac{\partial}{\partial x_k}\left(C_s \frac{k}{\varepsilon}\overline{u_k u_l}\frac{\partial \overline{u_i u_j}}{\partial x_l}\right) \tag{2.30}$$

Although this latter model is the most widely used, more advanced approaches were proposed. For instance, a Gallilean invariant alternative to Eq. 2.30 was proposed in Hanjalic and Launder (1972) whereas the model of Craft (1998) relies on implicit algebraic relations to obtain the triple correlations from their exact transport equations.

The dissipation tensor ε_{ij}:

Because of the complexity of the exact transport equations for ε_{ij} the following algebraic decomposition is used:

$$\varepsilon_{ij} = \frac{2}{3}\varepsilon\delta_{ij} + \underbrace{\left(\varepsilon_{ij} - \frac{2}{3}\varepsilon\delta_{ij}\right)}_{\varepsilon_D} \tag{2.31}$$

The first term is the isotropic dissipation rate, whereas ε_D represents the deviatoric contribution. Reynolds-stress models usually simply rely on an additional transport equation for the dissipation rate ε, whereas ε_D is generally lumped into the pressure strain-rate term model, on the basis that both terms have the same mathematical properties (Pope, 2008).

An empirical equation, proposed in Hanjalic and Launder (1972), is generally adopted (yet the analysis of Eq. 2.21 has guided the derivation of some RSM).

$$\frac{D\varepsilon}{Dt} = C_{\varepsilon 1}\frac{P_k\varepsilon}{k} - C_{\varepsilon 2}\frac{\varepsilon^2}{k} + \frac{\partial}{\partial x_k}\left(\nu + C_\varepsilon \frac{k}{\varepsilon}\overline{u_k u_l}\frac{\partial \varepsilon}{\partial x_l}\right) \tag{2.32}$$

The two first terms of the right hand side are proposed as a global model for the difference of the terms $P^4 - Y$ (see Eq. 2.21) and the last one represents the turbulent, molecular and pressure diffusion terms, whereas other terms of the exact ε equation (Eq. 2.21) only play a significant role in near-wall or low Reynolds number flows

(Hanjalic and Launder (1976)). Some more complex models (e.g. Hanjalic and Launder (1972), Hanjalic and Launder (1976), Jakirlic and Hanjalic (2002) and Mansour et al. (1988)) have attempted to follow a term-by-term modelling of Eq. 2.21.

The coefficients of this empirical equation are obtained by matching experimental results on simple cases. In a decaying isotropic turbulent flow (grid turbulence experiment of Comte-Bellot and Corrsin (1966)) the turbulent kinetic energy is observed to decay exponentially. Eq. 2.32 simply becomes:

$$\frac{d\varepsilon}{dt} = -C_{\varepsilon 2}\frac{\varepsilon^2}{k} \tag{2.33}$$

Therefore, the turbulent kinetic energy $k = 1/2\overline{u_i u_i}$ decays according to the following law: $k(t) = k_0(t - t_0)^{-n}$, where x is the distance downstream of the grid with $n = 1/(C_{\varepsilon 2} - 1)$. The decay rate is experimentally observed to be of order $n \sim 1.2$ which yields $C_{\varepsilon 2} = 1.8$. The coefficient $C_{\varepsilon 1}$ can be set for the model to match experimental results in the case of an ever growing turbulence generated by a constant shear. Whereas most models use the value of order $C_{\varepsilon 1} = 1.45$ recommended in Hanjalic and Launder (1972), some more advanced models have adopted a smaller value (*e.g.* $C_{\varepsilon 1} = 1.0$ in Craft (1998)). In some models the coefficients of the dissipation rate and the pressure strain-rate correlation are optimised together (e.g. Speziale et al. (1991)).

Justifications of focussing the modelling efforts on the isotropic part of ε_{ij} are only valid in regions where the largest and the smallest dissipative scales are well separated, that is when dissipation can be assumed to be isotropic [8]. When the Reynolds number is small or in near-wall regions alternative models for the decomposition Eq. 2.31 and for the model of ε_D are used, as it will be seen in the subsequent chapter. The modelled transport equation for ε also needs low-Reynolds and near-wall corrections.

[8] following Kolmogorov's hypothesis

2.3.2 Eddy viscosity models

The models presented in the previous section have the disadvantage of containing usually seven transport equations, six for the components of the Reynolds-stress tensor, and one for the dissipation rate. Apart from the added numerical cost of solving additional equations, numerical problems may arise in the resolution of the momentum equation (Eq. 2.19) as the term $-\frac{\partial}{\partial x_j}\overline{u_i u_j}$ is explicit.

A very appealing way to simplify this problem is the use of the analogy between the molecular random motion and the turbulence, leading to model the turbulent effects using a turbulent viscosity, noted ν_t, which enables to model the Reynolds stress tensor components with the Boussinesq formula:

$$\overline{u_i u_j} = -2\nu_t \overline{S_{ij}} + \frac{2}{3}k\delta_{ij} \tag{2.34}$$

A turbulent length-scale (noted L), velocity (V) or kinetic energy (K) can be combined to form the turbulent viscosity whose dimension is $m^2.s^{-1}$. Those quantities are either resolved by respective transport equations, given by algebraic relations or simply prescribed.

Zero-equation models The mixing-length hypothesis expresses the turbulent viscosity ν_t as the product of a velocity scale V and a prescribed mixing length l_m. In a shear layer, Prandtl (1925) proposed the velocity scale to take the form $V = l_m \left|\frac{d\overline{U}}{dy}\right|$ (where $\overline{U}$ and y are respectively the mean wall-parallel velocity component and the wall normal coordinate) hence the turbulent time-scale entering the definition of ν_t is taken equal to the inverse of the mean shear magnitude $\frac{d\overline{U}}{dy}$. To close the model only a turbulent length-scale is required which is a characteristic quantity depending on the flow considered. In the outer part of a boundary layer it is simply proportional to the boundary layer thickness, whereas closer to walls turbulent structures become smaller, as it will be seen, and the mixing-length needs to be reduced.

One of the shortcomings of this model is that existence of turbulence is linked to the simultaneous presence of its generator (*i.e.* mean velocity gradients).

One-equation models The one-equation model of Prandtl (1945) proposes to resolve an equation for the turbulent kinetic energy k in order to obtain the turbulent velocity scale $V = \sqrt{k}$ used in the mixing length model. Other more recent one-equation models have been proposed for specific industrial applications, such as the model of Spalart and Allmaras (1994). The latter is based on the derivation of a transport equation for the turbulent viscosity.

Two-equation models In order to produce more accurate predictions of the quantities involved in the turbulent viscosity without increasing too much the complexity and the number of equations, two transport equations are generally used, and derived models are the most widely employed in industrial CFD codes. The turbulent viscosity can be written as the combination of a turbulent velocity scale V and a turbulent length scale L. Similarly to the one-equation model described previously the turbulent velocity scale is related to the resolved variable $\sqrt{k}$.

The transport equation for the turbulent kinetic energy, which is defined as $k = \frac{1}{2}\overline{u_i u_i}$ can be found by taking the trace of the Eq. 2.20:

$$\frac{Dk}{Dt} = P_k + \phi^* - \varepsilon - \frac{1}{2}\frac{\partial \overline{u_j u_i u_i}}{\partial x_j} + \nu \frac{\partial^2 k}{\partial x_k^2} \tag{2.35}$$

where $P_k = \frac{1}{2}P_{ii}$ is the production of turbulent energy. It is closed using the Boussinesq formula: $P_k = 2\nu_t S_{ij} S_{ij}$. The sink term $\varepsilon = \frac{1}{2}\varepsilon_{ii}$ is the dissipation rate. The term $\phi^* = \frac{1}{\rho}\frac{\partial \overline{u_j p}}{\partial x_j}$ is the pressure diffusion. The pressure and diffusion terms are modelled together using a simple gradient diffusion hypothesis (SGDH):

$$\frac{1}{\rho}\frac{\partial \overline{u_j p}}{\partial x_j} - \frac{1}{2}\frac{\partial \overline{u_j u_i u_i}}{\partial x_j} = \frac{\partial}{\partial x_j}\left(\frac{\nu_t}{\sigma_k}\frac{\partial k}{\partial x_j}\right) \tag{2.36}$$

Where σ_k is the Prandtl number associated to the quantity k. In nearly all models $\sigma_k = 1$.

The second resolved variable is the means of determining the turbulent length scale required in the model for ν_t and enables to model the dissipation-rate term appearing in Eq. 2.35. One of the most popular two-equation models is the $k - \varepsilon$ model proposed by Jones and Launder (1972), and this resolves the following second

equation for ε (which is very similar to the one proposed by Hanjalic and Launder (1972) for a Reynolds Stress model):

$$\frac{D\varepsilon}{Dt} = C_{\varepsilon 1}\frac{P_k\varepsilon}{k} - C_{\varepsilon 2}\frac{\varepsilon^2}{k} + \frac{\partial}{\partial x_j}\left[\left(\nu + \frac{\nu_t}{\sigma_\varepsilon}\right)\frac{\partial \varepsilon}{\partial x_j}\right] \tag{2.37}$$

The two quantities are combined to form the turbulent viscosity:

$$\nu_t = C_\mu \frac{k^2}{\varepsilon} \tag{2.38}$$

The quantities σ_ε and C_μ are tuned to return the expected behaviour in the logarithmic layer of a channel flow (*i.e.* the value of the Von K'arm'an constant κ and the ratio $\overline{uv}/k$), whereas the coefficient $C_{\varepsilon 1}$ is calibrated to predict the correct turbulence growth rate in homogeneous shear flow. As in Hanjalic and Launder (1972), $C_{\varepsilon 2}$ is adjusted to return the correct isotropic turbulence decay.

Alternatively, following the approach of Kolmogorov (1941) the $k-\omega$ model of Wilcox (2006) solves for a second variable for the dissipation per unit turbulent kinetic energy using an empirical equation similar to Eq. 2.37.

$$\frac{D\omega}{Dt} = \alpha\frac{\omega}{k}P_k - \beta\omega^2 + \frac{\partial}{\partial x_j}\left[\left(\nu + \frac{\nu_t}{\sigma_\omega}\right)\frac{\partial \omega}{\partial x_j}\right] \tag{2.39}$$

where α and β are model constants. To close the k equation, the dissipation rate is related to ω as follows:

$$\varepsilon = C_\mu k\omega \tag{2.40}$$

Another popular modelling strategy is the $k-\omega$ SST model of Menter (1994). It consists in a blending between the $k-\varepsilon$ and the $k-\omega$ approaches with an additional modification of the turbulent viscosity to recover the proportionality link between the turbulent shear stress $\overline{uv}$ and the turbulent kinetic energy k in a boundary layer (Bradshaw's hypothesis). Equations and constants of this model are given in App. B.

2.3.3 Other RANS approaches

Non-linear eddy viscosity models: These formulations propose to improve the Boussinesq relation Eq. 2.34 by adding a non-linear dependance on the strain and

vorticity rates S_{ij} and Ω_{ij}. Some examples of these models are the quadratic models of Gatski and Speziale (1993) or Abe et al. (2003) or the cubic models of Craft et al. (1996), Apsley and Leschziner (1998) or Lien et al. (1996).

Algebraic Reynolds stress model: They are based upon simplifications of the Reynolds-stress-transport equations yielding algebraic relations linking the different Reynolds stresses to each other. Some of them further simplify to explicit expressions for the different stresses as functions only of turbulent scales and mean flow quantities. The later models, which can be cast into the form of non-linear eddy-viscosity models, are called Explicit Algebraic Reynolds-stress models. An example of such approach is the model of Wallin and Johansson (2000). It is noteworthy that the models of Gatski and Speziale (1993) or Apsley and Leschziner (1998), previously mentioned, were also derived from simplifications to Reynolds stress modelling.

Stress strain misalignement modelling: A feature that the two previous classes of models miss, however complex they may be, is an ability to reproduce the history effects of turbulence. To this end, the model of Revell et al. (2006) proposes to solve for a coefficient C_{as} defined as:

$$C_{as} = -\frac{a_{ij}S_{ij}}{||\underline{S}||} \tag{2.41}$$

besides the turbulent kinetic energy and the scale determining variable (ε or ω). This coefficient represents the cosine of the angle between the two matrices a_{ij} and S_{ij}, erroneously supposed to be aligned in a linear EVM framework. The turbulent kinetic energy production appearing in the turbulent equations is then rewritten:

$$P_k = C_{as}k||\underline{S}|| \tag{2.42}$$

Unsteady RANS Referred to as URANS, this method consists in using a RANS model to predict unsteady flows. This approach proves to be promising if the mean flow and turbulent scales are well separated, typically in the wake of a bluff body (vortex shedding).

2.4 RANS/LES coupling

With the usual assumptions, LES approach requires that modelled turbulence should be isotropic, which means that the computational grid should be able to capture all the anisotropic content. However near the wall the turbulence is anisotropic almost down to the viscous scale. Therefore, LES should be used on very fine grids in this region. The size of a grid suitable for LES in a wall-bounded flow scales as $\approx Re^{1.8}$ as shown in Chapman (1979). A cheaper strategy is to employ the RANS approach at walls, coupled with LES further away. A review of such hybrid methods is given in Fröhlich and von Terzi (2008). Some examples of this approach are the two-velocity method of Uribe et al. (2010), the Partially Integrated Turbulence Model of Chaouat and Schiestel (2009), the seamless approach of Fadai-Ghotbi et al. (2010) or the Detached Eddy Simulation (see Spalart (2009)).

Chapter 3

Near-wall turbulence and its modelling

This chapter gives a description of the characteristics of turbulent wall-bounded flows, in the general case first, then in the academic channel flow case. For the latter case, DNS data are analysed to highlight the different mechanisms of turbulence production, dissipation and transport and to assess the universality of the variables behaviour. As it will be seen, the models introduced in the previous section, calibrated for homogeneous flows, need substantial adaptations in order to be used near walls. The conclusions of this analysis are used in the next chapters, where new developments are proposed.

3.1 The effects of walls on turbulence

3.1.1 Influence of walls on instantaneous field

At the wall the flow adheres to the surface and progressively recovers its free-stream velocity further outwards. The strong inhomogeneities are the origin of a wide spectrum of turbulent instabilities, which can only be imperfectly described by the statistical approach of RANS modelling. The mechanisms of generation of instabilities, followed by the production of turbulence, in a near wall flow are different from those

due to the presence of mean velocity inflexion points in a simple shear layer. The turbulent transition of a boundary layer (whether by a "bypass" mechanism if the outer flow is already turbulent, or "natural" otherwise) and the sustenance of turbulence by a continuous production and transport outwards, has been the object of many experimental and numerical investigations. They provided evidences for a wide variety of vortical structures responsible for strong inhomogeneities and exchange mechanisms. Amongst these studies there is a consensus regarding the shape and location of the different structures, but not on their role, nor on the mechanisms they are involved in, although it is observed that quasi-cyclic events occur (referred to as "bursting"). Experimental techniques include dye or hydrogen bubbles injection (e.g. Kline et al. (1967); Kim et al. (1971)), hot-wire measurement or visualisation using colloidal size particles (Corino and Brodkey, 1969), but it is generally very difficult to experimentally monitor the near-wall flow[1]. Conditional sampling methods can be used to study the outwards transport of low-speed flow (called "ejection") and inwards transport of high-speed flow ("sweep"): these two processes correspond to the events $\{u < 0 \text{ and } v > 0\}$ and $\{u > 0 \text{ and } v < 0\}$ respectively, where u and v represent the stream-wise and wall-normal fluctuating velocity, respectively. The observation and the interpretation of these mechanisms may help to improve turbulent models and ascertain the postulated existence of a unique and universal behaviour of near-wall flows, but averaged data remain the main source of information for modellers.

3.1.2 Influence of walls on RANS statistical quantities

As far as RANS statistical quantities are concerned, the presence of a wall has several implications:

- Because of the molecular viscosity of the fluid, the wall induces viscous friction on the flow, characterised by the non slip condition at the wall (the velocity component parallel to the wall $U_{\parallel}$ is zero). This yields strong wall-normal

[1] In fact, the near-wall sublayer can be of the same size if not larger than the probe or injection device. Indeed $y^+ = 5$ corresponds to $y = 0.125\ mm$ for a pipe flow at $Re = 50000$ (Corino and Brodkey (1969)).

gradients of the wall-parallel mean velocity resulting in the production of high levels of turbulence, which is transported further away from walls.

- The turbulence itself is strongly affected by walls. The dynamic effects of viscous friction not only reduce the mean velocity but also impairs the turbulent intensity, as evidenced in the case of a flow along a wall moving at the same speed as the mean flow (*e.g.* the shear-free near-wall flow was experimentally studied in Aronson et al. (1997)).

- The impermeability condition (the velocity component perpendicular to the wall $U_\perp$ is zero), propagating through incompressibility in the wall neighbourhood (kinematic "non-local" effect, also known as wall-blocking effect), increases the turbulence anisotropy: as will be seen, the combined no-slip and impermeability conditions applied to turbulence results in the wall-normal fluctuations being reduced by two orders of magnitude above that of the stream-wise and span-wise components. Therefore, both the turbulent structure shape and size are noticeably altered, and these modifications need to be accounted for in models (the earliest near-wall corrections were proposed in Prandtl (1925) and van Driest (1956) who suggested to relate the mixing length to the wall distance).

- As direct consequence of the wall-induced turbulence-intensity reduction, the integral characteristics of turbulence become progressively closer to viscous scales as walls are approached. These low-Reynolds-number effects are characterised by $Re_t = \dfrac{k^2}{\varepsilon\nu} \to 0$. Large and small scales are no longer clearly distinct, and the dissipation-rate tensor becomes anisotropic.

- The integral solution of the Poisson equation for the fluctuating pressure, Eq. 2.24, contains two surface terms. If the boundary condition $\partial p/\partial y = 0$ is applied as first approximation [2], one can drop the last term. The surface term left can be turned into a volume integral, and combined with the first term. The pressure strain-rate correlation becomes :

[2] it will be seen that $\partial p/\partial y = \nu \partial^2 v/\partial y^2$

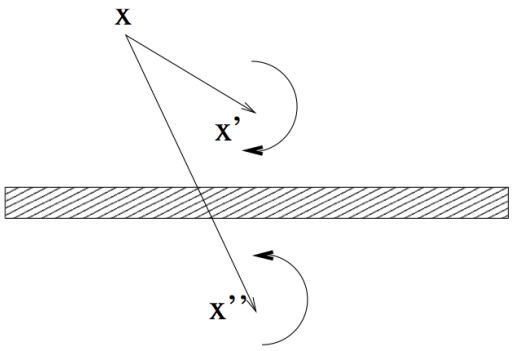

Figure 3.1: Illustration of the "wall-reflection" effect

$$\rho\phi_{ij}(\underline{x}) = -\int_{\Omega} \overline{\nabla^2 p(\underline{x}') \left(\frac{\partial u_i}{\partial x_j}(\underline{x}) + \frac{\partial u_j}{\partial x_i}(\underline{x}) \right)} \left(\frac{1}{4\pi \|\underline{x}' - \underline{x}\|} + \frac{1}{4\pi \|\underline{x}'_* - \underline{x}\|} \right) dV(\underline{x}') \tag{3.1}$$

Where $\underline{x}'_*$ is the mirror point of $\underline{x}'$ through the wall, as represented in Fig.3.1.2. This wall echo term, also called "wall-reflexion" term represents a contribution similar to that from point $\underline{x}'$ but from the mirror point $\underline{x}'_*$ and it actually increases the redistribution term, as pointed out in Manceau (1999).

The representation of wall turbulence damping, anisotropy enhancement and low-Reynolds number effects constitutes a real challenge for wall-bounded flow predictions and classical modelling often needs considerable modifications.

The following presents a description of a turbulent flow in a simple wall-bounded geometry, from which will emerge some guidelines for near-wall RANS models developments.

3.2 The channel flow

Due to the viscous nature of the wall friction, the fluid's molecular viscosity is a parameter involved in a wall-bounded flow. The viscous length scale δ_ν (ratio of the viscosity and a turbulent velocity scale noted u_τ (or friction velocity) constructed from the wall viscous shear stress) as well as the boundary-layer thickness, δ, are

two length-scales upon which a wall bounded flow motion depends. Some general conclusions about boundary-layer flows can be derived by considering the asymptotic state, for which the friction Reynolds number $Re_\tau = \dfrac{\delta}{\delta_\nu} \to \infty$. Then, asymptotic results and their validity for a finite Reynolds number can be studied in a channel flow or a boundary layer (using experimental or DNS data). We focus here on the channel-flow case.

3.2.1 Presentation of the case and flow equations

The analysis done in Tennekes and Lumley (1999) and Pope (2008) in an extensively detailed manner are summarised in what follows.

The study considers a flow between two infinite parallel surfaces separated by a distance 2δ, driven by a constant pressure gradient which exactly balances the wall friction, so that the flow is neither accelerated nor decelerated. The stream-wise, wall-normal and span-wise axis are respectively x, y and z. The mean velocity along the direction y and z is zero, and the mean quantities are constant along the z and x axis (except for the pressure). The mean pressure P and stream-wise velocity U, as well as the turbulent shear stress $\overline{uv}$ and wall normal stress $\overline{v^2}$ are related to each other by the momentum equation on the axes x and y:

$$0 = -\frac{1}{\rho}\frac{\partial \overline{P}}{\partial x} - \frac{d\overline{uv}}{\partial y} + \nu \frac{d^2\overline{U}}{dy^2} \tag{3.2}$$

$$0 = -\frac{1}{\rho}\frac{\partial \overline{P}}{\partial y} - \frac{d\overline{v^2}}{dy} \tag{3.3}$$

From Eq. 3.3, we deduce: $\dfrac{\partial^2 \overline{P}}{\partial y \partial x} = \dfrac{\partial^2 \overline{P}}{\partial x \partial y} = \dfrac{\partial^2 \rho\overline{v^2}}{\partial x \partial y} = 0$ since $\overline{v^2}$ is independent on x. Therefore, the pressure gradient $d\overline{P}/dx$ is independent of y, and is then a constant. The total stress $\tau_T = \mu \dfrac{d\overline{U}}{dy} - \rho\overline{uv}$ is then a linear function of y. At the wall it reduces to the viscous wall stress $\rho\nu \dfrac{d\overline{U}}{dy}$. The friction velocity, $u_\tau = \sqrt{\nu \dfrac{d\overline{U}}{dy}(0)}$ is used as velocity scale. At $y = \delta$, the flow symmetry imposes $\tau_T = 0$. This finally

leads to:

$$\nu\frac{dU}{dy} - \overline{uv} = u_\tau^2\left(1 - \frac{y}{\delta}\right) \tag{3.4}$$

3.2.2 The different regions of a channel flow

Two non-dimensional equations can be derived:

- Using the velocity scale u_τ and the inner space scale $\delta_\nu = \nu/u_\tau$:

$$\frac{d\overline{U}^+}{dy^+} - \overline{uv}^+ = 1 - \frac{y^+}{Re_\tau} \tag{3.5}$$

  where $y^+ = y/\delta_\nu$, $\overline{U}^+ = \overline{U}/u_\tau$ and $\overline{uv}^+ = \overline{uv}/u_\tau^2$

- Using the velocity scale u_τ and the outer space scale δ

$$\frac{1}{Re_\tau}\frac{d\overline{U}^+}{d\eta} - \overline{uv}^+ = 1 - \eta \tag{3.6}$$

  where $\eta = y/\delta$

The near-wall asymptotic state can be derived using the momentum equation expressed in viscous units (it will be shown later that $\overline{uv}^+ = O(y^{+3})$ at the wall):

$$\overline{U}^+ = y^+ - \frac{1}{2}\frac{y^{+2}}{Re_\tau} + O(y^{+4}) \tag{3.7}$$

The viscous sublayer is defined as the wall region where $\overline{U}^+ \sim y^+$ ($y^+ < 8$). The Reynolds number is involved in the near-wall asymptotic expansion Eq. 3.5 only from the second order term.

In order to study the behaviour of equations Eq. 3.5 and Eq. 3.6 further away from the wall, the mixing length theory (Prandtl (1925)) is used to express the turbulent shear stress: $\overline{uv} = -L_m^2\left|\frac{d\overline{U}}{dy}\right|\frac{d\overline{U}}{dy}$. This introduces the mixing length scale L_m. The two equations are respectively rewritten using L_m (where $L_m^+ = L_m/\delta_\nu$):

$$\left(1 + (L_m^+)^2\left|\frac{d\overline{U}^+}{dy^+}\right|\right)\frac{d\overline{U}^+}{dy^+} = 1 - \frac{y^+}{Re_\tau} \tag{3.8}$$

$$\left(\nu + (L_m)^2\left|\frac{d\overline{U}^+}{dy}\right|\right)\frac{d\overline{U}^+}{dy} = 1 - \frac{y}{\delta} \tag{3.9}$$

In the inertial subrange, when $Re_\tau \to \infty$, the flow does not depend either on δ_ν or δ. von Karman (1931) was one of the first to derive theoretical results concerning the mean velocity profile in the inertial layer proposing the following linear relation: $L_m = \kappa y$. In this region, Eq. 3.8 simplifies because $y \gg \delta_\nu$ (*i.e.* $L_m^+ \gg 1$) and $y \ll \delta$. This leads to the well known logarithmic profile:

$$\overline{U}^+ = \frac{1}{\kappa} ln y^+ + C \tag{3.10}$$

The logarithmic behaviour of the near-wall velocity is also present at finite Reynolds numbers, as observed in experimental and computational data. They give an estimate of the values of the constants $\kappa = 0.41$ and $C = 5.2$, even though those are dependent on Re_τ, especially C. This is due to interactions between very large structures and the wall. Moreover, the region between the logarithmic and the viscous sublayer is called the buffer layer.

In the outer part of the flow (for $y > 0.2\delta$) the mixing length becomes constant, $L_m = 0.2\kappa$. In this region (with again viscous shear negligible), Eq. 3.9 is used to obtain an expression for the difference between the velocity and its maximum value at the centre line (velocity defect, hence the name "defect" layer):

$$\frac{\overline{U} - U_{max}}{u_\tau} = \frac{2}{0.6\kappa} \left(1 - \frac{y}{\delta}\right)^{3/2} \tag{3.11}$$

Matching Eq. 3.10 and Eq. 3.11 at point $y = 0.2\delta$ enables to recover the value U_{max}.

The different zones in a channel flow can be well represented by plotting the variable $y^+ \dfrac{d\overline{U}^+}{dy^+}$, whose extrema can be visually associated to the bounds of these regions, as seen on Fig. 3.2. Similarly, they can be visually matched to the inflexion points of the velocity profile (when a logarithmic scale is used for the y^+ axis)[3].

3.2.3 Asymptotic behaviour of the turbulent variables

It has been seen previously that, very close to the wall, the mean-velocity profile is linear in the wall-normal direction, and this asymptotic behaviour holds over a large

[3]The plot of the function $f(x)$ with a logarithmic scale for the x axis is the plot of a function f_l such that $f_l(ln(x)) = f(x)$. Therefore $f_l''(ln(x)) = x(xf'(x))'$.

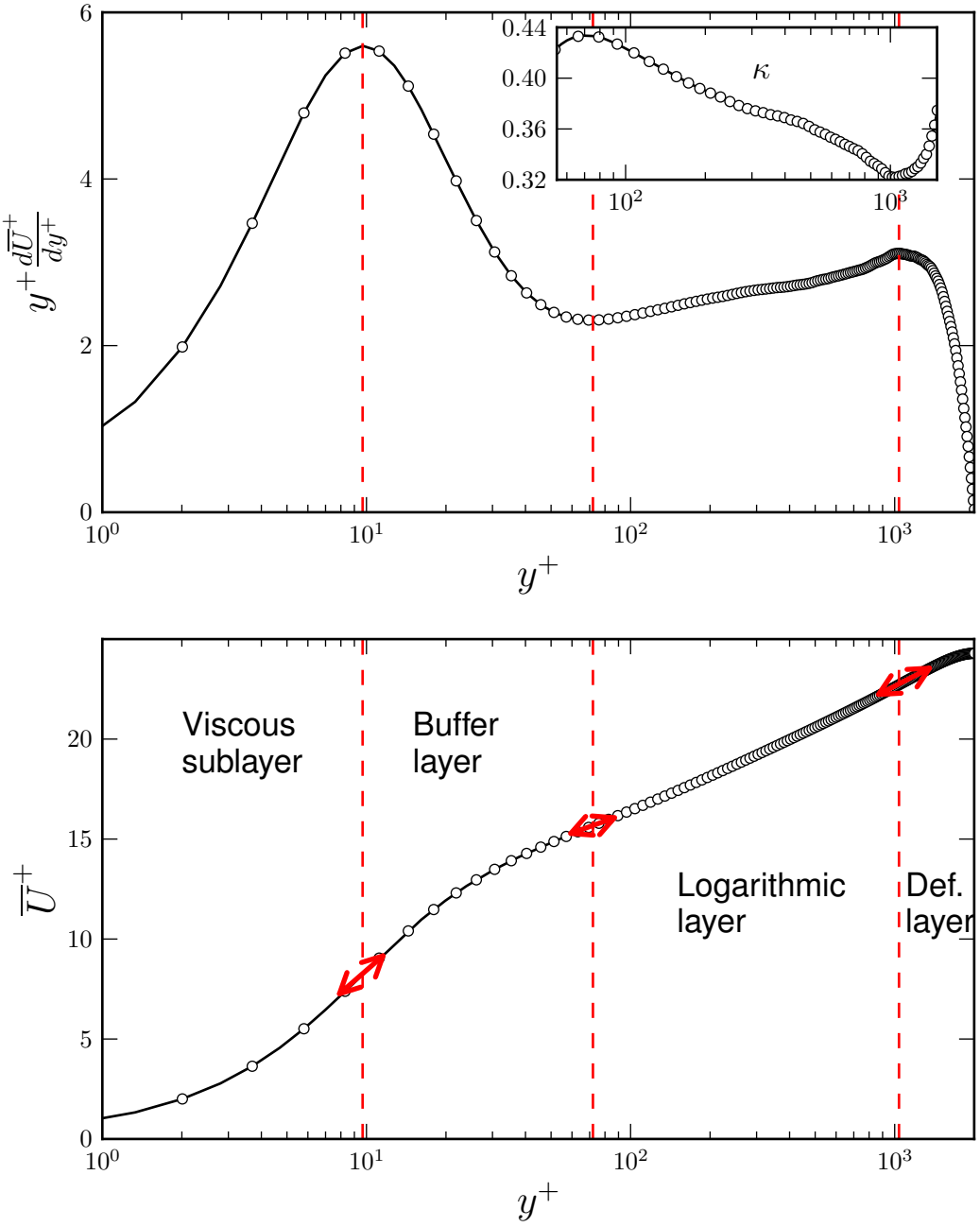

Figure 3.2: Profiles of $y^+\dfrac{d\overline{U^+}}{dy^+}$ and $\overline{U^+}$, represented in the case of a channel flow, for $Re_\tau = 2000$ (DNS data of Hoyas and Jiménez (2008))

part of the viscous sublayer. More generally the study of Taylor-series expansions of turbulent quantities provides insight into the relative near-wall importance of each Reynolds stress and the source terms of their respective transport equations.

The mean velocity $\overline{U}$, the fluctuating velocity components u, v and w as well as the fluctuating pressure p expend as follows:

$$\begin{cases} \overline{U} = \sum_{i=0}^{\infty} \mathcal{A}_i y^i \\ u = \sum_{i=0}^{\infty} a_i y^i \\ v = \sum_{i=0}^{\infty} b_i y^i \\ w = \sum_{i=0}^{\infty} c_i y^i \\ p = \sum_{i=0}^{\infty} p_i y^i \end{cases} \tag{3.12}$$

The $\mathcal{A}_i$'s are constant but the a_i's, b_i's, c_i's and p_i's are random variables which depend upon x, z and t. The wall impermeability leads to $\lim_{y\to 0} v = 0$ hence $b_0 = 0$. Moreover the no-slip condition imposes $\lim_{y\to 0} \overline{U} = \lim_{y\to 0} u = \lim_{y\to 0} w = 0$, hence $\mathcal{A}_0 = a_0 = c_0 = 0$. More relations between coefficients are derived from the continuity and Navier Stokes equations.

- The divergence of the turbulent velocity field expends as $\dfrac{\partial u}{\partial x} + \dfrac{\partial v}{\partial y} + \dfrac{\partial w}{\partial z} = b_1 + \left(\dfrac{\partial a_1}{\partial x} + \dfrac{\partial c_1}{\partial z} + 2b_2 \right) y + O(y^2)$. The continuity equation requires the latter relation to be 0, hence $b_1 = 0$, $\dfrac{\partial a_1}{\partial x} + \dfrac{\partial c_1}{\partial z} + 2b_2 = 0$, ...

- At the wall, the momentum equations for the fluctuating velocity in a channel flow reduces to $\dfrac{\partial p}{\partial x_i} = \mu \dfrac{\partial^2 u_i}{\partial x_j \partial x_j}$. This leads to $\dfrac{\partial p_0}{\partial x} = 2\mu a_2$, $p_1 = 2\mu b_2$ and $\dfrac{\partial p_0}{\partial z} = 2\mu c_2$.

The resulting near-wall asymptotic behaviour of the mean velocity and the turbulent variables is:

$$\begin{cases} \overline{U} = \mathcal{A}_1 y + O(y^2) \\ u = a_1 y + O(y^2) \\ v = b_2 y^2 + O(y^3) \\ w = c_1 y + O(y^2) \\ \frac{\partial p}{\partial x} = 2\mu a_2 + O(y) \\ \frac{\partial p}{\partial y} = 2\mu b_2 + O(y) \\ \frac{\partial p}{\partial z} = 2\mu c_2 + O(y) \end{cases} \tag{3.13}$$

One of the most important results of this analysis is that the wall-normal fluctuation $\overline{v^2}$ is two orders of magnitude smaller than the stream-wise and span-wise components $\overline{u^2}$ and $\overline{w^2}$. This two-component limit of turbulence is characterised by a strong anisotropy which should be reproduced in second-moment closure. Fig. 3.3 presents the Reynolds-stress components (DNS data of Moser et al. (1999) at $Re_\tau = 590$) as well as the first-order term in their Taylor series expansion. The turbulent kinetic energy and its dissipation rate are also represented. As seen, the first-order approximation seems to be a reasonable estimate for the quantities $\overline{u^2}$, $-\overline{uv}$ and k in the major part of the viscous sublayer. For $\overline{v^2}$ and ε noticeable departure starts at $y^+ = 1 - 2$.

These relations are also used to find the near-wall leading order term of the source terms of the Reynolds stresses and turbulent kinetic energy transport equations (Eq. 2.20 and Eq. 2.35 respectively). They are summarised in Tab. 3.1 and 3.2 and provide useful information for the near-wall RANS modelling requirement. For instance, in the k transport equation, the linear term D_k^p is lumped into the turbulent transport model and the model for the dissipation should balance the molecular diffusion (Eq. 3.14).

$$\lim_{y\to 0} \varepsilon = \lim_{y\to 0} \nu \frac{\partial^2 k}{\partial y^2} \tag{3.14}$$

	$(1,1)$	$(2,2)$	$(3,3)$	$(1,2)$
$\overline{u_i u_j}$	$\overline{a_1^2}y^2$	$\overline{b_2^2}y^4$	$\overline{c_1^2}y^2$	$\overline{a_1 b_2}y^3$
P_{ij}	$-2\mathcal{A}_1\overline{a_1 b_2}y^3$	0	0	$-\mathcal{A}_1\overline{b_2^2}y^4$
$-\varepsilon_{ij}$	$-2\nu\overline{a_1^2} - 8\nu\overline{a_1 a_2}y$	$-8\nu\overline{b_2^2}y^2$	$-2\nu\overline{c_1^2} - 8\nu\overline{c_1 c_2}y$	$-4\nu\overline{a_1 b_2}y$
ϕ^*_{ij}	$-4\nu\overline{a_1 a_2}y$	$-4\nu\overline{b_2^2}y^2$	$-4\nu\overline{c_1 c_2}y$	$-2\nu\overline{a_1 b_2}y$
ϕ_{ij}	$\frac{2}{\rho}\overline{p_0\frac{\partial a_1}{\partial x}}y$	$4\frac{1}{\rho}\overline{p_0 b_2}y$	$\frac{2}{\rho}\overline{p_0\frac{\partial c_1}{\partial z}}y$	$\frac{1}{\rho}\overline{p_0 a_1}$
D^p_{ij}	$-4\nu\overline{a_1 a_2}y - \frac{2}{\rho}\overline{p_0\frac{\partial a_1}{\partial x}}y$	$-4\frac{1}{\rho}\overline{p_0 b_2}y$	$-4\nu\overline{c_1 c_2}y - \frac{2}{\rho}\overline{p_0\frac{\partial c_1}{\partial z}}y$	$-\frac{1}{\rho}\overline{p_0 a_1}$
D^t_{ij}	$-4\overline{a_1^2 b_2}y^3$	$-6\overline{b_2^3}y^5$	$-4\overline{b_2 c_1^2}y^3$	$-5\overline{a_1 b_2^2}y^4$
D^ν_{ij}	$2\nu\overline{a_1^2} + 12\nu\overline{a_1 a_2}y$	$12\nu\overline{b_2^2}y^2$	$2\nu\overline{c_1^2} + 12\nu\overline{c_1 c_2}y$	$6\nu\overline{a_1 b_2}y$

Table 3.1: Near wall asymptotic behaviour of the Reynolds Stresses and of the terms of their transport equation

k	$\frac{1}{2}(\overline{a_1^2} + \overline{c_1^2})y^2$
P_k	$-\mathcal{A}_1\overline{a_1 b_2}y^3$
ε	$-\nu(\overline{a_1^2} + \overline{c_1^2})$
ϕ^*_k	$-2\nu(\overline{a_1 a_2} + \overline{c_1 c_2})y$
ϕ_k	0
D^p_k	$-2\nu(\overline{a_1 a_2} + \overline{c_1 c_2})y$
D^t_k	$-2\overline{b_2\,(a_1^2 + c_1^2)}y^3$
D^ν_k	$\nu\left(\overline{a_1^2} + \overline{c_1^2}\right)$

Table 3.2: Near wall asymptotic behaviour of k and of the terms of its transport equation

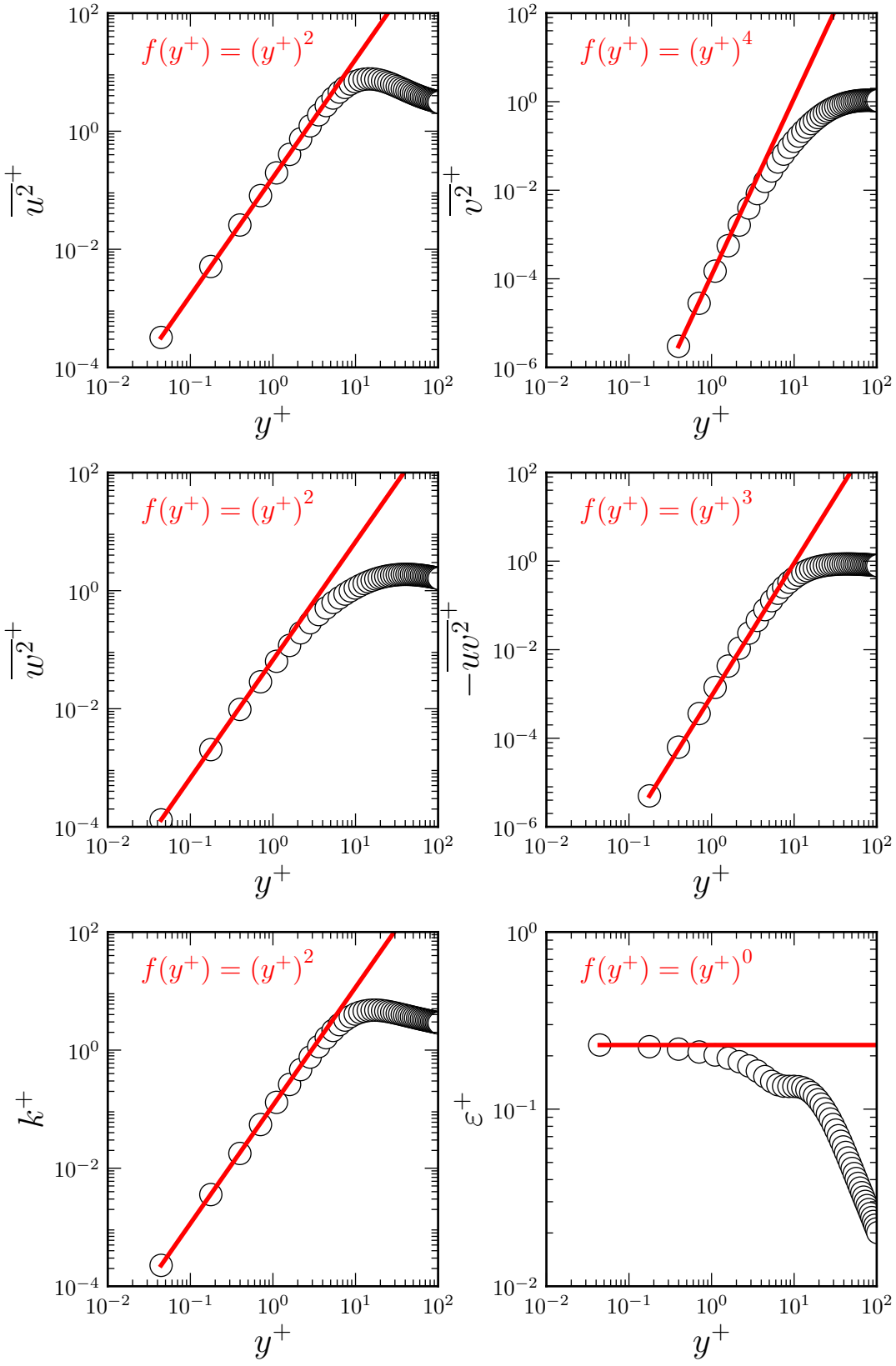

Figure 3.3: Asymptotic behaviour of the DNS variables, $Re_\tau = 590$

3.2.4 Budget of the Reynolds stresses and the dissipation rate

The budget of the Reynolds stress equations (Eq. 2.20) and of the dissipation rate (Eq. 2.21) taken from DNS channel flow data at different Reynolds numbers is now analysed using a "proportional" presentation: for a given variable m, the transport equation is written:

$$\frac{Dm}{Dt} = \sum_i T_i \tag{3.15}$$

The source terms T_i are decomposed as follows: $T_i = \underbrace{\min(T_i, 0)}_{T_i^-} + \underbrace{\max(T_i, 0)}_{T_i^+}$. Each source term T_i^+ is then represented as proportion of the total source term $\sum_i T_i^+$. Likewise, each sink term T_i^- is represented as a proportion of the total sink term $\sum_i T_i^-$. The absence of mean flow unsteadiness and convection imposes $\sum_i T_i^+ = \sum_i T_i^-$. This offers a clearer picture of the balance between generation, destruction and transport[4]. The aim of this analysis is to gain understanding in the role of the different terms of the equations for the turbulence, stresses and dissipation rate, and possibly draw some useful conclusions for the modelling.

The following presents the budget of k and $\overline{u_i u_j}$ in a channel flow using the data of Hoyas and Jiménez (2008) for $Re_\tau = 2000$ and Iwamoto et al. (2002) for $Re_\tau = 395$. Dissipation rate budgets are also presented using the data of Gilbert and Kleiser (1991) for $Re_\tau = 211$ and Rodi and Mansour (1993) for $Re_\tau = 395$.

The budgets of k, $\overline{u^2}$, $\overline{v^2}$, $\overline{w^2}$ as well as $\overline{uv}$ are presented on Fig. 3.5, 3.6, 3.7, 3.8 and 3.9, respectively. For the graphs corresponding to $Re_\tau = 2000$ no data is available in the white region (smallest y^+ values). Black regions represent data error (*i.e.* difference between sink and source terms). Figure 3.4 shows the different terms of the exact ε equation (terms notation taken from Eq. 2.21). In the outer part of the flow, the main ε source/sink terms are proportional to $1/(y^+)^2$. Therefore, all source terms in this region are premultiplied by $(y^+)^2$ for a better representation. It can be

[4]A traditional display of raw DNS budgets, for instance in a boundary layer or a channel flow, often becomes unclear in regions where the terms shrinks to 0 (*i.e.* towards the wall or at the edge of a boundary layer). A somehow similar "proportional" representation of the budget can be found in Pope (2008).

clearly seen that P_4 and Y are the main terms in the core region, but their difference is actually of the same order as the other terms. Therefore the proportional budget representation of the ε equation source terms (shown on Fig. 3.10) is clearer when applied directly to the groups $P^1 + P^2 + P^3$ and $P^4 - Y$. In light of these graphs some comments can be formulated:

• Since $P_{22} = P_{33} = 0$ in a channel flow the production of turbulent kinetic energy by mean velocity gradient only feeds the $\overline{u^2}$ component. As seen, in all the domain the pressure term then removes energy from the component $\overline{u^2}$ to feed $\overline{v^2}$ and $\overline{w^2}$ ($\phi^*_{11} < 0$, $\phi^*_{22} > 0$ and $\phi^*_{33} > 0$). However due to near-wall kinematic blockage (*i.e.* splat) there is some further transfer from $\overline{v^2}$ to $\overline{u^2}$ and $\overline{w^2}$ in the near-wall region through the term ϕ^*_{ij} (ϕ^*_{22} is actually negative near the wall).

• In the logarithmic region, at $Re_\tau = 2000$ the following equilibria may roughly be observed:

$$\begin{cases} P = \varepsilon \\ P_{11} = \varepsilon_{11}(33\%) + \phi^*_{11}(66\%) \\ \phi^*_{22} = \varepsilon_{22} \\ \phi^*_{33} = \varepsilon_{33} \\ P_{12} = \phi^*_{12}(95\%) + \varepsilon_{12}(5\%) \\ P_1 + P_2 + P_3(66\%) + D^T_\varepsilon(33\%) = P_4 - Y \end{cases} \tag{3.16}$$

• In the defect layer: After the log region, the velocity gradient decreases faster, and the turbulent diffusion of k progressively becomes the dominant source term of k. The excess of net production in the logarithmic layer is going to feed the channel centre. Conversely, pressure transport carries some k back to the lower edge of the log layer. At the channel centre, the pressure term ϕ^*_{ij} is still present for the component $(1,1)$, (3.3) and $(1,2)$ but vanishes for $(2,2)$

• Universality of the near-wall region: These proportional plots are very similar for the two Reynolds numbers, with one major difference however: for $Re_\tau = 395$ and for all the variables, particularly k, the turbulent flux plays a non-negligible role

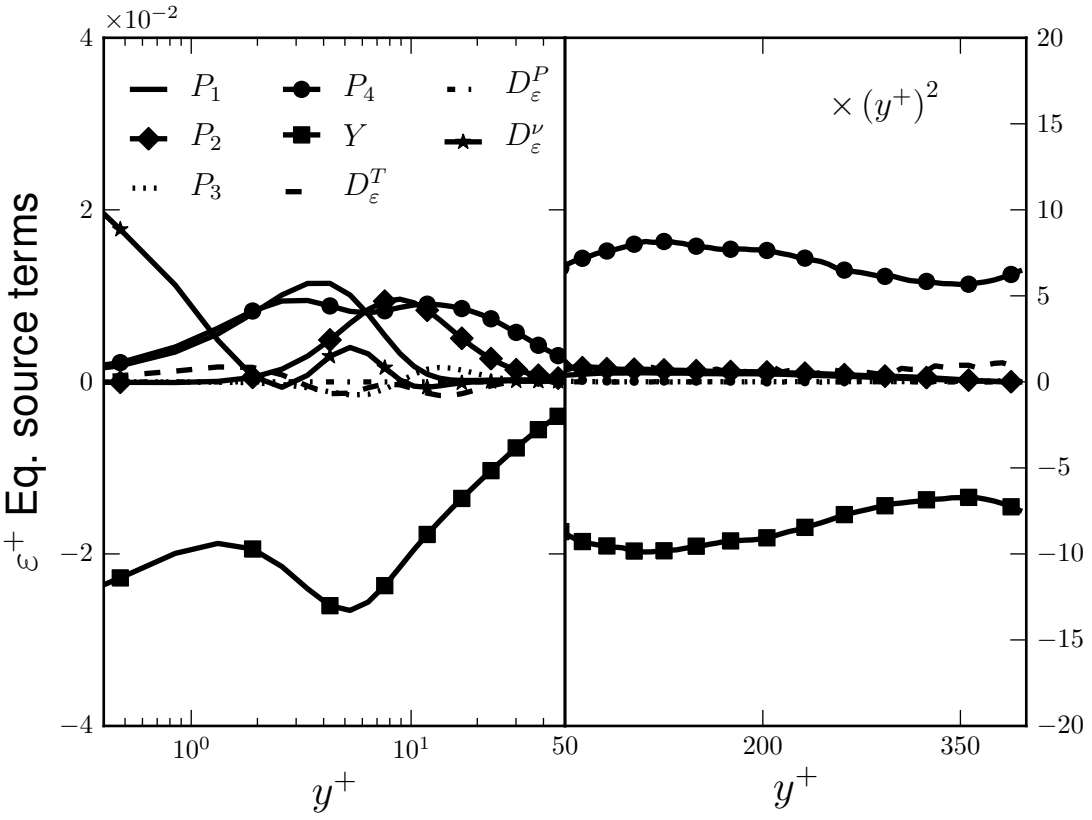

Figure 3.4: Budget of the dissipation rate ε, $Re_\tau = 395$ following the term decomposition of Eq. 2.21. Near-wall region ($y^+ \in [0.4, 50]$) in log-scale and outer part ($y^+ \in [50, 395]$) in linear scale. Terms in the outer part are pre-multiplied by $(y^+)^2$

in the logarithmic layer: it is responsible for the transfer between the near wall and the channel centre. This may be seen as a possible explanation for the dependence of the near-wall region on outer flow parameters, at low-Reynolds number, the two zones being in "connection" *via* turbulent transport. The dissipation rate ε is the variable for which turbulent transport is comparatively the largest in the logarithmic layer.

• Comparing budgets of k, Fig. 3.5, and ε, Fig. 3.10, justifies modelling the later as proportional to the former, with the following difference: as seen, turbulent transport of ε from the near-wall region to the centre is much more important than that of k (and visible in the log region even at high Reynolds number). Also "production" of ε reaches 100% at $y^+ = 4$ then again for $10 < y^+ < 30$, *i.e.* it has a "W" shaped profile which is then balanced by a complex redistribution by viscous and turbulent transport.

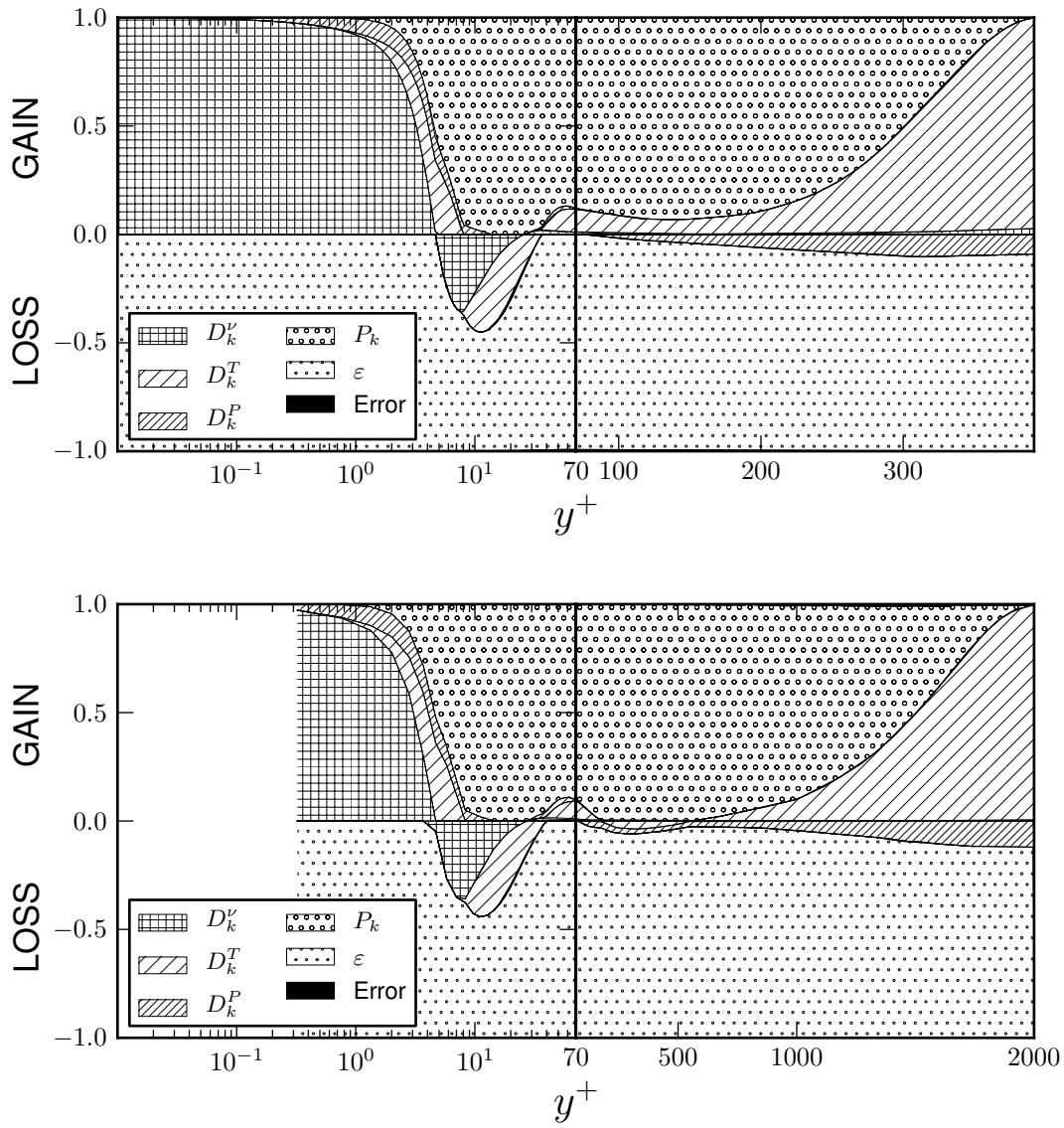

Figure 3.5: Budget of the turbulent kinetic energy k. Top: $Re_\tau = 395$, Bottom: $Re_\tau = 2000$

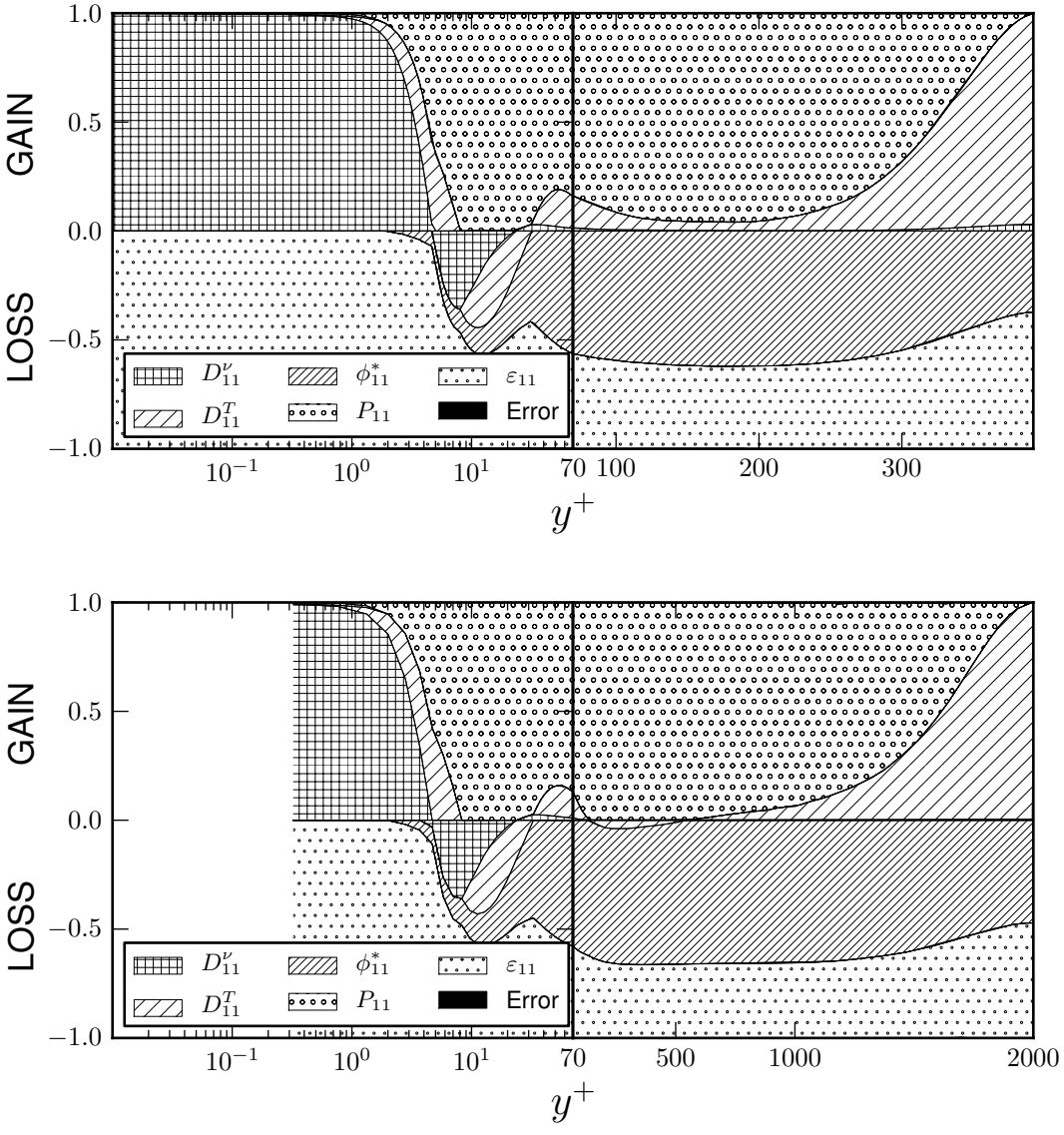

Figure 3.6: Budget of $\overline{u^2}$. Top: $Re_\tau = 395$, Bottom: $Re_\tau = 2000$

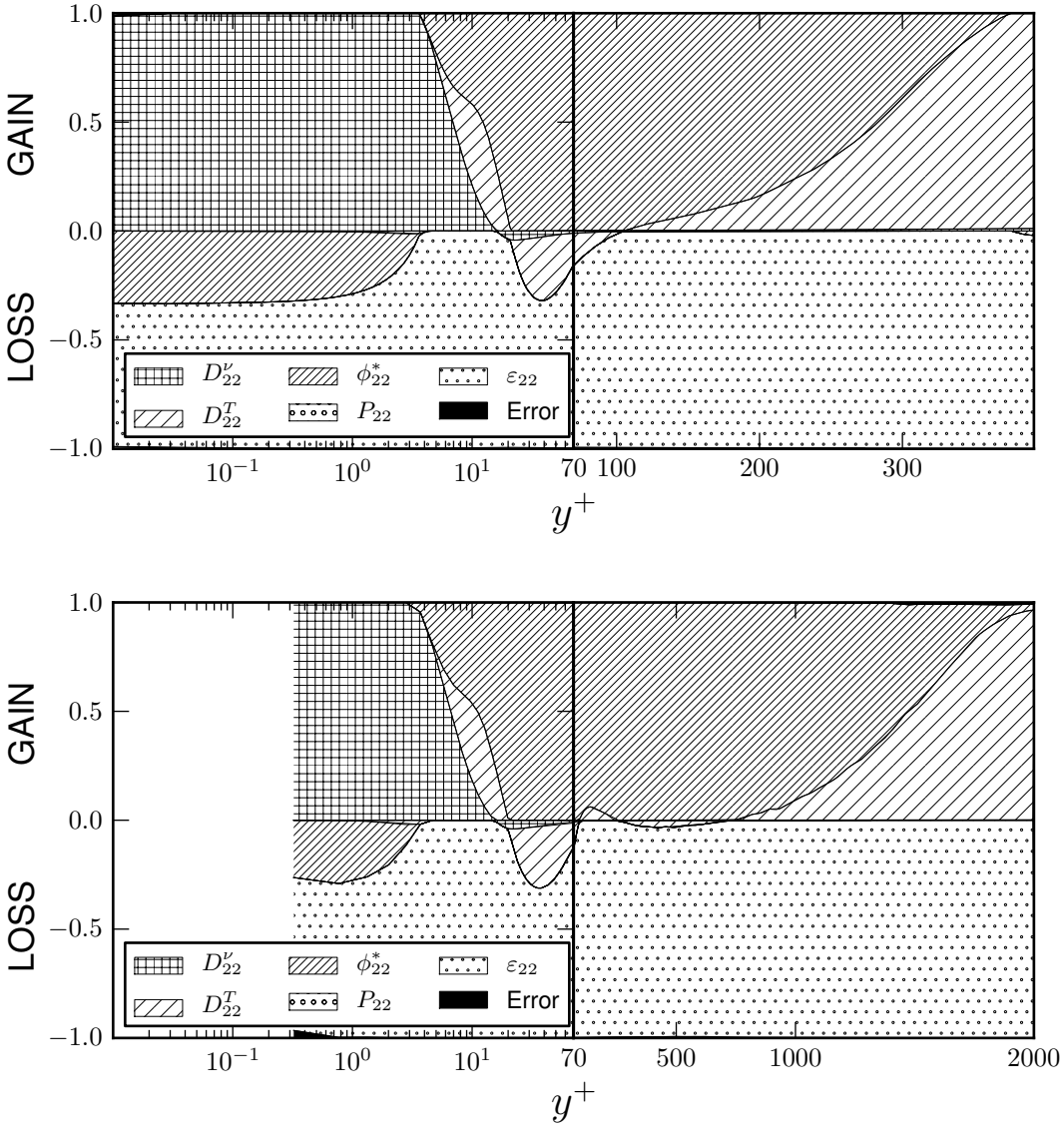

Figure 3.7: Budget of $\overline{v^2}$. Top: $Re_\tau = 395$, Bottom: $Re_\tau = 2000$

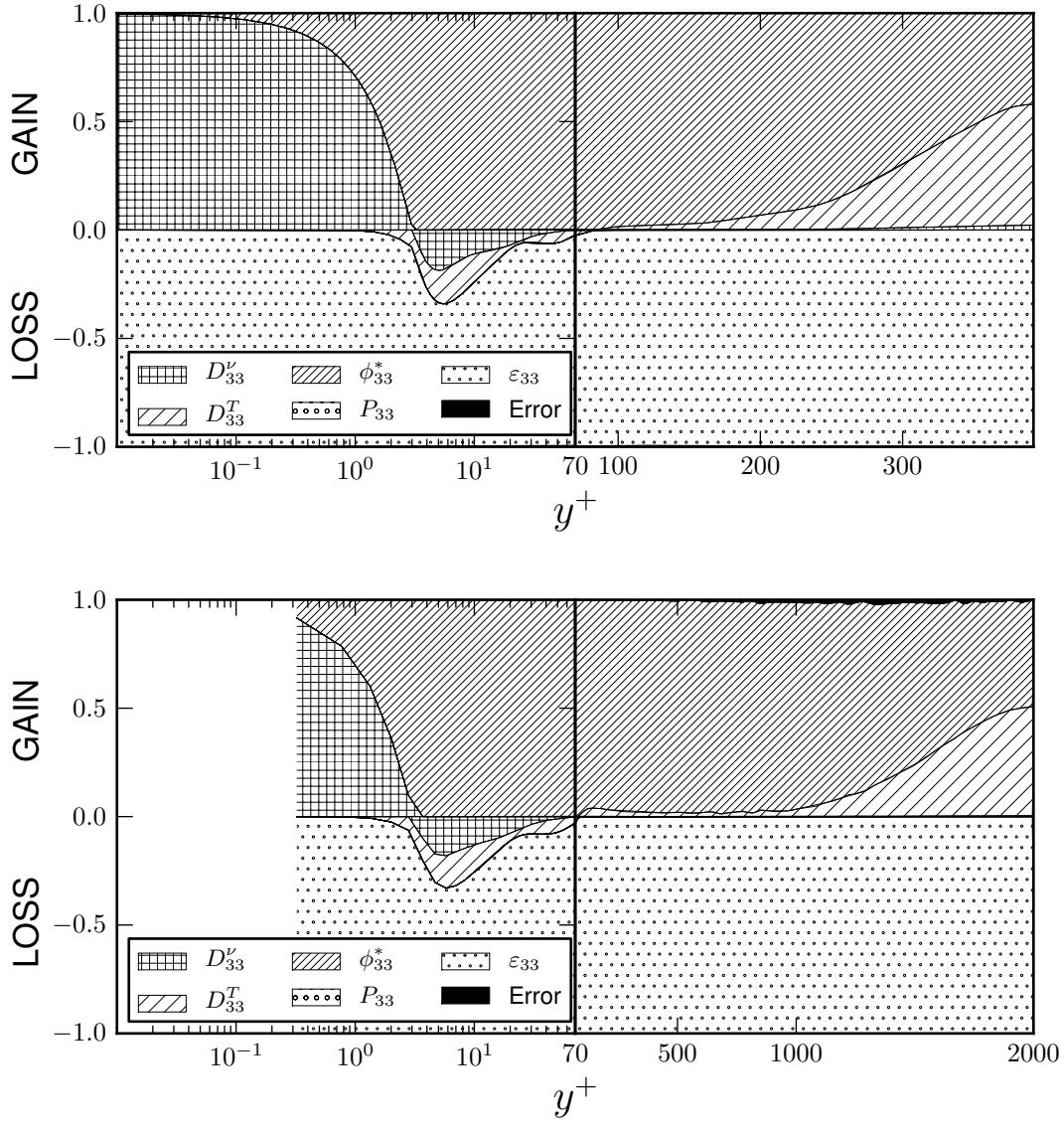

Figure 3.8: Budget of $\overline{w^2}$. Top: $Re_\tau = 395$, Bottom: $Re_\tau = 2000$

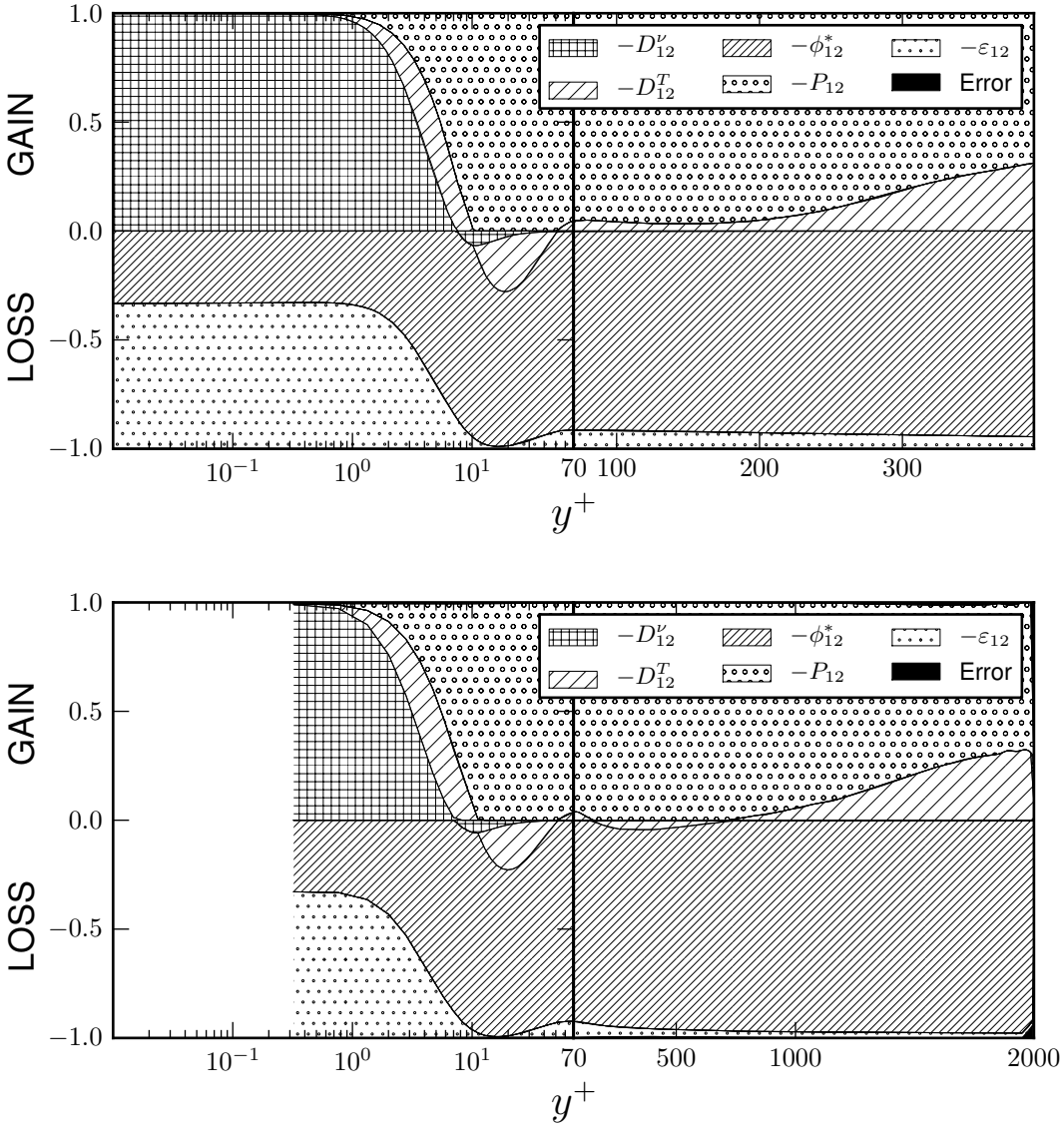

Figure 3.9: Budget of $\overline{uv}$. Top: $Re_\tau = 395$, Bottom: $Re_\tau = 2000$

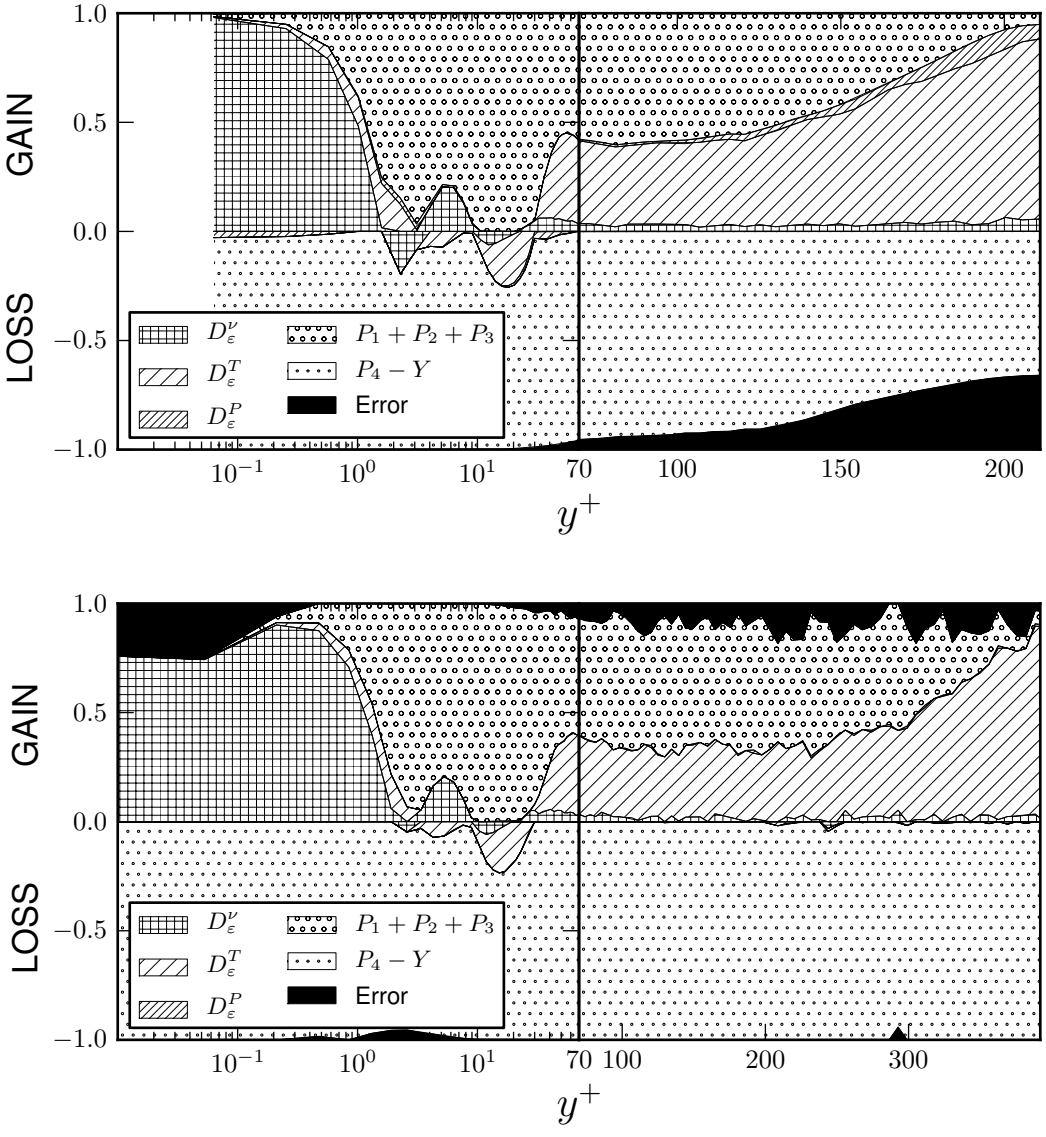

Figure 3.10: Budget of ε. Top: $Re_\tau = 211$, Bottom: $Re_\tau = 395$

3.2.5 Universality of the near-wall behaviour

This section focuses on the dependance of the mean velocity and the turbulence variables on the friction Reynolds number Re_τ: although it is expected that for infinite Reynolds-number the near-wall flow behaviour should be totally independent of the channel half-width δ (*i.e.* only be a function of $y^+ = y/\delta_\nu$) it is interesting to investigate the effects of this dependance for a finite value of Re_τ and in particular for which variables it is the most visible. This will provide rules for turbulence models developments.

To this end, DNS data for the set $Re_\tau \in \{180; 395; 590; 950; 2000\}$. The DNS data analysed are those of Hoyas and Jiménez (2008) for Re_τ = 180, 590, 950 and 2000, those of Iwamoto et al. (2002) for Re_τ = 395 and those of Moser et al. (1999) for $Re_\tau = 590$.

Fig. 3.11 shows the quantities $y^+\varepsilon^+$, k^+, $\dfrac{1}{y^+}(-\overline{uv}^+/\dfrac{d\overline{U}^+}{dy^+})$, $y^+\dfrac{d\overline{U}^+}{dy^+}$, $\dfrac{1}{y^+}(k^+/\varepsilon^+)$ and $\dfrac{1}{y^+}((k^+)^{3/2}/\varepsilon^+)$ plotted from DNS data simultaneously for all considered Reynolds numbers. An analysis of the turbulent quantities in the logarithmic layer (see Subsec. 4.2.2) shows that the dissipation rate ε^+ is proportional to $1/y^+$, and the turbulent viscosity $-\overline{uv}^+/(d\overline{U}^+/dy^+)$, the turbulent time scale k^+/ε^+ and the turbulent length-scale $(k^+)^{3/2}/\varepsilon^+$ are proportional to y^+. Therefore, they are pre-multiplied by y^+ and $1/y^+$, respectively, so the differences between plots is easier to spot. These graphs aim at representing the Reynolds-number dependence of the different variables.

The bottom plot of Fig. 3.11 shows a measure of the Reynolds number dependency: for each variable A^+, the parameter $\sigma(A^+(y^+))$ represents the standard deviation of the set $\{A^+_{Re^i_\tau}(y^+)/\overline{A}^+(y^+)\}$ for all Reynolds numbers Re^i_τ for which data are available for a given y^+ [5]. $\overline{A}^+(y^+)$ is the mean of the set $\{A^+_{Re^i_\tau}(y^+)\}$. $\sigma(A^+)$ is 0 if there is no Reynolds-number dependence. Fig 3.12 presents the normal Reynolds stresses and the associated σ parameter.

The parameter σ is a good indicator to show the universality of the variables in

[5] *e.g.* for $y^+ = 500$ only $Re^i_\tau \in \{550; 590; 900; 2000\}$ is considered.

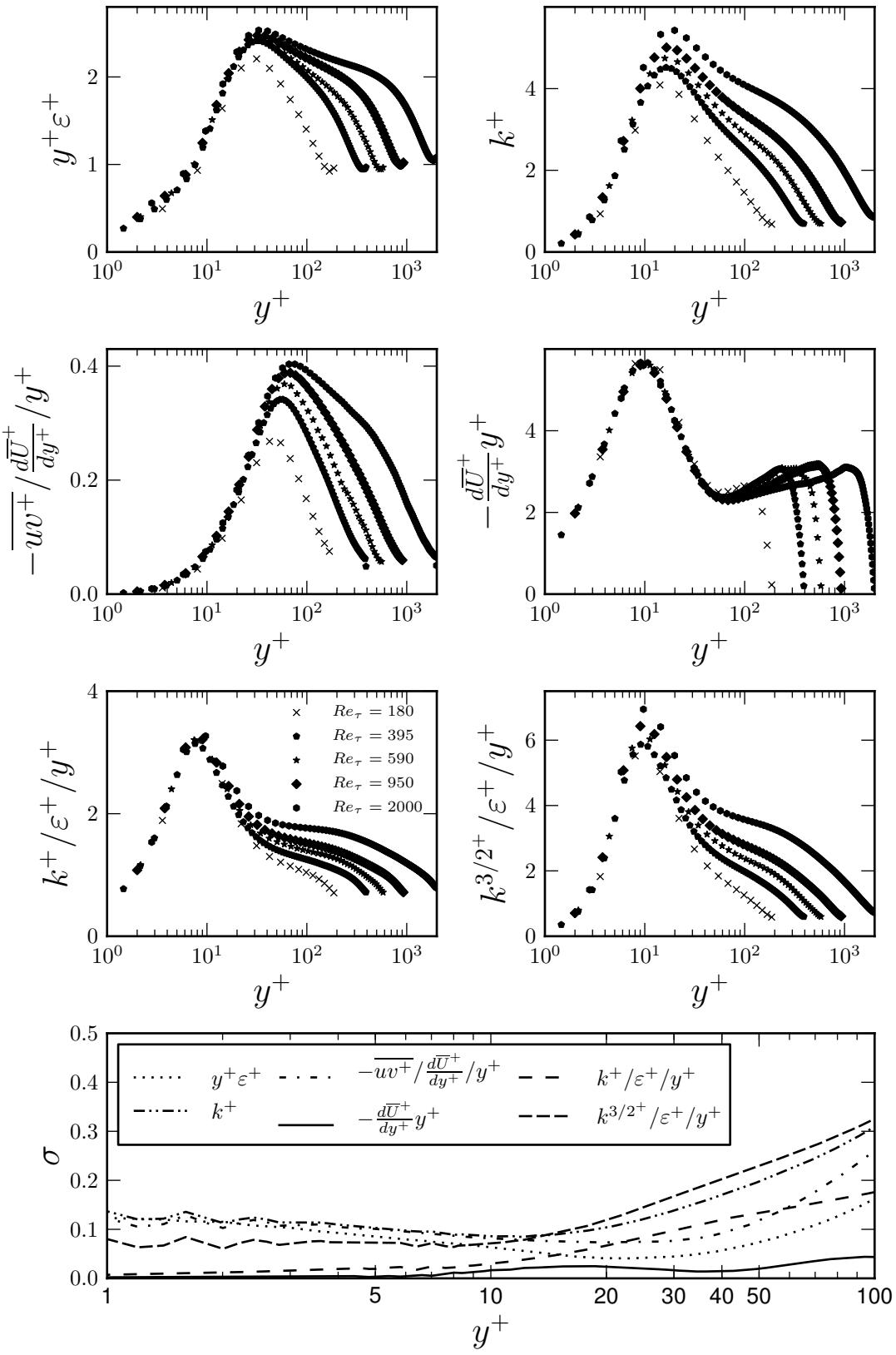

Figure 3.11: Top: turbulent variables from the DNS data for $Re_\tau \in \{180; 395; 590; 950; 2000\}$. Bottom: σ parameter for the different variables.

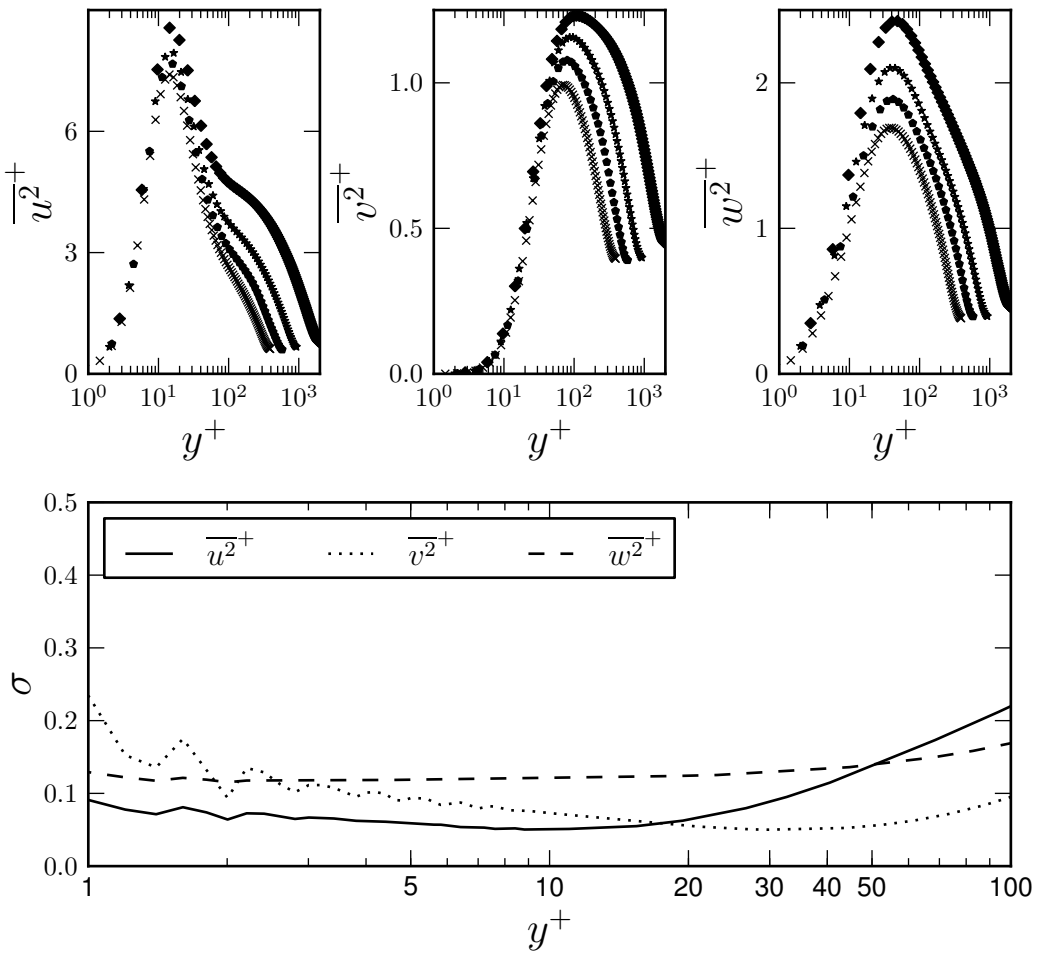

Figure 3.12: Top: Normal Reynolds stresses from the DNS data for $Re_\tau \in \{395; 590; 950; 2000\}$. Bottom: σ parameter for the different stresses.

the near-wall region, characterised by a lower Re_τ dependency near walls when the viscous scaling is used: this trend can clearly be observed for all variables though the upper limit of the region with lowest values of σ varies amongst variables.

The velocity is the variable where the universality in the near-wall region is the most obvious: very low and constant value of σ is observed in a region ranging from $y^+ = 0$ to $y^+ = 100$ for the variable $y^+ \dfrac{d\overline{U}^+}{dy^+}$ as shown on Fig. 3.11. As a consequence of the relation given by Eq. 3.5 in a channel flow, the same obvious trend is observed for the rescaled turbulent viscosity $-\overline{uv}^+ / \left(\partial \overline{U}^+ / \partial y^+\right) / y^+$. However, there is a clear Re_τ independence only for a region up to $y^+ = 50$ (Fig.3.11).

As for the turbulent variables, the normalised time scale $\dfrac{1}{y^+}(k^+/\varepsilon^+)$ is the only variable where the near-wall universality is observed to a large extent. In contrast, the dissipation rate has the lowest level of Re_τ dependency in a region extending from $y^+ = 10$ to $y^+ = 20$ because of the influence, closer to the wall, of the boundary condition $\lim\limits_{y\to 0} \varepsilon = \lim\limits_{y\to 0} \nu \partial_{jj} k$. Indeed, as also observed, the peak of turbulent kinetic energy k^+ in the buffer layer is strongly Re_τ dependant, which yields the same trend for $\lim\limits_{y\to 0} \varepsilon$. Moreover, a strong Re_τ dependency is also observed for the normalised length-scale $\dfrac{1}{y^+}((k^+)^{3/2}/\varepsilon^+)$ in the same region. Amongst the three normal Reynolds-stresses, Fig 3.12, the wall-normal component $\overline{v^2}^+$ seems to be the least Re_τ dependent in the buffer layer (from $y^+ = 10$ to $y^+ = 100$). The inner layer seems to be limited to the region from 0 to 10 for $\overline{u^2}^+$ however, as characterised by the lowest values of σ taken in this region.

As a conclusion of the analysis, it is clear that a low Re_τ dependence in the inner layer up to at least $y^+ = 50$ exists for the variables U^+, $y^+ \dfrac{d\overline{U}^+}{dy^+}$ and $\nu_t^+ = \overline{uv}^+ / \left(dU^+/dy^+\right)$. As far as the turbulent variables are concerned, a weak Re_τ dependence up to the buffer layer is observed for the time scale and the wall-normal fluctuations $\overline{v^2}$. It will be argued in the subsequent chapters that these rules, when respected in a RANS model development, can greatly help improve the predictions.

3.3 Classical near-wall RANS modelling

The mainstream of near-wall adaptations for the models introduced in Sec. 2.3 is now presented.

3.3.1 Damping functions

Isotropic damping: As the main characteristic feature of the simplest models is an isotropic representation of turbulence, the main feature of near-wall corrections is a damping of turbulence near walls to account for the severe reduction of mixing due to wall normal turbulent-fluctuation impairment. The earliest damping function was proposed by van Driest (1956) within the framework of the mixing length hypothesis.

$$l_m^+ = \kappa y^+ \left(1 - exp(-y^+/26)\right) \tag{3.17}$$

In eddy-viscosity models, damping functions are used primarily as a multiplier in the turbulent-viscosity to correct the poor reproduction of the turbulent shear stress $\overline{uv}$ by the Boussinesq relation.

Most of near-wall EVM's propose a correction for the constant $C'_\mu = f_\mu C_\mu$ defined as

$$f_\mu = \frac{\overline{uv}_{target}}{\overline{uv}_{model}} \tag{3.18}$$

The parameter on which the function f_μ depends is generally either y^+ (*e.g.* Chien (1982)), or the turbulent Reynolds number $Re_t = \dfrac{\sqrt{k}y}{\nu}$ or $Re_t = \dfrac{k^2}{\varepsilon\nu}$ (*e.g.* Launder and Sharma (1974), Wilcox (1994)) or both (*e.g.* Nagano and Tagawa (1990)). A review of near-wall corrections for EVMs is given in Patel et al. (1985).

The same type of damping functions is classically used in the Reynolds-stress-transport equations in the representation of the pressure/strain-rate correlation ϕ_{ij} in the vicinity of walls. Indeed, the hypothesis of quasi homogeneity on which most models for ϕ_{ij} are based no longer holds near walls. Moreover, the surface part of ϕ_{ij} (last terms of Eq. 2.24) is not represented by classical models, which assume that the distance to the wall is large. To this end, some models (*i.e.* Chen (1995) or the wall

reflection terms of Gibson and Launder (1978)) propose low Reynolds adaptations using damping functions.

Selective damping: As seen on Tab. 3.1, the decay of the different Reynolds stresses and their source terms (ϕ^*_{ij} and ε_{ij}) is generally smaller by several orders of magnitude for the wall normal component. To account for this selective damping, some advanced Reynolds-stress models rely on measures to identify the wall normal direction as an ingredient to near-wall terms (*e.g.* Craft (1998)).

3.3.2 Modelling of the dissipation rate

Near-wall adaptation is also required in the dissipation-rate equation, and whereas the empirical ε equation, Eq. 2.37, is mainly tuned to return the observed behaviour in fundamental flows, the analysis of the actual equation for the dissipation rate, Eq. 2.21, may be useful to improve the prediction of this quantity in a boundary layer. The study of Eq 2.21 proved worthwhile only when the first channel-flow DNS data were published, accurate enough to give the budget of the actual equation[6]. For instance, before the availability of DNS data, it was commonly assumed that the dissipation rate reaches its maximum value in the buffer layer, just like k, then decreases towards the wall, this intuition being proved wrong by DNS data. However, as seen in Fig 3.10, errors introduced in the post-processing of complex terms are far from negligible, suggesting that the analysis of the exact equation brings qualitative rather than quantitative guidance. Some authors (*e.g.* Rodi and Mansour (1993), Jakirlic and Hanjalic (2002)) proposed term-by-term models based on the analysis of the exact ε equation. Another approach simply consists in improving the empirical equation by analysing available data for the exact ε equation: however there are different ways of grouping terms and linking them to the source and sink terms of the empirical equation: one of these approaches is to link rapid terms (functions of mean velocity gradients, that is $P_1 + P_2 + P_3$) to $C_{\varepsilon 1} P\varepsilon/k$ and *slow terms* (function

[6]However *a priori* assessment of the ε equation can be hazardous as budget are only available for the lowest Reynolds number cases of the channel flow.

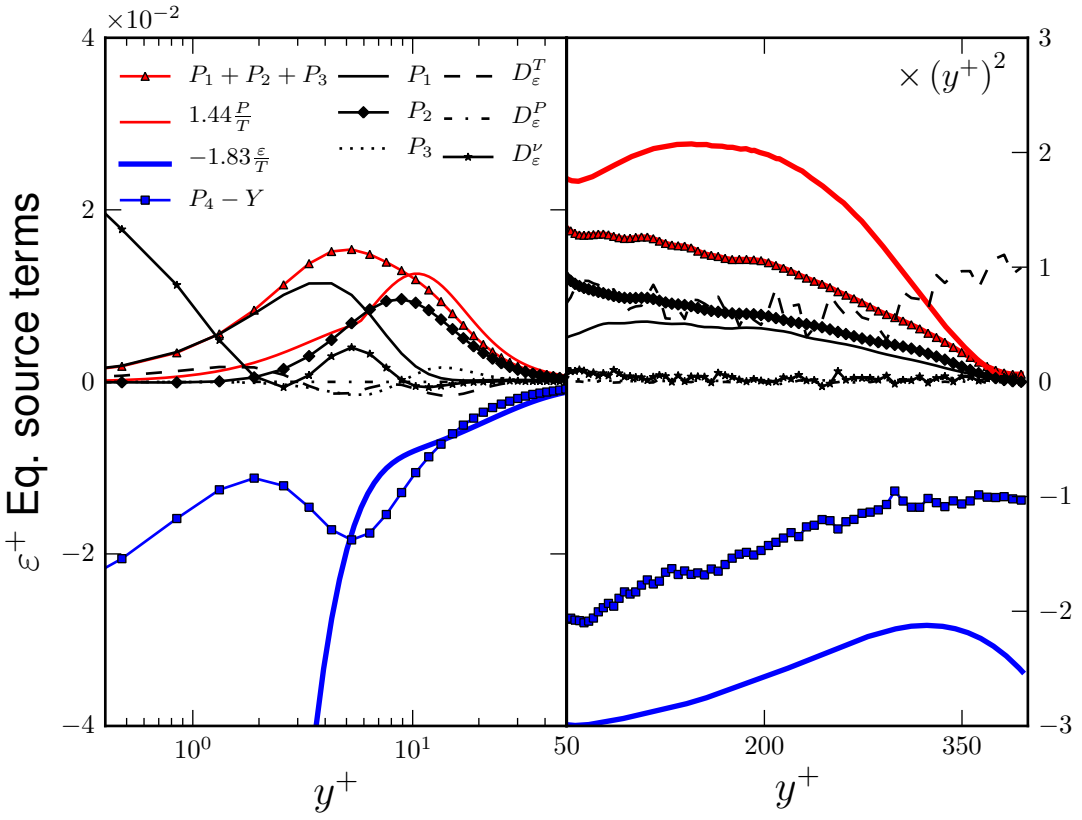

Figure 3.13: Budget of the exact epsilon equation Eq. 2.21. Data of Rodi and Mansour (1993), with the slow and rapid term groups and their respective model.

of turbulent quantities only, that is $P_4 - Y$) to $C_{\varepsilon 2}\varepsilon^2/k$.

Fig. 3.13 shows the ε equation budget (data from Rodi and Mansour (1993)) grouped as rapid (red) and slow (blue) terms.

Near wall region (Fig. 3.13, left) In the viscous sublayer ($y^+ < 5$) the correct modelling of the source terms is not necessary since ε is mainly ruled by its boundary condition in that region (for instance, for the $k-\varepsilon$ model, $\varepsilon_w = 2\nu k/y^2$). However, further outwards, the production term clearly under-predicts the sum $P_1 + P_2 + P_3$, and low-Reynolds-number models usually feature modifications of the ε equation, to take into account this weakness of the model. To circumvent the problem, Jones and Launder (1972) proposed to add the source term $E = 2\nu\nu_t \left(\frac{\partial^2 \overline{U}}{\partial y^2}\right)^2$ into the ε equation. This was first meant to improve the prediction of the turbulent kinetic

energy peak near $y^+ = 20$. This term was seen as model for the term P_3 and using a generalised gradient model for the unclosed term $\overline{u_k \partial u_i/\partial x_l}$, in the framework of second-moment-closure modelling, P_3 can be modelled by $-2\nu\frac{k}{\varepsilon}\overline{u_j u_k}\frac{\partial^2 \overline{U}_i}{\partial x_j \partial x_l}\frac{\partial^2 \overline{U}_i}{\partial x_k \partial x_l}$[7]. This term was, for instance, used in the first version of the elliptic blending Reynolds Stress Model of Manceau and Hanjalić (2002), but it was decided, for reasons of robustness, to replace it, using a variable $C_{\varepsilon 1}$ coefficient, by the term $C_{\varepsilon 1} \times 0.03(1-\alpha^2)\sqrt{\frac{k}{\overline{u_i u_j} n_i n_j}}$ with the vector $\underline{n}$ being the wall-normal vector. The idea of using a variable $C_{\varepsilon 1}$ coefficient to increase the production term was also used in most of the $\overline{v^2} - f$ based models since the original work of Durbin (1993a). The constant is replaced by $C^*_{\varepsilon 1} = C_{\varepsilon 1}(1 + C_{A1}\phi)$ with $\phi = P/\varepsilon$, $\phi = \sqrt{\frac{k}{\overline{v^2}}}$, or ϕ as a function of the Reynolds-stress anisotropy invariant, but there is no clear physical justifications in the use of these corrections.

Logarithmic and defect layer (Fig. 3.13, right) The magnitude of the rapid and slow terms is strongly over-predicted in the logarithmic layer but those errors seem to cancel out. However, in the defect layer the rapid terms decay to zero, and so does the model, but the slow term is still substantially over predicted in magnitude, by a factor of 2. This was noticed by Parneix et al. (1996) who proposed a model to reduce $C_{\varepsilon 2}$ in this region based on the turbulent transport to dissipation rate ratio.

Some other near-wall and low-Reynolds-number modifications have been proposed to the ε equation, which were not directly derived from the comparison to the exact equation. For instance, the coefficient $C_{\varepsilon 2}$ needs to take into account low-Reynolds-number effects induced by the vicinity of the wall. The grid-turbulence experiment shows that far from the grid, when turbulence weakens, the decay exponent increases. This is pointed out in Hanjalic and Launder (1976) who suggest a correction for the

[7] In reality the double peak seen earlier, Fig. 3.10, is related to the P_1 peak at $y^+ = 3$ then a separate P_2 peak at $y^+ = 8$, whereas P_3 is comparatively very small. Therefore the near-wall modelling of the dissipation rate cannot entirely rely upon the correct reproduction of the term P_3.

$C_{\varepsilon 2}$ coefficient based on the turbulent Reynolds number $Re_t = \dfrac{k^2}{\varepsilon\nu}$:

$$C^*_{\varepsilon 2} = \left[\underbrace{1 - \frac{2}{9} exp\left(-\left(\frac{Re_t}{6}\right)^2\right)}_{f_{\varepsilon 2}}\right] C_{\varepsilon 2} \tag{3.19}$$

Some Reynolds-stress models also propose a dependence on the Lumley anisotropy invariant A (*e.g* Craft (1998)). It may indeed seem reasonable to introduce a dependence on parameters representing the turbulence anisotropy, stronger in the near-wall region.

It is noteworthy that some equivalent near-wall modifications are also proposed for the ω equation when it is the scale determining variable used (*e.g* Wilcox (1994)).

3.4 The elliptic relaxation

An original idea, introduced in Durbin (1991), proposes another way to take into account the near-wall effects and inhomogeneities in the existing RSM. It is based on a better understanding of the non-local wall and pressure interactions, and a consideration of the near-wall asymptotic behaviour of the components of the Reynolds-stress tensor. The general approach applied to an RSM is first presented (the model of Durbin (1993b)), followed by a simplified version in an eddy-viscosity framework (the $\overline{v^2} - f$ model of Durbin (1991)). Finally the elliptic-blending technique of Manceau and Hanjalić (2002) is introduced.

3.4.1 The elliptic relaxation RSM of Durbin (1993b)

The elliptic equation: Durbin (1991) and Durbin (1993b) propose to model the two-point correlation present in Eq. 2.24 in the generic way :

$$\overline{f(\underline{x})g(\underline{x}')} = \overline{f(\underline{x}')g(\underline{x}')} exp(-\|\underline{x} - \underline{x}'\|/L) \tag{3.20}$$

Where L represents the turbulent length-scale. Using this model in Eq. 2.24, it can be shown that the kernel appearing in the integral is the Green's function in $\mathbb{R}^3$ of the

operator $1/L^2 - \Delta$. Hence the pressure strain-rate term is a solution of the following equation:

$$\phi_{ij} - L^2 \Delta \phi_{ij} = \phi^h_{ij} \tag{3.21}$$

Where ϕ^h_{ij} is an homogeneous model for the pressure strain-rate term in the regions where $\Delta^2 \phi_{ij} = 0$ (remote from the wall). This elliptic equation therefore enables to take into accounts non-local-effects due to the incompressibility at a turbulent scale, but unlike the Poisson equation for the pressure, the elliptic operator (Eq. 3.21) limits the propagation of information to a sphere of radius of the order of the turbulent length scale L. The solution of this equation, ϕ_{ij}, is directly used as source term of the $\overline{u_i u_j}$ equations.

However, in order to correctly reproduce the asymptotic near-wall behaviour of the different Reynolds stresses (as presented in Sec. 3.2.3) equation 3.21 is not solved for the pressure strain-rate correlation itself, but for a modified term, f_{ij}, whose nature is explained in what follows.

The elliptic variable: As the theoretical wall behaviour is $O(y^2)$ for $\overline{u^2}$ and $\overline{w^2}$, the balance between terms whose order is less than 2 must be ensured in their transport equation at walls, otherwise a residual source term will be predominant. As for $\overline{v^2}$, whose behaviour is $O(y^4)$, the terms whose order is less than 4 should balance. This means that ϕ_{ij}, D^P_{ij}, D^ν_{ij} and ε_{ij} should be modelled in order to balance each other[8] (See Tab. 3.1):

$$D^\nu_{ij} \sim -\phi_{ij} - D^P_{ij} + \varepsilon_{ij} \tag{3.22}$$

Firstly, it is to be noted that the split between pressure transport D^P_{ij} and pressure strain-rate correlation ϕ_{ij} is not relevant if one wants to ensure to correct asymptotic behaviour of the resolved variables. Indeed, for the components $(2,2)$ and $(1,2)$, the first leading-order terms of D^P_{ij} and ϕ_{ij} cancel out (again, as seen on Tab. 3.1), and this property should hold for the models of the two terms if they were to be independently represented (as already pointed out in Manceau (1999)). Therefore, to facilitate the modelling, the pressure term is then represented as a whole: ϕ^*_{ij}.

[8]This is also true for $\overline{uv}$

Consequently, the constant C_s (appearing in Eq. 2.30) in the model for the turbulent transport is modified, as D_{ij}^P is not lumped into this term anymore.

Secondly, the addition of the deviatoric part of the dissipation tensor $\varepsilon_{ij} - 2/3\varepsilon\delta_{ij}$ into the pressure term, as usually done in Reynolds-stress modelling (as seen in Sec.2.3.1) transforms this latter term into a new term which is a constant (*i.e.* $O(1)$) near the wall, and this does not help to model the asymptotic behaviour correctly. Instead, as proposed by Durbin (see Durbin and Reif (2001), p.170), the dissipation is written as : $\varepsilon_{ij} = \frac{\overline{u_i u_j}}{k}\varepsilon + \left(\varepsilon_{ij} - \frac{\overline{u_i u_j}}{k}\varepsilon\right)$ (using the model of Rotta (1951)). This latter term is modelled together with ϕ_{ij}^*. The composite term, entering the definition of the elliptic variable is noted φ_{ij} and defined as:

$$\varphi_{ij} = \phi_{ij} + D_{ij}^P - \left(\varepsilon_{ij} - \frac{\overline{u_i u_j}}{k}\varepsilon\right) \tag{3.23}$$

Thirdly, the near-wall equilibrium Eq. 3.22 rewritten using the variable φ_{ij} reads:

$$\varphi_{ij} \sim -D_{ij}^\nu + \frac{\varepsilon\overline{u_i u_j}}{k} \tag{3.24}$$

The elliptic equation is solved for $f_{ij} = \varphi_{ij}/k$ so that the non-zero wall Dirichlet boundary condition given to f_{ij} ensures Eq. 3.24 is respected to order $O(1)$.

The elliptic equation for the variable f_{ij} finally reads:

$$f_{ij} - \nabla^2 f_{ij} = \frac{\varphi_{ij}^h}{k} \tag{3.25}$$

Boundary conditions: Condition 3.24 is related to the simplified $\overline{u_i u_j}$ transport equation at the wall:

$$\nu\frac{\partial^2\overline{u_i u_j}}{\partial y^2} - \frac{\overline{u_i u_j}}{k}\varepsilon = -k f_{ij,w} \tag{3.26}$$

where $f_{ij,w}$ is the wall limit of f_{ij}.

Using the fact that $\overline{u_i u_j} = 0$ at the wall the solution of the differential equation can be written (invoking $\varepsilon = 2\nu k/y^2$):

$$\overline{u_i u_j} = Ay^2 - \frac{\varepsilon}{20\nu^2} f_{ij,w} y^4 \tag{3.27}$$

Firstly the behaviour $\overline{v^2} = O(y^4)$ is obtained for a value $f_{22,w}$ for which $A = 0$. This is achieved for

$$f_{22,w} = -20\frac{\nu^2}{\varepsilon^2}\lim_{y\to 0}\frac{\overline{v^2}}{y^4} \tag{3.28}$$

Secondly equation 3.27 shows that the quadratic behaviour for $\overline{u^2}$ and $\overline{w^2}$ is obtained for any value of $f_{11,w}$ and $f_{33,w}$, respectively. Therefore there is no unique set of values for $f_{11,w}$ and $f_{33,w}$. Here they are chosen as: $f_{11,w} = f_{33,w} = -1/2 f_{22,w}$.

Thirdly, the cubic behaviour of $\overline{uv}$ is impossible to achieve, as seen in equation 3.27. Therefore it is only sought to predict $\overline{uv}$ to be of order $O(y^4)$ (what is really important is the dominance of the viscous stress over the turbulent stress in the momentum equation) and this is achieved by imposing:

$$f_{12,w} = -20\frac{\nu^2}{\varepsilon^2}\lim_{y\to 0}\frac{\overline{uv}}{y^4} \tag{3.29}$$

A more detailed analysis of this topic can be found in Manceau (1999).

The only change needed for φ_{ij}^h/k when starting from a classical pressure strain-rate RSM model such as in LRR or SSG is to replace the Rotta's constant C_1 by $C_1 - 1$. Indeed what is "lumped" into the pressure strain-rate model is no longer $\frac{2}{3}\delta_{ij}\varepsilon - \varepsilon_{ij}$ but $\varepsilon\overline{u_i u_j}/k - \varepsilon_{ij}$.

The length-scale: The non-local effects introduced by this model represent the remote action of the incompressibility over a turbulent structure. Hence, the correlation length-scale is linked to the integral turbulent length-scale:

$$L = C_L max\left(\frac{k^{3/2}}{\varepsilon}, C_\eta\left(\frac{\nu^3}{\varepsilon}\right)^{1/4}\right) \tag{3.30}$$

The integral length-scale is bounded by the Kolmogorov scale, in order to prevent a singularity near the wall. Further analysis of the validity of Eq. 3.30 and recommendation for the values of C_L and C_η based on a 2-point correlation study using a DNS database can be found in Manceau et al. (2001).

The model for φ_{ij}^h: The homogeneous model for the modified pressure term is the sum of the Rotta's return to isotropy model and isotropisation of production:

$$f_{ij}^h = \frac{(1-C_1)}{T}\left(\frac{\overline{u_i u_j}}{k} - \frac{2}{3}\delta_{ij}\right) - \frac{C_2}{k}\left(P_{ij} - \frac{2}{3}P\delta_{ij}\right) \tag{3.31}$$

where $P = \frac{1}{2}P_{ii}$ and $k = \frac{1}{2}\overline{u_i u_i}$. T is the turbulent time scale and once again, the integral value is bounded by its Kolmogorov expression near the wall to avoid a singularity:

$$T = max\left(\frac{k}{\varepsilon}, C_T\sqrt{\frac{\nu}{\varepsilon}}\right) \tag{3.32}$$

Other equations and constants The dissipation rate equation reads:

$$\frac{D\varepsilon}{Dt} = \frac{C_{\varepsilon 1}^* P - C_{\varepsilon 2}\varepsilon}{T} + \frac{\partial}{\partial x_j}\left(\left(\nu + \frac{\nu_t}{\sigma_\varepsilon}\right)\frac{\partial \varepsilon}{\partial x_j}\right) \tag{3.33}$$

where $\nu_t = C_\mu k T$ and $C_{\varepsilon 1}^* = C_{\varepsilon 1}(1 + A_1 P/\varepsilon)$. As explained in Sec. 3.3.2 the modification to the $C_{\varepsilon 1}$ coefficient is required to take into account the near-wall terms of the exact dissipation rate equation. The constants of the model are given in Tab. 3.3.

C_1	C_2	C_T	C_L	C_η	C_μ	$C_{\varepsilon 1}$	$C_{\varepsilon 2}$	σ_ε	A_1
1.22	0.6	6.0	0.2	80	0.23	1.44	1.9	1.65	0.1

Table 3.3: Constants of the elliptic relaxation RSM model of Durbin (1993b)

This model has the advantage of avoiding damping functions, and takes into account non-locality, as it features an elliptic equation at the turbulent scale. Moreover, by giving specific limits to every f_{ij} (Eq. **??**) one ensures that the correct asymptotic behaviour of the Reynolds stresses is predicted. However 6 more equations have to be solved, compared to a classical RSM. A simpler way to use the elliptic relaxation is to combine it along with an eddy-viscosity model.

3.4.2 The $\overline{v^2} - f$ model (Durbin (1991))

This model stems from the standard $k - \varepsilon$ system (the ε equation being similar to that of the elliptic relaxation RSM, Eq. 3.33) and a third transport equation is solved for a scalar $\overline{v^2}$, which can be assimilated near solid walls to the wall-normal

fluctuations[9]. The $\overline{v^2}$ equation resembles the classical transport equation of the wall-normal Reynolds-stress component, and as in the RSM version, the difference between ϕ^*_{22} and ε_{22} is modelled as a whole:

$$\phi^*_{22} - \varepsilon_{22} = -\frac{2}{\rho}\overline{v\frac{\partial p}{\partial y}} - 2\nu\overline{\frac{\partial v}{\partial x_k}\frac{\partial v}{\partial x_k}} = \varphi_{22} - \varepsilon\frac{\overline{v^2}}{k} \tag{3.34}$$

and $\varphi_{22} = kf$ where f is solution of the elliptic equation:

$$f - L^2\Delta f = f_h \tag{3.35}$$

In order to ensure the correct asymptotic behaviour $\overline{v^2} = O(y^4)$ the following boundary condition should be used (similar to that of f_{22} (see Eq. **??**) in the RSM version):

$$\lim_{y\to 0} f = \lim_{y\to 0} \frac{-20\nu^2\overline{v^2}}{\varepsilon y^4} \tag{3.36}$$

Finally the model integrates $\overline{v^2}$ in the definition of the turbulent eddy viscosity:

$$\nu_t = C_\mu\overline{v^2}\max\left(\frac{k}{\varepsilon}, 6\sqrt{\frac{\nu}{\varepsilon}}\right) \tag{3.37}$$

Durbin (1991) showed that the use of the parameter $\overline{v^2}$ in Eq. 3.37 is the main feature allowing a correct reduction of the turbulent mixing in the buffer and viscous sublayer (as seen in Fig. 3.14).

Another feature of the model is an upper limiter for the turbulent time scale to avoid excessive turbulence level at stagnation point of impinging flows. The solution proposed in Durbin (1996) is similar to a strain rate S dependant C_μ included in some models (*e.g.* Craft et al. (1996); Menter (1994); Guimet and Laurence (2002)) and consists in an upper bound for the time scale (Eq. 3.32):

$$T = \min\left[\max\left(\frac{k}{\varepsilon}, C_T\sqrt{\frac{\nu}{\varepsilon}}\right), \frac{0.6k}{\sqrt{6}C_\mu\overline{v^2}S}\right] \tag{3.38}$$

3.4.3 The elliptic blending

The boundary conditions given for the elliptic variables f_{ij} require ratios of terms of order 4 to be evaluated at walls and this can constitute a numerical difficulty. This

[9]In the very general case, $\overline{v^2}$ can be seen as the normal stress in the direction aligned with the wall-distance gradient

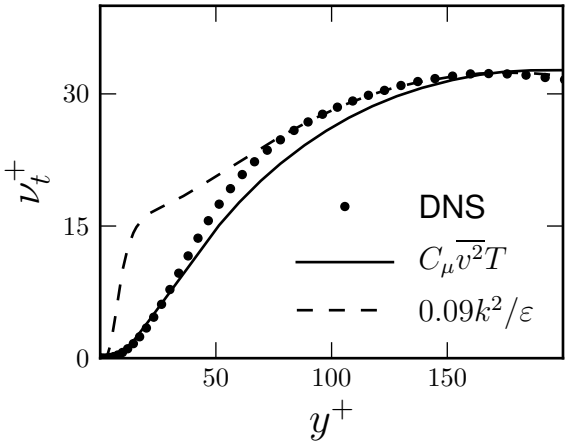

Figure 3.14: *A priori* evaluation of Eq. 3.37 and of the standard high Reynolds turbulent viscosity expression $C_\mu k^2/\varepsilon$, compared to the exact DNS value $-\overline{uv}/(\partial U/\partial y)$ for the channel flow case at $Re_\tau = 395$.

numerical problem holds also for the $\overline{v^2} - f$ version and this will be largely described in the next chapter. Based on this observation, and also noticing that there is a certain amount of redundancy in the 6 f_{ij} equations, Manceau and Hanjalić (2002) proposed a novel approach, consisting in solving an elliptic equation for a coefficient α taking the value 0 at walls and 1 in the remote region.

$$\alpha - L^2 \Delta\alpha = 1 \tag{3.39}$$

The blending parameter α is then used to define the pressure term ϕ_{ij}^* and the dissipation ε_{ij} as a blending between homogeneous and near-wall models. The near-wall model for ϕ_{ij}^*, noted $\phi_{ij,w}^*$ is defined such that the near-wall balance, Eq. 3.22, is respected. To this end, the following is prescribed:

$$\phi_{ij,w} = -5\frac{\varepsilon}{k}\left(\overline{u_i u_k} n_j n_k + \overline{u_j u_k} n_i n_k - \frac{1}{2}\overline{u_k u_l} n_k n_l (n_i n_j - \delta_{ij})\right) \tag{3.40}$$

Where the vector $\underline{n}$ is used to identify the wall normal direction, and defined as:

$$\underline{n} = \frac{\nabla\alpha}{||\nabla\alpha||} \tag{3.41}$$

Chapter 4

Comprehensive review of the $\overline{v^2} - f$ models

In the previous chapter, the use of an elliptic equation as a representation of the non-local effects of turbulence damping was presented in its general form as an alternative to the common damping-function-based near-wall RANS modelling. However, the eddy viscosity $\overline{v^2} - f$ approach as originally presented in Durbin (1991) would have remained in the academic world without further work on numerical aspects. In fact, it will now be seen that a main drawback of the original formulation of the $\overline{v^2} - f$ model is the requirement for $\overline{v^2}$ and f to be solved in a strongly coupled manner. For codes which solve the variables in a segregated way (*i.e.* one variable is solve at a time), that is in most popular codes, the original $\overline{v^2} - f$ model is highly unstable. After publication of the first version in 1991, a 20-year long period started, during which many fixes were proposed, leading to numerous subsequent versions, some of which were popularised by their availability in commercial codes, such as StarCD, StarCCM, Fluent or *Code_Saturne*. All the proposals are reviewed in the following, and their behaviour in different fundamental flows is assessed and compared. It will be seen that some variants, although more stable, results in inferior predictions. For some other versions, the deterioration is minimal, but the numerical problem is not quite solved.

Moreover during this 20-year long time span other variants of the $\overline{v^2} - f$ model

were proposed, whose aim was not to address the numerical issues but to improve the predictive capabilities of the original approach. The versions are also included in the review, not only for the sake of completeness, but also as a potential source of ideas for further developments.

4.1 Developments of the $\overline{v^2} - f$ model

4.1.1 Introduction

The purpose of the first version of the $\overline{v^2}-f$ model (Durbin, 1991) is to show the applicability of the elliptic relaxation technique, and the model proposed was only tested on the channel flow case, for $Re_\tau = 180$ and 395. A subsequent version (Durbin, 1993a) introduces a low-Reynolds-number modification for the dissipation-rate equation, and the model was validated for channel-flow and zero-pressure-gradient boundary-layer cases, without and with heat transfer. To further assess the model's abilities, simulation on a flat-plate boundary-layer with a heat transfer was also carried out, as well as on an adverse-pressure-gradient boundary-layer and a Couette flow. Not only was the model reported to perform well in all cases, but the author emphasises that the superiority of the model over virtually all low-Reynolds-number versions of the $k-\varepsilon$ formulation was due to the use of $\overline{v^2}$ as velocity scale in the turbulent viscosity expression. In Durbin (1995), the modification of the ε equation previously introduced is further refined to predict the correct shear-layer spreading rate both in a wall-bounded flow and in a free shear flow. This version is used to compute separated flows: a backward-facing-step flow and the asymmetric plane-diffuser case, as well as the vortex-shedding behind a triangular cylinder.

Some subsequent versions include proposals to enhance the $\overline{v^2} - f$ predictions in specific configurations (modification of the elliptic operator proposed in Wizman et al. (1996) (for the elliptic relaxation RSM) and adapted by Durbin and Laurence (1996) and Manceau et al. (2002b) to the $\overline{v^2} - f$ formulation to enhance predictions

in the logarithmic layer; distinction between wall-normal and wall-parallel eddy viscosity to improve the turbulent transport modelling (Davidson et al. (2003)); better integration of low-Reynolds-number effects to predict by-pass transition (Lien and Durbin, 1996)). However most of the work in the past 15 years focuses on simplifying the version of Durbin (1995) to make it more robust and code-friendly, thus enhancing the popularity of this approach, with the hope that the simplifications would not overly deteriorate the quality of predictions.

The major drawback of the $\overline{v^2} - f$ model is the stiffness implied by the boundary condition given to f, Eq. 3.36. The resolution of this problem is a prerequisite if the model is to be implemented in a segregated solver. The first solution was proposed by Lien and Durbin (1996) where a change of variable for f is introduced, which results in the f boundary condition being zero. This code-friendly version is later shown to strongly over-predict the pressure term in the logarithmic region, and other proposals were introduced and unlike Lien and Durbin (1996), they are based on the resolution of $\varphi = \overline{v^2}/k$ instead of $\overline{v^2}$. The latter modification reduces the boundary condition stiffness by two orders of magnitude (*i.e.* $O(y^2)$ instead of $O(y^4)$) and does not affect the prediction of the logarithmic layer. It has been simultaneously and independently implemented in two versions: Hanjalić et al. (2004) and Laurence et al. (2004). However, as will be seen the numerical robustness is not completely satisfactory in neither of them. The later version, with some further modifications (Uribe (2006)) is the model implemented in *Code_Saturne*.

In the early versions, numerical robustness is also impaired by additional terms in the ε equation (consisting of a modification of the $C_{\varepsilon 1}$ coefficient): its dependence on the production P_k (as done in Durbin (1993a)) introduces non-linearities, whereas its dependence on the wall distance y (in Durbin (1995) and Lien and Durbin (1996)) is in contradiction to the sought-after wall-distance free property of the elliptic relaxation concept. A coefficient $C_{\varepsilon 1}$ based on $\sqrt{\dfrac{k}{\overline{v^2}}}$ is proposed in Durbin and Laurence (1996). This removes the ability of the model to distinguish wall-bounded and free shear layers (because $\sqrt{\dfrac{k}{\overline{v^2}}}$ adopts roughly the same value in the two configurations), but the simplification makes the model easier to implement and more

stable. This modification is also added to the early models of Durbin (1995) (yielding Lien and Durbin (1996)) and Parneix and Durbin (1997) (yielding Lien and Kalitzin (2001)). The latter model is the one which is implemented in commercial codes such as StarCD, Fluent and StarCCM[1]. This simplified $C_{\varepsilon 1}$ coefficient is also retained in all other code-friendly models.

The issue of numerical robustness associated with the $\overline{v^2} - f$ model, being the main driving force of developments over the past 15 years, will now be described, along with the different solutions proposed.

4.1.2 Stability of the $\overline{v^2} - f$ model

The $\overline{v^2} - f$ model can be seen as a simplification of elliptic-relaxation-based RSM, and yet, this formulation paradoxically suffers from a serious lack of robustness. The use of $\overline{v^2}$ in ν_t is the main appealing feature of the model, and its relevance is undoubtedly demonstrated in Fig. 3.14 which shows that $\overline{v^2}$ is the appropriate near-wall turbulence damping parameter. For the variable $\overline{v^2}$ to correctly play its role, the correct asymptotic behaviour must be reproduced, that is $O(y^4)$, even though this matter is somehow nuanced in Durbin (1991)[2].

The origin of the numerical problem

The equation governing $\overline{v^2}$ reads:

$$\frac{D\overline{v^2}}{Dt} = \underbrace{\phi_{22}^* - \left(\varepsilon_{22} - \frac{\overline{v^2}}{k}\varepsilon\right)}_{\varphi_{22}} - \frac{\overline{v^2}}{k}\varepsilon + \nu\frac{\partial^2\overline{v^2}}{\partial x_j^2} - \frac{\partial\overline{vvu_k}}{\partial x_k} \tag{4.1}$$

The Taylor series expansion of the different right-hand-side terms are:

[1] for the later code, the definition of $C_{\varepsilon 1}$ is slightly altered.

[2] In the momentum equation the turbulent viscosity is indeed defined as $-\overline{uv}/(\partial U/\partial y)$ which behaves as $O(y^3)$, whereas Durbin's definition for ν_t $(= C_\mu\overline{v^2}T)$ behaves as $O(y^4)$. As pointed out by the same author what really matters near the wall is the molecular diffusion and its dominance with respect to the turbulent one. The model should then only ensure that the predicted ν_t is of order at least as high as the theoretical one, to preserve the dominance of ν.

$$\begin{cases} \varphi_{22} = A_\varphi y^2 + O(y^3) \\ \frac{\overline{v^2}}{k}\varepsilon = A_0 y^2 + O(y^3) \\ \nu \frac{\partial^2 \overline{v^2}}{\partial x_k} = A_\nu y^2 + O(y^3) \\ \frac{\partial \overline{vvu_k}}{\partial x_k} = O(y^5) \end{cases} \tag{4.2}$$

The correct reproduction of $\overline{v^2} << y^2$ requires $A_\varphi - A_0 + A_\nu = 0$ (from the near-wall balance Eq. 3.24) and this is achieved with the wall limit for f given in Eq. 3.36. In a segregated solver this ratio of two terms of order 4 is handled explicitly (because the term $\overline{v^2}$ appearing in the numerator of Eq. 3.36 is explicit) and is in practice evaluated at the first off-wall cell which can lead to a severe numerical stiffness.

Solutions in a segregated solver

The code-friendly solutions proposed to ensure the near-wall equilibrium of Eq. 4.1 are now presented (the notations of Taylor series expansions Eq. 4.2 are used herein).

Method 1: A near-wall equivalent for f is used in the $\overline{v^2}$ equation, if a decomposition of the following form can be derived: $\varphi_{22} = kf = k\overline{f} - \varphi_{22,w}\overline{v^2}$, with the auxiliary functions $\overline{f}$ and ψ having the following properties:

$$\begin{cases} -\psi \overline{v^2} = A_\varphi y^2 + O(y^3) \\ \lim\limits_{y \to 0} \overline{f} = 0 \end{cases} \tag{4.3}$$

The function $-\varphi_{22,w}\overline{v^2}$ which "carries" the boundary condition is handled implicitly in the $\overline{v^2}$ equation and an elliptic equation is solved for $\overline{f}$ with the homogeneous Dirichlet boundary condition.

Method 2: A transport equation is not solved for $\overline{v^2}$ but for $\varphi = \overline{v^2}/k^p$. The transport equation for φ becomes:

$$\begin{aligned}\frac{D\varphi}{Dt} &= \frac{f}{k^{p-1}} - \frac{\varphi}{k}\left[pP_k + (p-1)\varepsilon\right] + \frac{2p}{k}\left(\nu + \frac{\nu_t}{\sigma_k}\right)\frac{\partial\varphi}{\partial x_k}\frac{\partial k}{\partial x_k} + \\ & p(1-p)\frac{\varphi}{k^2}(\nu + \frac{\nu_t}{\sigma_k})\frac{\partial k}{\partial x_k}\frac{\partial k}{\partial x_k} + \frac{\partial}{\partial x_k}\left[\left(\nu + \frac{\nu_t}{\sigma_\varphi}\right)\frac{\partial\varphi}{\partial x_k}\right] \qquad (4.4)\end{aligned}$$

The near-wall dominant terms of Eq. 4.4 are now of order $O\left(y^{2-2p}\right)$.

In practice, code-friendly versions are combinations of the methods 1 and 2.

The solution introduced in Lien and Durbin (1996)

The method 1 is used and leads to the following change of variable: $\overline{f} = f + 5\varepsilon\frac{\overline{v^2}}{k^2}$, with the new limit $\lim_{y\to 0}\overline{f} = 0$. The term $\Delta\left(5\varepsilon\frac{\overline{v^2}}{k^2}\right)$ is neglected in the $\overline{f}$ equation and this leads to a strong over-prediction of $\overline{v^2}$ in the logarithmic layer, as it will be seen. This motivated further developments of code-friendly versions.

The reduced variable $\varphi = \overline{v^2}/k$

The method 2 is used in Laurence et al. (2004), Uribe (2006) and in Hanjalić et al. (2004) with $p = 1$. The transport equation is solved for $\varphi = \dfrac{\overline{v^2}}{k}$ and the leading-order terms of the φ equation, f, $\nu\dfrac{\partial^2\varphi}{\partial x_k^2}$ and $\dfrac{2\nu}{k}\dfrac{\partial k}{\partial x_k}\dfrac{\partial\varphi}{\partial x_k}$ are $O(1)$. The φ transport equation becomes:

$$\frac{D\varphi}{Dt} = f - \frac{\varphi}{k}P_k + \frac{\partial}{\partial x_k}\left[\left(\nu + \frac{\nu_t}{\sigma_\varphi}\right)\frac{\partial\varphi}{\partial x_k}\right] + \frac{2}{k}\left(\frac{\nu_t}{\sigma_\varphi} + \nu\right)\frac{\partial k}{\partial x_k}\frac{\partial\varphi}{\partial x_k} \qquad (4.5)$$

By noting $\varphi = A_\varphi y^2 + O(y^3)$, the Taylor series expansion of the near-wall leading order terms is:

$$\begin{aligned}\frac{2\nu}{k}\frac{\partial k}{\partial y}\frac{\partial\varphi}{\partial y} \sim 2\nu\frac{2A_k y}{A_k y^2}2A_\varphi y \sim 8\nu A_\varphi \sim 8\nu\frac{\varphi}{y^2} \\ \nu\frac{\partial^2\varphi}{\partial y^2} \sim 2\nu A_\varphi \sim 2\nu\frac{\varphi}{y^2} \qquad (4.6)\end{aligned}$$

Hence the balance between the three leading-order terms leads to:

$$f_w = -10\nu\frac{\varphi}{y^2} \qquad (4.7)$$

This is an improvement compared to Eq. 3.36 because the order of the stiffness is reduced from 4 to 2. The model of Hanjalić et al. (2004) solves the $\varphi - f$ system as just described, but the cross-diffusion term in the φ equation is neglected for the sake of simplicity. Due to this later simplification, the f boundary condition becomes $1/5\times$ Eq. 4.7. Observing that this boundary condition still strongly impairs the numerical stability[3] (compared to Lien and Durbin (1996)), Laurence et al. (2004) proposed an additional code-friendly modification[4].

The model of Laurence et al. (2004) combines method 1 and method 2: an equation is solved for the reduced variable φ, but a change of variable is made for f to enable a zero boundary condition for this variable. There are different possibilities for this change of variable. The aim is to find a decomposition $f = \overline{f} + g$ such that

$$\lim_{y\to 0} g = \lim_{y\to 0} f = \lim_{y\to 0} \left(-\frac{2\nu}{k}\frac{\partial k}{\partial y}\frac{\partial \varphi}{\partial y} - \nu\frac{\partial^2 \varphi}{\partial y^2} \right) \tag{4.8}$$

To find such a function, the molecular cross-diffusion and the molecular diffusion can be used in the form shown in Eq.4.6. Using a near-wall equivalent for the dissipation, $\varepsilon \sim 2\nu\dfrac{k}{y^2}$, an equivalent ε based function can also be used to reproduce the near-wall behaviour of φ:

$$\varepsilon\frac{\varphi}{k} \sim 2\nu\frac{\varphi}{y^2} \tag{4.9}$$

The most general form for the g function is then

$$g = -\frac{\alpha}{2}\left(\frac{\varepsilon}{k}\varphi\right) - \frac{\beta}{8}\left(\frac{2\nu}{k}\frac{\partial k}{\partial y}\frac{\partial \varphi}{\partial y}\right) - \frac{\gamma}{2}\left(\nu\frac{\partial^2 \varphi}{\partial y^2}\right) \tag{4.10}$$

The limit of g when y tends to zero reads $g_0 = (\alpha + \beta + \gamma)\nu\varphi/y^2$. Hence the coefficients must satisfy $\alpha + \beta + \gamma = 10$.

The $\varphi - \overline{f}$ system with the change of variable reads:

[3]This model was implemented into *Code_Saturne* in the course of this work and the time step had to be drastically reduced in order to get convergence.

[4]Noteworthily the model of Hanjalić et al. (2004) has very recently been improved in Popovac (2010) to accomodate an homogeneous boundary condition for f, following the same path as Uribe (2006), aiming at an improved numerical robustness.

$$\begin{aligned}\frac{\partial \varphi}{\partial t} + U_j \frac{\partial \varphi}{\partial x_j} &= \overline{f} - \frac{P_k}{k}\varphi - \frac{\varepsilon}{k}\varphi\frac{\alpha}{2} + \frac{2}{k}\left[\nu\left(1-\frac{\beta}{8}\right) + \frac{\nu_t}{\sigma_\varphi}\right]\frac{\partial k}{\partial x_k}\frac{\partial \varphi}{\partial x_k} \\ &\quad + \frac{\partial}{\partial x_k}\left[\left((1-\frac{\gamma}{2})\nu + \frac{\nu_t}{\sigma_\varphi}\right)\frac{\partial \varphi}{\partial x_k}\right] \end{aligned} \tag{4.11}$$

$$L^2\nabla^2\overline{f} - \overline{f} = \frac{1}{T}\left(C_1 - 1\right)\left(\varphi - \frac{2}{3}\right) - C_2\frac{P_k}{k} + g - L^2\Delta g \tag{4.12}$$

The choice for the three coefficients is ruled by the following constraints:

- The part of g included in the cross diffusive term cannot easily be handled implicitly (unless the convective velocity is changed), hence $\beta = 0$ should be preferred[5].

- The coefficient γ is involved in the φ molecular diffusion which should preferably be positive, thus $1 - \frac{\gamma}{2} > 0$.

- The term $L^2\Delta g$ in the $\overline{f}$ equation is likely to be neglected in some implementations, or in any case explicit, therefore the coefficients should be chosen so that it is as small as possible.

In the final set of equations used in Laurence et al. (2004), the choice ($\alpha = 0, \beta = 8, \gamma = 2$) has been made. Uribe (2006) showed that one can hardly decide whether or not the term $L^2\Delta g$ appearing in the $\overline{f}$ equation is negligible, but in isotropic cases, the term neglected vanishes unlike the one neglected in the model of Lien and Durbin (1996). However as it is the model is still unstable, because the choice $\gamma = 2$ leads to a zero molecular viscosity which yields instabilities. In the discretisation used in *Code_Saturne*, in which the model was intended, the wall boundary condition for φ expresses itself solely with the molecular diffusive flux. The later choice for β does not guarantee zero value for φ at walls. Therefore in the version finally implemented in *Code_Saturne* , the molecular diffusion is re-introduced in the φ equation. This model is described in Uribe (2006). This improves the numerical stability, but the near-wall asymptotic equilibrium is no longer ensured and in the model of Uribe (2006), the variable φ is erroneously predicted as linear instead of quadratic.

[5] an implicit treatment is preferred in a segregated solver for near-wall leading terms.

DUR91	Durbin (1991)
DUR93	Durbin (1993a)
DUR95	Durbin (1995)
DUR96	Durbin and Laurence (1996)
LIE96	Lien and Durbin (1996)
PAR97	Parneix and Durbin (1997)
LIE01	Lien and Kalitzin (2001)
MAN02	Manceau et al. (2002b)
HAN04	Hanjalić et al. (2004)
URI06	Uribe (2006)

Table 4.1: Acronyms used for models

4.2 Comparison of the different versions

The following presents a comparison of all the versions introduced and highlights some limitations, which motivates the present work. Hereafter, the models will be referred to by the acronyms given in Tab. 4.1.

The models equations and constants

The definition of all studied models (terms and constants) is given in the following. For a simpler comparison the following generic form is adopted for the equations[6].

$$\begin{aligned}
\frac{Dk}{Dt} &= P_k - \varepsilon + \frac{\partial}{\partial x_j}\left[\left(\nu + \frac{\nu_t}{\sigma_k}\right)\frac{\partial k}{\partial x_j}\right] \\
\frac{D\varepsilon}{Dt} &= \frac{C^*_{\varepsilon 1}P_k - C_{\varepsilon 2}\varepsilon}{T} + \frac{\partial}{\partial x_j}\left[\left(\nu + \frac{\nu_t}{\sigma_\varepsilon}\right)\frac{\partial \varepsilon}{\partial x_j}\right] \\
\frac{Dg}{Dt} &= \mathcal{P}_g + \frac{\partial}{\partial x_j}\left[\left(\nu + \frac{\nu_t}{\sigma_g}\right)\frac{\partial g}{\partial x_j}\right] \\
-L^2\Delta f + f &= f_h
\end{aligned} \tag{4.13}$$

$$\begin{aligned}
L &= C_L max\left[\frac{k^{3/2}}{\varepsilon}, C_\eta\left(\frac{\nu^3}{\varepsilon}\right)^{1/4}\right] \\
T &= max\left[\frac{k}{\varepsilon}, C_T\left(\frac{\nu}{\varepsilon}\right)^{1/2}\right]
\end{aligned} \tag{4.14}$$

[6]To prevent excessive growth of turbulence of impinging flows, the use of an upper bound for the time and length scale (as presented in the previous chapter, Eq. 3.38) was used in models LIE01, MAN02 and HAN04. For the sake of simplicity we do not mention it here given the present comparison does not cover impinging flows.

Model	f	f_h	C_1	C_2
DUR91	$\frac{\varphi_{22}}{k}$	$\frac{1}{T}(C_1-1)\left(\frac{2}{3}-\frac{\overline{v^2}}{k}\right)+C_2\frac{P_k}{k}$	1.2	0.3
DUR93	$\frac{\varphi_{22}}{k}$	$\frac{1}{T}(C_1-1)\left(\frac{2}{3}-\frac{\overline{v^2}}{k}\right)+C_2\frac{P_k}{k}$	1.3	0.3
DUR95	$\frac{\varphi_{22}}{k}$	$\frac{1}{T}(C_1-1)\left(\frac{2}{3}-\frac{\overline{v^2}}{k}\right)+C_2\frac{P_k}{k}$	1.4	0.3
DUR96	$L\frac{\varphi_{22}}{k}$	$L\left[\frac{1}{T}(C_1-1)\left(\frac{2}{3}-\frac{\overline{v^2}}{k}\right)+C_2\frac{P_k}{k}\right]$	1.3	0.35
LIE96	$\frac{\varphi_{22}}{k}+5\varepsilon\frac{\overline{v^2}}{k^2}$	$\frac{1}{T}\left[(C_1-1)\frac{2}{3}-(C_1-6)\frac{\overline{v^2}}{k}\right]+C_2\frac{P_k}{k}$	1.4	0.3
PAR97	$\frac{\varphi_{22}}{k}$	$\frac{1}{T}(C_1-1)\left(\frac{2}{3}-\frac{\overline{v^2}}{k}\right)+C_2\frac{P_k}{k}$	1.4	0.3
LIE01	$\frac{\varphi_{22}}{k}+5\varepsilon\frac{\overline{v^2}}{k^2}$	$\frac{1}{T}\left[(C_1-1)\frac{2}{3}-(C_1-6)\frac{\overline{v^2}}{k}\right]+C_2\frac{P_k}{k}$	1.4	0.3
MAN02	$\frac{\varphi_{22}}{\varepsilon k}$	$\frac{1}{\varepsilon T}(C_1-1)\left(\frac{2}{3}-\frac{\overline{v^2}}{k}\right)+\frac{2}{3}C_2\frac{P_k}{\varepsilon k}$	1.8	0.4
HAN04	$\frac{\varphi_{22}}{k}$	$\frac{1}{T}\left(C_1-1+C_2\frac{P_k}{\varepsilon}\right)\left(\frac{2}{3}-\frac{\overline{v^2}}{k}\right)$	1.4	0.65
URI06	$\frac{\varphi_{22}}{k}+\frac{2\nu}{k}\frac{\partial\left(\overline{v^2}/k\right)}{\partial x_j}\frac{\partial k}{\partial x_j}+\nu\frac{\partial^2\left(\overline{v^2}/k\right)}{\partial x_j^2}$	$\frac{1}{T}(C_1-1)\left(\frac{2}{3}-\frac{\overline{v^2}}{k}\right)+C_2\frac{P_k}{k}+2\frac{\nu}{\varepsilon T}\frac{\partial k}{\partial x_k}\frac{\partial\left(\overline{v^2}/k\right)}{\partial x_k}+\nu\frac{\partial^2\left(\overline{v^2}/k\right)}{\partial x_k^2}$	1.4	0.3

Table 4.2: Terms and coefficients of the f equation

$$
\begin{aligned}
L &= \sqrt{C_L^2\left(\frac{k^3}{\varepsilon^2}+C_\eta^2\frac{\nu^{3/2}}{\varepsilon^{1/2}}\right)} \\
T &= \sqrt{\frac{k^2}{\varepsilon^2}+C_T^2\frac{\nu}{\varepsilon}}
\end{aligned}
\tag{4.15}
$$

The f equation Tab. 4.2 gives the definition of the elliptic variable f, its homogeneous counterpart f_h as well as the constants used. The models DUR91, DUR93, DUR95, PAR97 and HAN04 resolve an equation for the variable φ_{22}/k whereas LIE96 and LIE01 use the change of variable $\overline{f} = f + 5\varepsilon\overline{v^2}/k^2$ as a code-friendly variation. In URI06 a change of variable for f is also performed as described in the previous section. DUR96 and MAN02 solve the elliptic equation for a "rescaled" variable $A \times f$ with $A = L$ for DUR96 and $A = \varepsilon^{-1}$ for MAN02. As it will be seen later this reduces the undesired amplification effect of the elliptic operator in the logarithmic layer. For f_h all models keep the original choice of DUR91 to use a LRR-IP model, except the model HAN04 which uses the SSG model.

Model	g	$\mathcal{P}_g$
DUR91	$\overline{v^2}$	$kf - \overline{v^2}\frac{\varepsilon}{k}$
DUR93	$\overline{v^2}$	$kf - \overline{v^2}\frac{\varepsilon}{k}$
DUR95	$\overline{v^2}$	$kf - \overline{v^2}\frac{\varepsilon}{k}$
DUR96	$\overline{v^2}$	$\frac{k}{L}f - \overline{v^2}\frac{\varepsilon}{k}$
LIE96	$\overline{v^2}$	$kf - 6\overline{v^2}\frac{\varepsilon}{k}$
PAR97	$\overline{v^2}$	$kf - \overline{v^2}\frac{\varepsilon}{k}$
LIE01	$\overline{v^2}$	$kf - 6\overline{v^2}\frac{\varepsilon}{k}$
MAN02	$\overline{v^2}$	$k\varepsilon f - \overline{v^2}\frac{\varepsilon}{k}$
HAN04	$\frac{\overline{v^2}}{k}$	$f - \frac{\overline{v^2}}{k^2}P_k$
URI06	$\frac{\overline{v^2}}{k}$	$f - \frac{\overline{v^2}}{k^2}P_k + \frac{2}{k}\frac{\nu_t}{\sigma_k}\frac{\partial k}{\partial x_k}\frac{\partial\left(\overline{v^2}/k\right)}{\partial x_k}$

Table 4.3: Terms and coefficients of the g equation. Note that $\sigma_g = 1.2$ for HAN04 and $\sigma_g = \sigma_k$ for all other models.

Model	$C^*_{\varepsilon 1}$	$C_{\varepsilon 2}$	σ_k	σ_ε
DUR91	1.7	2.0	1.3	1.6
DUR93	$1.44\left(1 + 0.1\frac{P_k}{\varepsilon}\right)$	1.9	0.9	1.3
DUR95	$1.3 + \frac{0.25}{\left[1+\left(\frac{C_L y}{2L}\right)^8\right]}$	1.9	1	1.3
DUR96	$1.44\left(1 + \frac{1}{30}\sqrt{\frac{k}{\overline{v^2}}}\right)$	1.85	1	1.5
LIE96	$1.55 + exp\left(-0.00285R_y^2\right)$	1.92	1	1.5
PAR97	$1.4\left(1 + 0.045\sqrt{\frac{k}{\overline{v^2}}}\right)$	1.9	1	1.3
LIE01	$1.4\left(1 + 0.05\sqrt{\frac{k}{\overline{v^2}}}\right)$	1.9	1	1.3
MAN02	$1.44\left(1 + 0.06\sqrt{\frac{k}{\overline{v^2}}}\right)$	1.91	1	1.3
HAN04	$1.4\left(1 + 0.012\frac{k}{\overline{v^2}}\right)$	1.9	1	1.3
URI06	$1.4\left(1 + 0.05\sqrt{\frac{k}{\overline{v^2}}}\right)$	1.85	1	1.3

Table 4.4: Terms and coefficients of the ε equation. In LIE96 $Re_y = y\sqrt{k}/\nu$

Model	expression for L and T	C_L	C_η	C_T	C_μ
DUR91	Eq. 4.14	0.17	80	6	0.2
DUR93	Eq. 4.14	0.2	90	6	0.23
DUR95	Eq. 4.14	0.3	70	6	0.19
DUR96	Eq. 4.15	0.2	60	4	0.16
LIE96	Eq. 4.14	0.17	70	6	0.19
PAR97	Eq. 4.14	0.25	85	6	0.22
LIE01	Eq. 4.14	0.23	70	6	0.22
MAN02	Eq. 4.14	0.23	100	6	0.22
HAN04	Eq. 4.14	0.36	85	6	0.22
URI06	Eq. 4.14	0.25	110	6	0.22

Table 4.5: Lengh and time scales

The g equation: Table 4.3 gives the definition of the variable g and its source term $\mathcal{P}_g$. For all models $g = \overline{v^2}$, except HAN04 and URI06 who solve, as noted previously, $g = \overline{v^2}/k$ to enhance the numerical stability.

The ε equation: Table 4.4 gives the expression of the $C_{\varepsilon 1}$ coefficient, as well as the other constants involved in the ε equation. The main difference between models lies in the definition of the variable coefficient $C^*_{\varepsilon 1}$. Only DUR93 uses a production based coefficient, which was later shown to introduce non-linearities. DUR95 and LIE96 use the distance to the nearest wall. The aim in DUR95 is to make a distinction between wall-bounded and free shear flows, whereas in LIE96 the presence of Re_y improves the by-pass transition prediction. All other models use the wall-normal anisotropy for the sake of robustness. The values taken by $C^*_{\varepsilon 1}$ for all models are shown in Fig. 4.1 in a channel flow for $Re_\tau = 2000$, and it can be seen that the effects and intentions of the different models are very different from one another.

- For all models for which $C^*_{\varepsilon 1}$ depends on $\overline{v^2}/k$ the behaviour is the same: $\lim_{y\to 0} C^*_{\varepsilon 1} = +\infty$ in order to increase the near-wall production term of the ε equation. The singularity introduced has no consequence because the product $C^*_{\varepsilon 1} P_k/T$ retains a finite near-wall limit. Further away from the wall, the variation of $C^*_{\varepsilon 1}$ is linked to that of $\sqrt{k/\overline{v^2}}$. The later variable levels off in the logarithmic layer then further decreases towards the channel centre[7]. The same trend is noticed for $C^*_{\varepsilon 1}$. The plateau observed for all models is far less obvious in HAN04. This is because $k/\overline{v^2}$ is used instead of $\sqrt{k/\overline{v^2}}$ in the latter case.

- The use of $exp\left(-aRe_y^2\right)$ by LIE96 results in a sharp boosting of the coefficient in the near-wall region and the constant value 1.55 is recovered elsewhere.

- By using P_k/ε, the resulting $C^*_{\varepsilon 1}$ of DUR93 peaks in the buffer layer as does the production, hence the purpose of increasing the near-wall dissipation is achieved (even though the coefficient decreases again towards the wall, it may be argued

[7]The theoretical isotropic relation $\overline{v^2} = 2/3\ k$ is not reached in a channel flow.

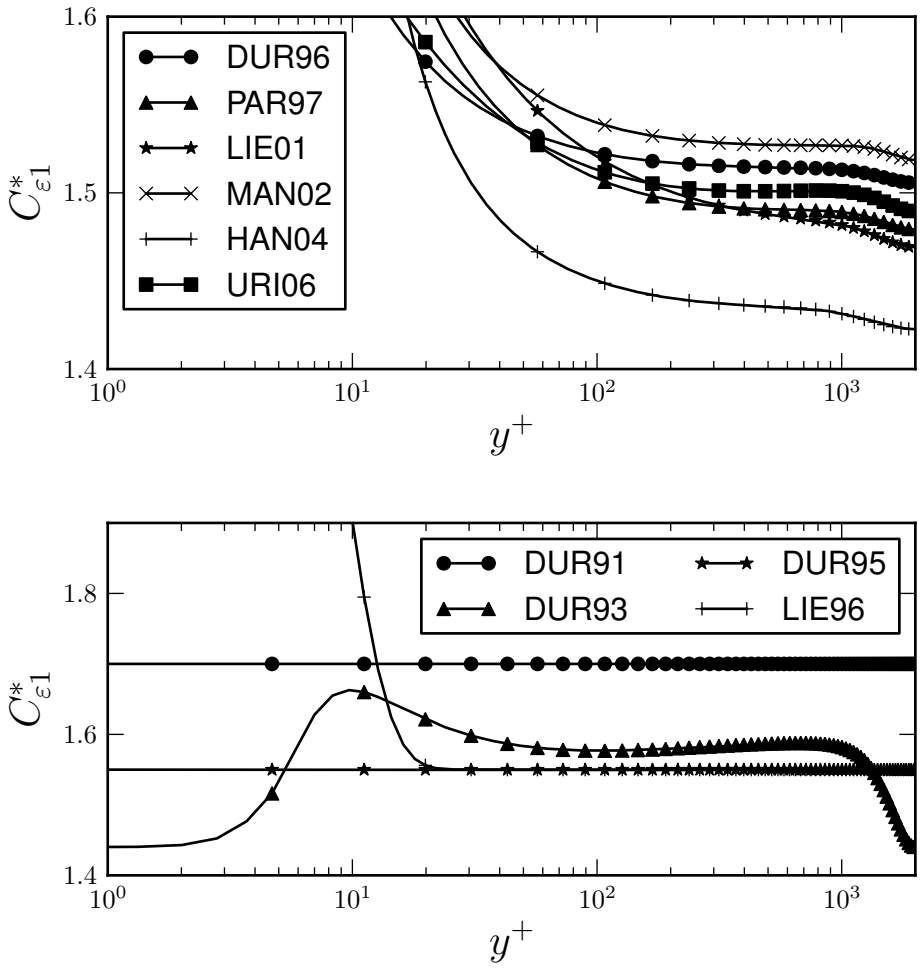

Figure 4.1: *A priori* evaluation of $C^*_{\varepsilon 1}$ in a channel flow for $Re_\tau \in \{2000\}$. Top: Models for which $C^*_{\varepsilon 1}$ depends on $\frac{\overline{v^2}}{k}$. Bottom: Other models

that the ε wall behaviour mainly depends on its boundary condition and no longer on the source terms of its equation).

- In the model of DUR95 the coefficient is intended to be exactly 1.55 in a boundary layer and this is achieved with the purposely designed function $0.25/\left[1+\left(\frac{C_L y}{2L}\right)^8\right]$ (y being the wall distance). L is taken from Eq. 4.14, and because of the lower limiter for L, there is no increase of the $C^*_{\varepsilon 1}$ coefficient in the near-wall region and hence the model inherits the shortcomings involved by using the high Reynolds $k-\varepsilon$ equations down to the wall[8].

- The coefficient $C^*_{\varepsilon 1}$ predicted by DUR93 and DUR95 reverts to a smaller value in the regions remote from walls. In channel-flow, this is much more obvious for DUR93 as seen in Fig. 4.1 where the coefficient varies from nearly 1.6 in the logarithmic layer to 1.44 in the defect layer. For DUR95 this change is less visible here but the $C^*_{\varepsilon 1}$ modification was shown to be active in the asymmetric diffuser case (Durbin (1995)).

The turbulent scales Tab. 4.5 gives the definition of the scales used (time and length) as well as the constants values. They are limited by a Kolmogorov scale to represent low-Reynolds-number effects. The switch is achieved in all models with the function max, except for DUR96 where a quadratic mean expression is used for a smoother transition between the two scales. Tab. 4.6 and 4.7 give the *a posteriori* location in wall-units of the switch for the length and time scales respectively, for all models except DUR96. The integral time-scale is used in most of the domain, the Kolmogorov time-scale being used only for $y^+ < 2$ for all models. However it can be seen that the Kolmogorov length-scale is used in a much larger extent. For $Re_\tau = 180$ it is used by all models over the whole domain, this being the case for URI06 and MAN02 also for $Re_\tau = 395$. For larger values of C_η Kolmogorov scaling is extended to a larger part of the domain[9].

[8] This shows, at light of the satisfactory results of Durbin (1995), that a careful constant tuning successfully helped limit the implications of this shortcoming.

[9] This is not straighforward since the values given here are *a posteriori*.

Model	$Re_\tau = 180$	$Re_\tau = 395$	$Re_\tau = 590$	$Re_\tau = 950$	$Re_\tau = 2000$
DUR91	180	320	279	226	195
DUR93	180	311	329	295	247
DUR95	180	182	156	136	118
DUR96	N/A	N/A	N/A	N/A	N/A
LIE96	180	203	192	170	155
PAR97	180	292	279	241	213
LIE01	180	228	209	183	164
MAN02	180	395	389	347	288
HAN04	180	283	260	226	195
URI06	180	395	486	460	375

Table 4.6: *A posteriori* location $y^+_{s,L}$ of the switch between the Kolmogorov and the integral length-scale in wall-unit, in a channel flow for $Re_\tau \in \{180; 395; 590; 950; 2000\}$

Model	$Re_\tau = 180$	$Re_\tau = 395$	$Re_\tau = 590$	$Re_\tau = 950$	$Re_\tau = 2000$
DUR91	2.6	2.4	2.2	2.0	2.0
DUR93	2.6	2.4	2.2	2.0	2.0
DUR95	1.9	1.9	2.2	2.0	2.0
DUR96	N/A	N/A	N/A	N/A	N/A
LIE96	2.6	2.4	2.8	2.5	2.8
PAR97	2.6	2.4	2.2	2.5	2.0
LIE01	2.6	2.4	2.2	2.0	2.0
MAN02	2.6	2.4	2.2	2.5	2.8
HAN04	2.6	2.4	2.8	2.5	2.8
URI06	2.6	2.4	2.2	2.0	2.0

Table 4.7: *A posteriori* location $y^+_{s,T}$ of the switch between the Kolmogorov and the integral time-scale in wall-unit, in a channel flow for $Re_\tau \in \{180; 395; 590; 950; 2000\}$

4.2.1 Behaviour in a channel flow

In the following, model predictions are compared in the channel flow case. Profiles for different variables are shown for $Re_\tau \in \{395; 2000\}$: $\overline{U}^+$ (Fig.4.2), $y^+ d\overline{U}^+/dy^+$ (Fig. 4.3), k^+ (Fig. 4.4), ε^+ (Fig. 4.5), $y^+\varepsilon^+$ (Fig.4.6), φ (Fig. 4.7) and $k^+/(y^+\varepsilon^+)$ (Fig.4.8). As seen in Fig. 4.2, the mean stream-wise velocities are consistently well predicted, this can be attributed to the fact that models are generally calibrated using this test case. Tab. 4.8 shows the friction coefficient C_f calculated for all models for five different Reynolds numbers. It confirms a generally good agreement consistent for all models and regardless of the Reynolds number, with an error often lying within the 5%. Some discrepancies can be noted, however:

- DUR93 depicts a consistent under-prediction of C_f (mirroring an over-prediction of the velocity profile).
- LIE96, PAR97, LIE01 and HAN04 show a relatively strong under-prediction of C_f for the lowest Re_τ, LIE01 being by far the worst.
- URI06 tends to over-predict C_f for high Re_τ.

However a closer look at the velocity predictions by scrutinising the variable $y^+\dfrac{d\overline{U}^+}{dy^+}$ (as introduced in Subsec. 3.2.2) shows substantial differences between models. They do not predict equally well the near-wall peak of $y^+\dfrac{d\overline{U}^+}{dy^+}$: the models LIE96, PAR97 and HAN04 seem to be the best ones in the near-wall region; all the other versions under-predicting the peak. In the logarithmic region, some models are unable to predict the correct von Kármán constant (even at $Re_\tau = 2000$) (recall that in this region, $y^+\dfrac{d\overline{U}^+}{dy^+}=1/\kappa$ at infinite Reynolds number). For instance, the variable $y^+\dfrac{d\overline{U}^+}{dy^+}$ is over-predicted for early models (DUR91, DUR93, DUR95) and under-predicted for LIE96 and LIE01. For the two latter models, it will be seen that this under-prediction (hence over-prediction of κ) becomes far more obvious for infinite Reynolds number. It is also noteworthy that none of the models (except for DUR95 to some extent) is able to represent the Re_τ independance of the variables indicated by the DNS data up to $y^+ = 60$.

The model for $C^*_{\varepsilon 1}$ (see Tab. 4.4) affects the behaviour of ε in the viscous and buffer layer, hence the near-wall behaviour of k (due to the ε boundary condition, Eq. 3.14). This explains the difference between models in the prediction of k and ε near the wall, as shown in Fig. 4.4 and Fig. 4.5, respectively. Note that the absence of near-wall modification for the ε equation in DUR95 leads to a strong over-prediction of k for this model. In the logarithmic layer ε^+ behaves as $(y^+)^{-1}$; hence it is easier to spot the differences between models with the variable $y^+\varepsilon^+$, as shown in Fig. 4.6. In this region, predictions of ε are mainly affected by the difference $C^*_{\varepsilon 1} - C_{\varepsilon 2}$, since it is expected that $P_k = \varepsilon$. The models performing the best are LIE96, PAR97 and HAN04, with other models over-predicting $y^+\varepsilon^+$ in the log layer. Finally, it is clear that all models under-predict ε^+ in the defect layer, as shown in Fig. 4.6.

Fig. 4.7 shows the predictions of $\varphi = \overline{v^2}^+/k^+$. Virtually all models over-predict φ in the logarithmic region, with LIE96 and LIE01 being the worst. It will be seen that this discrepancy is due to an ill-behaviour of the elliptic operator, amplifying the redistribution term in the log layer. For LIE96 and LIE01, a term is neglected in the $\overline{v^2}$ equation leading to an even more drastic overshoot. Lastly, this variable is somehow over-represented by URI06 in the near-wall region. This is due to the fact that it is erroneously predicted as $O(y)$ instead of $O(y^2)$, as previously stated.
More generally, the variability observed in the φ prediction in the log region depends on the model for the quasi-homogeneous part of the pressure term and the constant used, as detailed in Tab. 4.2.

Finally, Fig. 4.8 shows the prediction of $k^+/(\varepsilon^+ y^+)$ which represents the rescaled turbulent time scale. It naturally reflects the predictions of k and ε. The overshoot of this variable in the defect layer is explained by the observed undershoot of ε in the same region.

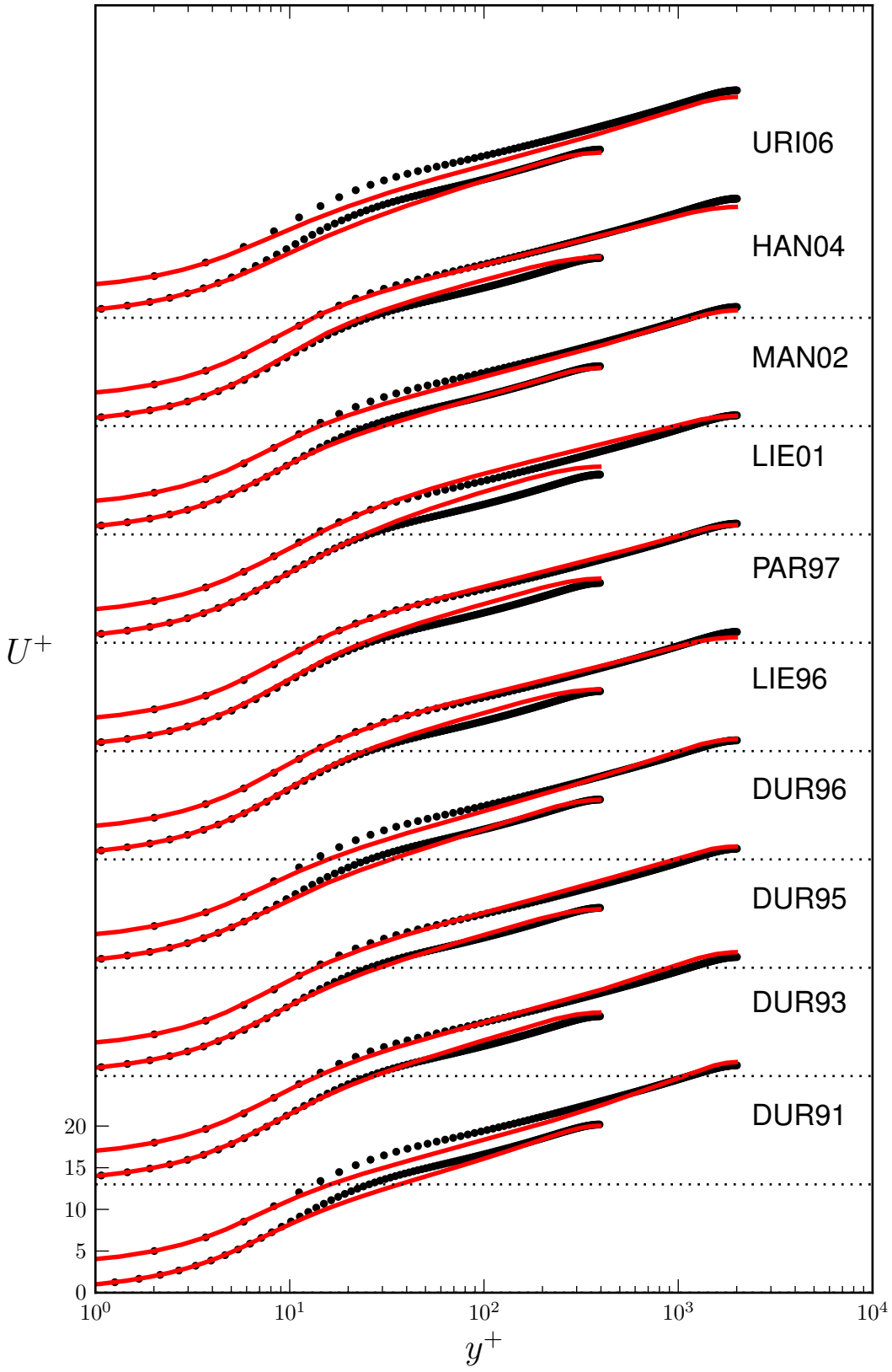

Figure 4.2: $\overline{U}^+$ in a channel flow for $Re_\tau \in \{395; 2000\}$ ($Re_\tau = 2000$ profiles are shifted upwards for clarity)

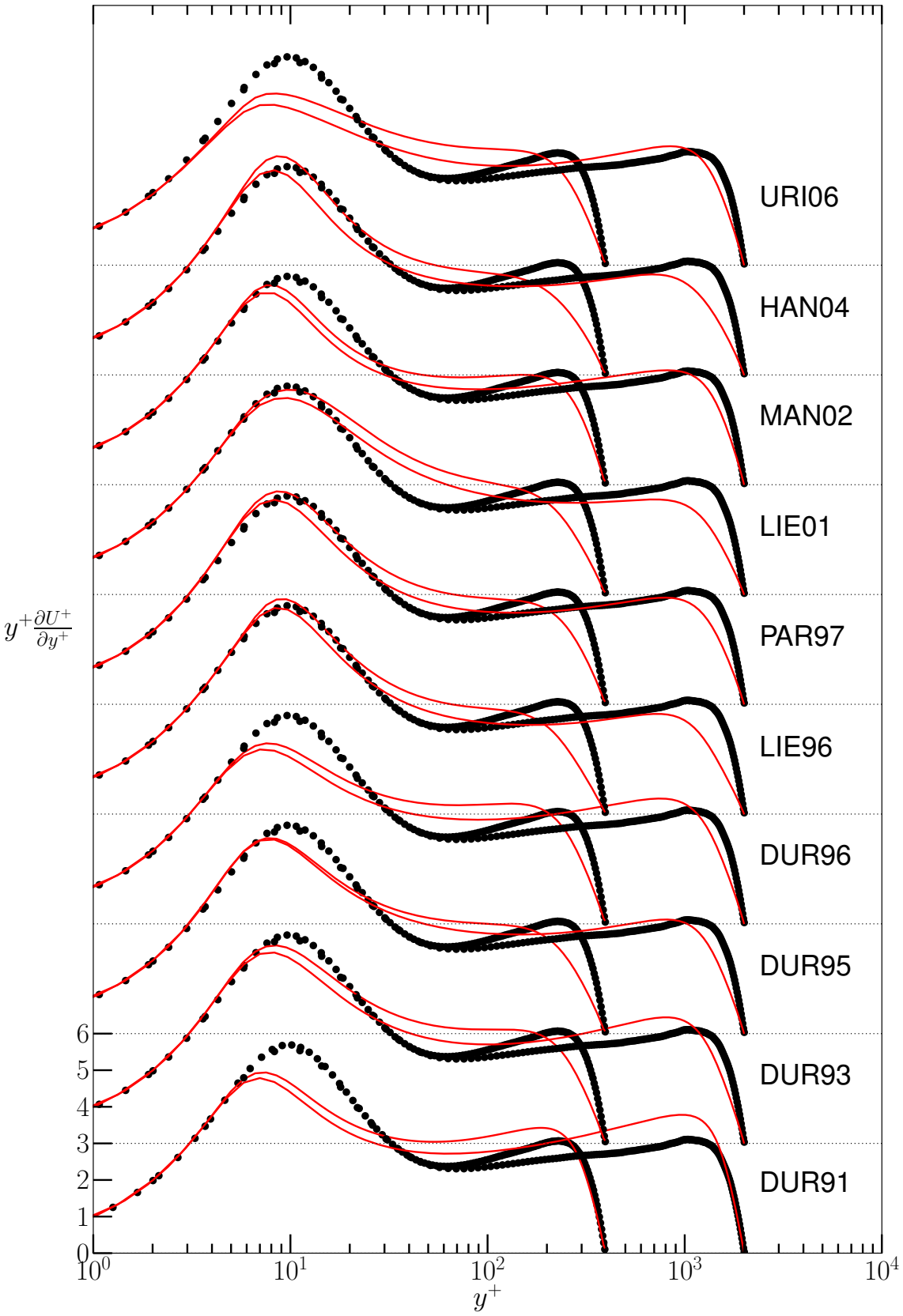

Figure 4.3: $y^+\dfrac{d\overline{U}^+}{dy^+}$ in a channel flow for $Re_\tau \in \{395; 2000\}$

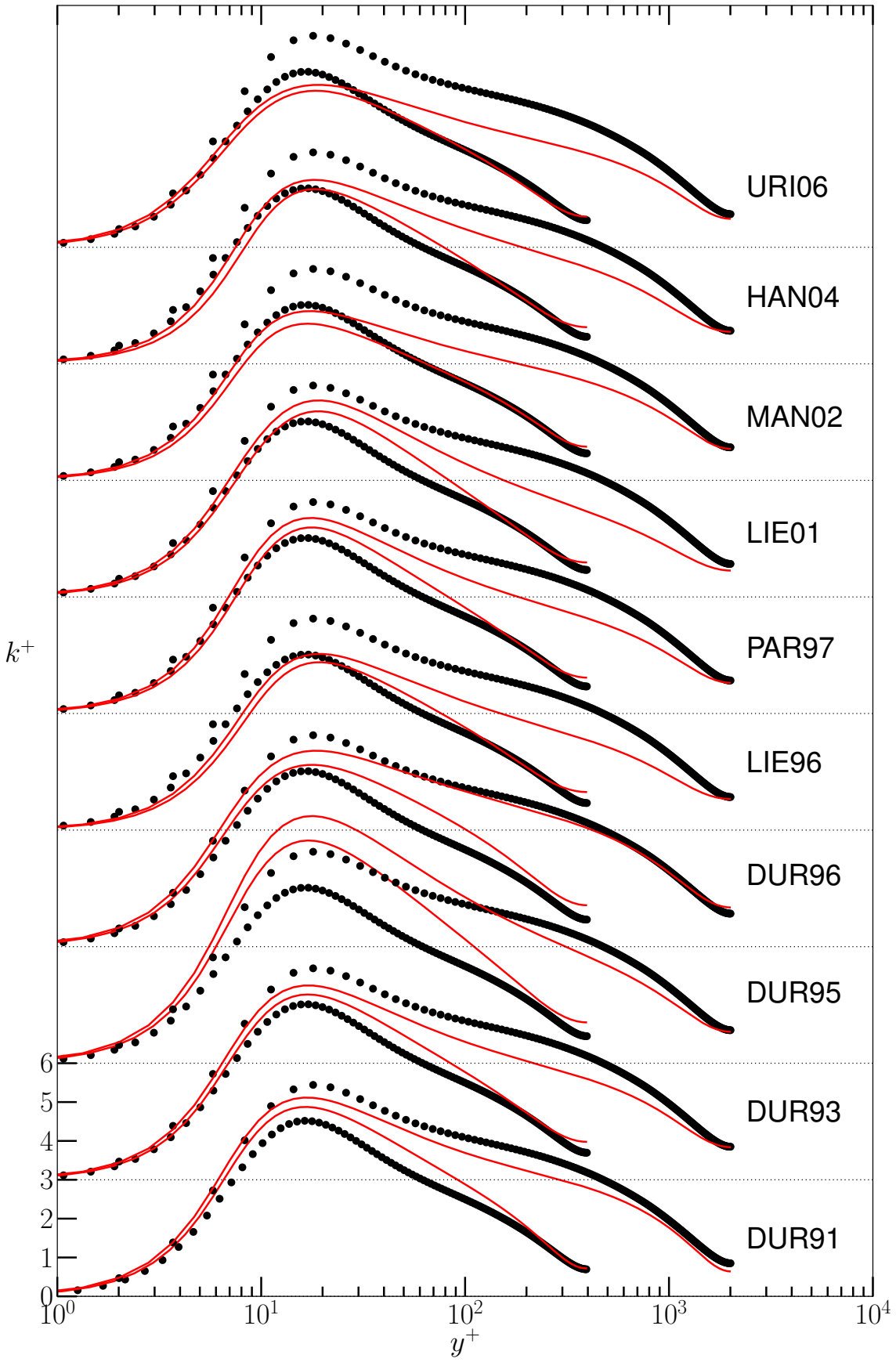

Figure 4.4: k^+ in a channel flow for $Re_\tau \in \{395; 2000\}$

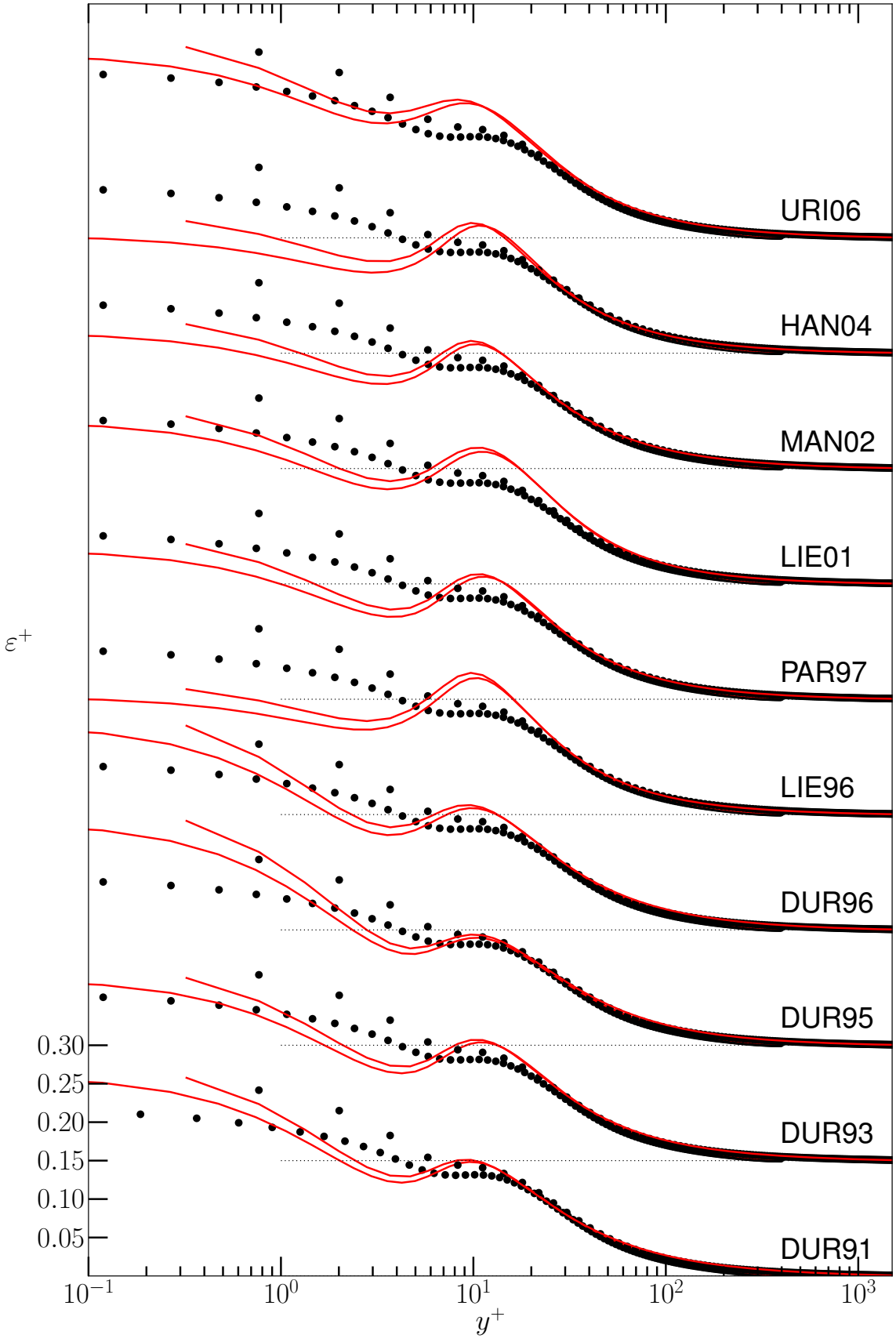

Figure 4.5: ε^+ in a channel flow for $Re_\tau \in \{395; 2000\}$

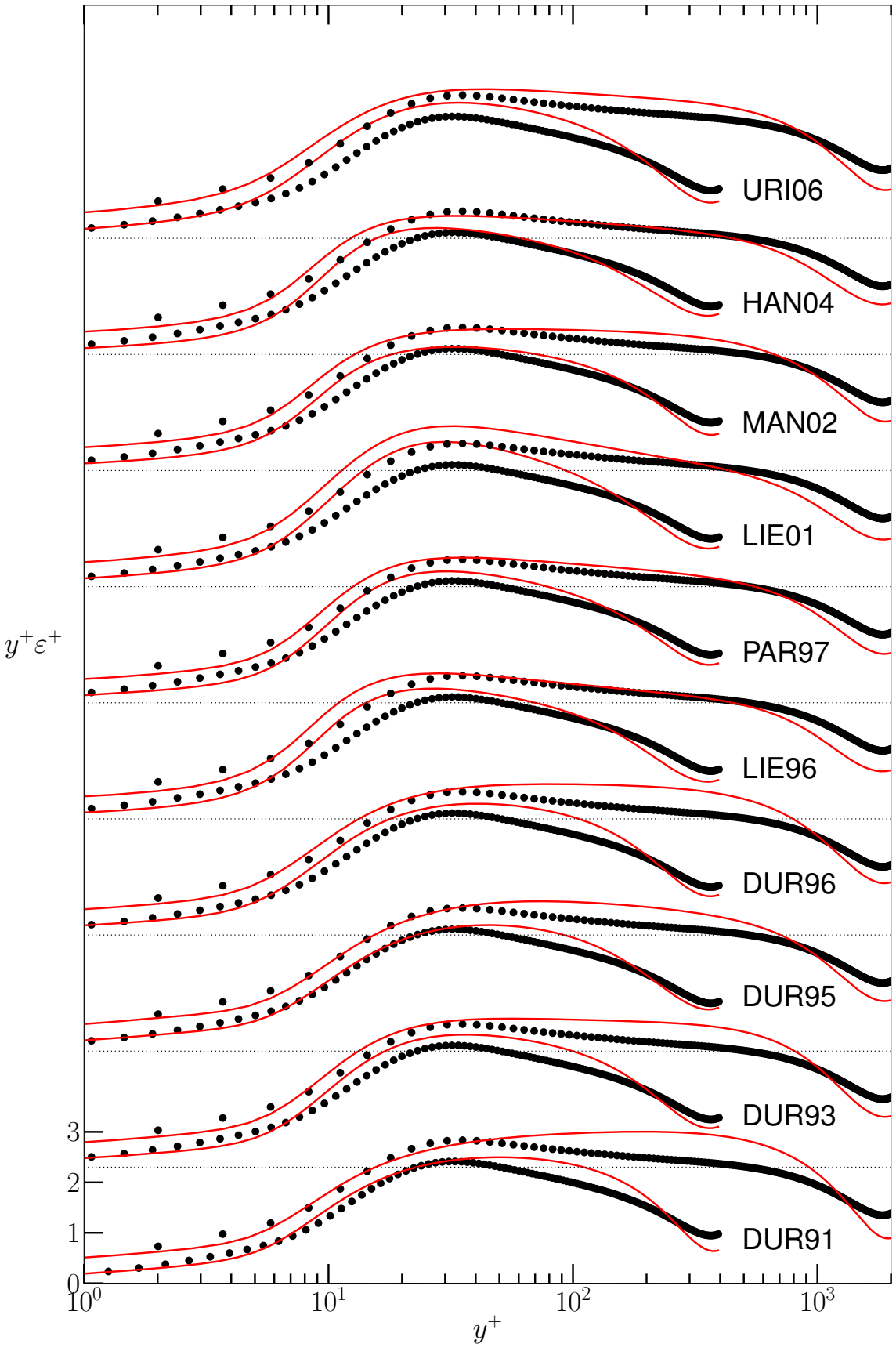

Figure 4.6: $y^+\varepsilon^+$ in a channel flow for $Re_\tau \in \{395; 2000\}$ ($Re_\tau = 2000$ profiles are shifted upwards for clarity)

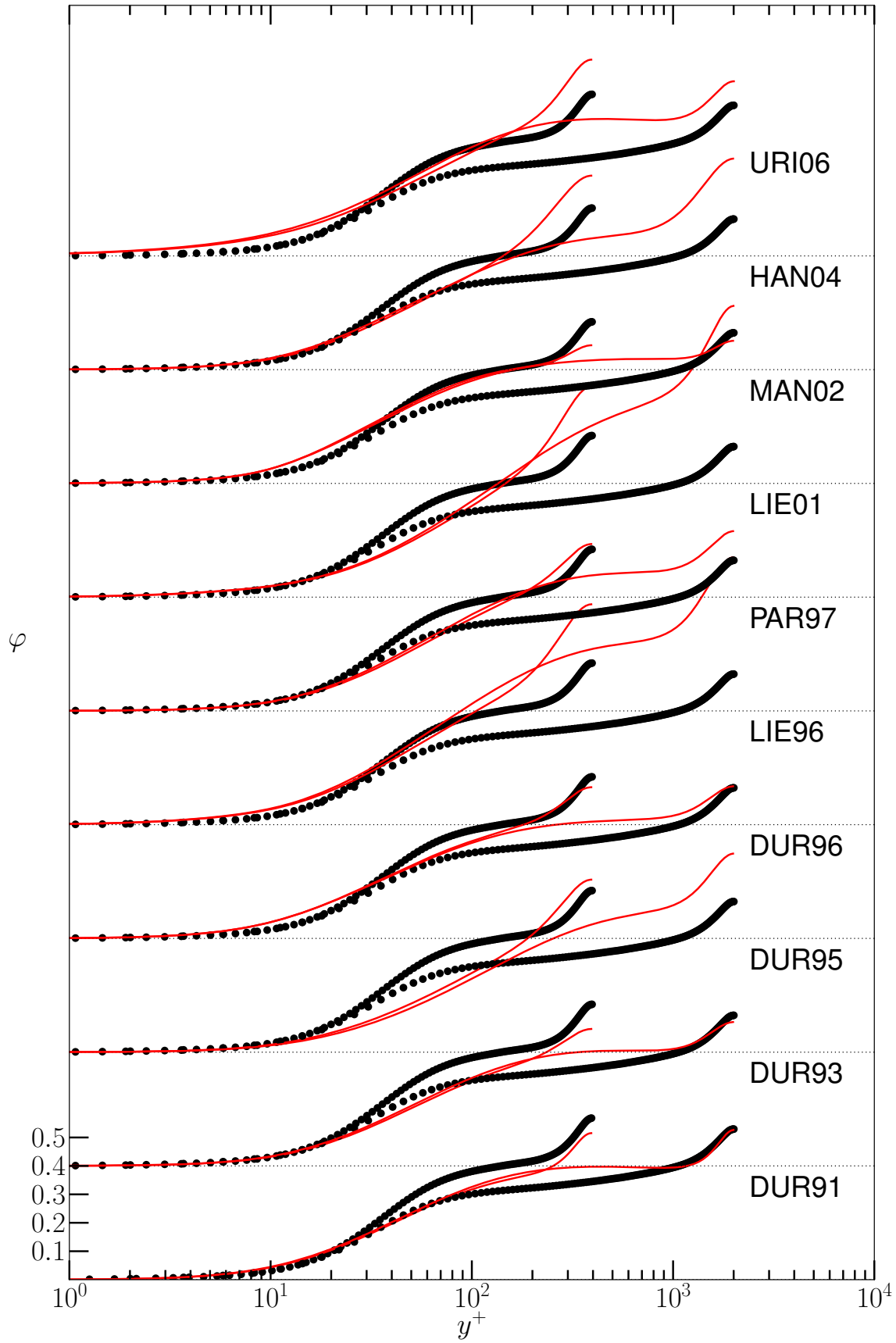

Figure 4.7: φ in a channel flow for $Re_\tau \in \{395; 2000\}$

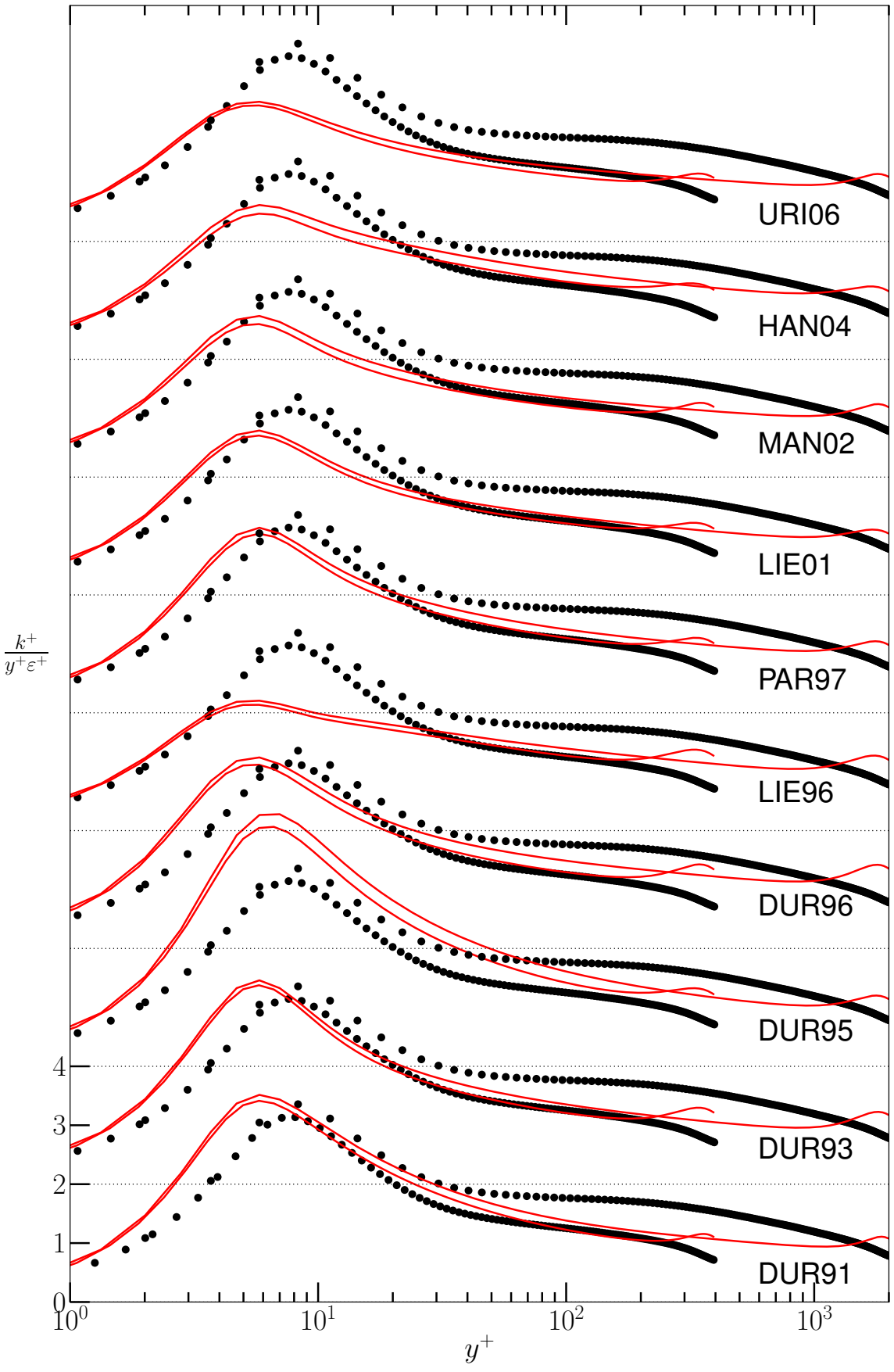

Figure 4.8: $\frac{k^+}{y^+\varepsilon^+}$ in a channel flow for $Re_\tau \in \{395; 2000\}$

Model	$Re_\tau = 180$	$Re_\tau = 395$	$Re_\tau = 590$	$Re_\tau = 950$	$Re_\tau = 2000$
DUR91	106	105	106	106	105
DUR93	95	96	97	97	97
DUR95	101	97	97	96	96
DUR96	101	99	100	99	98
LIE96	89	92	95	97	100
PAR97	87	91	94	96	98
LIE01	84	87	90	91	95
MAN02	99	100	101	102	102
HAN04	88	93	97	100	104
URI06	99	102	104	105	106

Table 4.8: Friction coefficient C_f compared to the DNS value for the same friction velocity based Reynolds number Re_τ (given in %)

4.2.2 Analysis of the logarithmic layer at infinite Reynolds number

The comparison of the models in a channel flow for $Re_\tau \leq 2000$ showed that the quality of predictions could depend on the Reynolds number and comparison now focuses on the logarithmic layer, which reflects what one would obtain in a channel flow for an infinite Reynolds number Re_τ. This layer, as already mentioned, is characterised by a local equilibrium $P_k = \varepsilon$ and a constant Reynolds shear stress $\overline{uv} = -u_\tau^2$. Moreover the mean stream-wise velocity gradient takes the value $\dfrac{\partial \overline{U}}{\partial y} = \dfrac{u_\tau}{\kappa y}$. Hence the production term can be calculated as $P_k = -\overline{uv}\dfrac{d\overline{U}}{dy} = \dfrac{u_\tau^3}{\kappa y}$. The following rationale is based upon the assumption that the models should predict the same eddy viscosity as the Prandtl's mixing length model. Hence $\nu_t = C_\mu \overline{v^2}\frac{k}{\varepsilon} = L_m^2 \dfrac{d\overline{U}}{dy} = \kappa y u_\tau$. The turbulent kinetic energy k can then be expressed as $k = u_\tau^2/\sqrt{C_\mu \dfrac{\overline{v^2}}{k}}$. The time derivative as well as the convection are zero. Diffusion terms becomes:

$$\frac{d}{dy}\left(\frac{\nu_t}{\sigma_k}\frac{dk}{dy}\right) = \frac{d}{dy}\left(\frac{\nu_t}{\sigma_g}\frac{dg}{dy}\right) = 0 \tag{4.16}$$

Moreover assuming $\varepsilon = \dfrac{u_\tau^3}{\kappa y}$ gives:

$$\frac{d}{dy}\left(\frac{\nu_t}{\sigma_\varepsilon}\frac{d\varepsilon}{dy}\right) = \frac{d}{dy}\left(\frac{\kappa y u_\tau}{\sigma_\varepsilon}\frac{d\varepsilon}{dy}\right) = \frac{u_\tau^4}{\sigma_\varepsilon y^2} = \frac{\varepsilon^2 \kappa^2}{\sigma_\varepsilon u_\tau^2} \tag{4.17}$$

In the logarithmic layer, as $\phi_{22}^* = O(y^{-1})$ the variable f behaves as y^n (with

$n = -1$ for all models except the "re-scaled" ones, DUR96 and MAN02 for which[10] $n = 0$). This leads to $\Delta f \sim fn(n-1)/y^2$. The length scale reduces in the log layer to $L = C_L \dfrac{k^{3/2}}{\varepsilon} = C_L \left(C_\mu \dfrac{\overline{v^2}}{k} \right)^{-3/4} \kappa y$, which results in the further simplification:

$$L^2 \Delta f = \kappa^2 f n (n-1) C_L^2 \left(C_\mu \frac{\overline{v^2}}{k} \right)^{-3/2} \tag{4.18}$$

The final system of equations to be solved then reads:

$$\begin{cases} \dfrac{\varepsilon^2}{u_\tau^2} \left((C_{\varepsilon 2} - C_{\varepsilon 1}) \sqrt{\dfrac{\overline{v^2}}{k} C_\mu} - \dfrac{\kappa^2}{\sigma_\varepsilon} \right) = 0 \\ \mathcal{P}_g = 0 \\ f \left(1 - C_L^2 (C_\mu \frac{\overline{v^2}}{k})^{-3/2} \kappa^2 n(n-1) \right) = f_h \end{cases} \tag{4.19}$$

The simplification leads to the following expression for the von Kármán constant:

$$\kappa^2 = \sigma_\varepsilon \left(C_{\varepsilon 2} - C_{\varepsilon 1} \right) \sqrt{\frac{\overline{v^2}}{k} C_\mu} \tag{4.20}$$

In DUR95, DUR96, PAR97, LIE01, MAN02, HAN04 and URI06 the coefficient $C_{\varepsilon 1}^*$ explicitly depends on $\varphi = \overline{v^2}/k$, and for DUR95 the expression for $C_{\varepsilon 1}^*$ is simplified in the logarithmic layer using $L = C_L \left(C_\mu \frac{\overline{v^2}}{k} \right)^{-3/4} \kappa y$, to the following:

$$C_{\varepsilon 1} = 1.3 + \frac{0.25}{1 + \left(\frac{C_L y}{2L} \right)^8} = 1.3 + \frac{0.25}{1 + \left(\frac{(\varphi C_\mu)^{3/4}}{2\kappa} \right)^8} \tag{4.21}$$

The simplifications performed in the $f - g$ system yields the following relation for φ:

- $\varphi = A \left[(C_1 - 1) \left(\frac{2}{3} - \varphi \right) + C_2 \right]$ for DUR91, DUR93, DUR95, DUR96, PAR97, MAN02 and URI06.
- $\varphi = \frac{1}{6} A \left[\frac{2}{3} (C_1 - 1) - \varphi (C_1 - 6) + C_2 \right]$ for LIE96 and LIE01.
- $\varphi = A (C_1 - 1 + C_2) \left(\frac{2}{3} - \varphi \right)$ for HAN04.

[10] we use here the fact that $\varepsilon = O(y^{-1})$ and $L = O(y)$ in the log layer.

The "amplification" factor is $A = \left(1 - 2\left(C_L\kappa\right)^2\left(C_\mu\varphi\right)^{-3/2}\right)^{-1}$ for all models except for DUR96 and MAN02 where $A = 1$.

For each model, the values of κ and φ_{log} are computed using an iterative process (φ_{log} denotes the value of φ in the log layer). They are given in Tab. 4.9, as well as the value for the turbulent to mean strain-rate time-scale ratio $\eta_{log} = \left(\frac{d\overline{U}}{dy}\frac{k}{\varepsilon}\right)_{log} = \left(\varphi_{log}C_\mu\right)^{-1/2}$, and the value of $C^*_{\varepsilon 1,log}$ taken in the log layer. A is the amplification factor for all models and is given in %. Finally the quantity $\varphi_{log}/\varphi^{A=1}_{log}$(also in %) shows the effective amplification, defined as the ratio between φ_{log} predicted by the model and φ_{log} predicted by the same model but when setting $A = 1$.

The most obvious difference between models in the logarithmic layer is due to the amplification effect of the original elliptic operator. This was extensively studied in Wizman et al. (1996), Manceau et al. (2001), Manceau and Hanjalić (2000) and Manceau et al. (2002a) in the framework of the Reynolds-stress modelling, and the problem was also raised in Durbin and Laurence (1996) (DUR96) concerning the $\overline{v^2} - f$ model. As previously derived the actual redistribution term in the logarithmic layer is greater than the quasi-homogeneous model by a factor A which exceeds 1 in the general case[11]. However, as stated in Durbin and Laurence (1996) "*the non local effects should not influence the log layer [...] supposed to be in local equilibrium*". Different ways were introduced to cancel this effect: Wizman et al. (1996) and Manceau et al. (2001) proposed alternative elliptic operators, whereas DUR96, MAN02 and Manceau et al. (2002a) introduced a "re-scaling" for f as seen previously, which leads to $A = 1$. Both were shown to give the best prediction for φ in a channel flow. For all other models, this amplification effect is not equally important. The dependance of A on φ leads to a positive feedback. Hence one should not only look at A but also at the effective amplification, which compares the prediction of φ of the model to what would be predicted by the equivalent neutral formulation. As seen, the positive feedback effect is actually dramatic for the code friendly models

[11] A model for which $A = 1$ is called neutral (using the terminology introduced in Manceau et al. (2001)).

of LIE96 and LIE01, with effective amplification of about 400% for the latter. This leads to an unrealisable value of 1.6 for φ (as seen on Fig. 4.7). The strong adverse effect of A in these two models is due to the neglected term in the f equation which is a second source of over-prediction of $\overline{v^2}$. The LIE01 model is the most popular and widely used version owing to its implementation in major commercial codes, despite this problem. However a quick fix consisting in solving the elliptic equation for a re-scaled variable, as done in DUR96 or MAN02, would be greatly beneficial.

It is also striking to see to which extent the prediction of models for the quantities κ and η_{log} differ from one another. The theoretical values for those two constants are acknowledged to be $\kappa = 0.42$ and $\eta_{log} = 3.33$ [12].

4.2.3 Behaviour in homogeneous sheared turbulence

The models are now compared on the case of homogeneous sheared turbulence. A uniform turbulence field is subjected to a constant and uniform mean velocity strain $S = y\frac{d\overline{U}}{dy}$. The turbulence equations are simplified and the evolution of the variables φ and $\eta = S\dfrac{k}{\varepsilon}$ with respect to the non-dimensional time $t^* = St$ is studied. The production term simplifies to $P = \nu_t S^2$.

The following equation is derived for η :

$$\frac{D\eta}{DSt} = -(C_{\varepsilon 1} - 1)C_\mu \varphi \eta^2 + (C_{\varepsilon 2} - 1) \tag{4.22}$$

The φ transport equation depends upon which model is used for the quasi-homogeneous pressure srambling term. For HAN04 where the SSG moodel is used:

$$\frac{D\varphi}{DSt} = -C_\mu \eta \varphi^2 + \frac{1}{\eta}\left(C_1 - 1 + C_2 C_\mu \eta^2 \varphi\right)\left(\frac{2}{3} - \varphi\right) \tag{4.23}$$

The converged solution (η_∞,φ_∞) corresponds to the intersections of the two null-clines in the (η,φ) plane, whose equations are $\dfrac{D\eta}{DSt} = 0$ and $\dfrac{D\varphi}{DSt} = 0$. The solution is:

$$\varphi_\infty = \frac{2}{3} \times \frac{C_1 - 1 + C_2 \frac{C_{\varepsilon_2 - 1}}{C_{\varepsilon_1 - 1}}}{C_1 - 1 + (C_2 + 1)\frac{C_{\varepsilon_2 - 1}}{C_{\varepsilon_1 - 1}}} \tag{4.24}$$

[12] The latter value is consistent with the choice $C_\mu = 0.09$ in a $k-\varepsilon$ model, based on the observation that the anisotropy $\left|\frac{\overline{uv}}{k}\right| = 0.3$ in many shear flows.

$$\eta_\infty = \sqrt{\frac{3}{2} \times \frac{C_{\varepsilon_2 - 1}}{C_\mu \left(C_{\varepsilon_1 - 1}\right)} \frac{C_1 - 1 + (C_2 + 1)\frac{C_{\varepsilon_2 - 1}}{C_{\varepsilon_1 - 1}}}{C_1 - 1 + C_2 \frac{C_{\varepsilon_2 - 1}}{C_{\varepsilon_1 - 1}}}} \tag{4.25}$$

For all other models, the φ transport equation reads:

$$\frac{D\varphi}{DSt} = -C_\mu \eta \varphi^2 + \frac{1}{\eta}\left(C_1 - 1\right)\left(\frac{2}{3} - \varphi\right) + C_2 C_\mu \varphi \eta \tag{4.26}$$

And the solutions are given by:

$$\varphi_\infty = \frac{\frac{2}{3}(C_1 - 1) + C_2\left(\frac{C_{\varepsilon 2} - 1}{C_{\varepsilon 1} - 1}\right)}{C_1 - 1 + \left(\frac{C_{\varepsilon 2} - 1}{C_{\varepsilon 1} - 1}\right)} \tag{4.27}$$

$$\eta_\infty = \sqrt{\frac{C_{\varepsilon_2} - 1}{C_\mu \left(C_{\varepsilon_1 - 1}\right)} \times \frac{C_1 - 1 + \left(\frac{C_{\varepsilon 2} - 1}{C_{\varepsilon 1} - 1}\right)}{\frac{2}{3}(C_1 - 1) + C_2\left(\frac{C_{\varepsilon 2} - 1}{C_{\varepsilon 1} - 1}\right)}} \tag{4.28}$$

It is useful to recall that with the standard $k - \varepsilon$ model, $\eta_\infty = \sqrt{\frac{C_{\varepsilon 2} - 1}{C_{\varepsilon_1} - 1} \times \frac{1}{C_\mu}}$. It approximately takes the value $\eta_\infty \simeq 4.578$ with the usual constants values $C_{\varepsilon_1} = 1.44$, $C_{\varepsilon 2} = 1.83$ and $C_\mu = 0.09$.

The values for φ_∞ and η_∞ for all the models are given in Tab. 4.9, right part. The predicted limit η_∞ is clearly of the same order as that for the standard $k - \varepsilon$ value, except for DUR95 and HAN04. Those values not only depend on the ε equation constants, but also on the quasi-homogeneous model for the redistribution term, due to the presence, for most of the models, of φ in the definition of $C^*_{\varepsilon 1}$.

The asymptotic values φ_∞ and η_∞ only partially characterise the behaviour in homogeneous sheared turbulence. Another aspect which might be worth looking at is the evolution towards the asymptotic values. Fig. 4.9 shows the streamlines of the vector $\left(\frac{d\eta}{dt^*}, \frac{d\varphi}{dt^*}\right)$ for the models DUR96 and LIE01. The thick (respectively dashed thick) line represents the null-cline of φ (respectively η), that is, the points where $\frac{d\varphi}{dt^*} = 0$ (respectively $\frac{d\eta}{dt^*} = 0$). The intersection corresponds to the equilibrium.

As seen in Fig. 4.9, the convergence towards the limit η_∞ seems to be somehow delayed especially for high values of η (Rapid Distortion Theory) and limiting values of φ ($\varphi \simeq 0$ or $\varphi \simeq \frac{2}{3}$). For instance starting from ($\eta = 9; \varphi = 0.1$), η increases first, to reach the η null-cline, and only then, decreases again towards the limit. This

Model	κ	φ_{log}	$\frac{\varphi_{log}}{\varphi_{log}^{A=1}}$ (%)	A (%)	η	$C^*_{\varepsilon 1,log}$	φ_∞	η_∞	$C^*_{\varepsilon 1,\infty}$
DUR91	0.38	0.48	132	141	3.24	1.70	0.35	4.55	1.70
DUR93	0.37	0.49	128	140	2.97	1.58	0.36	4.32	1.58
DUR95	0.41	0.71	176	253	2.72	1.55	0.34	6.78	1.30
DUR96	0.36	0.42	N/A	100	3.84	1.51	0.40	5.08	1.52
LIE96	0.51	1.13	278	117	2.16	1.55	0.37	4.87	1.55
PAR97	0.45	0.63	154	198	2.69	1.48	0.37	4.70	1.50
LIE01	0.59	1.60	394	121	1.69	1.46	0.37	4.64	1.52
MAN02	0.40	0.44	N/A	100	3.20	1.53	0.39	4.43	1.53
HAN04	0.49	0.7	206	N/A	2.55	1.42	0.31	5.42	1.45
URI06	0.41	0.59	146	180	2.77	1.49	0.37	4.49	1.51

Table 4.9: Predictions of the models in the log layer (left part) and in homogeneous sheared turbulence (right part)

illustrates the role of the temporal evolution of $\overline{v^2}$ in adding a lag in the response of the turbulence to the mean strain-rate. The latter feature is obviously lacking in a two-equation eddy-viscosity model, even those using algebraic relations to determine the Reynolds stresses (a more detailed study of flow response to time evolving mean velocity gradient and the superiority of Reynolds-stress models in that case can be found in Hadžić et al. (2001)).

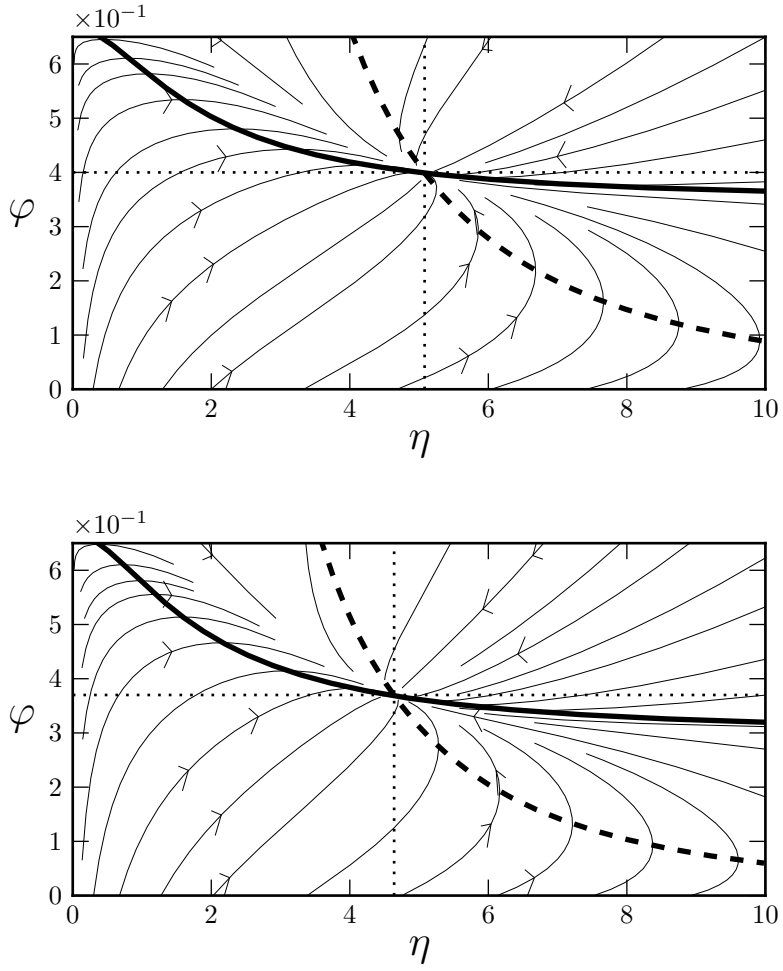

Figure 4.9: Phase-plane portrait of Eq. 4.22 and Eq. 4.26 for model DUR96 (top) and LIE01 (bottom). $\longrightarrow$: Streamlines of the vector $\left(\frac{\partial \eta}{\partial t}, \frac{\partial \varphi}{\partial t}\right)$ as a function of η and φ , —— :φ nullcline, — — —: η nullcline

Chapter 5

Development of new $\overline{v^2} - f$ models

From the review of the different $\overline{v^2} - f$ models proposed in the past 20 years two conclusions emerge.

Firstly the solutions to address the numerical problem linked to the original proposal are not satisfactory. The "code-friendly" versions of LIE96, LIE01 and URI06 do significantly reduce the numerical issue, but at the expense of the quality of the predictions. The models of LIE96 and LIE01 return a strongly excessive, occasionally unphysical, value for $\overline{v^2}$ in the logarithmic layer, and more generally, in the core region of a boundary layer, and in URI06 the damping of the variable $\overline{v^2}$ is not correct as seen previously. In HAN04 the modifications proposed do not entirely solve the numerical problems. The first part of this chapter therefore proposes to fully address the numerical issue of the original $\overline{v^2} - f$ approach with no deterioration of the predictive capabilities: this is achieved by combining the model of URI06 (which solves for the variable $\varphi = \overline{v^2}/k$) and the elliptic blending approach (which uses the non dimensional parameter α as elliptic variable): this new model will be denoted by $\varphi - \alpha$.

Secondly, the comparison of all models equations shows a large variability of values adopted for the constants, which yields differences amongst models for the prediction of fundamental flows (channel flow, logarithmic layer at infinite Reynolds number and homogeneous-shear turbulence). This is partly because solutions brought by modellers to address various practical problems, such as the numerical stability issue

or the near-wall modelling of the dissipation rate equation, also have an influence in cases where they should not. Another reason is that the constitutive relation proposed by Durbin (1991) (consisting in using $\overline{v^2}$ as damping parameter in the definition of ν_t) yields a turbulent shear stress to mean velocity gradient ratio (modelled by ν_t) which is too strongly dependent on the Reynolds number in a channel flow (as compared to the DNS data available in such flows). Because of this flaw in the baseline formulation at such a fundamental level, the model calibration in a channel flow at various Reynolds numbers becomes cumbersome and often imperfect (as seen in the channel flow results shown in the previous chapter). Based on the $\varphi-\alpha$ model, successive modifications, mainly located in the $k-\varepsilon$ system, are proposed to cope with this shortcoming. All these modifications are integrated in a final version, referred to as BL-$\overline{v^2}/k$ which will be presented at the end of this chapter. All developments are implemented in the unstructured finite volume code *Code_Saturne* which will be introduced in Chap. 7.

5.1 The $\varphi - \alpha$ model

Comparing the existing ways of resolving the numerical issue, one can identify two requirements. Firstly, for numerical stability to be ensured, the near-wall balance of leading-order terms in the $\overline{v^2}$ equation should be handled implicitly. This is the case in a segregated solver only if the f wall boundary condition is 0. Secondly extra terms introduced to ensure the above requirement should not deteriorate the predictions. In the course of this work, alternative ways of ensuring the correct near-wall behaviour of $\overline{v^2}$ were explored. Using analytical profiles $\overline{v^2} = \overline{v^2}(y^+)$ (either analytically derived from the $\overline{v^2}-f$ equations (Kalitzin et al., 2005) or resulting from DNS data interpolation) can be a way to prescribe the correct boundary condition, but shortcomings are obvious (lack of universality of such a function, ill-representation of low-Reynolds number effects, definition of the viscous velocity scale to be used in the y^+ definition in general flows (*e.g.* impinging flows), ...). The path eventually followed is the adaptation of the elliptic blending of Manceau and Hanjalić (2002) to

the $\overline{v^2} - f$ model. The model proposed in the following is referred to as $\varphi - \alpha$ (Billard et al. (2008)).

5.1.1 Presentation of the $\varphi - \alpha$ model

As seen in the previous chapter, the elliptic blending was introduced in the framework of second-moment-closure, but the adaptation to a simpler eddy-viscosity model is rather straightforward. The proposed new model stems from the model of URI06 (Laurence et al. (2004)) but handles the near-wall resolution using a blending coefficient α which is solved by the same modified Helmholtz equation, as done in Manceau and Hanjalić (2002). The resulting variable takes the value $\alpha = 0$ at the wall and relaxes towards 1 further away.

Derivation of the model The same equation for $\varphi = \overline{v^2}/k$ (Eq. 4.5) is used here, the source term f, connected to pressure redistribution, is then defined as a blending between two different forms as follows:

$$f = (1 - \alpha^p)\, f_w + \alpha^p f_h \tag{5.1}$$

The functions f_w and f_h are defined, respectively, as the model for f at the wall and away from the wall. The purpose of the term f_w is to balance the two other leading order terms in the φ equation, namely the molecular cross-diffusion and the molecular diffusion (whose Taylor series expansion is derived in Eq. 4.6). This leads to the following requirement: $f_w \sim -10\nu\varphi/k^2$. It was already seen that using the near-wall behaviour of ε yields $\varepsilon\varphi/k \sim 2\nu\varphi/y^2$. This yields the choice $f_w = -5\varphi\varepsilon/k$. Moreover the viscous cross-diffusion term is decomposed as follows (using Eq. 4.6 and Eq. 4.9 to obtain the near-wall part):

$$\frac{2\nu}{k}\frac{\partial k}{\partial y}\frac{\partial \varphi}{\partial y} = (1 - \alpha^p)\left[4\frac{\varphi\varepsilon}{k}\right] + \alpha^p\left[\frac{2\nu}{k}\frac{\partial k}{\partial y}\frac{\partial \varphi}{\partial y}\right] \tag{5.2}$$

The equations of the model read:

$$\begin{cases} \dfrac{Dk}{Dt} = P_k - \varepsilon + \dfrac{\partial}{\partial x_j}\left[\left(\nu + \dfrac{\nu_t}{\sigma_k}\right)\dfrac{\partial k}{\partial x_j}\right] \\ \dfrac{D\varepsilon}{Dt} = \dfrac{C^*_{\varepsilon 1}P_k - C_{\varepsilon 2}\varepsilon}{T} + \dfrac{\partial}{\partial x_j}\left[\left(\nu + \dfrac{\nu_t}{\sigma_\varepsilon}\right)\dfrac{\partial \varepsilon}{\partial x_j}\right] \\ \lim\limits_{y\to 0} k = 0 \\ \lim\limits_{y\to 0} \varepsilon = \lim\limits_{y\to 0} \dfrac{2\nu k}{y^2} \end{cases} \qquad \begin{cases} \alpha - L^2\Delta\alpha = 1 \\ \lim\limits_{y\to 0} \alpha = 0 \end{cases} \tag{5.4}$$

(5.3)

$$\begin{cases} \dfrac{D\varphi}{Dt} = (1-\alpha^p)\left[-\varphi\dfrac{\varepsilon}{k}\right] + \alpha^p f_h - P_k\dfrac{\varphi}{k} + \dfrac{2}{k}\left(\dfrac{\nu_t}{\sigma_k} + \alpha^p\nu\right)\dfrac{\partial k}{\partial x_j}\dfrac{\partial \varphi}{\partial x_j} + \dfrac{\partial}{\partial x_j}\left[\left(\nu + \dfrac{\nu_t}{\sigma_\varphi}\right)\dfrac{\partial \varphi}{\partial x_j}\right] \\ f_h = -\dfrac{1}{T}\left(C_1 - 1 + C_2\dfrac{P_k}{\varepsilon}\right)\left(\varphi - \dfrac{2}{3}\right) \\ \lim\limits_{y\to 0}\varphi = 0 \end{cases} \tag{5.5}$$

$C^*_{\varepsilon 1}$	$C_{\varepsilon 1}$	C_{A1}	$C_{\varepsilon 2}$	σ_k	σ_ε	ν_t	C_μ
$C_{\varepsilon 1}\left(1 + C_{A1}\left(1-\alpha^p\right)\sqrt{\frac{1}{\varphi}}\right)$	1.44	0.04	1.83	1	1.22	$C_\mu\varphi kT$	0.22

Table 5.1: Constants of the $\varphi - \alpha$ model. k and ε equations.

T	C_T	L	C_L	C_η
$\max\left[\frac{k}{\varepsilon}, C_T\sqrt{\frac{\nu}{\varepsilon}}\right]$	6	$C_L \max\left[\frac{k^{3/2}}{\varepsilon}, C_\eta\left(\frac{\nu^3}{\varepsilon}\right)^{1/4}\right]$	0.161	90

Table 5.2: Constants of the $\varphi - \alpha$ model. Expression for the scales and associated constants.

C_1	C_2	σ_φ	p
1.7	1.2	1	3

Table 5.3: Constants of the $\varphi - \alpha$ model. φ equation.

Using the elliptic blending approach addresses the numerical instability problem even if the $\varphi - \alpha$ system is solved sequentially. At each time step, the α equation is first solved with the homogeneous Dirichlet boundary condition. This then enables to resolve the φ equation with the terms involved in the near-wall region all being handled implicitly: $-(1-\alpha^p)\varphi\dfrac{\varepsilon}{k} + \nu\Delta\varphi$.

It can be seen from Fig. 5.1 that the predicted α scales remarkably well with viscous units, therefore is virtually Re_τ independent.

The present choice for the exponent p differs from the one ($p = 2$) in the early formulation of the elliptic blending (Manceau and Hanjalić (2002)), because $p = 3$ is necessary to ensure that the term $\alpha^p f_h$ is not involved in the near-wall balance, which involves terms of order $O(y^2)$. It can be shown indeed that $\alpha = O(y)$ at wall. The same conclusion was reached in Lecocq (2008).

Tab. 5.1, Tab. 5.2 and Tab. 5.3 give the chosen values for the constants, as well as the expression for $C^*_{\varepsilon 1}$. It can be noted that the presence of $(1 - \alpha^p)$ in $C_{\varepsilon 1}$ limits the near-wall boosting of ε to the near-wall region. The quasi-linear SSG model has been preferred to the LRR-IP model for its better behaviour in the logarithmic layer. Finally it is to be noted that $\alpha = 1$ in the log layer, therefore there is no amplification effect with the $\varphi - \alpha$ model.

5.1.2 Preliminary results

Fig. 5.2 and Fig. 5.3 show the predictions of the $\varphi - \alpha$ model compared to the URI06 model[1], Tab. 5.4 summarises the predictions of the skin-friction coefficient for the two models for various Re_τ, and Tab. 5.5 presents the results of the two models in the logarithmic layer at infinite Re_τ and in homogeneous sheared turbulence (with the same notation as in Tab. 4.9). The velocity profile prediction in the buffer layer is improved, and this is reflected by a better prediction of the peak and dip of the function $y^+ \frac{d\overline{U}^+}{dy^+}$ in the same region. The $\varphi - \alpha$ model gives very good predictions for C_f at higher Re_τ, but under-predicts this quantity for $Re_\tau = 180$. It also predicts slightly smaller values for the near-wall dissipation. Predictions of k^+ and ε^+ are very similar for the two models in the logarithmic region and the predictions are also close for the κ constant. As expected, the near-wall prediction of φ, and hence ν_t^+, is greatly improved by the $\varphi - \alpha$ model due its the compliance with near-wall budget

[1]The model URI06 is used as benchmark for two reasons. First it is the model already implemented in the code *Code_Saturne* which will be later used for applications and second it can be considered as the closest to the presently proposed versions, as it solves for φ: therefore the comparison is expected to provide an idea of the improvements specifically derived in this work.

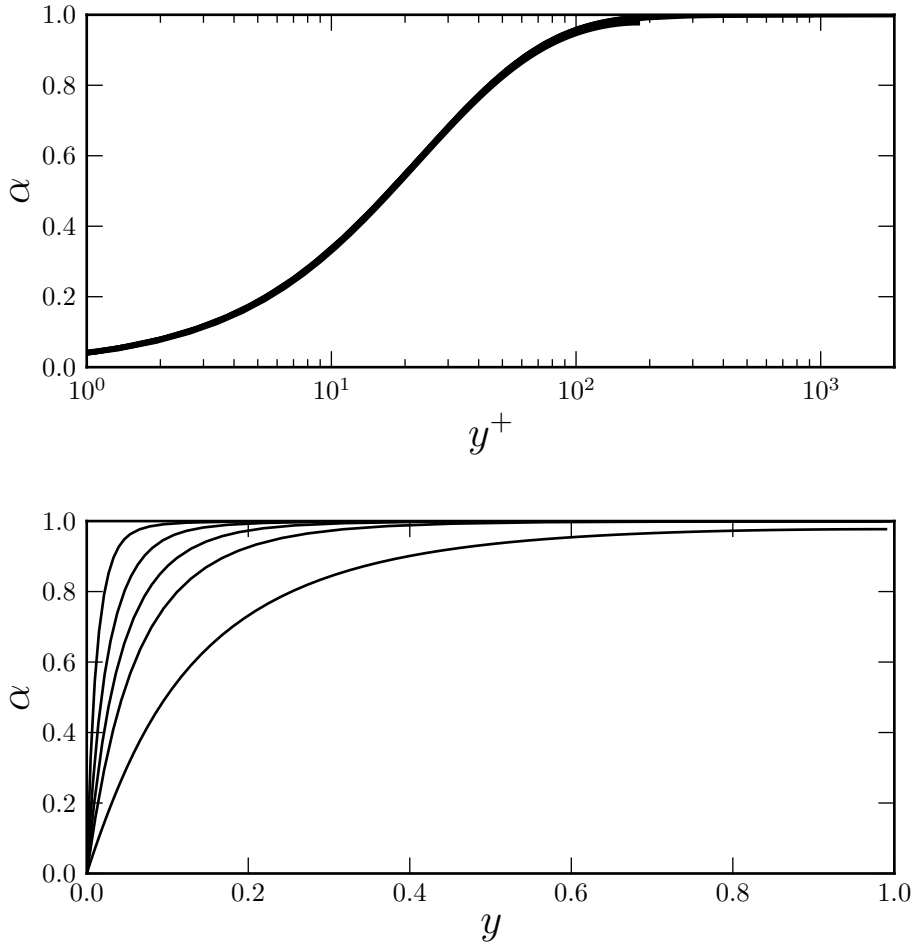

Figure 5.1: Prediction of α in the channel flow given by the $\varphi - \alpha$ model. $Re_\tau \in \{180; 395; 590; 950; 2000\}$. Top: $\alpha = f(y^+)$. Bottom: $\alpha = f(y)$.

balance, unlike URI06. Finally, the values of φ in the logarithmic region and in the defect layer are in closer agreement with the DNS thanks to the neutrality of the elliptic blending formulation and to the use of the SSG model. Wizman et al. (1996) indeed showed that the SSG pressure strain-rate term needed much less "damping" by the elliptic operator than the earlier LRR-IP model. The improved representation of φ in these regions is also visible in the prediction of the turbulent viscosity ν_t^+, for which URI06 shows substantial over-prediction.

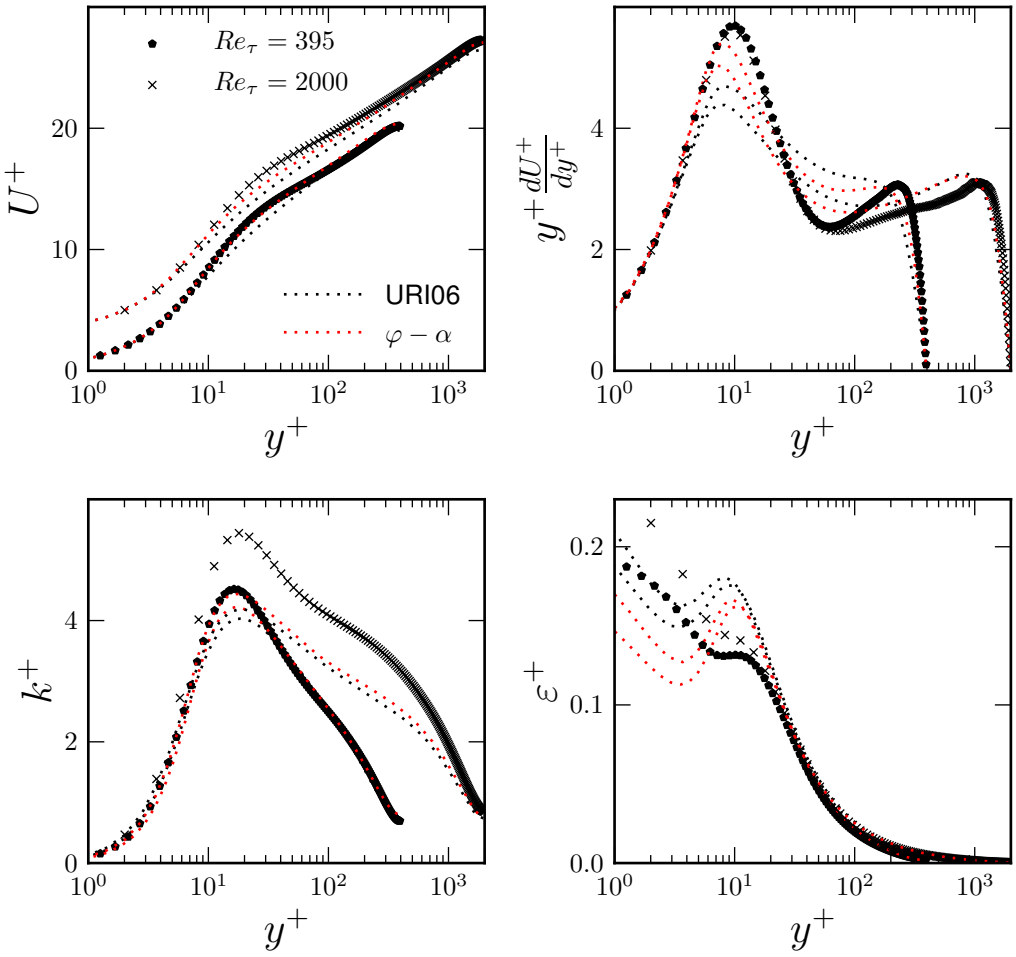

Figure 5.2: Predictions of the $\varphi - \alpha$ model in the channel flow for $Re_\tau \in \{395; 2000\}$ for the variables $\overline{U}^+$, $y^+ d\overline{U}^+/dy^+$, k^+ and ε^+.

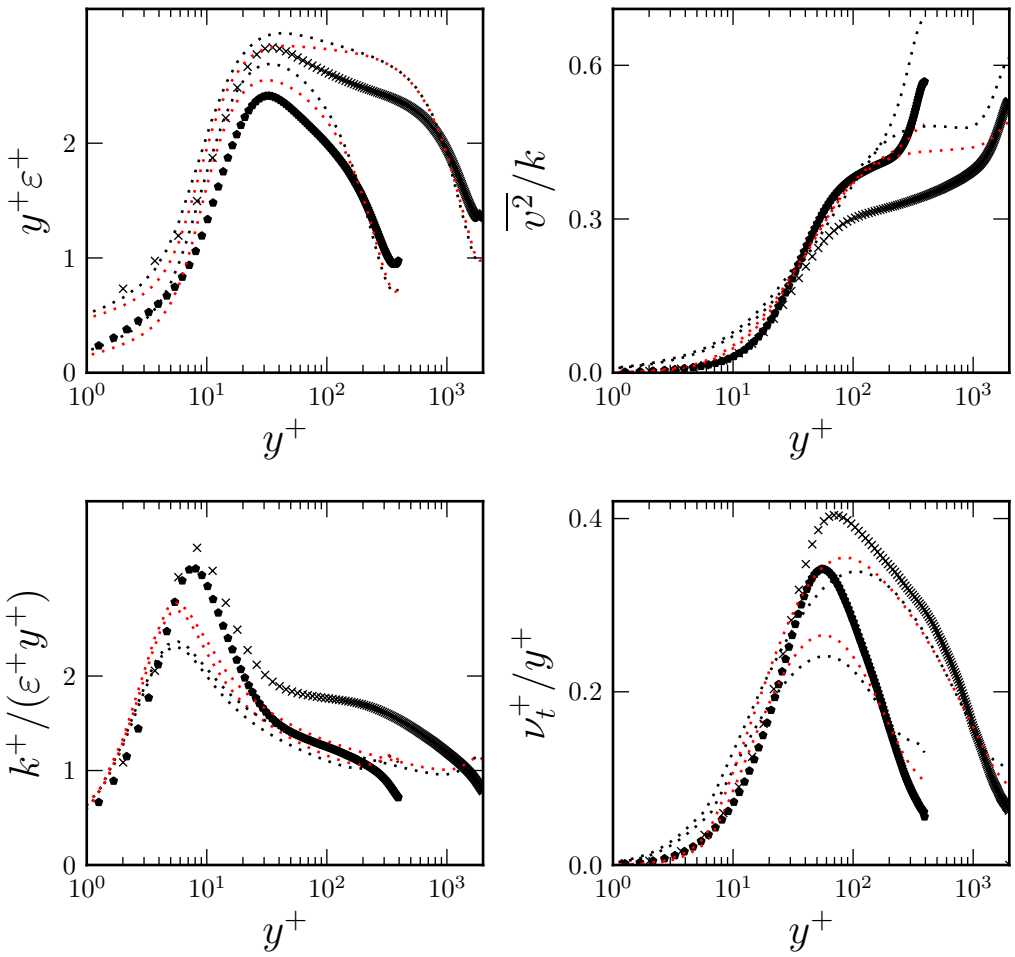

Figure 5.3: Predictions of the $\varphi - \alpha$ model in the channel flow case for $Re_\tau \in \{395; 2000\}$, for the variables $y^+\varepsilon^+$, $\overline{v^2}^+/k^+$, $k^+/(\varepsilon^+ y^+)$ and ν_t^+/y^+. See Fig. 5.2 for legends.

Model	$Re_\tau = 180$	$Re_\tau = 395$	$Re_\tau = 590$	$Re_\tau = 950$	$Re_\tau = 2000$
URI06	99	102	104	105	106
$\varphi - \alpha$	94	97	100	101	102

Table 5.4: Friction coefficient C_f compared to the DNS value for the same friction velocity based Reynolds number Re_τ (given in %) for URI06 and the $\varphi - \alpha$ model.

Model	κ	φ_{log}	$\frac{\varphi_{log}}{\varphi_{log}^{A=0}}$ (%)	A (%)	η	$C^*_{\varepsilon 1,log}$	φ_∞	η_∞	$C^*_{\varepsilon 1,\infty}$
URI06	0.41	0.59	146	180	2.77	1.49	0.37	4.49	1.51
$\varphi - \alpha$	0.38	0.44	100	100	3.23	1.44	0.41	4.59	1.44

Table 5.5: Predictions in the log layer (left part) and in homogeneous sheared turbulence (right part) for URI06 and the $\varphi - \alpha$ model.

5.2 The ν_t definition issue

The natural damping parameter $f_\mu = \overline{v^2}/k$ is a sounder alternative to empirical functions, but has a fundamental deficiency: Fig. 5.4 shows the Reynolds number dependance measure (introduced in Subsec. 3.2.5) for ν_t, $\sigma(\nu_t)$, computed for Durbin's model (*i.e.* with $\nu_t = 0.22\overline{v^2}T$) and for the quantity it is supposed to model (*i.e.* with $\nu_t = -\overline{uv}/\frac{\partial \overline{U}}{\partial y}$), both being evaluated *a priori* using DNS values. It can clearly be seen that Durbin's model leads to a turbulent viscosity that is strongly Reynolds-number dependent in the critical buffer layer ($5 < y^+ < 50$), twice as large as for the exact term. In Fig. 5.5 *a-priori* evaluation of both quantities are plotted in the channel flow for Reynolds number ranging from 180 to 2000, which also shows a persistent over-prediction of the model for high Reynolds numbers. In order to assess to what extent this discrepancy has a noticeable consequence for the predicted mean-velocity profile, the velocity is reconstructed from the model ν_t, integrating the momentum equation:

$$\frac{dU/u_\tau}{dy^+} - \frac{\overline{uv}}{u_\tau^2} = 1 - \frac{y^+}{Re_\tau} \tag{5.6}$$

with $\overline{uv}$ *a priori* calculated using Durbin's model $\overline{uv} = -0.22\overline{v^2}T\frac{d\overline{U}}{dy}$ (*i.e.* k, $\overline{v^2}$ and T are evaluated using DNS data). The reconstructed velocity is plotted in Fig. 5.6 against the DNS velocity. As expected this leads to a strongly over-predicted velocity for $Re_\tau < 395$ and under-predicted for $Re_\tau > 395$. The presence of such a mismatch

between the model and the DNS at such a fundamental level (the entry point of the turbulence to mean-flow feedback) greatly puts into question the relevance of *a-priori* modelling of individual turbulent variables in this framework.

In fact, the dramatic differences depicted in Fig. 5.6 is not reflected in the model predictions. As seen in the previous chapter, the velocity-profile prediction of all $\overline{v^2}-f$ models are rather satisfactory and it could be concluded that the models are able to cope with the previously mentioned shortcoming, by introducing compensating errors or favourable feedback in the turbulent variables prediction, to generate a turbulent viscosity whose low-Reynolds-number dependence is recovered. This conclusion is over-optimistic however. Fig. 4.3 shows a strong Reynolds number dependence of the variable $yd\overline{U}/dy$ in the near-wall region, hence of ν_t for all $\overline{v^2}-f$ models, with one exception (DUR95). Without solving this original problem, this has led the calibration of all the $\overline{v^2}-f$ models all the more tedious, and this explains why there is such differences in the models behaviour in the fundamental flows studied in the previous chapter. The most striking result is the variability of the predicted von Kármán constant κ and it would not be surprising to see unexpected differences between models arising in very high Reynolds number flows. According to Durbin and Laurence (1996), "[the] *set of constant can be varied without significantly altering predictions, as long as the whole set is readjusted"*. This acknowledged coefficients interdependence renders the model calibration more difficult and may also explain why the $\varphi-\alpha$ predictions at low Reynolds number (see Tab. 5.4) are not so satisfactory.

The only $\overline{v^2}-f$ model which does not depict this near-wall Reynolds dependance of ν_t is DUR95 (again this is most visible when looking at $y\frac{d\overline{U}}{dy}$, Fig. 4.3). There are two possible explanations:

- It does not feature any near-wall modification for the $k-\varepsilon$ system[2], therefore it is the standard $k-\varepsilon$ equations which are integrated all the way to walls. However, the same is also true for DUR91 (whereas the latter model predicts a ν_t which is Re_τ dependant as seen on Fig. 4.3) and therefore this fact alone is

[2]Because in the expression of $C^*_{\varepsilon 1}$ it uses (see Tab. 4.4), the length-scale being limited by its Kolmogorov lower bound, $C^*_{\varepsilon 1}$ remains constant in the near-wall region.

not a sufficient reason.

- This model uses the remarkably small $C_\eta = 70$. And yet some other models use similar value for this coefficient, DUR95 is the model for which the switch between the Kolmogorov and the integral length-scale is by far the earliest (*i.e.* the closest to the wall), as seen on Tab. 4.6, possibly leading to a smaller Re_τ dependence for $\overline{v^2}$, hence for ν_t.

These latter observations will drive the present work, which will aim at finding solutions to reduce the Re_τ dependence of ν_t in focussing the efforts in two directions: the near-wall modelling of the dissipation-rate equation and the length-scale determining the α coefficient.

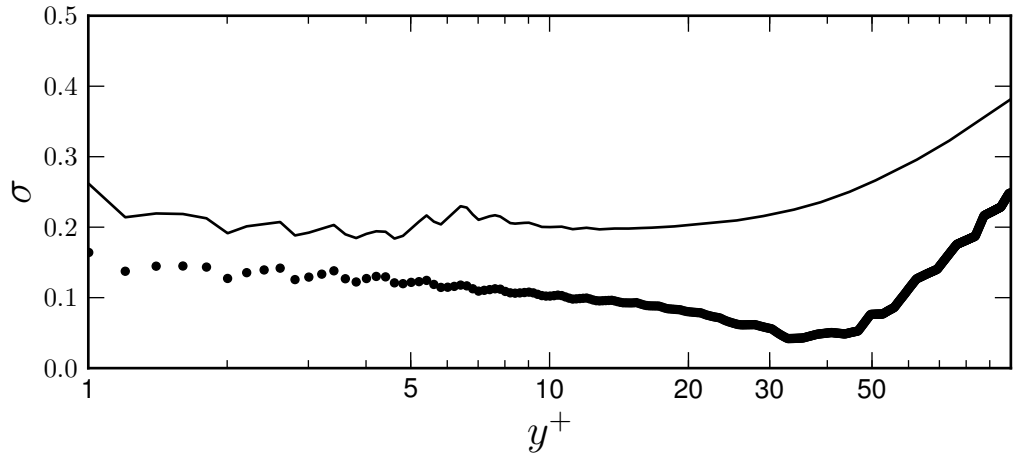

Figure 5.4: Reynolds number dependance coefficient $\sigma(\nu_t^+)$ in a channel flow: $\bullet\bullet\bullet$: with $\nu_t^+ = -\overline{uv}^+ / \frac{d\overline{U}^+}{dy^+}$, ——: with $\nu_t^+ = 0.22\overline{v^2}^+ T^+$.

5.3 Solution 1: Near-wall modelling of the ε equation

In the course of this research major "trial-and-error" efforts were made to improve the ε equation in the near-wall region, and most of these will not be mentioned in the present thesis. In the light of a term-by-term analysis, performed in Jakirlic

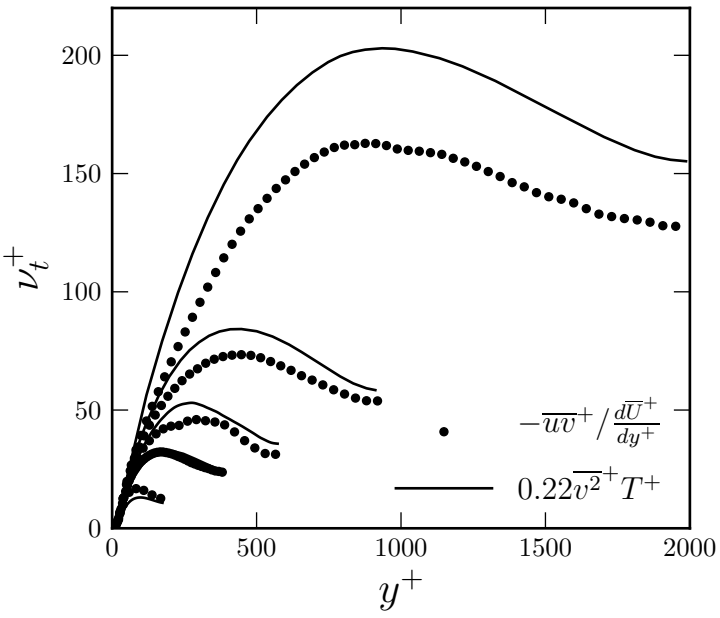

Figure 5.5: A priori evaluation of ν_t^+ in a channel flow, for $Re_\tau \in \{180; 395; 590; 950; 2000\}$

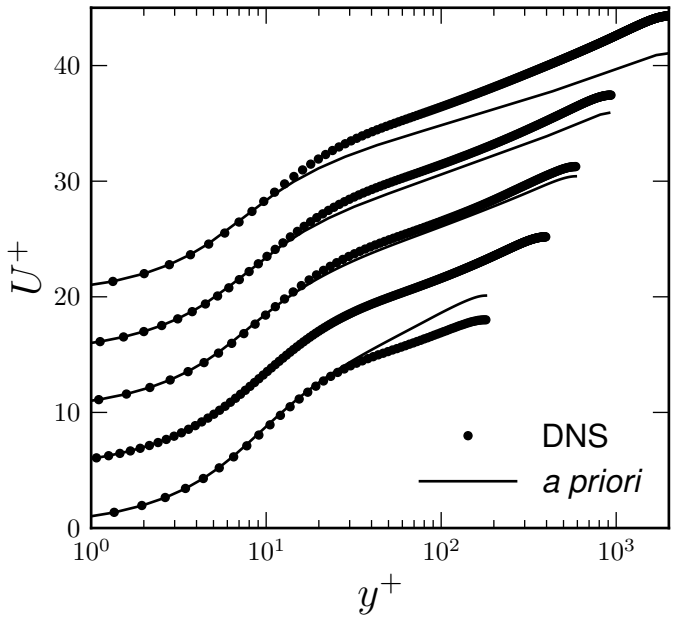

Figure 5.6: Velocity profile in a channel flow: *a priori* evaluation using Eq. 5.6 with $\overline{uv} = -C_\mu \overline{v^2} T \frac{d\overline{U}}{dy}$, for $Re_\tau \in \{180; 395; 590; 950; 2000\}$

and Hanjalic (2002), different alternatives to the commonly used $C^*_{\varepsilon 1}$ were tried, and attention was also paid to the possible numerical instabilities the modifications could cause. The most noticeable consequence of those alterations (and admittedly the most beneficial) is their influence on the resulting ν_t Re_τ-dependence. Three modifications are now presented, and it will be seen that combining the three of them enables to considerably reduce the Reynolds-number-dependence of ν_t.

Modification 1 (M1): As suggested in Jakirlic and Hanjalic (2002) the variable ε'_h, representing the homogeneous dissipation rate and defined as $\varepsilon'_h = \varepsilon - \frac{1}{2}\nu\Delta k$, is solved for instead of ε. This leads to several changes in the $\varphi - \alpha$ equations:

- ε is replaced by ε'_h in the k equation. The change of variable implies that the molecular diffusion of k is halved. For consistency the dissipation term ε_{22} in the $\overline{v^2}$ equation is replaced by $\varepsilon'_{22,h}$ (with $\varepsilon_{22} = \varepsilon'_{22,h} + \frac{1}{2}\nu\Delta\overline{v^2}$). In the derived φ equation, this results in the molecular diffusion of φ being halved as well.

- The wall boundary condition for ε'_h is also halved: $\varepsilon'_{w,h} = \nu k/y^2$. Likewise, the near-wall term of the φ equation reads: $(1-\alpha^p)\left[-\frac{1}{2}\varphi\frac{\varepsilon'_h}{k}\right]$

- Neglecting higher order terms, it can be shown (Jovanovic et al. (1995)) that the transport equation for ε'_h is similar to the one for ε except that, again, the molecular diffusion of ε'_h is halved.

Modification 2 (M2): The $C^*_{\varepsilon 1}$ coefficient is taken as constant ($C^*_{\varepsilon 1} = C_{\varepsilon 1}$) and the near-wall increase of the dissipation is modelled by the Jones and Launder (1972) E term $2\nu\nu_t\left(\frac{\partial^2\overline{U_i}}{\partial x_j \partial x_k}\right)^2$ (as already introduced in Sec. 3.3.2): this consists in an additional source term S_ε in the ε equation which reads $S_\varepsilon = C_{A1}(1-\alpha)^3 2\nu\nu_t\left(\frac{\partial^2\overline{U_i}}{\partial x_j \partial x_k}\right)^2$. The "$E$" term is here multiplied by a factor $(1-\alpha)^3$ to restrict its influence in the near-wall region.

Modification 3 (M3): $C^*_{\varepsilon 1} = C_{\varepsilon 1}$ and the S_ε term is moved from the ε equation to the k equation. This formally corresponds to a change of variable which, when

combined to the one performed in M1, takes the form

$$\varepsilon = \underbrace{\varepsilon_h + k/\varepsilon_h C_{A1}(1-\alpha)^3 2\nu\nu_t \left(\frac{\partial^2 \overline{U_i}}{\partial x_j \partial x_k}\right)^2}_{\varepsilon'_h} + \frac{1}{2}\nu\Delta k \tag{5.7}$$

The source term of the k equation becomes $P - \varepsilon - k/\varepsilon_h C_{A1}(1-\alpha)^3 2\nu\nu_t \left(\frac{\partial^2 \overline{U_i}}{\partial x_j \partial x_k}\right)^2 - \frac{1}{2}\nu\Delta k$ and this will be the only modification. The formal change of variable would involve more terms which are deliberately neglected in the present approach, on the basis that they would only play a role in the vicinity of walls. This might seem a crude assumption, but we recall in light of the shortcoming in Durbin's model for ν_t that we do not seek to obtain the best representation for each turbulent variable individually.

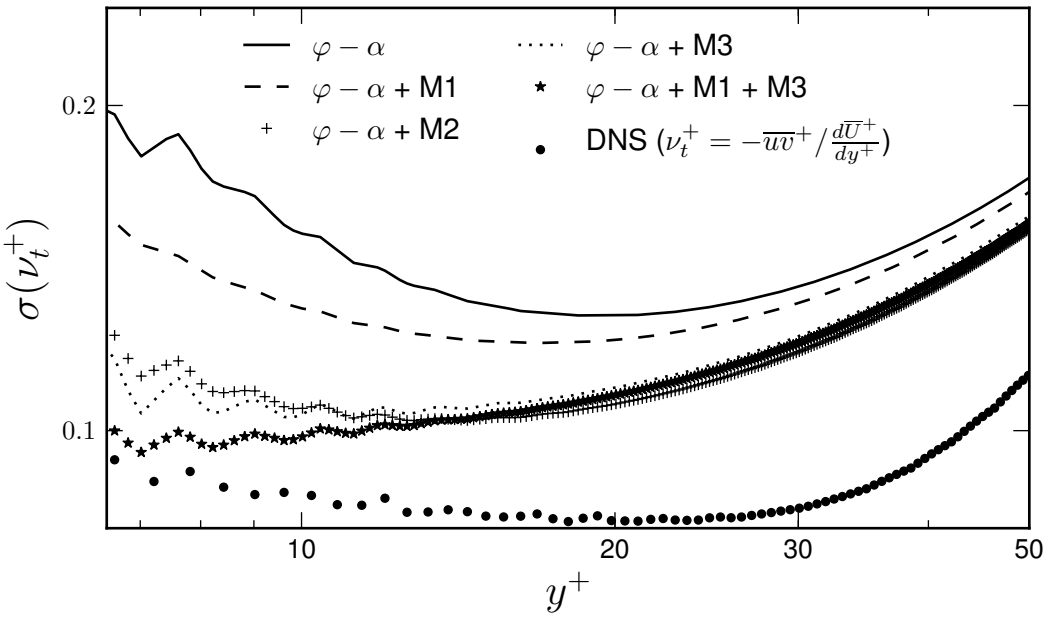

Figure 5.7: ν_t^+ Reynolds dependance coefficient $\sigma(\nu_t^+)$ in a channel flow for different variants of the model.

Fig. 5.7 shows the ν_t^+ Re_τ-dependance measure $\sigma(\nu_t^+)$ for the $\varphi - \alpha$ model with different modifications. It can be seen that the simple use of the modification M1 enables to substantially reduce $\sigma(\nu_t^+)$ compared to the original $\varphi - \alpha$, essentially in the lower edge of the buffer layer, where viscous terms are still active. This can be explained by the reduction of the near-wall limit of ε^h involved by the modification

M1. Indeed ε_w is linked to the near-wall behaviour of k which is linked to the production. Since as already mentioned the production peak is strongly Reynolds-dependent, reducing the link between k and ε_w helps limit the propagation of this undesired feature. It can be seen that using the E term instead of the variable $C^*_{\varepsilon 1}$ coefficient (modification M2) also strongly helps decrease $\sigma(\nu_t^+)$ and in a larger part of the buffer layer compared to what was obtained with the modification M1. Moving the E term into the k equation (modification M3) helps further reduce $\sigma(\nu_t^+)$ compared to modification M2. Finally the combination of modifications M1 and M3 is seen to be the one giving the lowest level of $\sigma(\nu_t^+)$.

The final BL-$\overline{v^2}/k$ model will include modifications M1 and M3: ε will be assimilated to ε_h (defined in Eq. 5.7) wherever it is used (therefore the notation "ε" will be retained).

These modifications are not solely motivated by the effect they have on the reproduction of $\sigma(\nu_t^+)$, but they also improve the predictive capabilities and the robustness of the model.

Improved prediction in the buffer-layer In the $\varphi - \alpha$ model, the near-wall modification of $C^*_{\varepsilon 1}$ is multiplied by $(1 - \alpha^p)$ in order to reduce its influence in the near-wall region. As seen in Fig. 5.2, this helps improve the prediction of $\overline{U}^+$ in the buffer layer (characterised by a bump), which is also visible for the variable $y^+ \frac{d\overline{U}^+}{dy^+}$ where the peak in the buffer layer is much better represented by the $\varphi - \alpha$ model. With the factor $(1 - \alpha^p)$ the side effects are reduced and the main effect of the coefficient C_{A1} tuning (recalling C_{A1} is involved in the $C^*_{\varepsilon 1}$ definition, Tab. 5.1) concentrates in the buffer layer whose prediction can therefore be optimised.

It will be seen now that the influence of the needed extra ε production term is even more localised when it is modelled by the E term: Fig. 5.8 compares the behaviour of the $\varphi - \alpha$ formulation with different variants for the near-wall dissipation modelling: using $C^*_{\varepsilon 1}$ from its definition in Tab. 5.1 without and with the factor $(1 - \alpha^p)$ or applying modification M2 or modification M3. Curves in Fig. 5.8 show predictions for $y^+ \frac{d\overline{U}^+}{dy^+}$ for C_{A1} varying over a range of values. The link between the coefficient

C_{A1} and the near-wall peak of the predicted term $y^+\frac{d\overline{U}^+}{dy^+}$ is clear. Without the factor $(1-\alpha^p)$ (Fig. 5.8 top left), an increase of C_{A1} results in shifting the whole profile upwards, whereas the use of this factor in the $C^*_{\varepsilon 1}$ definition (See Fig. 5.8 top right) restricts the shifting to the near-wall region, but in both cases the influence of the C_{A1} modification is still present in a large part of the log layer. With modification M2 (Fig. 5.8 bottom left), the influence in the logarithmic layer is considerably reduced and the shape of the $y^+\frac{d\overline{U}^+}{dy^+}$ peak more closely represented. This is further improved with the presence of the E term in the k equation (modification M3), as shown on the bottom right graph.

Improved numerical stability The E term (Jones and Launder, 1972), as sounder and less empirical alternative to the commonly used variable $C^*_{\varepsilon 1}$, was adopted in the early version of the elliptic blending Reynolds Stress model of Manceau and Hanjalić (2002). This choice was later abandoned due to the numerical problems it raised, the main drawback of the E term being that it is handled explicitly in the ε equation. Second derivatives of the velocity, whose evaluation can represent a computational challenge when handled explicitly, result in error in its computation that are likely to be of the same order as the other source terms in the near-wall region. When "moved" to the k equation, the E term is multiplied by a time scale, chosen to be k/ε. Its presence on the form "$-k\times\ldots$" allows an easy implicit discretisation in the $k-\varepsilon$ system resolution.

5.4 Solution 2: The length-scale L definition

The elliptic operator enables the variable f to switch from its near-wall value f_w to its homogeneous value f_h with an exponential like behaviour (if L were constant, one would have $f = f_w + (1-e^{-y/L})(f_h - f_w)$). The choice for the coefficients C_L and C_η involved in the length-scale definition (See Tab. 5.2) determines the values of the elliptic variable α, hence the importance of the near-wall terms in the φ equation, and consequently it influences the behaviour of ν_t in the near-wall region. Therefore, to

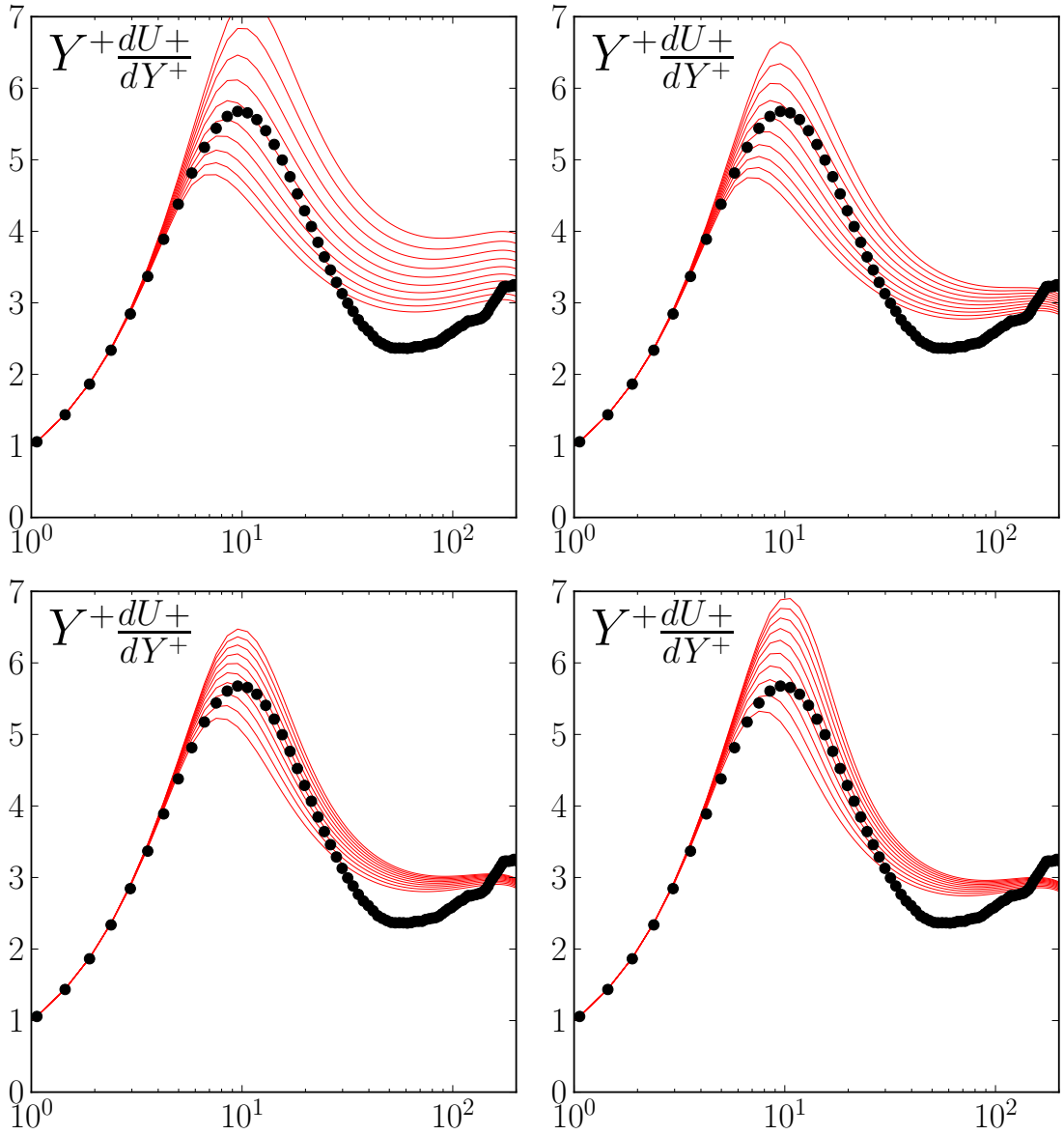

Figure 5.8: Prediction of the variable $y^+ \frac{d\overline{U}^+}{dy^+}$ in a channel flow for $Re_\tau = 395$ with the $\varphi - \alpha$ model. •••: DNS., ——: $\varphi - \alpha$. **Top left:** $\varphi - \alpha$ with $C^*_{\varepsilon 1} = 1.4\left(1 + C_{A1}\sqrt{\frac{1}{\varphi}}\right)$, $C_{A1} \in [0.02, 0.07]$. **Top right:** $\varphi - \alpha$ with $C^*_{\varepsilon 1} = 1.4\left(1 + C_{A1}\left(1-\alpha^3\right)\sqrt{\frac{1}{\varphi}}\right)$, $C_{A1} \in [0.02, 0.07]$. **Bottom left:** $\varphi - \alpha$ with term $C_{A1} \times 2\nu\nu_t \left(1-\alpha\right)^3 \left(\frac{\partial^2 \overline{U}_i}{\partial x_j \partial x_k}\right)^2$ added into the ε equation (modification M2), $C_{A1} \in [1.40, 4.55]$. **Bottom right:** $\varphi - \alpha$ with term $-\frac{k}{\varepsilon} C_{A1} \times 2\nu\nu_t \left(1-\alpha\right)^3 \left(\frac{\partial^2 \overline{U}_i}{\partial x_j \partial x_k}\right)^2$ added into the k equation (modification M3), $C_{A1} \in [0.80, 2.60]$.

further reduce the Re_τ dependance of ν_t, we seek coefficients C_L and C_η yielding for α the least Re_τ dependence. This aim also finds justification in Lecocq (2008). While studying the elliptic blending RSM of Manceau and Hanjalić (2002) he performed, for different Re_τ, *a-priori* evaluation of the DNS quantity α_{DNS} which is modelled by α, and defined as:

$$\alpha^{DNS} = \frac{\left(\phi_{22}^{DNS} - \varepsilon_{22}^{DNS}\right) - \left(\phi_{22}^{w} - \varepsilon_{22}^{w}\right)}{\left(\phi_{22}^{h} - \varepsilon_{22}^{h}\right) - \left(\phi_{22}^{w} - \varepsilon_{22}^{w}\right)} \tag{5.8}$$

where $\bullet^h$ and $\bullet^w$ respectively denote the homogeneous and the near-wall model. It is shown that α^{DNS} does not depend on Re_τ in the near-wall region[3].

The low-Re_τ-dependence of the α parameter predicted by the $\varphi-\alpha$ model, seen in Fig. 5.1, is a property which actually strongly depends on the choice for C_L and C_η. Even though the switch location between the Kolmogorov and the integral length-scale only depends on C_η, the evolution of α depends on the independent choice for both coefficient. The importance of this independence was minimised in Durbin and Laurence (1996) which state that in the model tuning a decrease of C_η can be balanced by an increase of C_L, suggesting a redundancy in the two coefficients, with the product $C_L \times C_\eta$ being the ultimate adjustment parameter. This statement will now be nuanced.

In the following we study the relation between the pair (C_L, C_η) and the resulting variable α. The latter can be characterised by a single parameter, the recovery length, noted $y^+_{\alpha=0.9}$ which corresponds to the non-dimensional distance to the wall at which $\alpha = 0.9$. In this analysis DNS values are taken for the variables k and ε entering the length-scale definition, and the elliptic equation $\alpha - L^2\Delta\alpha = 1$ is solved for different pairs (C_L, C_η), using the same DNS grid, and $y^+_{\alpha=0.9}$ is calculated. Fig. 5.9 shows the map of the function $y^+_{\alpha=0.9}(C_L, C_\eta)$ evaluated using DNS values of two different Reynolds numbers ($Re_\tau = 395$ and 2000). On the top of the map, the isoclines of the function $C_L \times C_\eta$ are displayed. Several conclusions can be drawn:

- It is clear for $Re_\tau = 2000$, that C_η does not influence much $y^+_{\alpha=0.9}$ even though

[3]This no longer being the case from the logarithmic region for $Re_\tau = 2000$ and according to Lecocq (2008) it is due to the discrepancies of the SSG model used in Manceau and Hanjalić (2002).

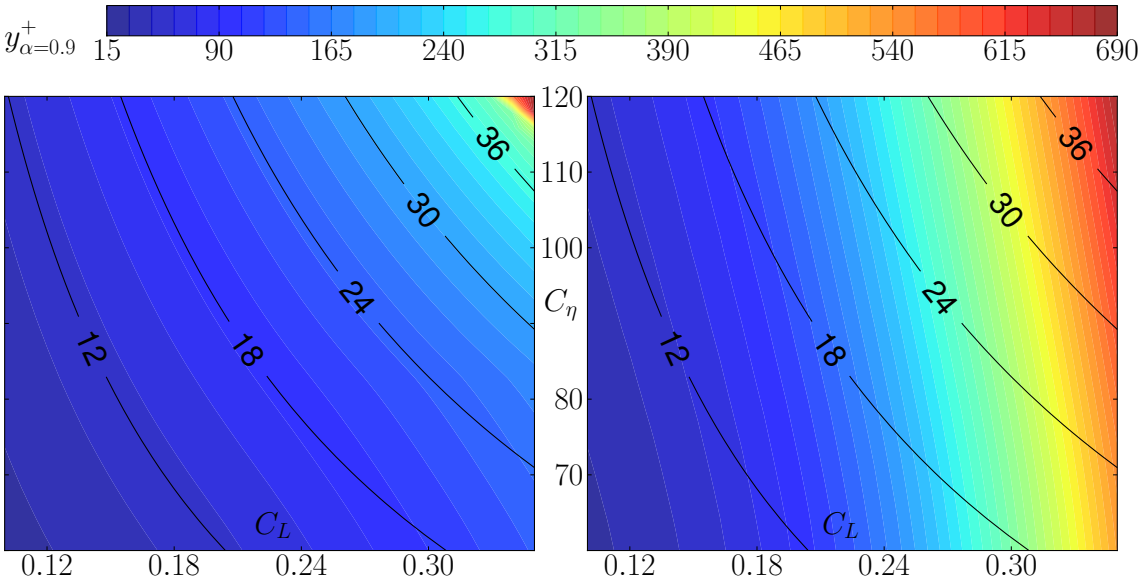

Figure 5.9: $y^+_{\alpha=0.9}$ map as function of C_L and C_η for $Re_\tau = 395$ (left) and $Re_\tau = 2000$ (right). $C_L \times C_\eta$ isoclines are plotted on top of the map.

the Kolmogorov / integral length-scale switch location, $y^+_{s,L}$ (see Tab. 4.6) solely depends on C_η.

- For $Re_\tau = 395$, $y^+_{\alpha=0.9}$ is very well correlated with $C_L \times C_\eta$, the isoclines of the two functions being parallel. However this is no longer true for $Re_\tau = 2000$ especially for high values of C_L. This proves the independence of the two coefficients for high Re_τ.

- Very low-Reynolds-number dependence of $y^+_{\alpha=0.9}$ can be achieved for low values of C_L and C_η. On the other hand, for $C_\eta = 110$ and $C_L = 0.35$, $y^+_{\alpha=0.9}$ varies from 200 for $Re_\tau = 395$ to 600 for $Re_\tau = 2000$.

This analysis focuses on the elliptic blending coefficient but it is believed that the same conclusion could be drawn for the other elliptic relaxation based models. As seen on Tab. 4.5 there is a high variability for the choice (C_L, C_η) amongst the different versions of the $\overline{v^2} - f$ models therefore leading to different levels of Re_τ dependence for $\overline{v^2}$, hence ν_t. In the final BL-$\overline{v^2}/k$ model, the coefficients $(C_L = 0.164, C_\eta = 75)$ are used, ensuring a low Re_τ-dependence of α, thanks to the low value adopted for C_η. The value of C_L is taken equal to its theoretical value determined via the

von Kármán constant in the logarithmic layer. As seen previously, in this region, $L = C_L \frac{k^{3/2}}{\varepsilon} = C_L \left(C_\mu \frac{\overline{v^2}}{k}\right)^{-3/4} \kappa y$. $L = \kappa y$ implies $C_L = 0.09^{3/4} = 0.164$ (in the $\overline{v^2} - f$ model, the value of $C_\mu = 0.22$ is chosen so that in the log layer $C_\mu \dfrac{\overline{v^2}}{k} = 0.09$ (with $\dfrac{\overline{v^2}}{k} = 0.41$)).

5.5 Dissipation rate in the defect layer

In addition to the modifications done to reduce the ν_t Reynolds-number dependence, an improvement of the dissipation rate equation is now proposed to yield better predictions in the defect layer of a channel flow and in separated flows.

Turbulence submitted to constant and uniform shear builds up at a rate P/ε whose asymptotic value is $\dfrac{C_{\varepsilon 2} - 1}{C_{\varepsilon 1} - 1}$[4]. More generally this parameter controls the spreading rate of a mixing layer, which is then determined by the choice for $C_{\varepsilon 1}$ and $C_{\varepsilon 2}$ (note that it only depends on φ if $C_{\varepsilon 1}$ does). There are several ways to calibrate $C_{\varepsilon 1}$ and $C_{\varepsilon 2}$ (because a round jet, a plane mixing layer or a boundary layer have different spreading rates) and therefore a trade-off is needed[5]. This is all the more true as the value for the coefficient $C_{\varepsilon 2}$ is already determined by the homogeneous isotropic turbulence rate of decay, so that $C_{\varepsilon 1}$ is the true spreading rate controlling parameter. In most of the reviewed $\overline{v^2} - f$ models $C^*_{\varepsilon 1}$ is influenced by the near-wall modification of the coefficient $C^*_{\varepsilon 1}$ (see Tab. 4.4) which does not vanish outside the near-wall region and this results in a value for $C^*_{\varepsilon 1}$ generally of order 1.5 in all the flow regions, as seen in Fig. 4.1. Even though this is a satisfactory value for a boundary layer this was shown to lead to an insufficient spreading rate in the case of a mixing layer, for which a smaller value of $C_{\varepsilon 1} = 1.3$ was recommended in Durbin (1995). On the other hand in the $\varphi - \alpha$ model the factor $(1 - \alpha^p)$ in the $C^*_{\varepsilon 1}$ definition (Tab. 5.1) leads to $C_{\varepsilon 1} = 1.44$ in all the regions outside the near-wall layer. This leads to an over-predicted spreading rate in a wall-bounded flow and this actually has adverse

[4]Using notations introduced in Subsec. 4.2.3 in homogeneous sheared turbulence the limiting value of $(P/\varepsilon)_\infty = C_\mu \varphi_\infty \eta^2_\infty = (C_{\varepsilon 2} - 1)/(C_{\varepsilon 1} - 1)$.

[5]For instance Craft and Launder (1996) use $C_{\varepsilon 1} = 1$ and $C_{\varepsilon 2} = f(A, A_2)$ to resolve the plane / round jet anomaly

effects on separated flows, as it will be seen in the results chapter (Chap. 6).

The present work proposes to revisit the idea introduced by Durbin (1995), consisting in returning a different spreading rate for a boundary layer and a plane mixing layer, in a more code friendly manner (*i.e.* without using the parameter y): as it was seen in Fig. 3.5, the turbulent diffusion of k, $D_k^T = \frac{\partial}{\partial x_j}\left(\nu_t \frac{\partial k}{\partial x_j}\right)$, starts to be important from the upper edge of the logarithmic layer, and the equilibrium $D_k^T = \varepsilon$ settles further up, whereas there is no turbulent transport in homogeneous sheared turbulence. Therefore it is proposed to introduce the parameter D_k^T/ε to characterise the defect layer of a wall-bounded flow and it is used to reduce the $C_{\varepsilon 2}$ coefficient. This has the same effect as a $C_{\varepsilon 1}$ increase and results in the diminution of the spreading rate. The following modification is proposed:

$$C_{\varepsilon 2}^* = C_{\varepsilon 2} + \alpha^3 \left(C_{\varepsilon 4} - C_{\varepsilon 2}\right) \tanh\left(\left|\frac{D_k^T}{\varepsilon}\right|^{3/2}\right) \tag{5.9}$$

As it was noticed in Chap. 3 the ε source term $P_1 + P_2 + P_4 - Y$ is unsatisfactorily represented by the model

$$\frac{C_{\varepsilon 1} P - C_{\varepsilon 2}\varepsilon}{T} \tag{5.10}$$

with $C_{\varepsilon 1} = 1.44$ and $C_{\varepsilon 2} = 1.83$, and Parneix et al. (1996) suggested the coefficient $C_{\varepsilon 2}$ should be halved in the defect layer. This is achieved by the present model Eq. 5.9 as seen in Fig. 5.10 which compares the two models to the exact ε source term (these terms, whose behaviour in the logarithmic layer is $O(y^{-2})$ are multiplied by y^2 for clarity). Fig. 5.11 shows the *a priori* evaluation of Eq. 5.9 ($C_{\varepsilon 2}^* = f(y)$) for various Re_τ. This shows a Re_τ independent characterisation of the outer region of the flow by the proposed model.

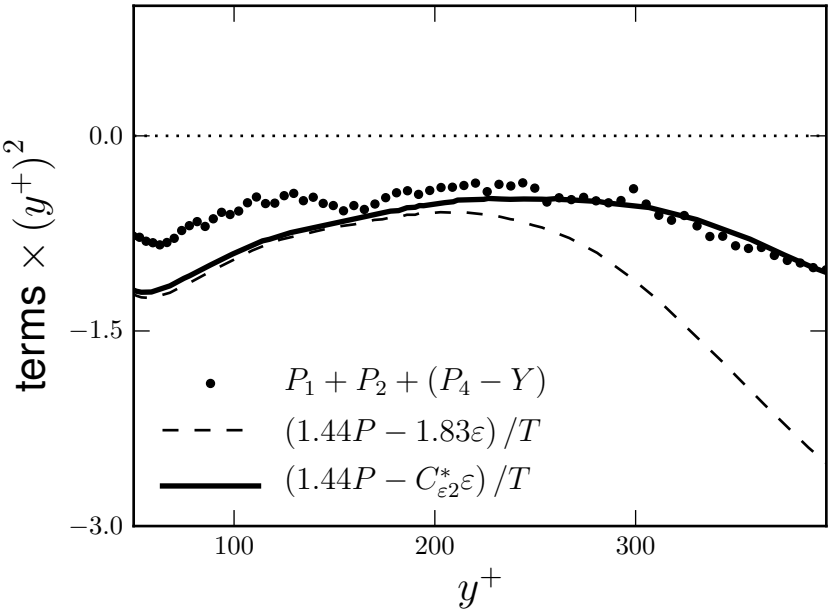

Figure 5.10: Model for the ε source term using a variable $C_{\varepsilon 2}$ coefficient ($C^*_{\varepsilon 2}$ from Eq. 5.9). *A priori* comparison for $Re_\tau = 395$.

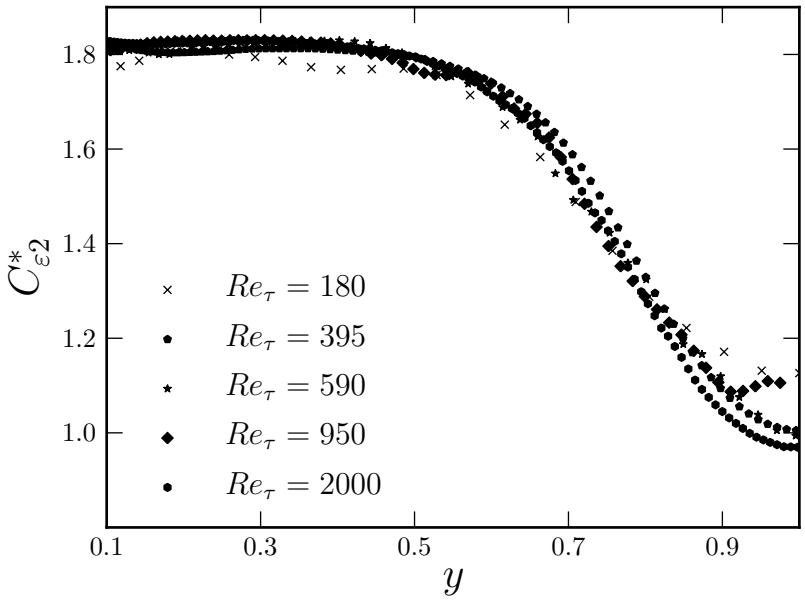

Figure 5.11: $C^*_{\varepsilon 2}$ from Eq. 5.9 for $Re_\tau \in \{180; 395; 590; 950; 2000\}$

5.6 The BL-$\overline{v^2}/k$ model

5.6.1 Presentation of the model

The modifications proposed in the three previous sections were integrated into a new model, namely the BL-$\overline{v^2}/k$ model (Billard and Laurence (2011)), whose equations

and constants are now given[6].

$$\begin{cases} \dfrac{Dk}{Dt} = P - \varepsilon - 2C_{\varepsilon 3}\nu\nu_t(1-\alpha)^p \dfrac{k}{\varepsilon}\left(\dfrac{\partial^2 \overline{U}_i}{\partial x_k \partial x_j}\right)^2 + \dfrac{\partial}{\partial x_j}\left[\left(\dfrac{\nu}{2} + \dfrac{\nu_t}{\sigma_k}\right)\dfrac{\partial k}{\partial x_j}\right] \\ \dfrac{D\varepsilon}{Dt} = \dfrac{C_{\varepsilon 1}P - C^*_{\varepsilon 2}\varepsilon}{T} + \dfrac{\partial}{\partial x_j}\left[\left(\dfrac{\nu}{2} + \dfrac{\nu_t}{\sigma_\varepsilon}\right)\dfrac{\partial \varepsilon}{\partial x_j}\right] \\ \lim\limits_{y\to 0} k = 0 \\ \lim\limits_{y\to 0} \varepsilon = \lim\limits_{y\to 0} \dfrac{\nu k}{y^2} \end{cases} \tag{5.11}$$

$$\begin{cases} \dfrac{D\varphi}{Dt} = -(1-\alpha^p)\dfrac{\varepsilon}{2}\dfrac{\varphi}{k} + \alpha^p f_h - P\dfrac{\varphi}{k} + \dfrac{2}{k}\dfrac{\nu_t}{\sigma_k}\dfrac{\partial k}{\partial x_j}\dfrac{\partial \varphi}{\partial x_j} + \dfrac{\partial}{\partial x_j}\left[\left(\dfrac{\nu}{2} + \dfrac{\nu_t}{\sigma_\varphi}\right)\dfrac{\partial \varphi}{\partial x_j}\right] \\ f_h = -\dfrac{1}{T}\left(C_1 - 1 + C_2\dfrac{P}{\varepsilon}\right)\left(\varphi - \dfrac{2}{3}\right) \\ \lim\limits_{y\to 0}\varphi = 0 \end{cases} \tag{5.12}$$

$$\begin{cases} \alpha - L^2\Delta\alpha = 1 \\ \lim\limits_{y\to 0}\alpha = 0 \end{cases} \tag{5.13}$$

$C_{\varepsilon 1}$	$C^*_{\varepsilon 2}$	$C_{\varepsilon 2}$	$C_{\varepsilon 3}$	$C_{\varepsilon 4}$	σ_k	σ_ε
1.44	$C_{\varepsilon 2} + \alpha^p\left(C_{\varepsilon 4} - C_{\varepsilon 2}\right)\tanh\left(\left\lvert\dfrac{\partial}{\partial x_j}\left(\dfrac{\nu_t}{\sigma_k}\dfrac{\partial k}{\partial x_j}\right)/\varepsilon\right\rvert^{3/2}\right)$	1.83	2.3	0.4	1	1.5

Table 5.6: Constants of the BL-$\overline{v^2}/k$ model. k and ε equations

T	C_T	L	C_L	C_η	ν_t	C_μ
$\sqrt{\left(\dfrac{k}{\varepsilon}\right)^2 + C_T^2\left(\dfrac{\nu}{\varepsilon}\right)}$	4	$C_L\sqrt{\dfrac{k^3}{\varepsilon^2} + C_\eta^2\left(\dfrac{\nu^3}{\varepsilon}\right)^{1/2}}$	0.164	75	$C_\mu\varphi k T$	0.22

Table 5.7: Constants of the BL-$\overline{v^2}/k$ model. Turbulent time, length and viscosity scale, and associated constants.

[6]The coefficient C_{A1} is renamed $C_{\varepsilon 3}$ for consistency

C_1	C_2	σ_φ	p
1.7	0.9	1	3

Table 5.8: Constants of the BL-$\overline{v^2}/k$ model. φ and α equations.

5.6.2 Preliminary results

The predictions of the BL-$\overline{v^2}/k$ model (Fig. 5.12 and Fig. 5.13) are improved for all variables. The model behaviour in the buffer layer is enhanced and the near-wall peak of $y^+\dfrac{d\overline{U}^+}{dy^+}$ is well represented. The variable $y^+\dfrac{d\overline{U}^+}{dy^+}$ is satisfactorily Re_τ independent. In fact with the new model the variable ε is only very weakly Re_τ dependent, as a result of the modifications performed on the $k-\varepsilon$ system. The correct prediction of κ (see Tab. 5.10) yields improved predictions of $y^+\varepsilon^+$ and $y^+\dfrac{d\overline{U}^+}{dy^+}$ in the logarithmic layer. Finally, the effect of the diminution of the $C_{\varepsilon 2}$ coefficient in the defect layer is reflected by the correct representation of $\dfrac{k^+}{y^+\varepsilon^+}$, hence ν_t^+/y^+, in this region, where all other $\overline{v^2}-f$ based models over-predict those two variables (as seen on Fig. 4.8). Tab. 5.9 compares the skin friction coefficient for URI06, the $\varphi-\alpha$ and the BL-$\overline{v^2}/k$ models. As seen the latest BL-$\overline{v^2}/k$ version corrects the discrepancy observed with the $\varphi-\alpha$ model for the lowest Reynolds number. Tab. 5.10 presents the behaviour in the logarithmic layer and in homogeneous sheared turbulence. The correct theoretical behaviour in the logarithmic layer ($\kappa = 0.42$ and $\eta = 3.33$) is recovered.

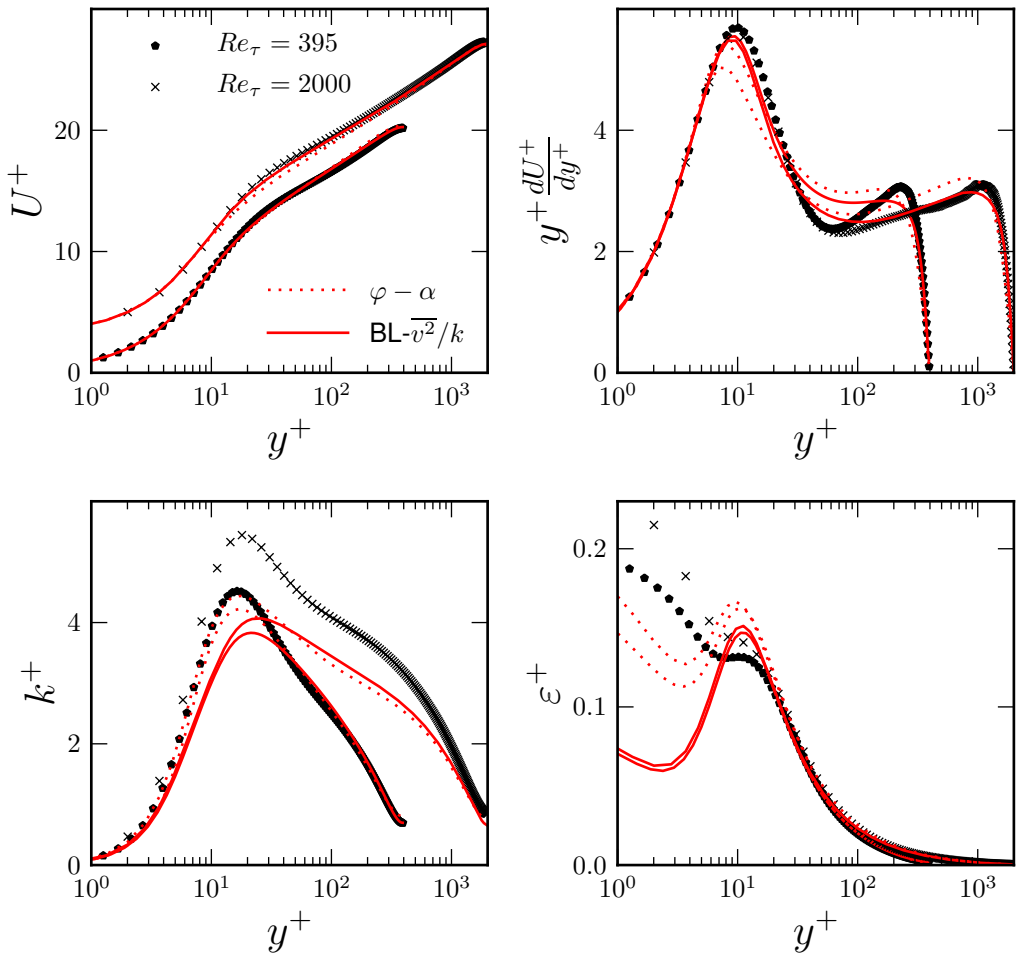

Figure 5.12: Predictions of the model in the channel flow for $Re_\tau \in \{395; 2000\}$, for the variables $\overline{U}^+$, $y^+ d\overline{U}^+/dy^+$, k^+ and ε^+

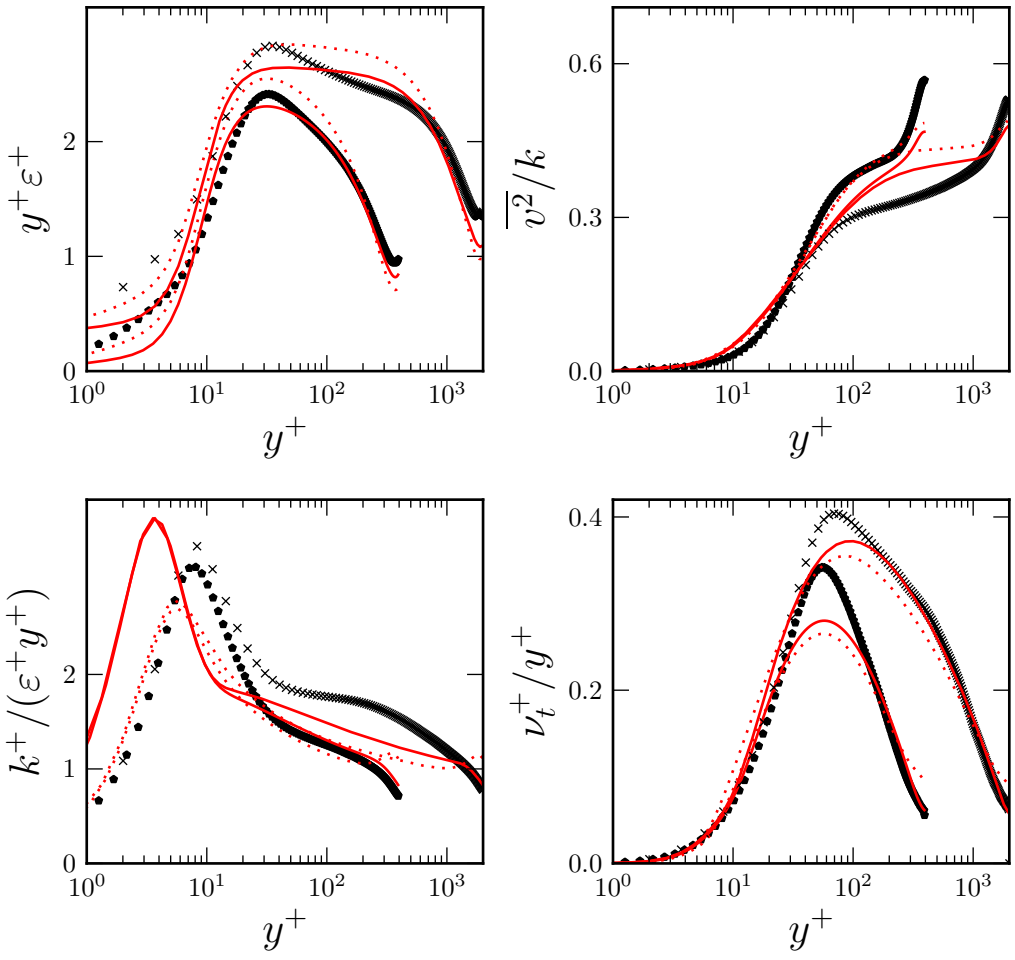

Figure 5.13: Predictions of the model in the channel flow for $Re_\tau \in \{395; 2000\}$, for the variables $y^+\varepsilon^+$, φ, $k^+/(\varepsilon^+ y^+)$ and ν_t^+/y^+. See Fig. 5.12 for legends.

Model	$Re_\tau = 180$	$Re_\tau = 395$	$Re_\tau = 590$	$Re_\tau = 950$	$Re_\tau = 2000$
URI06	99	102	104	105	106
$\varphi - \alpha$	94	97	100	101	102
BL-$\overline{v^2}/k$	100	98	100	100	101

Table 5.9: Friction coefficient C_f compared to the DNS value for the same friction velocity based Reynolds number Re_τ (given in %) for URI06, the $\varphi - \alpha$ and the BL-$\overline{v^2}/k$ models

Model	κ	φ_{log}	$\frac{\varphi_{log}}{\varphi_{log}^{A=1}}$ (%)	A (%)	η	$C^*_{\varepsilon 1,log}$	φ_∞	η_∞	$C^*_{\varepsilon 1,\infty}$
URI06	0.41	0.59	146	180	2.77	1.49	0.37	4.49	1.51
$\varphi - \alpha$	0.38	0.44	100	100	3.23	1.44	0.41	4.59	1.44
BL-$\overline{v^2}/k$	0.42	0.41	100	100	3.33	1.44	0.37	4.79	1.44

Table 5.10: Predictions of the models in the log layer (left part) and in homogeneous shear turbulence (right part) for URI06, the $\varphi - \alpha$ and the BL-$\overline{v^2}/k$ models

Chapter 6

Performance of the models

The first version developed, the $\varphi - \alpha$ model (Billard et al., 2008), and the second version, the BL-$\overline{v^2}/k$ model (Billard and Laurence, 2011), have been validated on a set of generic flows presenting some challenging features for turbulence modelling. They fall into two categories: pressure induced separating flows (flow through a periodically constricted channel flow (adapted from Almeida et al. (1993)) and in an asymmetric plane diffuser (Obi et al., 1993; Buice and Eaton, 1997)) and configurations featuring heat transfer (natural convection in a tall enclosed cavity (Betts and Bokhari, 2000) and mixed natural and forced convection in an vertical heated channel flow (Kasagi and Nishimura, 1997). Most of the configurations tested in the present study are popular benchmark cases for RANS models, and in particular $\overline{v^2} - f$ models. As will be seen, the early $\overline{v^2} - f$ formulations are shown to return fairly good results, and it will be investigated whether the present proposals provide results at least of the same level of accuracy. Moreover, the effects of the suggested improvements of the k and ε equations developed in the BL-$\overline{v^2}/k$ model will be assessed: to this end, the model will be compared to the early $\varphi - \alpha$ formulation (which simply addresses the numerical stability issue by solving for both φ and α), the main differences between both models being located in the k and ε equations modelling.

The $\varphi - \alpha$ and BL-$\overline{v^2}/k$ models are systematically compared to the code friendly $\overline{v^2} - f$ version of LIE01 (which is the one implemented in most commercial codes), the URI06 model (Laurence et al. (2004)) and the $k - \omega$ SST model (Menter (1994)). All

simulations are performed with the unstructured finite volume code *Code_Saturne* which is be introduced in Appendix. A.

6.1 Separating flows

This section focuses on the study of two configurations of pressure-induced separating flows for which well-documented reference data are available.

6.1.1 Periodic hill flow

Presentation of the case

This is an adaptation of the experiment of Almeida et al. (1993) who studied the flow over a single hill and between the last two consecutive hills of a series. The case was the subject of highly resolved LES (Temmerman and Leschziner, 2001; Fröhlich et al., 2005) which assume the flow is periodic in the stream-wise direction. The LES calculations were carried out using a configuration different from the experimental one: the channel height is halved and the inter-hill distance is twice as large so as to decrease the stream-wise coupling. Moreover span-wise homogeneous boundary conditions are applied, so that the LES flow is statistically truly 2-D. In the LES configuration, the hill topology is the same as in Almeida et al. (1993), and the domain is represented in Fig. 6.1. The inter-crest distance is $L_x = 9h$, and the two walls are separated by a distance of $L_y = 3.036h$, h being the hill height. The simplifications of this reference simulation case makes it a popular benchmark for assessing both coarser LES and RANS models, and it was the object of two ERCOFTAC workshops[1]. The flow is fully turbulent, with a Reynolds number of 10595, based on h and the bulk velocity above the hill crest.

The flow separates early after the hill crest, due to the strong curvature and reattaches half way between the two hills. Downstream, the flow recovers and is

[1] `http://www.ercoftac.org/special_interest_groups/15_turbulence_modelling/`

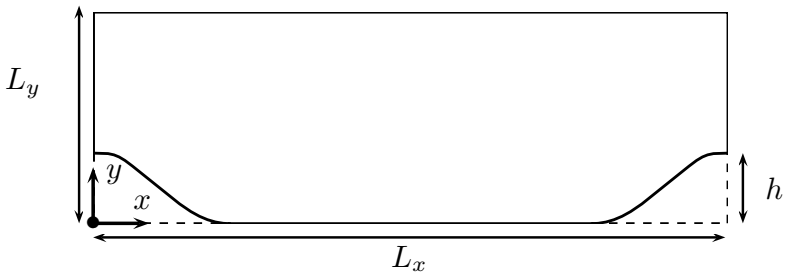

Figure 6.1: Geometry of the periodic hill flow configuration

accelerated on the wind-ward face of the next hill. It was shown that the flow in the separation was only little influenced by the behaviour downstream (Jang et al. (2002)) evidencing the desired stream-wise coupling reduction whose LES configuration is the purpose. However the flow presents some challenging features for turbulence modelling:

- The separation occurs on a highly curved surface and the re-circulation size and the gross flow features highly depend on the separation location (Temmerman and Leschziner (2001))

- The flow within the re-circulation also depends on its interaction with the bulk flow, governed by the turbulent shear stress. Therefore, the main prerequisite for a RANS model in this case is its ability to represent the correct level of shear-stress along the boundary layer.

- The flow is strongly accelerated on the wind-ward face and features a thin boundary layer at the top of the crest.

- The study of the LES flow field (Fröhlich et al., 2005) highlights flow mechanisms whose modelling is out of reach of RANS models, such as the strong intermittent nature of the flow in the re-circulation zone, the trend towards formation of two secondary vortices downstream of the separation and of a second small recirculation on the windward face. This raises questions about the relevance of RANS model results on this case, which may return the correct prediction for the wrong reasons.

Performance of RANS modelling

Jang et al. (2002) compared the capabilities of numerous RANS models of different complexity: linear and non-linear eddy viscosity models as well as second moment closure, with high and low Reynolds versions and resolving either ε and ω for the length-scale determining parameter, amongst others the $k-\omega$ model of Wilcox (2006), the $k-\varepsilon$ model of Launder and Sharma (1974), the non-linear ω based model of Wallin and Johansson (2000) and the low-Reynolds number Reynolds Stress model of Chen et al. (2000). The performances of the $k-\omega$ SST model of Menter (1994), the $\overline{v^2}-f$ model of Durbin (1991), the code-friendly version of LIE96 and the URI06 version were studied in Uribe (2006).

The main difference between models is the shear-stress $\overline{uv}$ prediction across the recirculation region. The $k-\varepsilon$ model of Launder and Sharma (1974) predicts high level of $\overline{uv}$, leading to a recirculation region that is considerably too small, whereas most other models, such as the ε-based non-linear eddy-viscosity models and the Reynolds-stress model of Chen et al. (2000) strongly under-predict the shear-stress in this region and especially its near-wall behaviour, leading to excessively large recirculation zones.

However, a correctly-sized recirculation is predicted by the $k-\omega$ model, the non-linear ω-based model of Wallin and Johansson (2000) and the $\overline{v^2}-f$ models. Leaving aside elliptic-relaxation-based models, Jang et al. (2002) highlighted the superiority of ω-based models, for which a better representation of the shear-stress in the re-circulating flow and a better rate of recovery is observed. Jang et al. (2002) also emphasised the importance of the quadratic terms of non-linear eddy viscosity models, compared to cubic terms. For these reasons, the quality of predictions of the flow pattern in the re-circulation region does not reflect the complexity of a turbulence model. This is best expressed in the accelerating windward face, where the RSM of Chen et al. (2000) predicts the best levels of shear-stress (compared to other models consistently over-representing this quantity) and the correct velocity profile at the hill crest, characterised by a thin boundary layer, whereas this model is paradoxically one

predicting the poorest results elsewhere.

The "shear stress transport" improvement (Menter (1994)) supplemented to the $k-\omega$ model had adverse effects: as shown in Uribe (2006), the $k-\omega$ SST model massively under-predicts $\overline{uv}$, resulting in a bubble 1.6 times larger than the one of the LES. It is shown in Uribe (2006) that both standard and SST $k-\omega$ models predict the separation at the exact same location, this being due to the two models expected to behave identically in the near-wall region (*i.e.* being in $k-\omega$ mode).

Uribe (2006) reports very good predictions with the three $\overline{v^2}-f$ based models tested. However, the recovery rate is too slow. The correct level of shear-stress in the accelerated region, correctly picked up by RSMs (Jang et al. (2002)) is also satisfactorily captured by the $\overline{v^2}-f$ models. However the latter are not able to predict the correct thickness of the resulting accelerated boundary layer. The difference between $\overline{v^2}-f$ models is relatively small. In particular URI06 and the original $\overline{v^2}-f$ models yield remarkably similar predictions, reflecting the efforts undertaken in the URI06 model to minimise the consequences of the code-friendly modifications.

Results of the present approaches: Simulation were performed on a grid with $N_x \times N_y = 172 \times 120$ cells (simulations on finer grids did not evidence noticeable differences). Results of the $\varphi-\alpha$ and BL-$\overline{v^2}/k$ models are compared to the URI06 , LIE01 and $k-\omega$ SST models in the following. Reference LES data of Temmerman and Leschziner (2001) are also shown for comparison. Profiles of the mean stream-wise velocity $\overline{U}$, the turbulent shear stress $\overline{uv}$ and the wall-normal anisotropy $\overline{v^2}/k$ are shown on Fig. 6.2, Fig. 6.4 and Fig. 6.5, respectively. The flow pattern is represented in Fig. 6.3. The characteristics of the observed recirculation are given in Tab. 6.1. The stream-wise velocity predictions (Fig. 6.2) show a very similar flow pattern returned by URI06, LIE01 and BL-$\overline{v^2}/k$ models, whereas the $\varphi-\alpha$ model yields a dramatically under-represented re-circulation. It is worthy of note that the intensity of the reverse flow is better captured by the BL-$\overline{v^2}/k$ model, which is mostly visible at $x/h=3$, but adversely this model predicts a delayed reattachment. Most

models also tend to over-predict the velocity along the top wall. Finally, all models under-predict the acceleration magnitude in the wind-ward face. The good prediction of the $\varphi - \alpha$ model in this latter region is simply a consequence of an erroneously larger size of the recovery region.

As expected, the smaller re-circulation size of the $\varphi - \alpha$ model is linked to a larger amount of predicted shear stress, as seen in Fig. 6.4. The shear-stress predictions of the BL-$\overline{v^2}/k$, URI06 and LIE01 models are almost identical, whereas the strong $\overline{uv}$ under-estimation returned by the $k - \omega$ SST model is clear.

The predictions of the near-wall anisotropy $\varphi = \overline{v^2}/k$ differ noticeably amongst models (Fig. 6.5). As seen in Chap. 4, for the $\overline{v^2} - f$ model of Lien and Kalitzin (2001) the amplification of $\overline{v^2}$ in the logarithmic region is one of the most dramatic. In this case, this is clearly reflected by a strong over-prediction of $\varphi = \overline{v^2}/k$ by this model in the upper region. The URI06 model also returns a considerable over-representation of φ near the top wall whereas both the $\varphi - \alpha$ and BL-$\overline{v^2}/k$ models predict fairly similar levels, closer to the reference data. Moreover a consistent earlier switch from the near-wall to homogeneous form of φ can be noted for the URI06 model along the lower wall (characterised by a sudden increase of φ from right above the wall).

The erroneous behaviour of the $\varphi - \alpha$ model (*i.e.* over-predicted shear stress hence smaller re-circulation bubble) is due to its expression for $C^*_{\varepsilon 1}$, Tab. 5.1. The inclusion of the factor $(1 - \alpha^3)$ makes the coefficient revert to the value 1.44 from right above the viscous sub-layer (unlike virtually all other $\overline{v^2} - f$ models for which the value is between 1.5 and 1.55 throughout the channel flow domain, as seen on Fig. 4.1), hence producing an exaggerated mixing layer spreading rate and thus too strong a momentum transfer from the bulk to the re-circulating flow. The correction proposed by the BL-$\overline{v^2}/k$ model has a beneficial effect, the decrease of $C^*_{\varepsilon 2}$ having the same consequences as an increase of $C^*_{\varepsilon 1}$. Fig. 6.6 shows the values taken by $C^*_{\varepsilon 2}$ (defined by Eq. 5.9). The conventional value 1.83 is used in most of the domain, but it is reduced at the edge of the re-circulation, and at the edge of the top boundary layer.

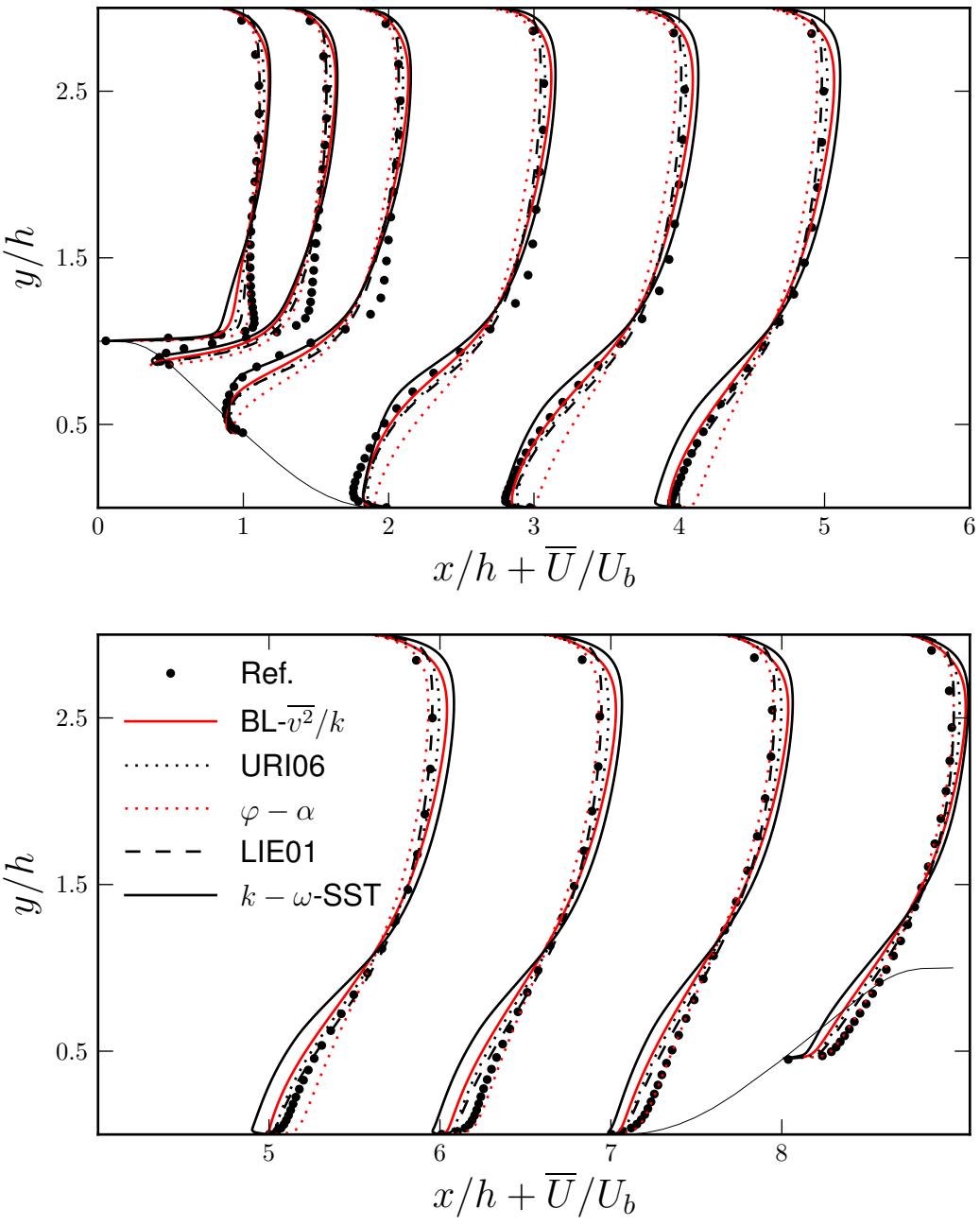

Figure 6.2: Prediction of the mean stream-wise velocity in the periodic hill case.

Model	Separation	Reattachement	Length	% / LES
LES	0.22	4.72	4.5	100
$k-\omega$ SST	0.24	7.58	7.34	163
URI06	0.38	4.65	4.27	95
$\varphi-\alpha$	0.39	3.01	2.62	58
BL-$\overline{v^2}/k$	0.33	5.14	4.81	107
LIE01	0.39	4.78	4.39	98

Table 6.1: Prediction of the periodic hill flow re-circulation size

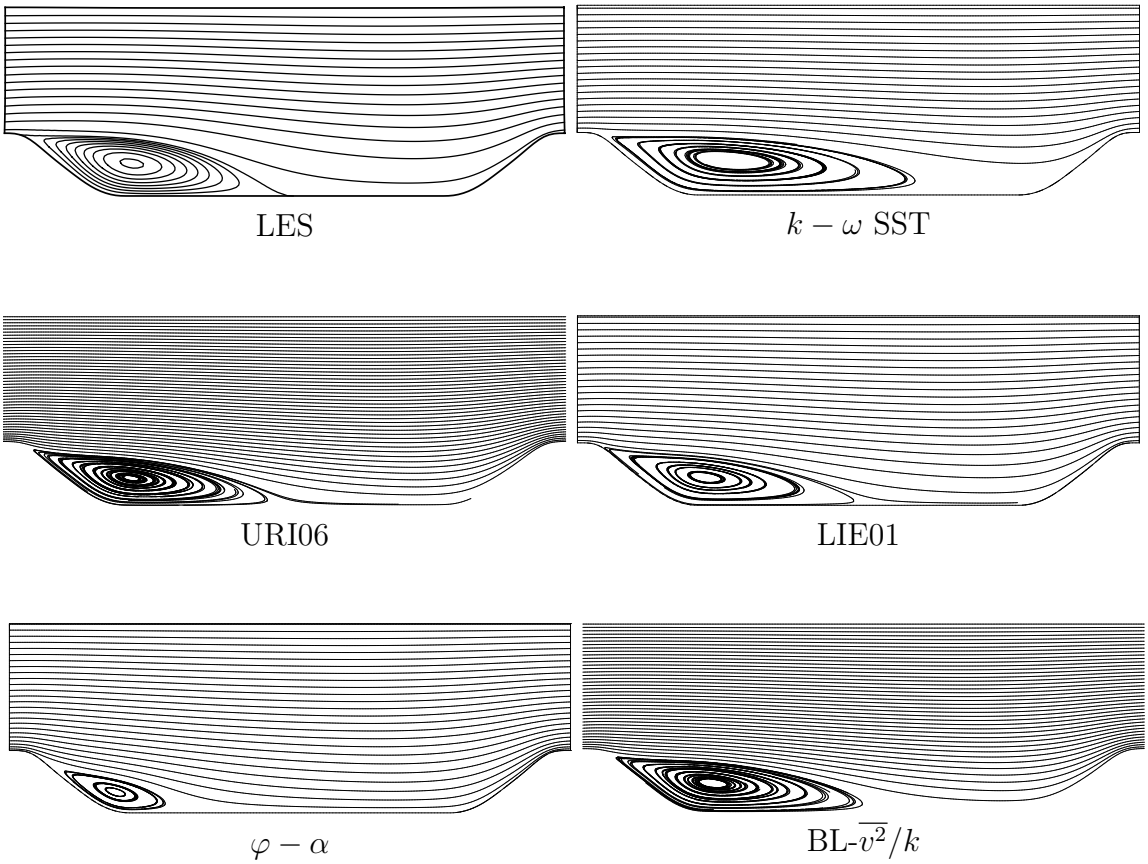

Figure 6.3: Mean stream-wise velocity streamlines predicted for the periodic hill case

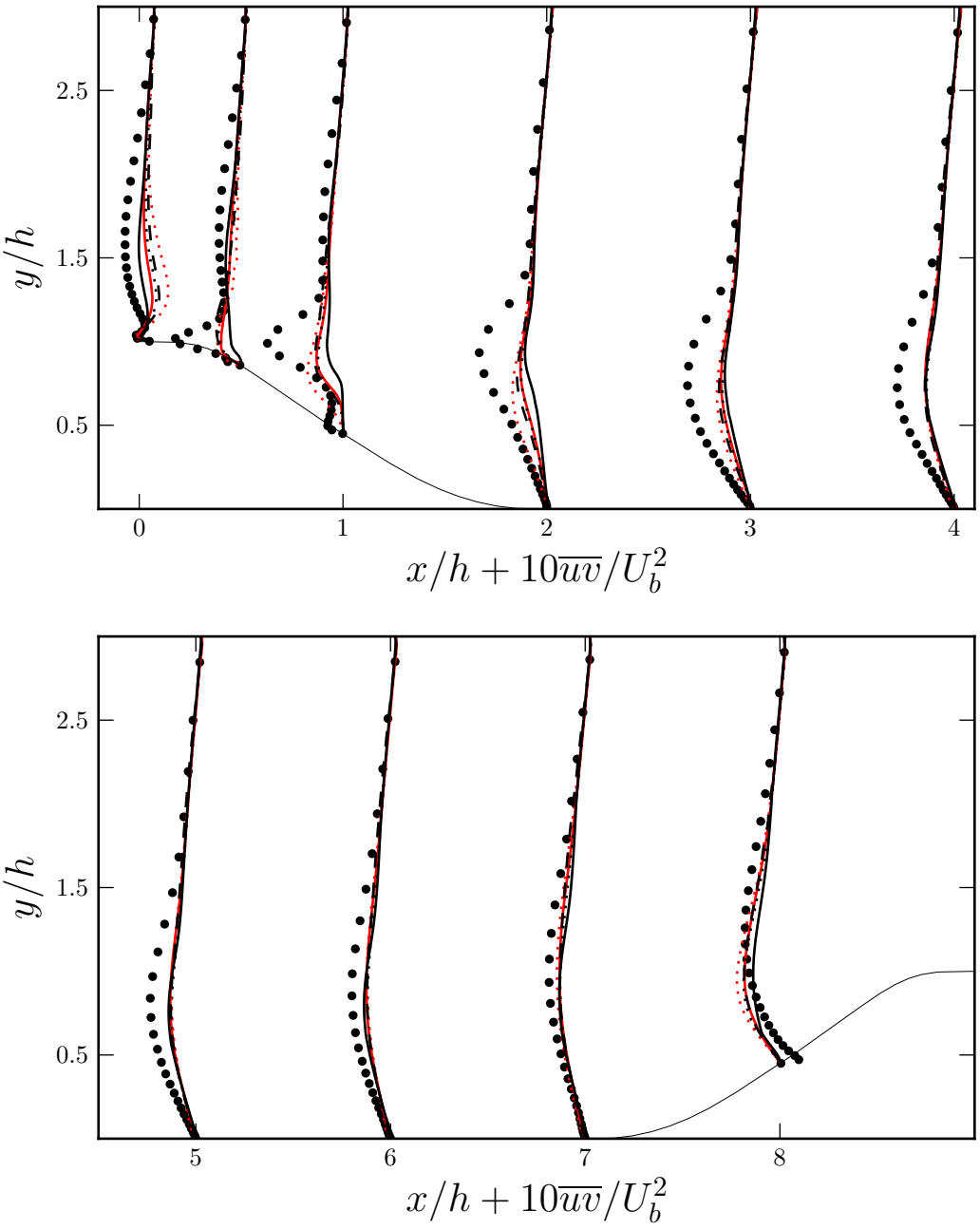

Figure 6.4: Prediction of the turbulent shear stress in the periodic hill case. See Fig. 6.2 for legends.

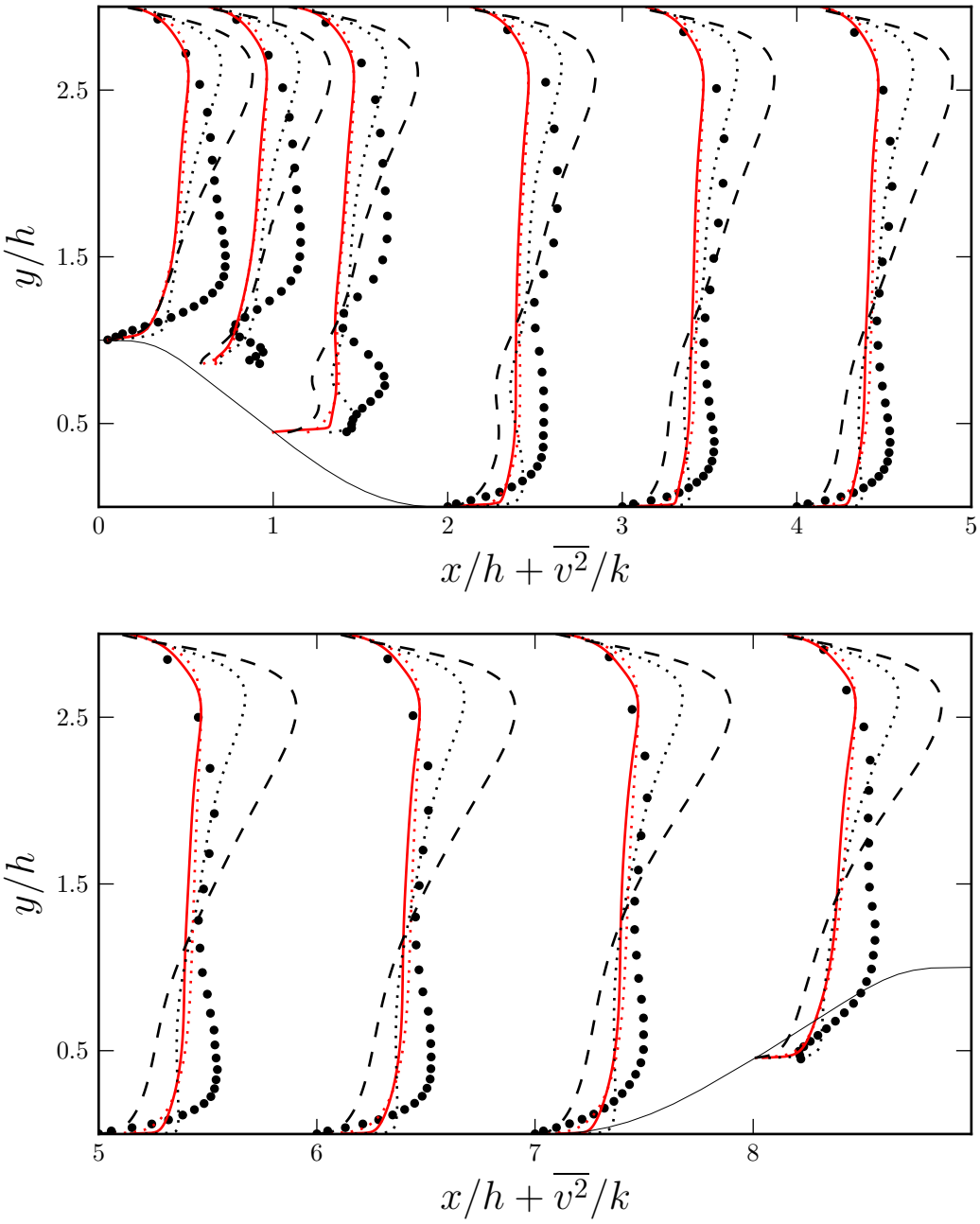

Figure 6.5: Prediction of the wall-normal anisotropy in the periodic hill case. See Fig. 6.2 for legends

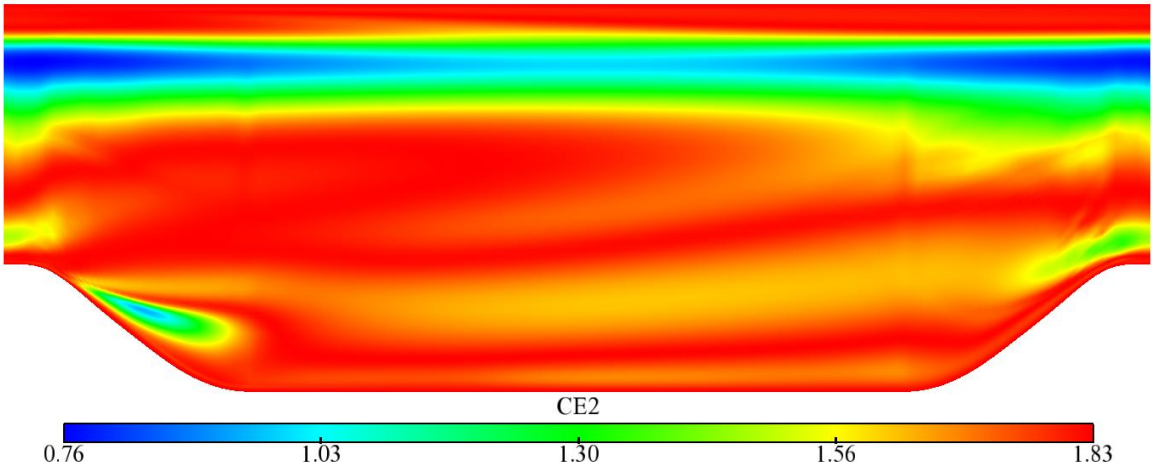

Figure 6.6: Periodic hill flow case: Values of $C^*_{\varepsilon 2}$ as predicted by the BL-$\overline{v^2}/k$ model ($C^*_{\varepsilon 2}$ defined by Eq. 5.9)

6.1.2 Asymmetric plane diffuser

Presentation of the case

The asymmetric plane diffuser case represents another widely used test case for assessing the ability of models to predict pressure-induced separation. It consists in a channel with one of the walls diverging, thus inducing a re-circulation along the inclined surface. The geometry is given in Fig. 6.7. The Reynolds number based on the inlet height H and the bulk velocity is $Re = 18000$. The case was studied experimentally in Obi et al. (1993) and later in Buice and Eaton (1997) and Eaton (2000). The later experiment is the most reliable since it endeavours to eliminate three dimensional effects. It was also the subject of a large eddy simulation by Kaltenbach et al. (1999). Unlike the periodic hill case, the role of the geometry in the flow separation is not as important as it would be for a higher angle of inclination. Therefore the flow separation is mainly a consequence of adverse pressure gradient, thus making it a challenging case of study for RANS modelling: Apsley and Leschziner (2000) emphasise the importance of the correct modelling of the response of the shear stress and the normal stresses to the deceleration in the boundary layer prior to separation. Again, the flow analysed in the experiment and in the LES exhibits patterns which

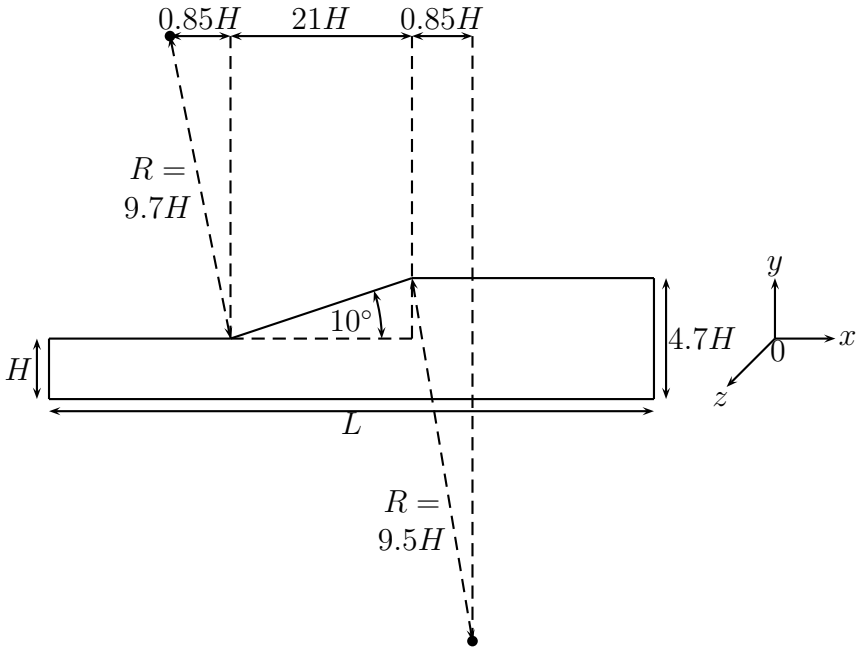

Figure 6.7: Geometry of the asymmetric plane diffuser flow configuration

cannot be accurately reproduced by a RANS model, and is characterised by the presence of a smaller re-circulation right at the corner of the diffuser and by a periodic shear-layer instability leading to a flapping motion throughout the separating flow. The strong resulting turbulent shear stress downstream the separation is generally missed by RANS models (Apsley and Leschziner (2000)).

Moreover it is another case where more advanced models can lead to degraded results. For instance Apsley and Leschziner (2000) highlighted the poor performances of low-Reynolds-number second-moment-closure models compared to their high-Reynolds number wall-function-based counterparts.

Performance of RANS modelling

Apsley and Leschziner (2000) presented the predictions of various RANS turbulence models: amongst others the $k-\varepsilon$ model of Launder and Sharma (1974), the $k-\omega$ model of Wilcox (2006), the $k-\omega$ SST of Menter (1994), three ε based non-linear eddy-viscosity models, and both high- and low-Reynolds number ε- and ω-based Reynolds-stress models. The study performed in Apsley and Leschziner (2000) shows that as far as Reynolds-stress models are concerned, results depend a great deal on the

near-wall treatment employed, high-Reynolds-number versions combined with wall functions seem to give the best results, whereas low-Reynolds-number models fail to predict separation. The comparison of predictions of the non-linear eddy-viscosity models highlights the important role of the eddy-viscosity coefficient as being function of the mean strain and vorticity rate, over the quadratic and cubic terms present in the non-linear relation. This shows that good predictions in this case are more affected by the modelling of the response to the strain present in the adverse-pressure-gradient region rather than curvature effects and turbulence anisotropy modelling. As far as linear eddy viscosity models are concerned, the $k-\varepsilon$ model of Launder and Sharma (1974) does not yield separation whereas the back flow intensity and the re-circulation extent are only weakly represented by the $k-\omega$ model of Wilcox (2006). The $k-\omega$ SST model of Menter (1994) is shown to give better overall performances, this being due to the ν_t limiter being active in the separation region[2], resulting in the turbulent viscosity being sensitised to the strain-rate. Despite the benefits of this feature in the case of the $k-\omega$ SST model, some adverse effects however and yields to a far too early separation.

Results for the $\overline{v^2}-f$ models are presented in Durbin (1995) (for the version DUR95), in Iaccarino (2000) (the model LIE01 is compared to the $k-\varepsilon$ model of Launder and Sharma (1974) with results provided by three commercial codes), in Manceau et al. (2002b) (for MAN02) and in Uribe (2006) (for LIE96 and URI06). The results are very good for all models, with predicted separation and reattachment points very close to the experimental observation. The variants in the $\overline{v^2}-f$ modelling have the following consequences:

- The effect of the "rescaled" model of MAN02 highlights the consequences of the neutral formulation of the elliptic operator. The resulting improved prediction

[2]The study of the blending functions F_1 and F_2 used by the model are performed in Apsley and Leschziner (2000) and Uribe (2006) and shows that the SST model uses the $k-\omega$ equations over most of the domain. Therefore the strong differences between standard and SST $k-\omega$ models results is due to the turbulent viscosity limiter.

of the central region of a channel flow is made at the expense of an over-prediction of $\overline{v^2}$ and an under-prediction of the peak of k near the wall (Manceau et al. (2002b)). This yields slightly over-predicted turbulent viscosity in the diffuser near-wall flow resulting in a noticeable degradation of the results with the re-scaled model.

- The differences between LIE96 and URI06 (Uribe (2006)) show the consequences of the strong over-prediction of $\overline{v^2}$ the former model depicts. This results in exaggerated level of turbulence shear stress and flatter stream-wise velocity profile around its maximum value.

- Durbin (1995) shows the consequences, for the predictions of DUR95, of the use of the variable $C^*_{\varepsilon 1}$ coefficient (given in Tab. 4.4 and built to return $C_{\varepsilon 1} = 1.3$ in free shear turbulence and $C_{\varepsilon 1} = 1.55$ in wall-bounded flows) compared to the constant $C_{\varepsilon 1} = 1.55$. The reduction of $C^*_{\varepsilon 1}$ in the regions farthest from walls results in a smaller separation (this is consistant with the resulting increase of mixing layer spreading rate hence a stronger momentum exchange between the bulk and the re-circulating flow).

Finally, Sveningsson et al. (2005) compared linear and non-linear versions of the $\overline{v^2} - f$ model and evidenced the adverse effect of a non-linear constitutive relation compared to the linear model. They showed that the superiority of the linear formulation was a due to an error compensation in the evaluation of the momentum turbulent flux in the entrance zone of the diffuser.

Results of the present approaches: Results shown here are those of simulations performed on a grid with $N_x \times N_y = 292 \times 96$ cells, which was found sufficiently fine after a grid sensitivity study. Fig. 6.8 and Fig. 6.9 show the evolution of the skin-friction C_f and the pressure coefficient C_p along the inclined wall. The evolution of C_f shows a very good prediction of the separation and the reattachment location for both URI06 and the BL-$\overline{v^2}/k$ model, with the re-circulation being slightly shifted downstream for the latter model. Both formulations also tend to under-predict the

extent of reverse flow characterised by an over-estimation of the pressure coefficient. Moreover the $\varphi - \alpha$ model predicts a very small and weak re-circulation. The mean steam-wise velocity profiles given by the four $\overline{v^2} - f$ models and the $k - \omega$ SST are shown in Fig. 6.10. The absence of re-circulating flow for the $\varphi - \alpha$ model yields an under-predicted velocity along the straight wall, consecutively to the mass-flow-rate conservation. The better profiles observed with this model in the final section of the domain is simply a consequence of the ill-prediction upstream, yielding a larger zone for recovery. The main difference between the URI06 and the BL-$\overline{v^2}/k$ model lies in the recovery region, with the former model showing a strong over-prediction of the skin-friction coefficient. The models also predict too slow a rate of recovery.

The values taken by the coefficient $C^*_{\varepsilon 2}$ (defined with Eq. 5.9)for the BL-$\overline{v^2}/k$ model are shown on Fig. 6.11. The coefficient is mostly reduced in the defect layer of the inlet channel and at the edge of the boundary layer along the straight wall, but also noticeably decreased (around 1.6) at the edge of the re-circulation yielding the correct spreading rate of the layer mixing the re-circulating and the bulk flow, hence the correct flow pattern.

The good performance of the $\overline{v^2} - f$ modelling seems to be in contradiction with the conclusion of Apsley and Leschziner (2000) stating that a strain or vorticity rate dependence of the proportionality coefficient of the linear part of the stress / strain rate relation is crucial to secure good predictions of eddy-viscosity models in this case. It may be argued that the time-scale limiter present in some $\overline{v^2} - f$ models to ensure the releasability constrain (Durbin, 1996) achieves the same purpose. However, present simulations using the $\varphi - \alpha$ and the BL-$\overline{v^2}/k$ models have shown no activation of the limiter in this case, and the good performance should simply be attributed to a careful calibration and an accurate near-wall effect representation.

The robustness of the $\varphi - \alpha$ and the BL-$\overline{v^2}/k$ models in these two cases will be presented in Chap. 7. It is worth mentioning that inter-code comparisons were undertaken in Jang et al. (2002) for the case of the periodic hill and in Iaccarino (2000) for the diffuser flow. It is reported a noticeable code dependance of the Launder

and Sharma (1974) $k - \varepsilon$ results, this being attributed to the possible difference in implementation of the second-order-gradient derivative present in the ε equation. Since the BL-$\overline{v^2}/k$ model uses the same "E" term as in the Launder and Sharma (1974) model, the similar inter-code comparison should be carried out with the new model.

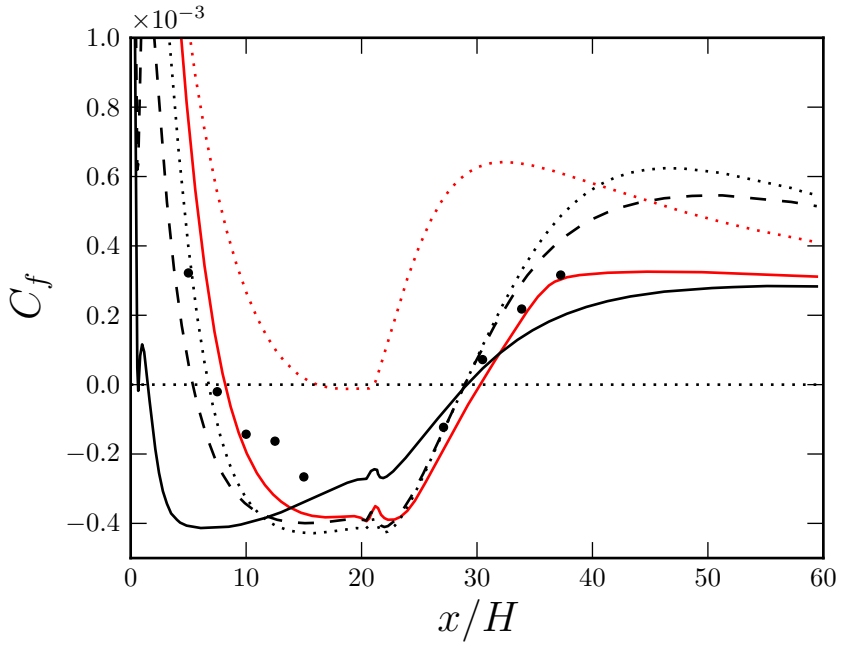

Figure 6.8: Prediction of the skin friction coefficient along the inclined wall in the asymmetric plane diffuser case. See Fig. 6.9 for legends.

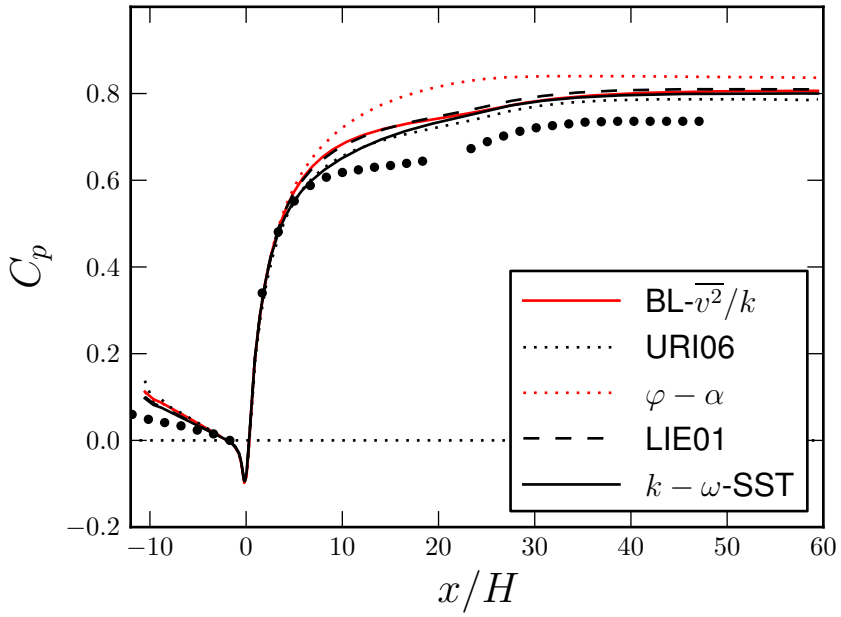

Figure 6.9: Prediction of the pressure coefficient along the inclined wall in the asymmetric plane diffuser case.

6.2 Buoyant flows

Heat transfer and implied density inhomogeneities play an important role in many industrial configurations: for instance, the role of natural convection in the cooling

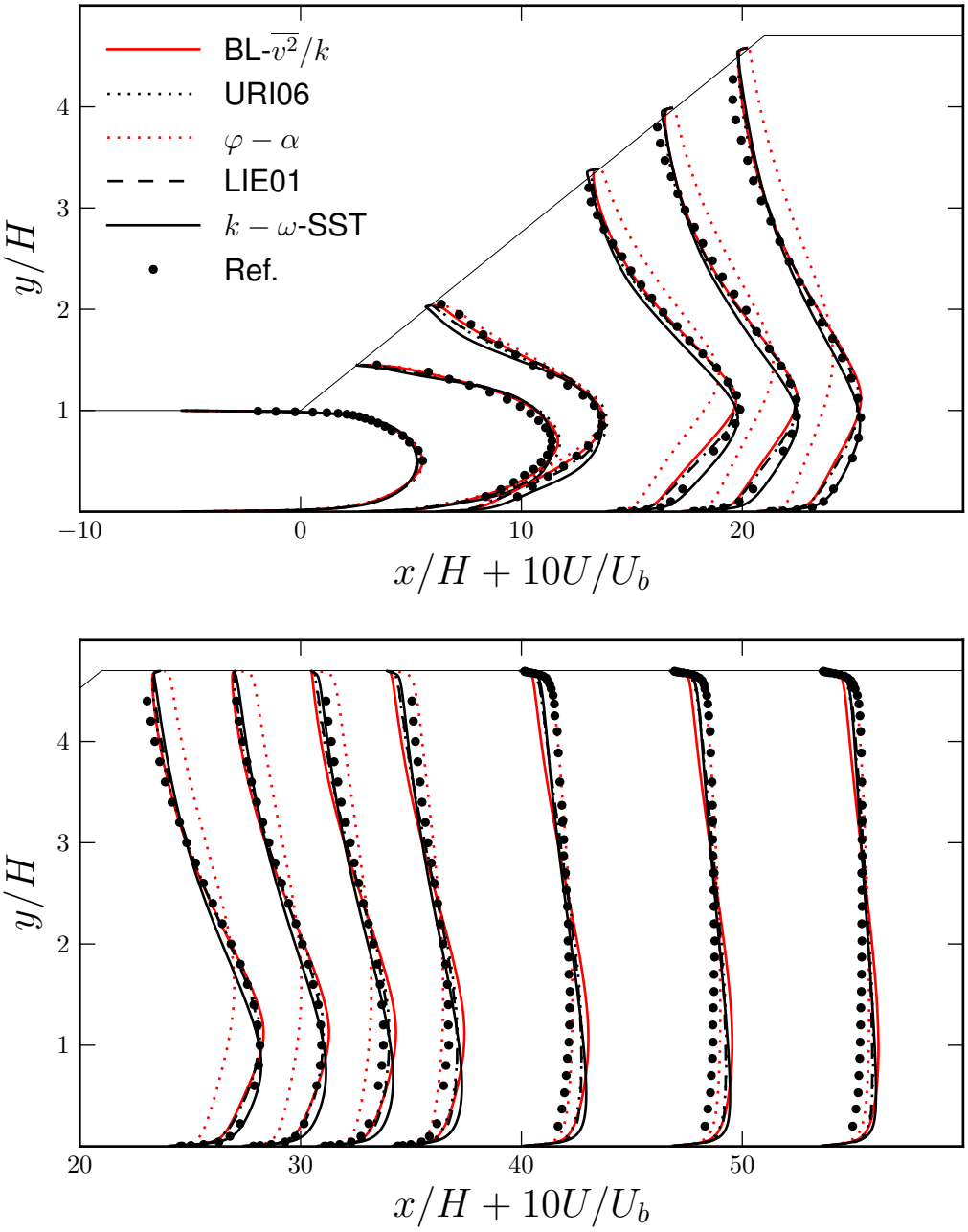

Figure 6.10: Prediction of the mean stream-wise velocity in the asymmetric plane diffuser case.

system of nuclear power plants is of utmost importance. Similar to the Reynolds number for momentum-driven flows, the Grashof number characterises buoyant flows, and is defined as the ratio of buoyancy to viscous force. This non-dimensional parameter is considerable in domestic-heating systems, solar panels, heat exchangers, amongst others. Boudjemadi et al. (1997) emphasises the importance of heat removal through

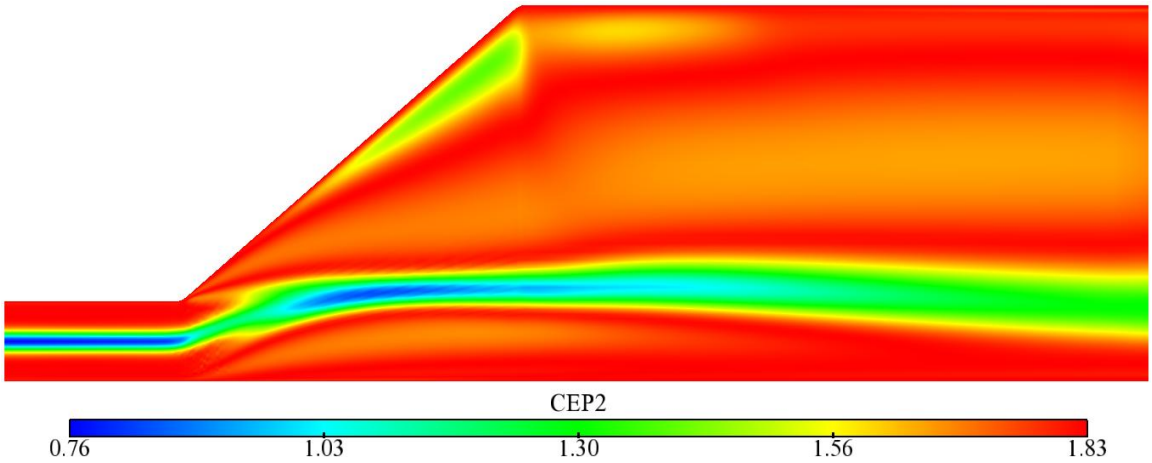

Figure 6.11: Asymmetric diffuser case: Values of $C^*_{\varepsilon 2}$ as predicted by the BL-$\overline{v^2}/k$ model ($C^*_{\varepsilon 2}$ defined by Eq. 5.9).

natural convection (instead of forced convection) in future plants for increased safety. Heat transfer in wall-bounded flows falls into two categories: configuration with horizontal walls (with Rayleigh-Bénard convection if the bottom wall is heated, or a stable stratification if the top wall is heated) and vertical walls. In most cases a turbulent boundary layer develops but the latter presents significant differences with the pressure driven boundary layer.

This section first introduces the implications of the buoyancy effects on the turbulence, and their representation in the framework of RANS modelling. Then applications are studied by reference to the following cases: a flow purely driven by buoyancy (natural convection) and one featuring a combination of buoyancy and pressure effects (mixed natural and forced convection), for which cases the behaviour of the $\varphi - \alpha$ and the BL-$\overline{v^2}/k$ models are assessed.

6.2.1 Effects of buoyancy on turbulent flows

Temperature and density inhomogeneities are linked through the thermal expansion coefficient β defined as :

$$\beta = -\frac{1}{\rho}\frac{\partial \rho}{\partial T} \tag{6.1}$$

Following Archimede's principle the buoyancy force due to density inhomogeneities appearing in the momentum equation reads: $\underline{F} = (\rho - \rho_0)\,\underline{g}$. The density is assumed to vary little about its reference value ρ_0 and the Boussinesq approximation is used: the flow is assumed incompressible and density variations are only taken into account in the buoyant force expression. For small variations of ρ about ρ_0 the buoyant force can be linearised: $\underline{F} = \rho_0\beta(T_0 - T)\underline{g}$. The Reynolds decomposition of this added body force ($F_i = \overline{F_i} + f_i'$) reads:

$$\begin{cases} \overline{F_i} = \rho_0\beta(T_0 - \overline{T})g_i \\ f_i' = -\rho_0\theta\beta g_i \end{cases} \tag{6.2}$$

The quantity θ represents the fluctuating temperature. The presence of buoyancy thus adds new production terms for the Reynolds stresses $\overline{u_iu_j}$:

$$G_{ij} = \overline{u_jf_i} + \overline{u_if_j} = -\rho_0\beta\left(\overline{u_i\theta}g_j + \overline{u_j\theta}g_i\right) \tag{6.3}$$

The corresponding term $G_k = \frac{1}{2}G_{kk}$ appears in the k equation. A term also appears in the transport equation of $\overline{u_iu_ju_k}$ and ε_{ij} as well as in the pressure scrambling term.

The mean-temperature equation reads:

$$\rho\frac{\partial\overline{T}}{\partial t} + \rho\overline{U_j}\frac{\partial\overline{T}}{\partial x_j} = \frac{\partial}{\partial x_j}\left(\frac{\mu}{\mathrm{Pr}}\frac{\partial\overline{T}}{\partial x_j} - \rho\overline{u_j\theta}\right) \tag{6.4}$$

The Prandtl number Pr is defined as the viscous to thermal viscosity ratio.

The buoyant force influences turbulence either indirectly (*i.e.* the temperature field affects the mean-flow field, whose resulting distortion will produce or impair turbulence) or directly, through G_{ij} and G_k present in the equations of turbulence. The relative importance of direct compared to indirect effects depends on the flow considered, and for some flows the modelling of G_{ij} is not crucial. In the calculations presented herein, the Boussinesq approximation is not completely used. Indeed the density ρ is updated at each time step using the linearisation of Eq. 6.1, and then, spatial variations of ρ are taken into account everywhere. The only assumption which is introduced is, therefore, the linearisation of the expansion coefficient.

6.2.2 Modelling of the buoyancy effects on turbulence

Using the linearisation of the buoyancy force, as implied by the Boussinesq approximation, the accuracy in the representation of the buoyant term G_{ij} relies upon the modelling of the turbulent heat flux $\overline{u_i\theta}$. This can be divided into four categories of increasing complexity:

- The simple gradient diffusion hypothesis (SGDH): In the framework of eddy viscosity modelling, the heat flux $\overline{u_i\theta}$ present in the transport equation of T as well as in G is modelled using the simple gradient-diffusion hypothesis (SGDH)($\overline{u_i\theta} = \nu_t/Pr_t \frac{\partial \overline{T}}{\partial x_i}$). The turbulent Prandtl number Pr_t (ratio of momentum to temperature turbulent diffusion) is generally taken equal to 0.9. The value used in the present simulations is the default value of the *Code_Saturne*: $Pr_t = 1$.

- The generalised gradient diffusion hypothesis (GGDH): Second-moment-closure models without further modelling of the heat flux use the following relation (Daly and Harlow (1970)): $\overline{u_i\theta} = -c_\theta \frac{k}{\varepsilon} \overline{u_i u_j} \frac{\partial \overline{T}}{x_j}$. The GGDH can also be employed with eddy viscosity models by using the Boussinesq relation for the Reynolds stresses (Eq. 2.34).

- Additionnal transport equations are solved for $\overline{\theta^2}$ and its dissipation term ε_θ to enrich any of the two above models.

- Algebraic models, linear (e.g. Hanjalić (2002)) or non-linear, explicit or implicit, are used. They also solve equations for $\overline{\theta^2}$ and ε_θ. Models integrating wall effects are also proposed, amongst others the elliptic-blending based versions of Shin et al. (2008) and Lecocq (2008).

In all $\overline{v^2} - f$ models including the $\varphi - \alpha$ and the BL-$\overline{v^2}/k$ models the SGDH is used and the buoyancy production term G_k is added to the mean velocity gradient production term P_k wherever it appears in the k, ε, $\overline{v^2}/\varphi$ and f/α equations[3].

[3]The SSG model proposes an extra term $C_6\left(G_{ij} - \frac{1}{3}G_{kk}\right)$ to account for buoyancy effects, which is not included however in the $\varphi - \alpha$ and BL-$\overline{v^2}/k$ model for the sake of simplicity.

6.2.3 Natural convection

A purely buoyancy-driven wall flow is encountered, for example, in the case of a heated room, characterised by a recirculating motion of the air. The configuration is experimentally reproduced in a cavity where opposing vertical walls (separated by a distance D) are heated at different temperatures ($T_h - T_c = \Delta T$).

- In the momentum equation, the Grashof number is defined as the ratio between buoyant and viscous force: $Gr = g\beta\Delta T D^3/\nu^2$

- In the temperature equation, the Rayleigh number is defined as the ratio between convection and viscous transport of temperature: $Ra = PrGr$

In such flows, heat tends to build up at the top and the resulting stratification dampens turbulence. The experiment of Betts and Bokhari (2000) uses a high aspect-ratio cavity to avoid an influence of the corners, and a fully turbulent flow is obtained at moderate Rayleigh number, so the temperature differences are comparatively small and the Boussinesq approximation is not violated. The ideal buoyancy-driven, fully developed turbulence boundary layer in infinitely tall vertical channel flow was the subject of two DNS studies: Boudjemadi et al. (1997) and Versteegh and Nieuwstadt (1998)[4] for Rayleigh numbers of 10^5 and 5.4×10^5 for the former and values ranging between 5.4×10^5 and 5×10^6 for the latter. Unlike a pressure-driven flow, the core region of the present flow is dominated by a constant shear, similar to a Couette flow, and it is in this case that the largest values of the Reynolds-stresses and their production term are found, whereas the near-wall flow is viscous. The budgets of the Reynolds stresses provided by the DNS help understand the near-wall turbulence impairment (Boudjemadi et al. (1997)). Production terms P_{ij} and G_{ij} are active only for components $\overline{uu}$ and $\overline{uv}$[5].

[4]The latter showed that the former DNS domain was perhaps too small.

[5]u (resp. v) represents the stream-wise (resp. wall-normal) component (*i.e.* along the x axis (resp. the y axis)).

$$\begin{cases} P_{11} + G_{11} = -\overline{uv}\dfrac{\partial \overline{U}}{\partial y} + 2\beta g \overline{u\theta} \\ P_{12} + G_{12} = -\overline{v^2}\dfrac{\partial \overline{U}}{\partial y} + \beta g \overline{u\theta} \end{cases} \tag{6.5}$$

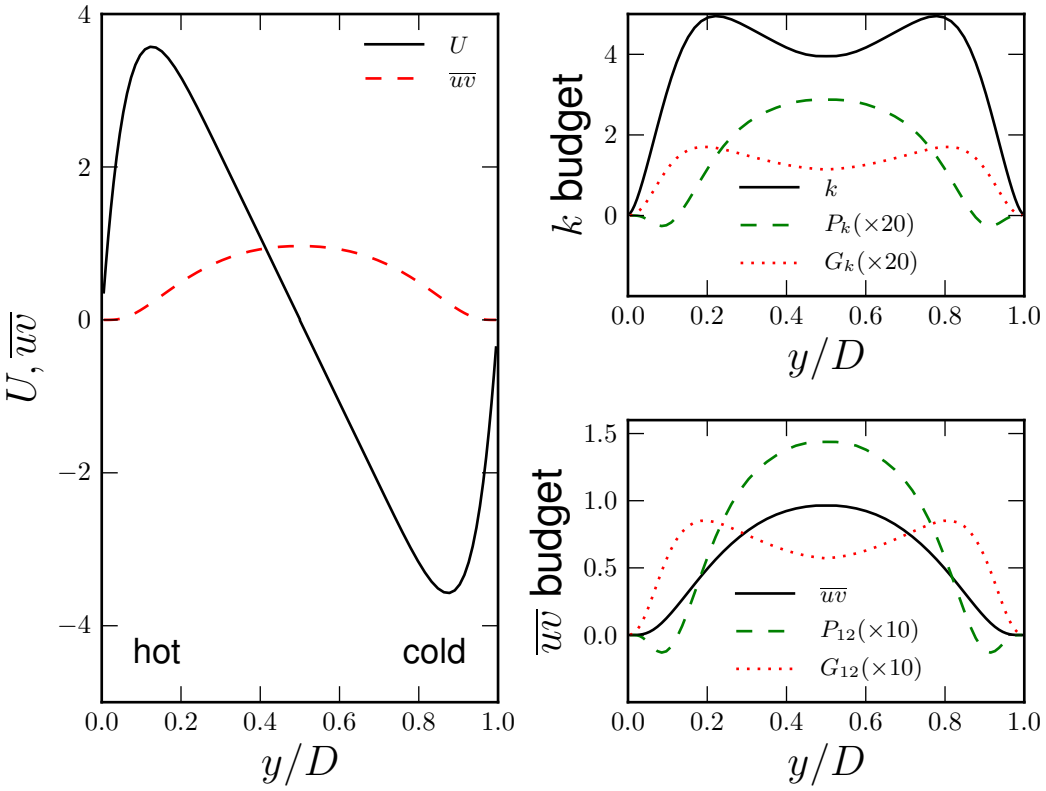

Figure 6.12: Natural convection in a vertical slot. DNS data of Boudjemadi et al. (1997), for $Ra = 10^5$ Left: Mean upward velocity profile and turbulent shear stress. Right top: Budget of k. Right bottom: Budget of $\overline{uv}$ (Production by shear and gravity only)

Fig. 6.12 presents the DNS data of Boudjemadi et al. (1997) for $Ra = 10^5$ across the channel. The flow is driven upward near the hot wall (left) and downward near the cold wall (right). Profile of the mean velocity and shear stress $\overline{uv}$ are shown as well as the budget of the turbulent kinetic energy k and $\overline{uv}$ equations.

- A constant mean velocity gradient appears in the core region where the production by shear (both P_k and P_{12}) is maximum.

- In the near-wall region, the gravity production term G_{12} (always positive) has a larger magnitude than that of the shear stress production P_{12} (which is of the

same sign as $-\dfrac{\partial \overline{U}}{\partial y}$), hence $P_{12} + G_{12} > 0$: this yields $\overline{uv}$ being positive everywhere, even in the near-wall region where $\frac{\partial \overline{U}}{\partial y}$ is also positive. This particularity (counter-gradient turbulent transport) yields a negative k production P_k near walls and is not reproducible by eddy viscosity models.

- Eddy viscosity models use the SGDH model for $\overline{u_i\theta}$ which implies that the buoyant production term G_k is zero for horizontal temperature gradients, which is the case here. As pointed out in Boudjemadi et al. (1997) the correctly low levels of turbulence predicted by some low Reynolds number eddy viscosity models is simply due to an under representation of both negative P_k and positive G_k (error cancellation).

The absence of modelling for gravity production when the SGDH model is used was shown to be not so crucial in some flow configurations. For instance, its consequences for the performance of the $\overline{v^2} - f$ model was studied in Tieszen et al. (1998), for the case of natural convection in a heated vertical plate and a heated rectangular box of aspect ratio 5 : 1. Comparisons of $\overline{v^2} - f$ simulations using the SGDH and the GGDH show no noticeable differences for the heated vertical plate flow, but the SGDH implies a considerably delayed turbulent transition in the heated cavity flow.

Simulation of natural convection in a tall cavity

The following presents the results for the case of Betts and Bokhari (2000), which is presented in Fig. 6.13. The height H and width W are related by the aspect ratio $H/W = 28.68$. The recirculating flow is computed for the two Rayleigh numbers $Ra = 0.86 \times 10^6$ and 1.43×10^6 for the models $k - \omega$ SST, URI06, $\varphi - \alpha$ and BL-$\overline{v^2}/k$ as well as the LIE01 model. The simulations are performed on a 2-D grid with 100 and 200 computational points in the vertical and horizontal directions respectively. Vertical velocity profiles are shown on Fig. 6.14 and Fig. 6.16 for the two Rayleigh numbers respectively. Temperature profiles are shown on figures Fig. 6.15 and Fig. 6.17, respectively.

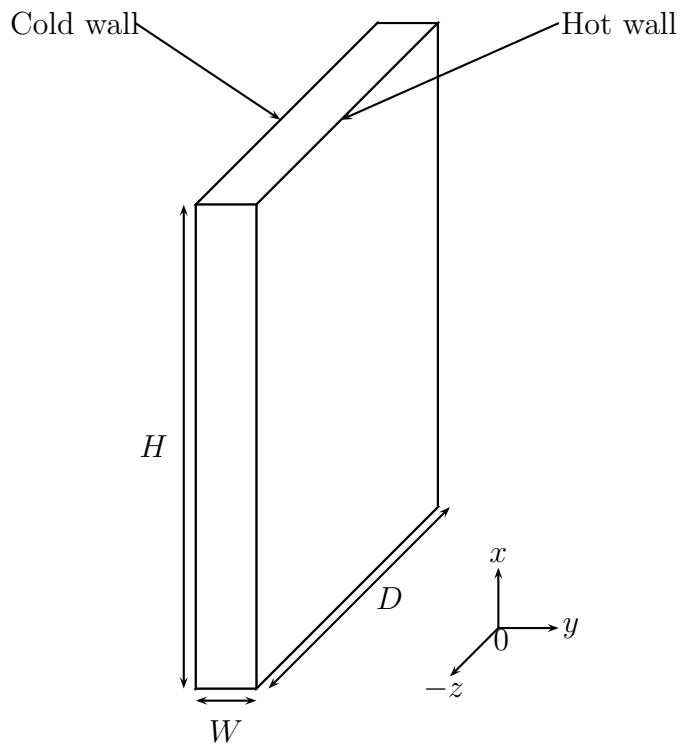

Figure 6.13: Configuration of the case of Betts and Bokhari (2000)

It is worth comparing the maximum of the quantity ν_t/ν, over the whole domain, predicted by the different models (not shown here). For the smaller Rayleigh number the models BL-$\overline{v^2}/k$, URI06 and $k-\omega$ SST predicts very similar values ($(\nu_t/\nu)_{max} = 24$, 26 and 25 respectively), whereas the LIE01 is much less turbulent ($(\nu_t/\nu)_{max} = 17$) and the $\varphi - \alpha$ is sensibly more turbulent ($(\nu_t/\nu)_{max} = 33$). The same was noticed for the higher Rayleigh number. This explains why the velocity profiles are strongly over-predicted by the LIE01 model (due to the lower turbulent mixing) and noticeably under-predicted by the $\varphi - \alpha$. Other models predict fairly similar profiles for the velocity, particularly in the central region, close to the experimental observation. For both Rayleigh numbers the velocity peaks are best predicted by the BL-$\overline{v^2}/k$ model, especially in the mid-height region, where the boundary layer is fully developed.

The temperature prediction does not vary much amongst models, with values close to the experimental ones, expect for the LIE01 model for which the temperature is

over-predicted (respectively under-predicted) in the upper part (respectively in the lower part), this being a direct consequence of the poorly predicted velocity. Note that the same conclusion is pointed out in Uribe (2006) for the LIE96 model.

6.2.4 Mixed convection

The added effect of buoyancy on a pressure-driven fully turbulent flow was investigated in the DNS of Kasagi and Nishimura (1997): the configuration (Fig. 6.19) consists in a flow between two vertical plates, driven upwards by a pressure gradient (the Reynolds number based on the averaged friction velocity u_τ on the two walls and the channel half-width δ is $Re_\tau = 150$). Buoyancy effects are added by heating walls at different temperatures. The resulting Grashof number defined with δ and the temperature difference is $Gr = 9.6 \times 10^6$. Fig. 6.18 compares the mixed convection flow with the equivalent without heat transfer (*i.e.* $G = 0$), with the same Re_τ value) (DNS of Kuroda et al. (1994)). On these figures the data are normalised by the friction velocity (for the mixed convection case, the averaged on the two walls is considered).

The pressure gradient drives the flow upward whereas the buoyant force drives the flow upwards near the hot wall, aiding flow, and downwards near the cold wall, opposing flow. Owing to the buoyant force, the turbulence is decreased in the hot side and increased in the cold side.

- With added buoyancy the mean velocity is accelerated near the hot wall and decelerated near the cold wall.

- Turbulent variables ($\overline{uv}$, k,$\overline{u^2}$,$\overline{v^2}$,$\overline{w^2}$) are decreased in the hot side and increased near the cold side. The near-wall peak of $\overline{v^2}$, $\overline{w^2}$ no longer exist with added buoyancy.

- In the hot side the indirect effects of buoyancy reduce $\overline{v^2}$ and $\overline{w^2}$ to a much larger extent than $\overline{u^2}$. Therefore the wall normal and span-wise anisotropy are greatly enhanced.

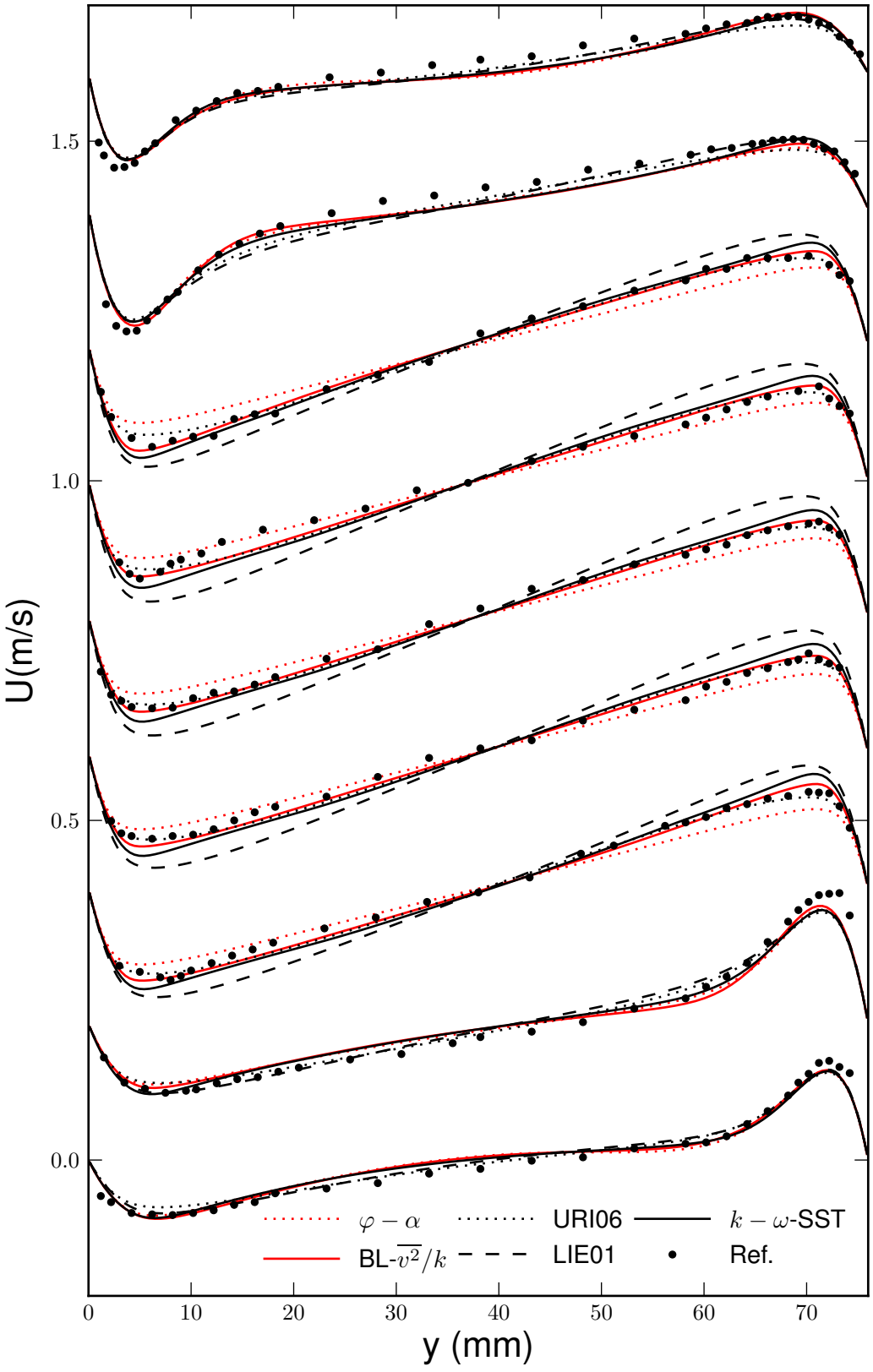

Figure 6.14: Prediction of the vertical velocity in the Betts cavity case ($Ra = 0.86 \times 10^6$)

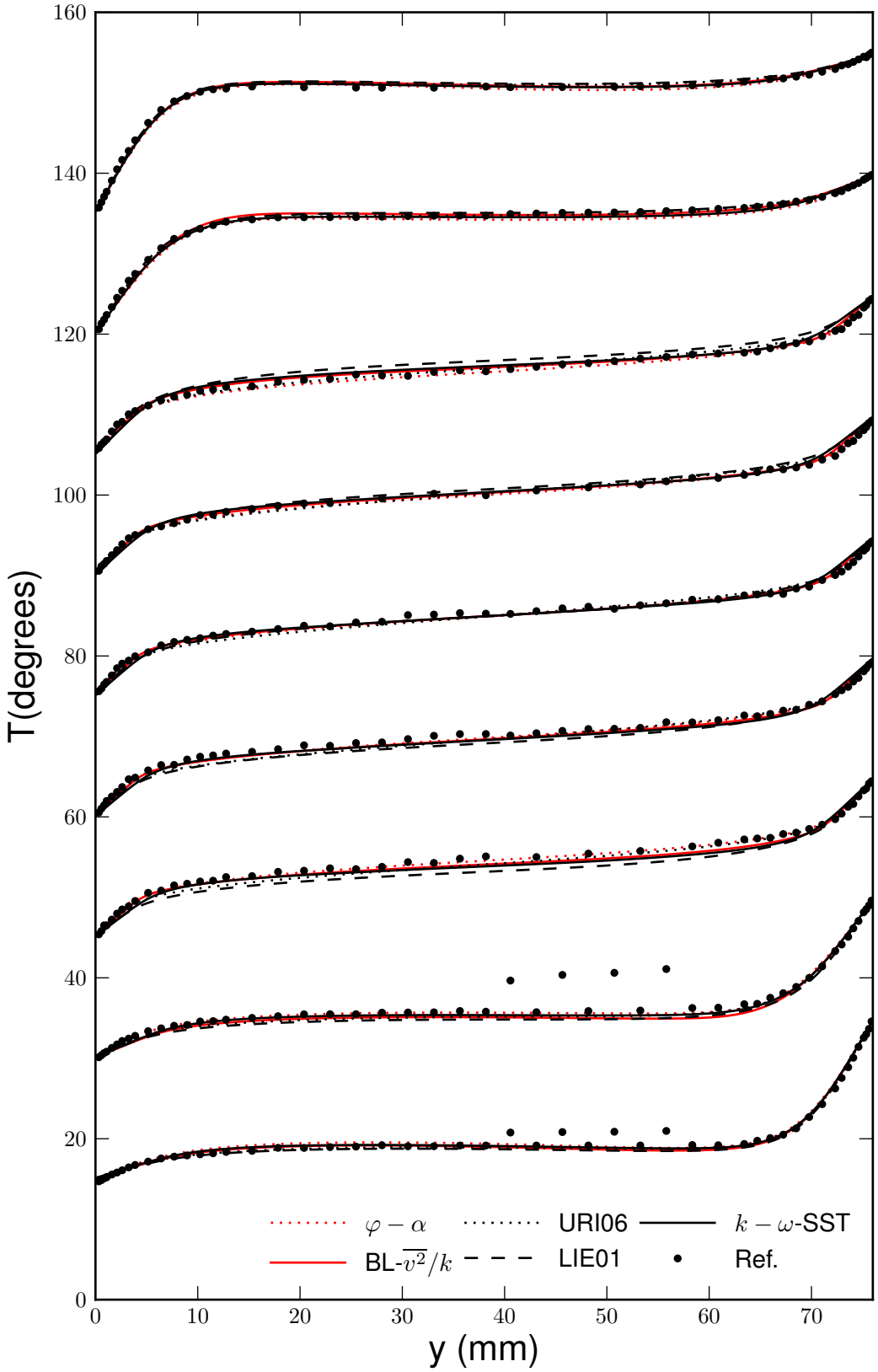

Figure 6.15: Prediction of the temperature in the Betts cavity case ($Ra = 0.86 \times 10^6$)

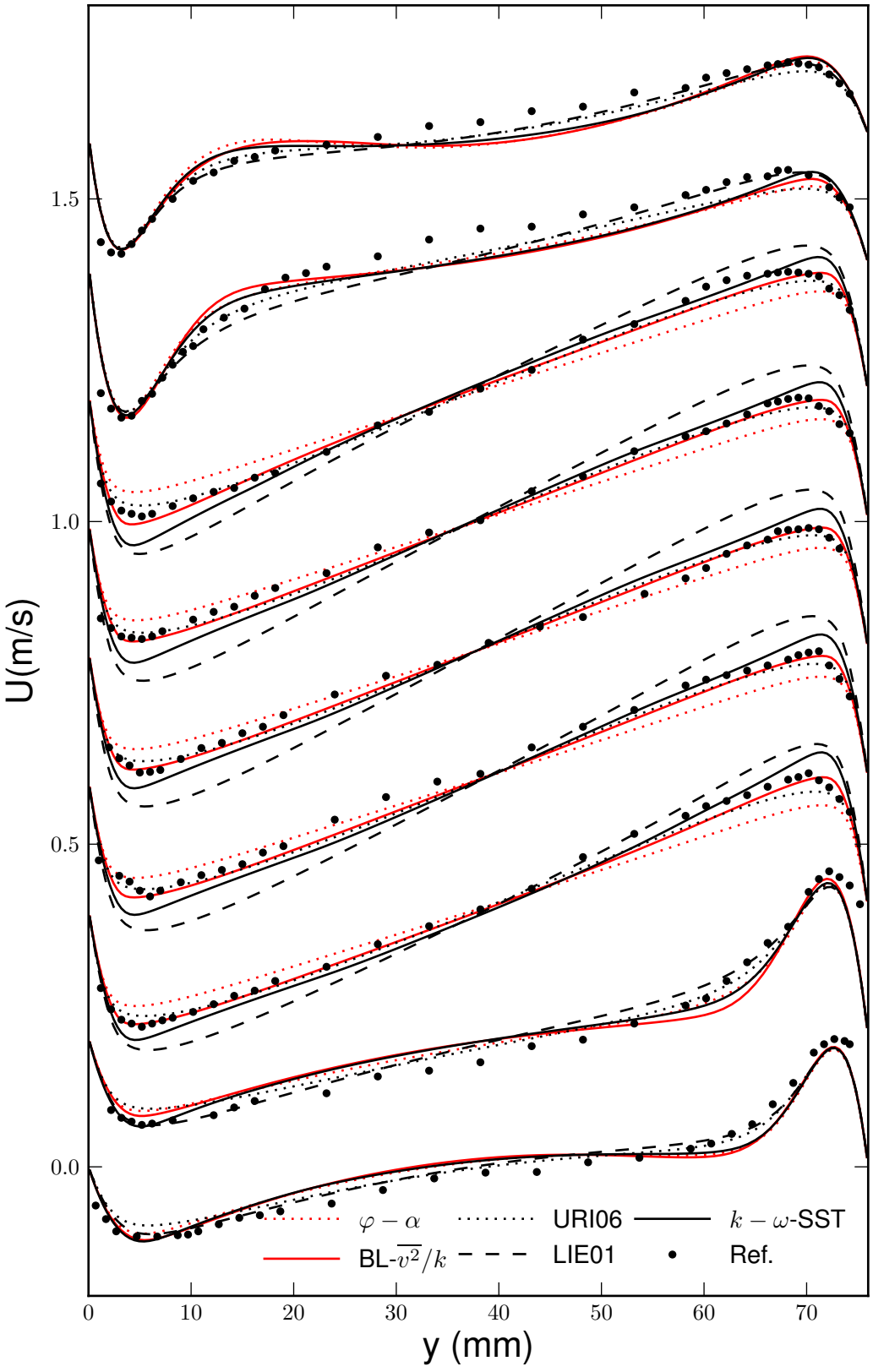

Figure 6.16: Prediction of the vertical velocity in the Betts cavity case ($Ra = 1.43 \times 10^6$)

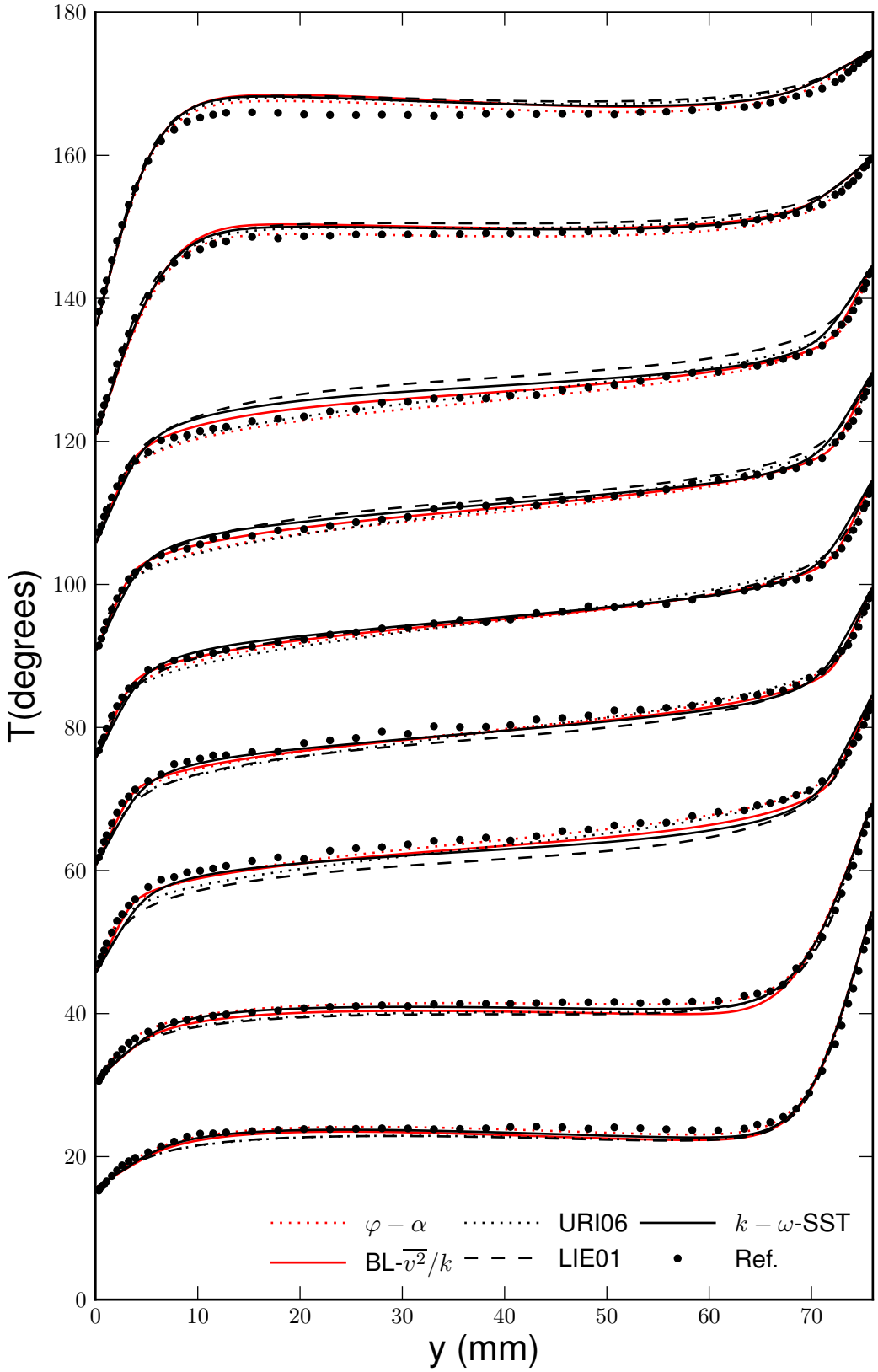

Figure 6.17: Prediction of the temperature in the Betts cavity case ($Ra = 1.43 \times 10^6$)

Behaviour of turbulence models The predictions of the mean velocity, the turbulent kinetic energy, the wall-normal anisotropy and the turbulent shear stress are presented on Fig. 6.20 and Fig. 6.21 for the models $k-\omega$ SST , URI06 , $\varphi-\alpha$ and BL-$\overline{v^2}/k$ as well as the LIE01 model. The simulations are performed on a 1-D grid with 60 cells from wall to wall. In the buoyancy aiding side, the turbulence impairment observed is somehow captured by all models, whose returned level for k are significantly decreased, whereas in the opposing side only the $\varphi-\alpha$, the BL-$\overline{v^2}/k$ and URI06 return fairly correct level of turbulent kinetic energy. The $k-\omega$ SST consistently yields under predicted levels of k on both sides.

The turbulent shear-stress is very well predicted for the BL-$\overline{v^2}/k$ and the URI06 models yielding correct velocity predictions. The under-prediction of $\overline{uv}$ by the LIE01 model on the aiding side leading to excessively large values of the velocity is unexpected since the model captures the correct near-wall values of the stress anisotropy and level of k similar to other models. This again highlights the presence of error cancellations in eddy viscosity modelling. The near-wall anisotropy is somehow over-predicted by the URI06 model. This might be due to the near-wall balance of the φ equation terms not being achieved with this model, as already pointed out in Chap. 4, whereas the $\varphi-\alpha$ and the BL-$\overline{v^2}/k$ model successfully address this shortcoming.

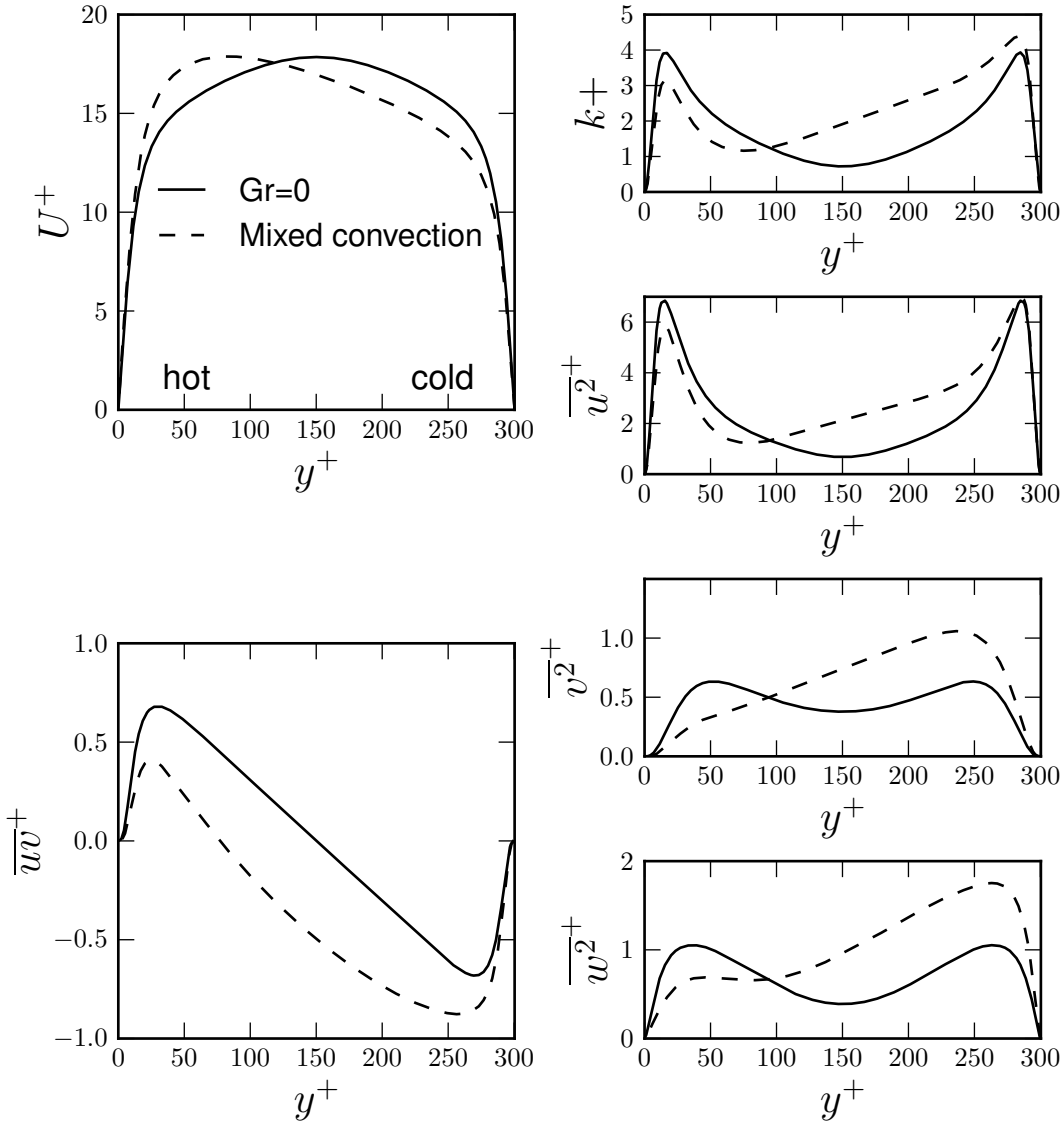

Figure 6.18: DNS data of Kasagi and Nishimura (1997) (mixed convection, $Gr = 9.6 \times 10^5$) and Kuroda et al. (1994) ($Gr = 0$), for $Re_\tau = 150$. Left: Mean upward velocity profile and turbulent shear stress. Right: Profile of k^+ and normal Reynolds stresses.

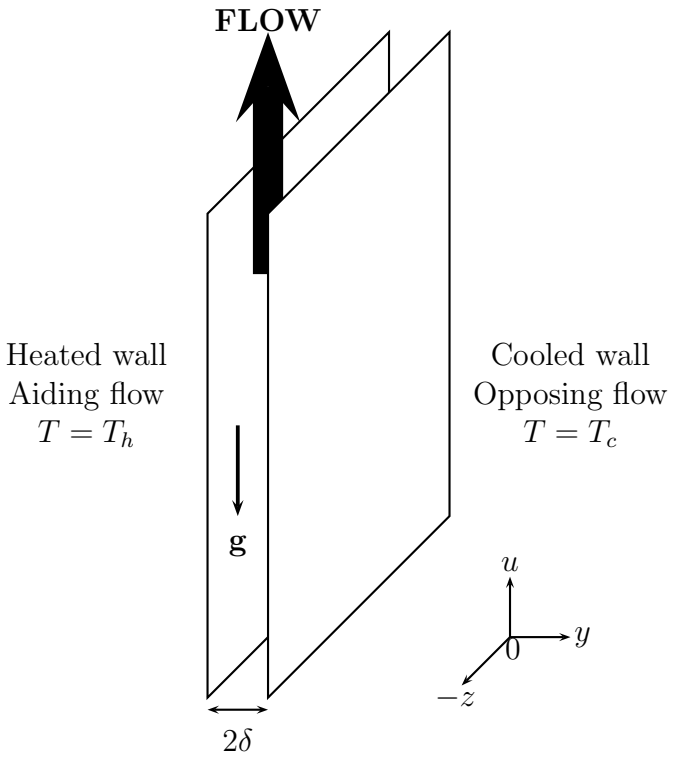

Figure 6.19: Schematic of the case of Kasagi and Nishimura (1997)

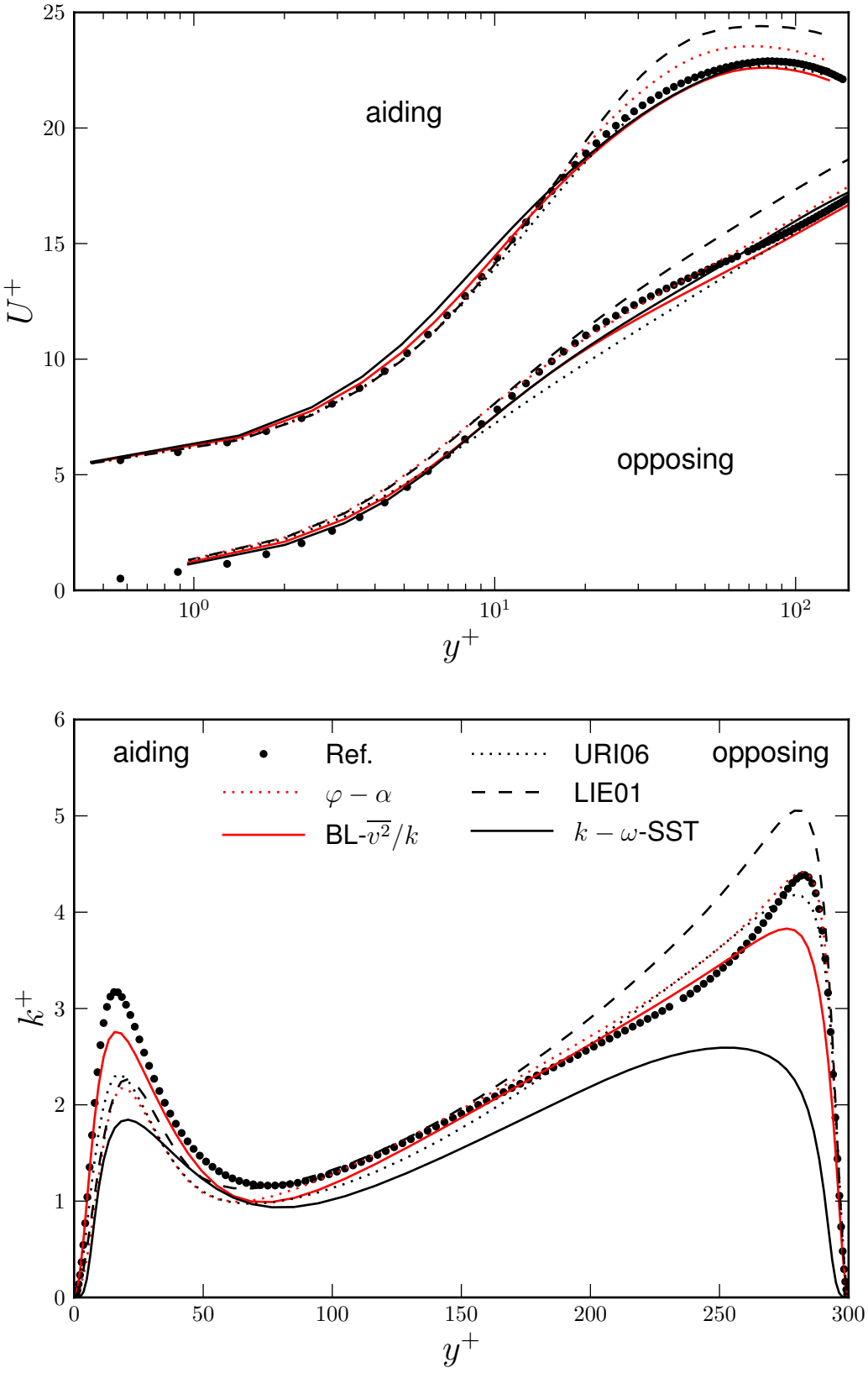

Figure 6.20: Prediction of the non-dimensional velocity (top) and non-dimensional turbulent kinetic energy (bottom) in the vertical heated channel (velocity profile on the aiding side are shifted for clarity).

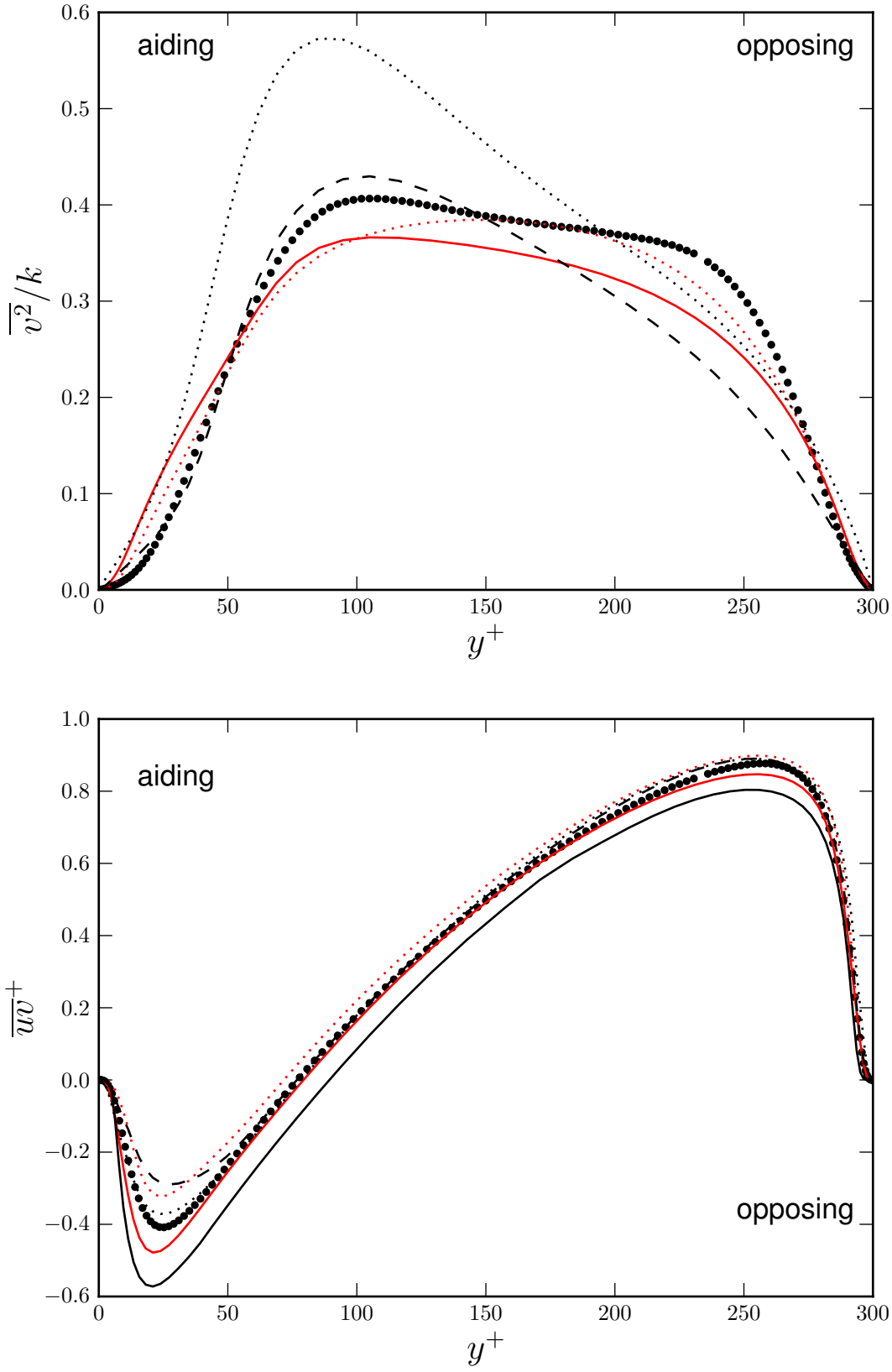

Figure 6.21: Prediction of the wall-normal anisotropy $\overline{v^2}/k$ (top) and the non-dimensional turbulent shear stress (bottom) in the vertical heated channel. See Fig. 6.20 for legends.

Chapter 7

Comparative "code friendliness" in an industrial code

All results presented in the previous section were obtained using an industrial CFD code where the $\varphi - \alpha$ and the BL-$\overline{v^2}/k$ models were implemented (*Code_Saturne* , see Appendix A). This chapter gives details about the code execution on the cases presented in Chap. 6 in order to assess the robustness of the newly developed models as compared to other eddy-viscosity formulations.

7.1 Description of the comparison

The following compares the execution of four models ($k-\omega$ SST, LIE01, URI06 and BL-$\overline{v^2}/k$) on four cases: the Betts cavity (for $Ra = 0.86 \times 10^6$ and $Ra = 1.46 \times 10^6$), the mixed convection case between vertical plates, the asymmetric plane diffuser and the periodic hill flow (simply referred to as Betts, Kasagi, diffuser and periodic hill in the following). The cases considered are run on two-dimensional grids and the steady state algorithm is used. The following criteria are used to analyse the convergency properties of the different variables for all models:

- For each variable V, V^∞ denotes the solution at the end of the calculation and

a convergency parameter R_V is defined as:

$$R_V^k = \frac{1}{N} \sum_{i=1}^{N} \left| \frac{V^k(\underline{x_i}) - V^\infty(\underline{x_i})}{V^\infty(\underline{x_i})} \right| \tag{7.1}$$

where V^k and R_V^k are the variable and the convergency parameter at the k^{th} iteration and N is the number of probes on which the time evolution is recorded.

- The CPU time T_V spent for the resolution of each variable and the total resolution time T (note that the total time spent is generally greater than the sum of the time spent on each variable)

To ease convergence, relaxation factors are used with the steady state algorithm: 0.9 is used for all variables except pressure for which $\alpha_P = 0.1$. Those are the default values used in *Code_Saturne*.

All variables (expect temperature) are initialised with a uniform field calculated from two user-specified reference velocities $\underline{U}_\infty$ and U_{ref}, a turbulent intensity I_t and a turbulent length-scale L_t). From these parameters the initial values of the variables are determined:

$$\begin{cases} \underline{U}^0 = \underline{U}_\infty \\ k^0 = \frac{3}{2} \left(I_t U_{ref} \right)^2 \\ \varepsilon^0 = C_\mu (k^0)^{3/2} / L_t \\ \omega^0 = \sqrt{k^0} / L_t \\ \varphi^0 = \frac{2}{3} \end{cases} \tag{7.2}$$

The values of $\underline{U}_\infty$, U_{ref}, I_t and L_t are given in Tab. 7.1.

Case	$\underline{U}_\infty$	U_{ref}	I_t	L_t
Betts ($Ra = 0.86 \times 10^6$)	0	4	0.02	8
Betts ($Ra = 1.43 \times 10^6$)	0	4	0.02	8
Kasagi	14.5	14.5	0.02	$\Omega^{1/3}$
Diffuser	1	1	0.02	$\Omega^{1/3}$
Periodic hill	1	1	0.02	$\Omega^{1/3}$

Table 7.1: Parameters determining the initial values used for the calculations. Ω represents the volume of the calculation domain.

For the Betts case, temperature is initialised by a field following constant gradient between the two walls. For the Kasagi case, it is given the initial value $25°C$.

7.2 Presentation of the results

For each case and for all models the calculations are run for the same number of time step and on the same type of processor: Intel(R) Xeon(TM) CPU 2.80GHz. Two processors are used for all simulations except for the Kasagi case (for which only 1 processor is used).

7.2.1 Execution time

The time T_V spent for the resolution of a given variable V is directly linked to the number of sub-iterations required to resolve the linear system associated to the governing equation of the variable[1]. The total execution time T does not equal the sum of variable-wise execution times. Indeed, calculation of source terms, matrix assembly, inter-node communication and post-processing can amount to a considerable part of the time spent as well.

Tab. 7.2, Tab. 7.3, Tab. 7.4, Tab. 7.5 and Tab. 7.6 present the variable-wise and total execution time for all models for the Betts case for both Rayleigh numbers, the Kasagi, diffuser and periodic hill cases, respectively.

For all present simulations, T is not so meaningful to spot differences between models. As seen from the tables the sum of all variable-wise resolution time T_V is always at least one order of magnitude smaller than the total time T, evidencing that the variables resolution is a negligible fraction of the total time. This may no longer be the case in larger configurations, however, and it is believed that variable-wise time figures can bring valuable insight on models numerical properties.

The resolution of ω by the $k-\omega$ SST is noticeably quicker than that of ε by the $\overline{v^2}-f$ based models. This is the most marked in the Kasagi case (nearly 10

[1]The Jacobi method is used for all variables except when the nature of the problem is elliptic (*i.e.* for the pressure and the $f/\overline{f}/\alpha$ variable) for which the conjugate gradient method is used instead.

times quicker). This may reflect better numerical properties of the ω equation (the high values of ω in the near-wall region (recall $\lim_{y\to 0}\omega = \infty$) beneficially augments the diagonal dominance of the linear system matrix, through the term proportional to ω^2).

In the Betts cavity case for both Rayleigh numbers the resolution of the turbulent variables for the BL-$\overline{v^2}/k$ model is the quickest compared to the URI06 and the LIE01 model (by a factor of 6 for k, 7 for ε and 4 for $\varphi/\overline{v^2}$). This can be associated to a better treatment of the near-wall terms in the BL-$\overline{v^2}/k$ formulation (implicit E term in the k equation, resolution of φ instead of $\overline{v^2}$, zero boundary condition for α)

The resolution of the non-dimensional parameter α by the BL-$\overline{v^2}/k$ is noticeably quicker than that of the elliptic variables of the URI06 and the LIE01 approaches. This is the most marked on the Betts case.

7.2.2 Convergence parameter

Fig. 7.1, Fig. 7.2, Fig. 7.3, Fig. 7.4 and Fig. 7.5 show the evolution of the convergence parameter R_V for each variable V for the Betts case for both Rayleigh numbers, the Kasagi, diffuser and periodic hill cases respectively.

In the Betts case the quality of the BL-$\overline{v^2}/k$ convergence is far better than that of the two other $\overline{v^2} - f$ based models(*i.e.* for the newly developed model R_V decreases faster and to lower values). The same final level of residuals is reached for the BL-$\overline{v^2}/k$ and the $k-\omega$ SST model but the latter model is slightly quicker to converge.

The Kasagi case shows a similar trend for all models, with a somehow faster and better convergency for the URI06 model.

In the diffuser case, the $k-\omega$ SST convergence is considerably slower than that of $\overline{v^2}-f$ based models. The former model also goes through a transient phase during the 1000 first iterations. For this case the BL-$\overline{v^2}/k$ is a little slower to converge than the LIE01 and the URI06 models as far as turbulent variables are concerned, with the exception of the elliptic variable.

In the periodic hill case, the $k-\omega$ SST is the fastest to converge. The three

$\overline{v^2} - f$ based models globally converge at the same pace but the variable φ seems to reach lower values of R_V with the BL-$\overline{v^2}/k$ model. For the latter model the convergence of α is also the quickest compared to other elliptic variables.

Model	T $\times 10^4 s$	T_k $\times 10^3 s$	T_ε/T_ω $\times 10^2 s$	$T_\varphi/T_{\overline{v^2}}$ $\times 10^3 s$	$T_{\overline{f}}/T_\alpha$ $\times 10^2 s$	T_U $\times 10^3 s$	T_V $\times 10^3 s$	T_P $\times 10^3 s$	T_T $\times 10^1 s$
$k-\omega$ SST	5.18	.243	.872			1.21	1.98	4.25	9.13
URI06	6.32	1.31	25.2	1.02	7.90	.951	1.95	4.37	9.54
BL-$\overline{v^2}/k$	6.37	.219	3.65	.239	1.88	.957	2.11	4.46	9.48
LIE01	6.41	1.20	24.4	.825	8.37	1.27	1.96	4.46	9.50

Table 7.2: Simulation of the Betts case ($Ra = 0.86 \times 10^6$): Total CPU time spent in total and for each variable for a 40000 iterations run.

Model	T $\times 10^4 s$	T_k $\times 10^3 s$	T_ε/T_ω $\times 10^2 s$	$T_\varphi/T_{\overline{v^2}}$ $\times 10^3 s$	$T_{\overline{f}}/T_\alpha$ $\times 10^2 s$	T_U $\times 10^3 s$	T_V $\times 10^3 s$	T_P $\times 10^3 s$	T_T $\times 10^2 s$
$k-\omega$ SST	5.31	.221	.871			1.04	1.88	4.87	.983
URI06	6.40	1.31	24.6	1.03	7.89	.991	1.92	4.94	1.00
BL-$\overline{v^2}/k$	6.38	.238	3.81	.207	1.85	.921	1.77	4.90	1.02
LIE01	6.38	1.20	23.4	.828	8.87	1.05	1.89	4.89	1.02

Table 7.3: Simulation of the Betts case ($Ra = 1.43 \times 10^6$): Total CPU time spent in total and for each variable for a 40000 iterations run.

Model	T $\times 10^2 s$	T_k $\times 10^0 s$	T_ε/T_ω $\times 10^0 s$	$T_\varphi/T_{\overline{v^2}}$ $\times 10^0 s$	$T_{\overline{f}}/T_\alpha$ $\times 10^- 1 s$	T_U $\times 10^0 s$	T_T $\times 10^0 s$
$k-\omega$ SST	1.62	2.22	.202			2.07	2.52
URI06	2.00	1.86	1.74	1.59	5.05	1.38	2.58
BL-$\overline{v^2}/k$	2.04	2.29	2.18	1.90	4.23	1.97	2.76
LIE01	1.78	2.27	2.01	2.01	5.31	1.61	3.00

Table 7.4: Simulation of the Kasagi case: Total CPU time spent in total and for each variable for a 10000 iterations run.

Model	T $\times 10^3 s$	T_k $\times 10^2 s$	T_ε / T_ω $\times 10^1 s$	$T_\varphi / T_{\overline{v^2}}$ $\times 10^1 s$	$T_{\overline{f}} / T_\alpha$ $\times 10^1 s$	T_U $\times 10^2 s$	T_V $\times 10^2 s$	T_P $\times 10^3 s$
$k-\omega$ SST	5.12	1.57	4.26			2.10	2.54	1.05
URI06	5.54	1.03	6.25	9.65	3.82	1.38	1.92	1.08
BL-$\overline{v^2}/k$	6.10	1.06	7.84	8.80	2.61	1.41	1.96	1.11
LIE01	5.49	.997	6.40	7.95	3.45	1.37	1.82	1.04

Table 7.5: Simulation of the diffuser case: Total CPU time spent in total and for each variable for a 2000 iterations run.

Model	T $\times 10^3 s$	T_k $\times 10^2 s$	T_ε / T_ω $\times 10^2 s$	$T_\varphi / T_{\overline{v^2}}$ $\times 10^2 s$	$T_{\overline{f}} / T_\alpha$ $\times 10^2 s$	T_U $\times 10^2 s$	T_V $\times 10^2 s$	T_P $\times 10^3 s$
$k-\omega$ SST	7.58	3.78	.986			4.91	5.47	1.28
URI06	9.22	4.63	5.37	4.21	1.82	5.57	5.71	1.22
BL-$\overline{v^2}/k$	9.79	4.21	4.60	3.59	1.38	5.23	5.60	1.26
LIE01	9.25	4.69	5.38	3.77	1.73	5.28	5.63	1.21

Table 7.6: Simulation of the periodic hill case: Total CPU time spent in total and for each variable for a 4000 iterations run.

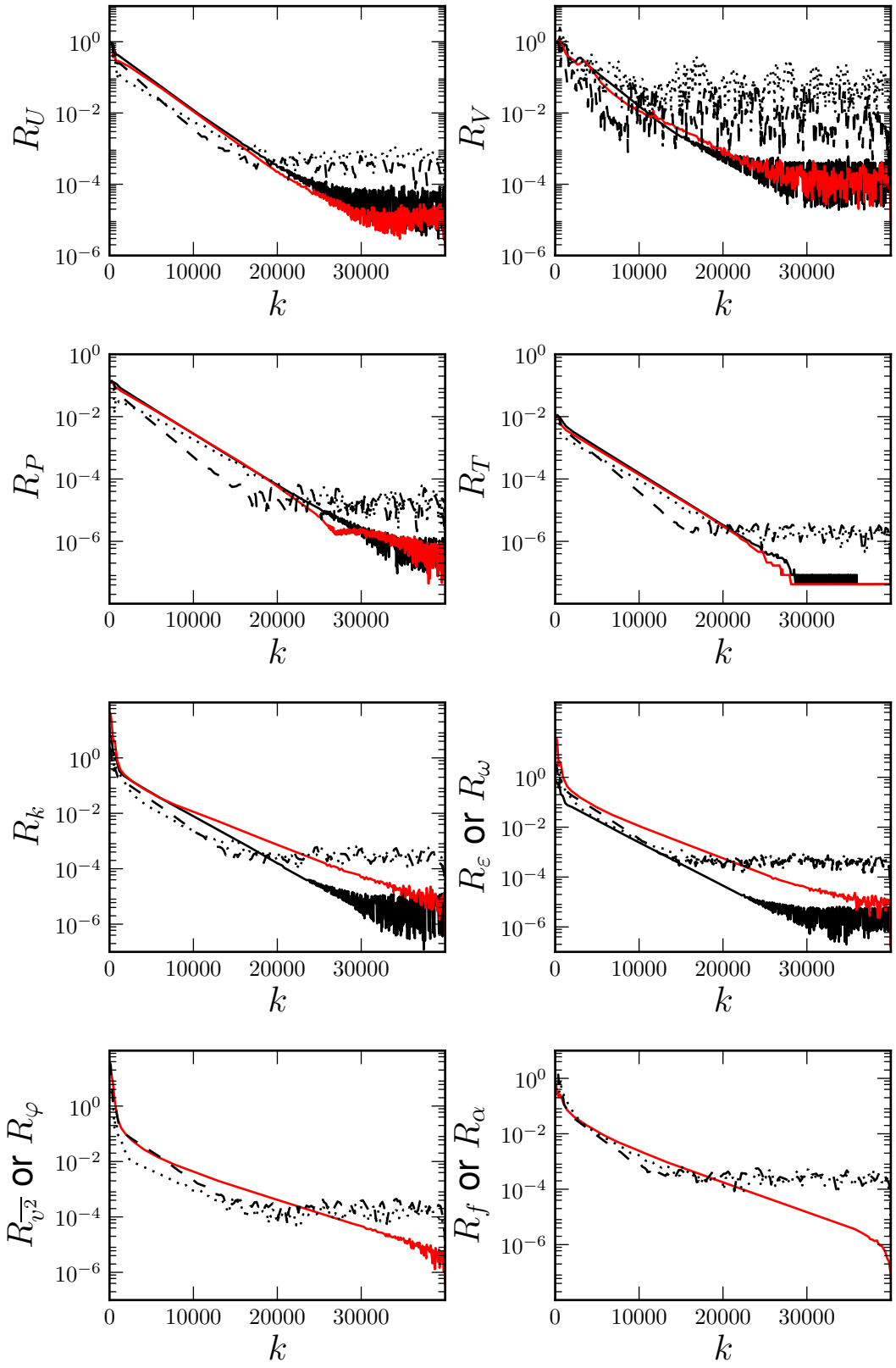

Figure 7.1: Convergency parameter for the Betts case ($Ra = 0.86 \times 10^6$) (8 probes). See Fig. 7.4 for legends

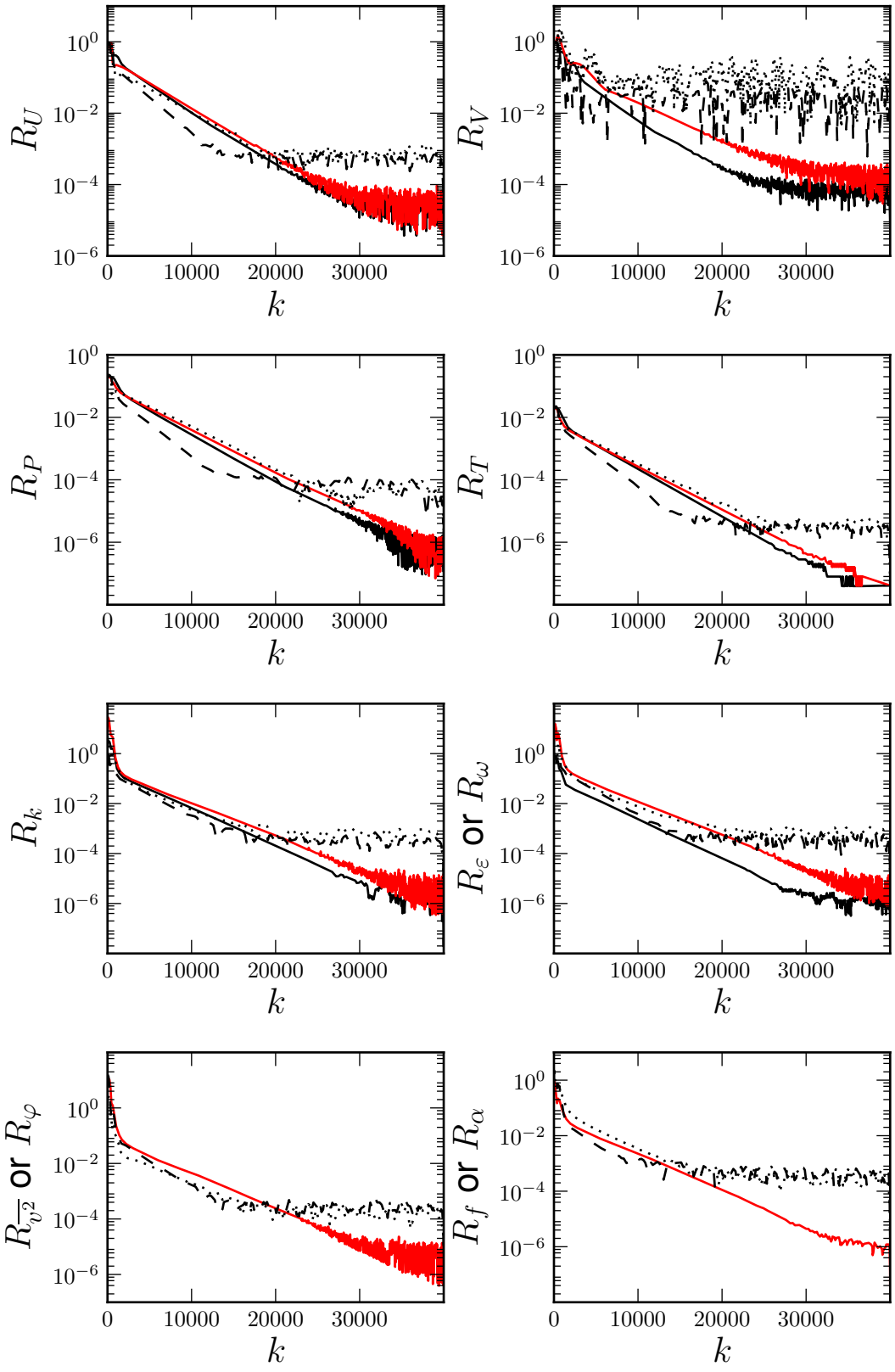

Figure 7.2: Convergency parameter for the Betts case ($Ra = 1.43 \times 10^6$) (8 probes). See Fig. 7.4 for legends.

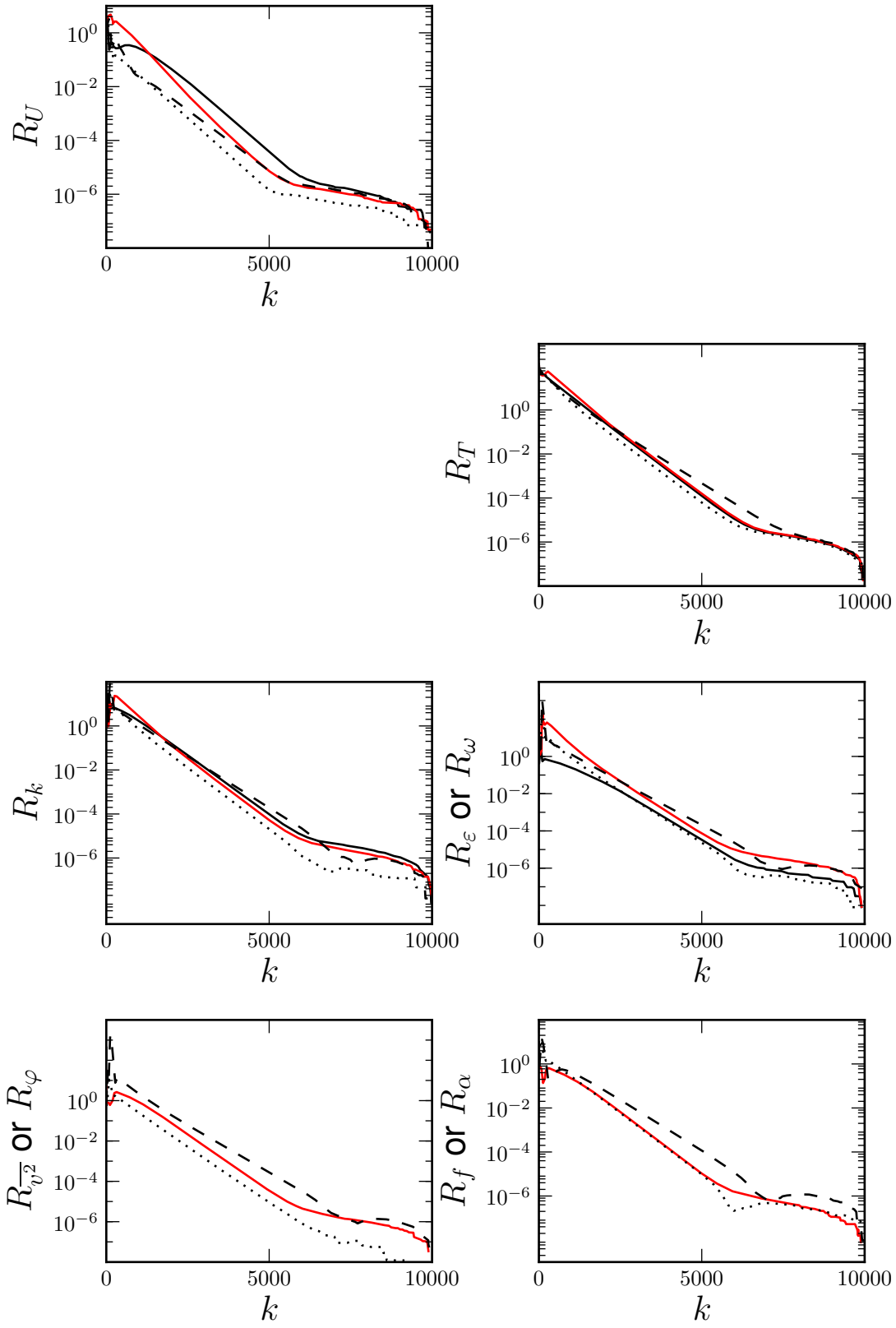

Figure 7.3: Convergency parameter for the Kasagi case (13 probes). See Fig. 7.4 for legends

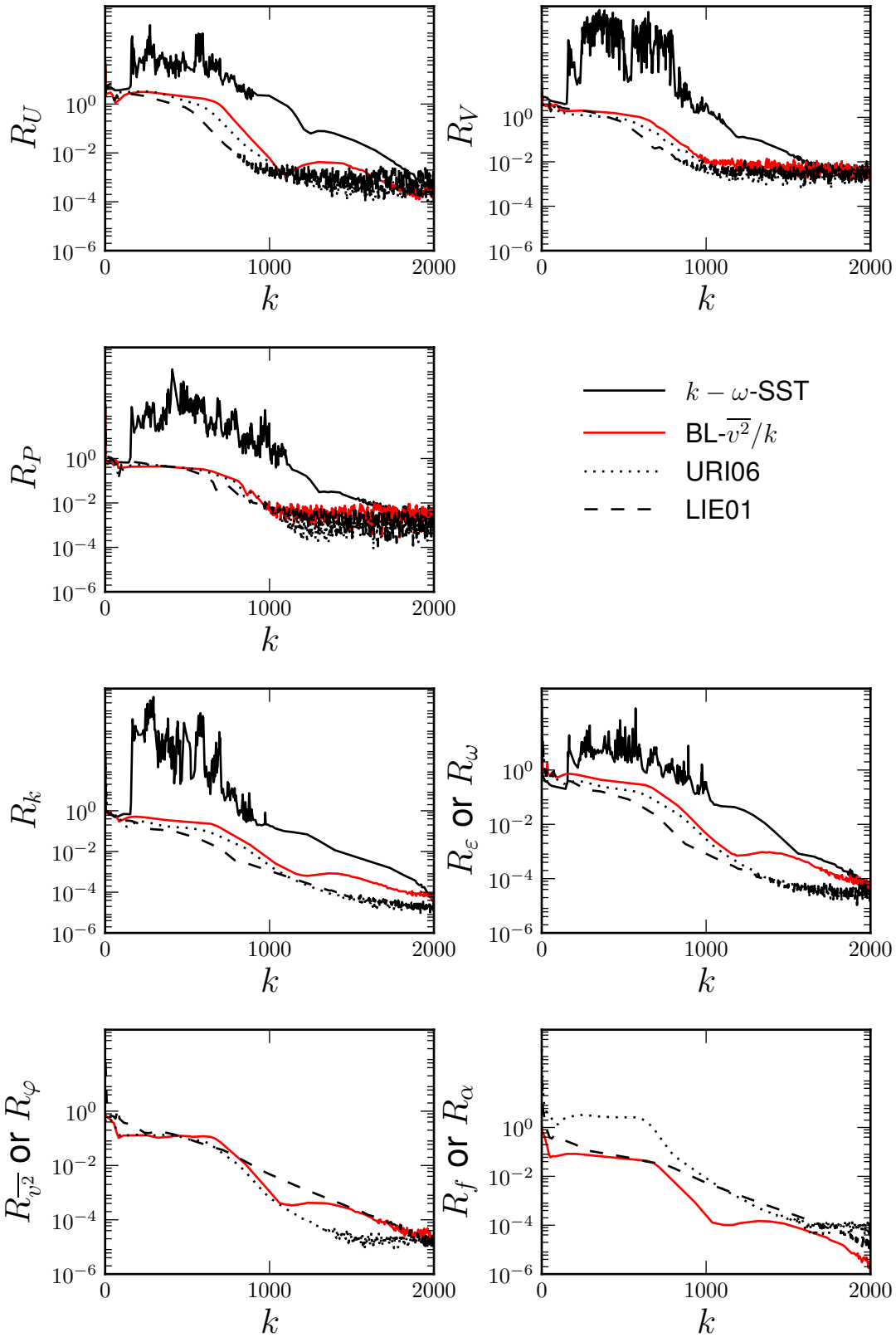

Figure 7.4: Convergency parameter for the diffuser case (16 probes)

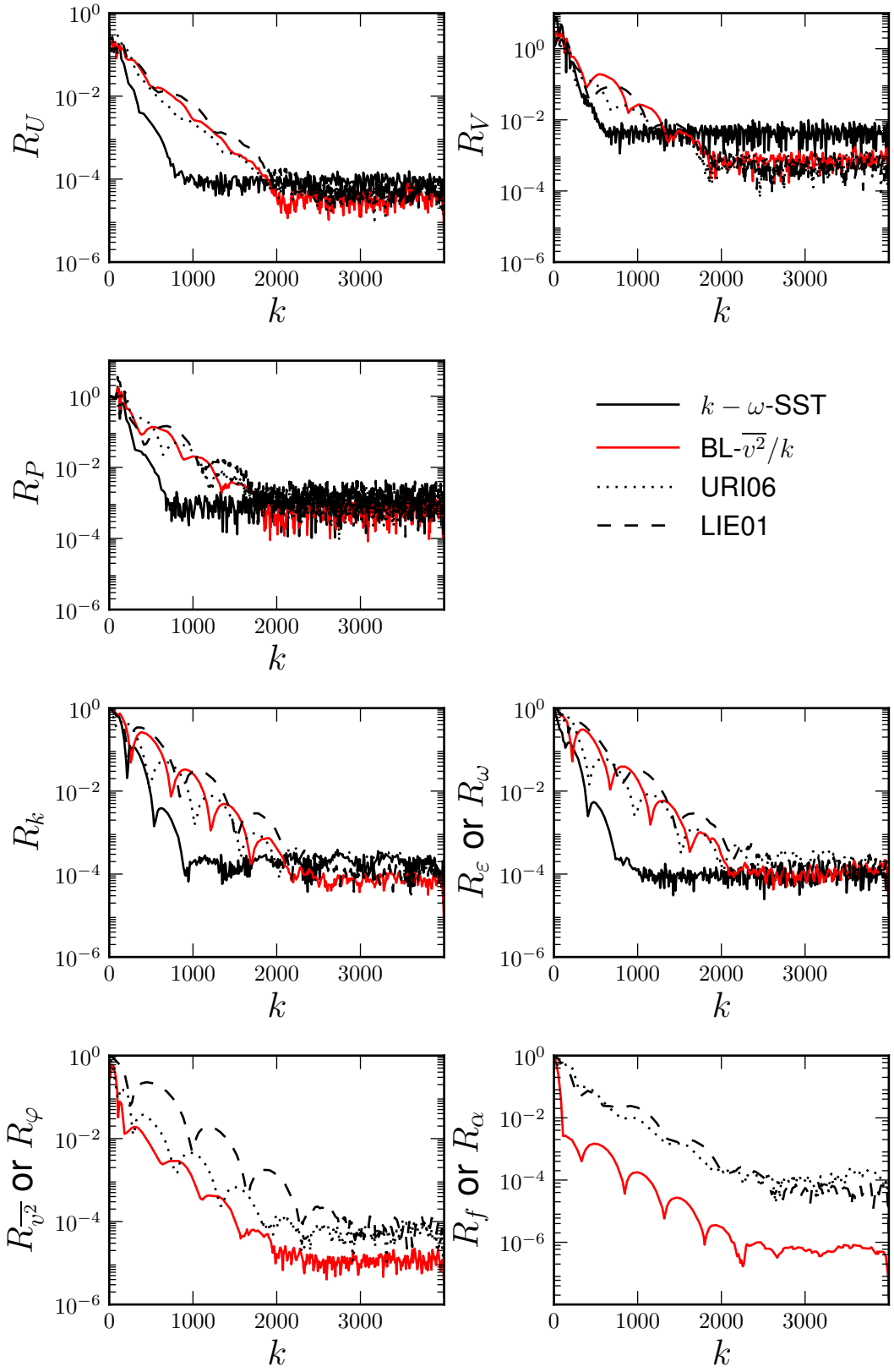

Figure 7.5: Convergency parameter for the periodic hill case (6 probes)

Chapter 8

Conclusions

This thesis has described the developments and the validation of a new near-wall eddy viscosity turbulence model which combines the principles of the $\overline{v^2} - f$ approach and the elliptic blending method. The proposed model is denoted as BL-$\overline{v^2}/k$ (Billard and Laurence, 2011, See Appendix D). Numerical and predictive performances of the model, implemented in an industrial CFD code, have then been successfully assessed in the case of pressure induced separating flows as well as buoyancy impairing turbulent flows. Applications of the model to 3-dimensional flows can be found in Billard et al. (2011) (See Appendix E).

8.1 Summary of the work

The chapters presenting the original work of the present thesis are now summarised.

Chap. 4 gave a comprehensive review of the $\overline{v^2} - f$ models, including those specifically derived to address the numerical problems associated to the original version. It was shown that the "code friendly" modifications are always detrimental to the predictive capabilities (for the versions of Lien and Durbin (1996) and Lien and Kalitzin (2001) this results in the variable $\overline{v^2}$ being strongly over-predicted in the logarithmic layer while the version of Uribe (2006) does not reproduce the correct $\overline{v^2}$ asymptotic

near-wall behaviour). Another code-friendly attempt, the version of Hanjalić et al. (2004), does not quite satisfactorily alleviate the numerical stiffness. In the review all the versions were compared for a set of fundamental flows, including the channel flow for various Reynolds numbers, the logarithmic layer at infinite Reynolds number and the case of homogeneous sheared turbulence. A large variability of behaviour was noted. This was shown to be partly due to the $C^*_{\varepsilon 1}$ modification proposed by most models to reproduce dominance of dissipation against production, in the viscous and buffer layer. For most models it was shown that this modification had an influence far beyond the mere viscosity-affected region, thus requiring a full retuning of all the constants, now departing from their standard values calibrated in homogeneous or infinite Re_τ cases (*i.e.* $C_{\varepsilon 1}$, $C_{\varepsilon 2}$ as well as the LRR-IP or the SSG model).

In Chap. 5 a simple adaptation of the elliptic blending method of Manceau and Hanjalić (2002) was performed based on the model of Uribe (2006). The resulting model, denoted as $\varphi - \alpha$, solves for the non-dimensional near-wall anisotropy parameter $\varphi = \overline{v^2}/k$ and the elliptic-blending coefficient α, which goes from 0 at walls to 1 in the remote region. The numerical stiffness associated to the original version was shown to be totally removed with the $\varphi - \alpha$ model. Moreover the needed $C^*_{\varepsilon 1}$ modification is multiplied by $(1-\alpha^p)$ so that it only has an influence in the very near-wall viscous and buffer regions. However, as it is, the $\varphi - \alpha$ model does not perform well in low Reynolds number flows, and this was shown to be due to a more general discrepancy of the $\overline{v^2} - f$ approach: indeed the constitutive relation defining ν_t, as proposed in Durbin (1991) yields a shear-stress-to-mean-velocity-gradient ratio which is too Reynolds number dependent in channel flow. This explains why the quality of predictions of the various models is quite Reynolds dependent, and behaviour in the logarithmic region at infinite Reynolds number, in particular the predicted value of the Von Kármán constant κ, is very different amongst models.
To facilitate the calibration of the $\varphi - \alpha$ model for both low and high Reynolds number flows, a reduction of the Reynolds number dependence of the predicted ν_t was

sought, firstly by performing successive modifications of the $k-\varepsilon$ system (mainly consisting in re-introducing the E extra dissipation production term originally proposed by Jones and Launder (1972) directly into the k equation) and secondly by adopting a smaller value for the length-scale coefficient C_η. The resulting and final model, referred to as BL-$\overline{v^2}/k$ thus performs well at both low and high Reynolds number flows, and the value adopted by the constants are exactly equal to their theoretical values ($C_{\varepsilon 1}, C_{\varepsilon 2}, \sigma_\varepsilon$, C_L and the constants of the SSG model). The correct behaviour in the considered fundamental flows is fully recovered. Finally the BL-$\overline{v^2}/k$ model includes a $C^*_{\varepsilon 2}$ coefficient correction active in the defect layer of a channel flow to avoid excessive growth of the turbulent viscosity and the turbulence time and length-scale in this region. This modification finds its justification in the analysis of the budget of the exact dissipation rate equation, from which it is shown that the constant $C_{\varepsilon 2}$ should be decreased in the defect layer.

In Chap. 6 the two models, namely the $\varphi - \alpha$ and the BL-$\overline{v^2}/k$ were compared to other $\overline{v^2} - f$ versions (the models of Uribe (2006) and Lien and Kalitzin (2001), respectively denoted URI06 and LIE01) as well as the $k-\omega$ SST model on separated flows (the periodic hill flow and the plane asymmetric diffuser flow) and turbulent buoyant flows (in a tall enclosed cavity (Betts) and between two differentially heated walls). Those cases are known to be fairly well predicted by $\overline{v^2} - f$ models in general and the performances of the present BL-$\overline{v^2}/k$ are at least as good. For the periodic hill and the diffuser cases the BL-$\overline{v^2}/k$ performs as well as other $\overline{v^2} - f$ models, and considerably improves the flow predictions downstream the diffuser recirculation. The BL-$\overline{v^2}/k$ also returns the best predictions for the Betts cavity at different Rayleigh numbers and is also the only one to correctly capture the turbulence level reduction near the hot wall (buoyancy aiding flow) of a differentially heated channel. In particular the near-wall anisotropy enhancement near the hot wall is well predicted with the present BL-$\overline{v^2}/k$ model. The LIE01 version generally returns strongly over-predicted values for $\overline{v^2}$, often non-physical due to the combined effects of a change of variable performed to improve robustness and a default of the original elliptic operator used

by the model. Paradoxically this version certainly is the most widely used as it is the one implemented in major commercial CFD codes. As the main differences between the $\varphi - \alpha$ and the BL-$\overline{v^2}/k$ models are the modifications performed on the $k - \varepsilon$ system it is interesting to compare both on the considered applications to investigate the consequences of these further developments on the results. They prove to be always beneficials as the BL-$\overline{v^2}/k$ is superior to the $\varphi - \alpha$ on all cases. The latter model strongly under-predicts the recirculation length for the two separating flows.

The last chapter, Chap. 7, presents the code used and reports the execution time and the evolution of residuals for each variable for all the cases and for all the models considered in Chap. 6. First, the $k - \omega$ SST is generally the fastest to converge but not always: the $k - \omega$ SST convergency in the diffuser is noticeably slower than that of the other models. As far as $\overline{v^2} - f$ based models are concerned, the BL-$\overline{v^2}/k$ is the fastest to converge and generally the model giving the best quality of convergence (*i.e.* lowest residuals) which is particularly true for the Betts cavity case. The convergence of the non-dimensional variable α is also quicker with the lowest residuals, compared to the other elliptic variables.

8.2 Future work

Some further developments should be performed to increase the predictive capabilities of the model in two configurations:

- The model inherits the general shortcoming of the $\overline{v^2} - f$ approach which is an under representation of truly low Reynolds number effects (*i.e.* close to transition). In fact those are mainly taken into account if they are a consequence of wall effects, by the use of the Kolmogorov length and time-scale, which are mainly introduced to avoid a singularity in the f/α and ε equations respectively. It is shown (see Appendix C) that the model can yield a spurious laminar solution in the case of homogeneous sheared turbulence for some low initial values of the turbulent quantities. Even though this was not experienced in the

cases investigated in the present work, this may also impair the convergence of the solution and activate clippings the codes generally employ to preserve stability. Elements accounting for low-Reynolds number effects in the more general case (*i.e.* not only in near-wall flows) should then be incorporated: these could take the form of damping terms made function of the turbulent Reynolds number for instance.

- The predictions of the BL-$\overline{v^2}/k$ model in non-equilibrium and unsteady flows could be improved. The third variable, $\overline{v^2}$, solved for by $\overline{v^2} - f$ models may somehow account for turbulence history effects, feature which is not even taken into account in non-linear eddy viscosity models or explicit algebraic Reynolds stress models. However the $\overline{v^2} - f$ approach cannot be considered as a simplified Reynolds stress model and $\overline{v^2}$ has little meaning in homogeneous flows. An alternative 3-equation model is the recent development of Revell et al. (2006), the C_{as} model which accounts for stress-strain misalignment and is clearly defined as a contraction of these two tensors. An essential ingredient present in the C_{as} equation is the material derivative of the strain rate DS/Dt which improves predictions in non-equilibrium and unsteady flows. The φ variable of the BL-$\overline{v^2}/k$ could be beneficially replaced by a compound quantity derived from the equations of $\overline{v^2}/k$ and C_{as} thus helping the third resolved variable of the model to play a more relevant role away from walls.

- Finally it was shown in Chap. 5 that the variables of the new model, in particular ε and ν_t are virtually independent of Re_τ at a wall. The recent work of Osman (2011) takes advantage of this model's property to devise an adaptive wall-function based BL-$\overline{v^2}/k$ suitable for coarse near-wall meshes. In this approach, analytical behaviour is prescribed to the BL-$\overline{v^2}/k$ variables at walls when the first computational grid point is not located in the viscous sub-layer. In Osman (2011) the proposed methodology, yet still in its early stages, was successfully applied to the channel flow case for various near-wall grid refinements and the ribbed channel flow of Rau et al. (1998).

Bibliography

K. Abe, Y.J. Jang, and MA Leschziner. An investigation of wall-anisotropy expressions and length-scale equations for non-linear eddy-viscosity models. *International journal of heat and fluid flow*, 24(2):181–198, 2003.

GP Almeida, DFG Durao, and MV Heitor. Wake flows behind two-dimensional model hills. *Experimental Thermal Fluid Science*, 7:87–101, 1993.

DD Apsley and MA Leschziner. A new low-reynolds-number nonlinear two-equation turbulence model for complex flows. *International journal of heat and fluid flow*, 19(3):209–222, 1998.

DD Apsley and MA Leschziner. Advanced turbulence modelling of separated flow in a diffuser. *Flow, Turbulence and Combustion*, 63(1):81–112, 2000.

F. Archambeau, N. Mechitoua, and M. Sakiz. A finite volume method for the computation of turbulent incompressible flows - industrial applications. *International Journal on Finite Volumes*, 1(1), 2004.

D. Aronson, A.V. Johansson, and L. LOeFDAHL. Shear-free turbulence near a wall. *Journal of Fluid Mechanics*, 338:363–385, 1997.

PL Betts and IH Bokhari. Experiments on turbulent natural convection in an enclosed tall cavity. *International Journal of Heat and Fluid Flow*, 21(6):675–683, 2000.

P.L. Bhatnagar, E.P. Gross, and M. Krook. A model for collision processes in gases. i. small amplitude processes in charged and neutral one-component systems. *Physical Review*, 94(3):511, 1954.

F Billard and D Laurence. A robust $k-\varepsilon-\overline{v^2}/k$ elliptic blending turbulence model with improved predictions in near-wall, wake, separated and buoyant flows. *Submitted to International Journal of Heat and Fluid Flow*, 2011.

F Billard, J.C. Uribe, and D Laurence. A new formulation of the $\overline{v^2}-f$ model using elliptic blending and its application to heat transfer prediction. In *Proceedings of the* 7^{th} *International Symposium on Engineering Turbulence Modelling and Mesurements*, pages 89–94, 2008.

F. Billard, A. Revell, and T. Craft. Applications of advanced reynolds stress transport models to highly separated flows. In *Proceedings, Seventh Symp. on turbulence and shear flow phenomena, Ottawa*, 2011.

R. Boudjemadi, V. Maupu, D. Laurence, and P. Le Quere. Budgets of turbulent stresses and fluxes in a vertical slot natural convection flow at rayleigh $ra = 10^5$ and 5.4×10^5. *International journal of heat and fluid flow*, 18(1):70–79, 1997.

CU Buice and JK Eaton. Experimental investigation of flow through an asymmetric plane diffuser. Report TSD-107, Department of mechanical engineering, 1997.

B. Chaouat and R. Schiestel. Progress in subgrid-scale transport modelling for continuous hybrid non-zonal RANS/LES simulations. *International Journal of Heat and Fluid Flow*, 30(4):602–616, 2009.

D.R. Chapman. Computational aerodynamics development and outlook. *AIAA J*, 17(12):1293–1313, 1979.

H.C. Chen. Submarine flows studied by second-moment closure. *Journal of engineering mechanics*, 121:11–36, 1995.

H.C. Chen, Y.J. Jang, and J.C. Han. Computation of heat transfer in rotating two-pass square channels by a second-moment closure model. *International Journal of Heat and Mass Transfer*, 43(9):1603–1616, 2000.

K.Y. Chien. Predictions of channel and boundary-layer flows with a low-reynolds-number turbulence model. *AIAA journal*, 20:33–38, 1982.

G. Comte-Bellot and S. Corrsin. The use of a contraction to improve the isotropy of grid-generated turbulence. *J. Fluid Mech*, 25(4):657–682, 1966.

E.R. Corino and R.S. Brodkey. A visual investigation of the wall region in turbulent flow. *Journal of Fluid Mechanics*, 37(01):1–30, 1969.

TJ Craft. Developments in a low-reynolds-number second-moment closure and its application to separating and reattaching flows. *International journal of heat and fluid flow*, 19(5):541–548, 1998.

TJ Craft and BE Launder. A Reynolds stress closure designed for complex geometries. *International Journal of Heat and Fluid Flow*, 17(3):245–254, 1996.

TJ Craft, BE Launder, and K. Suga. Development and application of a cubic eddy-viscosity model of turbulence. *International Journal of Heat and Fluid Flow*, 17 (2):108–115, 1996.

B.J. Daly and F.H. Harlow. Transport equations in turbulence. *Physics of Fluids*, 13:2634, 1970.

L. Davidson, PV Nielsen, and A. Sveningsson. Modification of the v2f model for computing the flow in a 3D wall jet. *Turbulence, Heat and Mass Transfer*, 4: 577–84, 2003.

F. Dubois. *Une introduction au schéma de Boltzmann sur réseau. Notes de cours donné dans le cadre du groupe Groupe de Travail Numérique de l'équipe "Analyse Numérique et Equations aux Dérivées Partielles" de l'Université Paris-Sud*, June 2006.

P.A. Durbin. Near-wall turbulence closure modeling without "damping functions". *Theoretical and Computational Fluid Dynamics*, 3(1):1–13, 1991.

P.A. Durbin. Application of a near-wall turbulence model to boundary layers and heat transfer. *International Journal of Heat and Fluid Flow*, 14(4):316–323, 1993a.

P.A. Durbin. A Reynolds stress model for near-wall turbulence. *Journal of Fluid Mechanics*, 249:465–498, 1993b.

P.A. Durbin. Separated Flow Computations with the $k-\varepsilon-\overline{v^2}$ Model. *AIAA journal*, 33(4):659–664, 1995.

P.A. Durbin. On the $k-\varepsilon$ stagnation point anomaly. *International Journal of Heat and Fluid Flow*, 17(1):89–90, 1996.

P.A. Durbin and D. Laurence. Nonlocal effects in single point closure. In 3^{rd} *Advances in Turbulence Research Conference*, pages 109–120, 1996.

PA Durbin and B.A.P. Reif. *Statistical theory and modeling for turbulent flows*. John Wiley & Sons, 2001.

J.K. Eaton. Experimental investigation of flow through an asymmetric plane diffuser. *Journal of Fluids Engineering*, 122:433, 2000.

A. Fadai-Ghotbi, C. Friess, R. Manceau, T.B. Gatski, and J. Borée. Temporal filtering: A consistent formalism for seamless hybrid RANS-LES modeling in inhomogeneous turbulence. *International Journal of Heat and Fluid Flow*, 2010.

Y. Fournier, J. Bonelle, C. Moulinec, Z. Shang, AG Sunderland, and JC Uribe. Optimizing Code_Saturne Computations on Petascale Systems. *Computers & Fluids*, 2011. ISSN 0045-7930.

J. Fröhlich and D. von Terzi. Hybrid LES/RANS methods for the simulation of turbulent flows. *Progress in Aerospace Sciences*, 44(5):349–377, 2008.

J. Fröhlich, C.P. Mellen, W. Rodi, L. Temmerman, and M.A. Leschziner. Highly resolved large-eddy simulation of separated flow in a channel with streamwise periodic constrictions. *Journal of Fluid Mechanics*, 526:19–66, 2005.

T.B. Gatski and CG Speziale. On explicit algebraic stress models for complex turbulent flows. *Journal of Fluid Mechanics*, 254(-1):59–78, 1993.

M. Germano. Turbulence: The filtering approach. *Journal of Fluid Mechanics*, 238: 325–336, 1992.

M. Germano, U. Piomelli, P. Moin, and W.H. Cabot. A dynamic subgrid-scale eddy viscosity model. *Physics of Fluids A: Fluid Dynamics*, 3(7):1760–1765, 1991.

MM Gibson and BE Launder. Ground effects on pressure fluctuations in the atmospheric boundary layer. *Journal of Fluid Mechanics*, 86(03):491–511, 1978.

N. Gilbert and L. Kleiser. Turbulence model testing with the aid of direct numerical simulation results. In *8th Symposium on Turbulent Shear Flows, Volume 2*, volume 2, pages 26–1, 1991.

V. Guimet and D. Laurence. A linearised turbulent production in the k- ε model for engineering applications. *Engineering Turbulence and Measurements*, 5:101, 2002.

I. Hadžić, K. Hanjalić, and D. Laurence. Modeling the response of turbulence subjected to cyclic irrotational strain. *Physics of fluids*, 13:1739, 2001.

K. Hanjalić. One point closure models for buoyancy-driven turbulent flows. *Annual Review of Fluid Mechanics*, 34(1):321–347, 2002.

K. Hanjalic and BE Launder. A reynolds stress model of turbulence and its application to thin shear flows. *J. Fluid Mech*, 52(4):609–638, 1972.

K. Hanjalic and BE Launder. Contribution towards a reynolds-stress closure for low-reynolds-number turbulence. *Journal of fluid mechanics*, 74(04):593–610, 1976.

K. Hanjalić, M. Popovac, and M. Hadžiabdić. A robust near-wall elliptic-relaxation eddy-viscosity turbulence model for CFD. *International Journal of Heat and Fluid Flow*, 25(6):1047–1051, 2004.

S. Hoyas and J. Jiménez. Reynolds number effects on the reynolds-stress budgets in turbulent channels. *Physics of Fluids*, 20, 2008.

G. Iaccarino. Prediction of the turbulent flow in a diffuser with commercial CFD codes. *Center for Turbulence Research, Annual Research Briefs*, pages 271–278, 2000.

K. Iwamoto, Y. Suzuki, and N. Kasagi. Reynolds number effect on wall turbulence: toward effective feedback control. *International journal of heat and fluid flow*, 23 (5):678–689, 2002.

S. Jakirlic and K. Hanjalic. A new approach to modelling near-wall turbulence energy and stress dissipation. *Journal of fluid mechanics*, 459(1):139–166, 2002.

YJ Jang, MA Leschziner, K. Abe, and L. Temmerman. Investigation of anisotropy-resolving turbulence models by reference to highly-resolved les data for separated flow. *Flow, turbulence and combustion*, 69(2):161–203, 2002.

WP Jones and BE Launder. The prediction of laminarisation with a two equation turbulence model. *International Journal of Heat and Mass Transfer*, 15(2):301–314, 1972.

J. Jovanovic, Q.Y. Ye, and F. Durst. Statistical interpretation of the turbulent dissipation rate in wall-bounded flows. *Journal of Fluid Mechanics*, 293:321–347, 1995.

G. Kalitzin, G. Medic, G. Iaccarino, and P. Durbin. Near-wall behavior of RANS turbulence models and implications for wall functions. *Journal of Computational Physics*, 204(1):265–291, 2005.

H.J. Kaltenbach, M. Fatica, R. Mittal, TS Lund, and P. Moin. Study of flow in a planar asymmetric diffuser using large-eddy simulation. *Journal of Fluid Mechanics*, 390:151–185, 1999.

N. Kasagi and M. Nishimura. Direct numerical simulation of combined forced and natural turbulent convection in a vertical plane channel. *International Journal of Heat and Fluid Flow*, 18(1):88–99, 1997.

H.T. Kim, SJ Kline, and WC Reynolds. The production of turbulence near a smooth wall in a turbulent boundary layer. *Journal of Fluid Mechanics*, 50(01):133–160, 1971.

J. Kim. On the structure of pressure fluctuations in simulated turbulent channel flow. *Journal of Fluid Mechanics*, 205(1):421–451, 1989.

SJ Kline, WC Reynolds, FA Schraub, and PW Runstadler. The structure of turbulent boundary layers. *J. Fluid Mech*, 30(4):741–773, 1967.

A.N. Kolmogorov. The local structure of turbulence in incompressible viscous fluid for very large reynolds numbers. In *Dokl. Akad. Nauk SSSR*, volume 30(4), pages 9–13, 1941.

A. Kuroda, N. Kasagi, and M. Hirata. Direct numerical simulation of turbulent plate couette-poiseuille flow: Effects of mean shear rate on the near-wall turbulence structures. *Turbulent Shear Flows*, 9:241–258, 1994.

BE Launder and BI Sharma. Application of the energy-dissipation model of turbulence to the calculation of flow near a spinning disc. *Letters in Heat and Mass Transfer*, 1(2):131–138, 1974.

BE Launder, GJ Reece, and W. Rodi. Progress in the development of a reynolds-stress turbulence closure. *Journal of Fluid Mechanics*, 68(03):537–566, 1975.

D. Laurence, J.C. Uribe, and S.V. Utyuzhnikov. A robust formulation of the $\overline{v^2} - f$ model. *Flow, Turbulence and Combustion*, 73(1):169–185, 2004.

Y. Lecocq. *Contribution l'analyse et la modlisation des coulements turbulents en rgime de convection mixte : application l'entreposage des dechets radioactifs*. PhD thesis, Universit de Poitiers, 2008.

F.S. Lien and P.A. Durbin. Non-linear $k - \varepsilon - \overline{v^2}$ modeling with application to high lift. In *Proceedings of the Summer Program, Center for Turbulence Research*, pages 5–26, 1996.

F.S. Lien and G. Kalitzin. Computations of transonic flow with the $\overline{v^2} - f$ turbulence model. *International Journal of Heat and Fluid Flow*, 22(1):53–61, 2001.

FS Lien, WL Chen, and MA Leschziner. Low-reynolds-number eddy-viscosity modelling based on non-linear stress-strain/vorticity relations. *Engineering turbulence modelling and experiments*, 3:91–100, 1996.

R. Manceau. *Modélisation de la turbulence. Prise en compte de l'influence des parois par relaxation elliptique.* PhD thesis, Université de Nantes, 1999.

R. Manceau and K. Hanjalić. A new form of the elliptic relaxation equation to account for wall effects in RANS modeling. *Physics of Fluids*, 12(9):2345–2351, 2000.

R. Manceau and K. Hanjalić. Elliptic blending model: A new near-wall Reynolds-stress turbulence closure. *Physics of Fluids*, 14(2):744–754, 2002.

R. Manceau, M. Wang, and D. Laurence. Inhomogeneity and anisotropy effects on the redistribution term in Reynolds-averaged Navier-Stokes modelling. *Journal of Fluid Mechanics*, 438:307–338, 2001.

R. Manceau, JR Carlson, and TB Gatski. A rescaled elliptic relaxation approach: Neutralizing the effect on the log layer. *Physics of Fluids*, 14(11):3868–3879, 2002a.

R. Manceau, S. Carpy, and D. Alfano. A rescaled $\overline{v^2} - f$ model: First application to separated and impinging flows. In W. Rodi and N. Fueyo, editors, *Proceedings of the 5^{th} International Symposium on Engineering Turbulence Modelling and Measurements, Mallorca, Spain, 16-18 September 2002*, pages 107–116. Elsevier Science, 2002b.

NN Mansour, J. Kim, and P. Moin. Reynolds-stress and dissipation-rate budgets in a turbulent channel flow. *Journal of Fluid Mechanics*, 194(1):15–44, 1988.

F.R. Menter. Two-equation eddy-viscosity turbulence models for engineering applications. *AIAA journal*, 32(8):1598–1605, 1994.

R.D. Moser, J. Kim, and N.N. Mansour. Direct numerical simulation of turbulent channel flow up to re= 590. *Physics of Fluids*, 11:943, 1999.

Y. Nagano and M. Tagawa. An improved k-ε model for boundary layer flows. *Journal of fluids engineering*, 112(1):33–39, 1990.

D. Naot, A. Shavit, and M. Wolfshtein. Interactions between components of the turbulent velocity correlation tensor due to pressure fluctuations(interactions between components of turbulent flow velocity correlation tensor due to pressure fluctuations). *Israel Journal of Technology*, 8(3):259–269, 1970.

S. Obi, K. Aoki, and S. Masuda. Experimental and computational study of turbulent separating flow in an asymmetric plane diffuser. In *Ninth Symposium on Turbulent Shear Flows, Kyoto, Japan*, page 305, 1993.

K. Osman. Adaptive wall functions for convective heat transfer simulations with an industrial code. Master's thesis, The University of Manchester, 2011.

S. Parneix and P. Durbin. Numerical simulation of 3D turbulent boundary layer using the $\overline{v^2} - f$ model. *Annual Research Briefs, Center for Turbulence Research, NASA Ames/Stanford University*, pages 135–148, 1997.

S. Parneix, D. Laurence, and P. Durbin. Second moment closure analysis of the backstep flow database. In *Proceedings of the Summer Program, Center for Turbulence Research*, pages 47–66, 1996.

V.C. Patel, W. Rodi, and G. Scheuerer. Turbulence models for near-wall and low Reynolds number flows- A review. *AIAA journal*, 23(9):1308–1319, 1985.

BA Pettersson-Reif, TB Gatski, and CL Rumsey. On the behavior of two-equation models in nonequilibrium homogeneous turbulence. *Physics of Fluids*, 18, 2006.

S.B. Pope. *Turbulent flows*. Cambridge Univ. Press, 2008.

M Popovac. Conjugate heat transfer simulations using zero wall boundary condition eddy viscosity turbulence model with elliptic relaxation. In *Proceedings of the* 8^{th}

International Symposium on Engineering Turbulence Modelling and Mesurements, pages 958–964, 2010.

L. Prandtl. Bericht
"uber untersuchungen zur ausgebildeten turbulenz. *Z. Angew. Math. Mech*, 5(2): 136–139, 1925.

G. Rau, M. Cakan, D. Moeller, and T. Arts. The effect of periodic ribs on the local aerodynamic and heat transfer performance of a straight cooling channel. *Journal of turbomachinery*, 120:368, 1998.

AJ Revell, S. Benhamadouche, T. Craft, and D. Laurence. A stress-strain lag Eddy viscosity model for unsteady mean flow. *International Journal of Heat and Fluid Flow*, 27(5):821–830, 2006.

CM Rhie and WL Chow. A numerical study of the turbulent flow past an isolated airfoil with trailing edge separation. In *American Institute of Aeronautics and Astronautics and American Society of Mechanical Engineers, Joint Thermophysics, Fluids, Plasma and Heat Transfer Conference, 3 rd, St. Louis, MO*, pages 1525–1532, 1982.

LF Richardson. Weather prediction by numerical processes, 1922.

W. Rodi and NN Mansour. Low reynolds number k—ε modelling with the aid of direct simulation data. *Journal of Fluid Mechanics*, 250(1):509–529, 1993.

J. Rotta. Statistische theorie nichthomogener turbulenz. *Zeitschrift f
"ur Physik A Hadrons and Nuclei*, 129(6):547–572, 1951. ISSN 0939-7922.

P. Sagaut. *Large eddy simulation for incompressible flows: an introduction*. Springer Verlag, 2006.

J.K. Shin, J.S. An, Y.D. Choi, Y.C. Kim, and M.S. Kim. Elliptic relaxation second moment closure for the turbulent heat fluxes. *Journal of Turbulence*, 9(3):1–29, 2008.

J. Smagorinsky. General circulation experiments with the primitive equations. *Monthly weather review*, 91(3):99–164, 1963.

P.R. Spalart. Detached-eddy simulation. *Annual Review of Fluid Mechanics*, 41: 181–202, 2009.

P.R. Spalart and S.R. Allmaras. A one-equation turbulence model for aerodynamic flows. *La recherche aérospatiale*, 1(1):5–21, 1994.

CG Speziale, S. Sarkar, and TB Gatski. Modelling the pressure-strain correlation of turbulence: an invariant dynamical system approach. *Journal of Fluid Mechanics*, pages 245–272, 1991.

A. Sveningsson, B.A. Pettersson-Reif, and L. Davidson. Modelling the entrance region in a plane asymmetric diffuser by elliptic relaxation. In *Proceedings of the* 4^{th} *International Symposium on Turbulence and Shear Flow Phenomena, Williamsburg, VA, USA*, 2005.

L. Temmerman and MA Leschziner. Large eddy simulation of separated flow in a streamwise periodic channel constriction. In *Int. Symp. Turb. Shear Flow Phenomena, Stockholm, Sweden*, 2001.

H. Tennekes and J.L. Lumley. *A first course in turbulence*. MIT press, 1999.

S. Tieszen, A. Ooi, P. Durbin, and M. Behnia. Modeling of natural convection heat transfer. In *Proceedings of the Summer Program, Center for Turbulence Research*, pages 287–302, 1998.

J.C. Uribe. *An industrial approach to near wall turbulence modelling for unstructured finite volume method*. PhD thesis, The University of Manchester, 2006.

J.C. Uribe, N. Jarrin, R. Prosser, and D. Laurence. Development of a Two-velocities Hybrid RANS-LES Model and its Application to a Trailing Edge Flow. *Flow, Turbulence and Combustion*, 85(2):181–197, 2010.

E.R. van Driest. On turbulent flow near a wall. *J. Aerospace Sci.*, 23:1007–1011, 1956.

TAM Versteegh and FTM Nieuwstadt. Turbulent budgets of natural convection in an infinite, differentially heated, vertical channel. *International Journal of Heat and Fluid Flow*, 19(2):135–149, 1998.

T. von Karman. Mechanical similitude and turbulence. *NACA TM*, 611, 1931.

S. Wallin and A.V. Johansson. An explicit algebraic Reynolds stress model for incompressible and compressible turbulent flows. *Journal of Fluid Mechanics*, 403: 89–132, 2000.

D.C. Wilcox. Simulation of transition with a two-equation turbulence model. *AIAA journal*, 32(2):247–255, 1994.

D.C. Wilcox. *Turbulence modeling for CFD*. DCW industries La Canada, CA, 2006.

V. Wizman, D. Laurence, M. Kanniche, P. Durbin, and A. Demuren. Modeling near-wall effects in second-moment closures by elliptic relaxation. *International Journal of Heat and Fluid Flow*, 17(3):255–266, 1996.

Appendix A

Introduction to code saturne

The code used in this work is *Code_Saturne* (Archambeau et al., 2004; Fournier et al., 2011)[1]. It is a finite-volume unstructured code developed by EDF (Electricité de France) to solve CFD problems. The code solves Navier-Stokes equations for two- and three-dimensional flows, steady or transient, single phase, laminar or turbulent, incompressible or slightly compressible, and also solves the transport equations for the temperature, enthalpy or passive scalar and their fluctuations. The code features many other components to handle a wide range of physical problems, such as a Lagrangian module or a model for combustion. The turbulence models available are: the standard $k-\varepsilon$, with or without linear production (variant of Guimet and Laurence (2002)), $k-\omega-SST$, Second moment closure (models of Launder et al. (1975) and Speziale et al. (1991)), v^2-f (URI06 and newly added BL-$\overline{v^2}/k$ version) and LES (both standard and dynamic sub-grid scale model of Germano et al. (1991)).

With the finite-volume method (FVM), the equations are solved over control volumes, and the velocity and pressure are both considered at the cells centre (collocated arrangement). The finite-volume method consists in writing the equations in a conservative form and integrating them over control volumes. Gauss' theorem is used to transform volume integrals of convective and diffusive flux divergence into surface integral of the fluxes over the cell faces. The conservative form of the momentum equation reads (the equation is cast into a tensorial form to highlight later use of the

[1]The code is open source and available at `www.code-saturne.org`

divergence operator)[2]:

$$\frac{\partial u}{\partial t} + \underline{div}(\underline{u} \otimes \rho\underline{u}) = \underline{div}(-P\rho\underline{\underline{Id}} + \mu_{eff}(\underline{\underline{grad}}(\underline{u}) + {}^{t}\underline{\underline{grad}}(\underline{u}))) \tag{A.1}$$

where the effective dynamic viscosity μ_{eff} represents the sum of the molecular viscosity and an eddy or sub-grid scale viscosity if a linear EVM or an LES model is used. The time discretisation is achieved through a fractional-step scheme (Euler implicit) that can be associated with the SIMPLEC method. At each time step n, the momentum equation is first solved with the pressure taken explicitly. The predicted velocity $\underline{u}^{n+\frac{1}{2}}$ is then modified by the corrector step, in order to yield a divergence free field.

A.1 The prediction step

In this step, the following equation is solved (an Euler implicit scheme is used here):

$$\rho\frac{\underline{u}^{n+\frac{1}{2}} - \underline{u}^{n}}{\Delta t} + \underline{div}(\underline{u}^{n+\frac{1}{2}} \otimes (\rho\underline{u})^{n}) = \underline{div}(-P^{n}\underline{\underline{Id}} + \mu_{eff}(\underline{\underline{grad}}(\underline{u}^{n+\frac{1}{2}}) + {}^{t}\underline{\underline{grad}}(\underline{u}^{n}))) \tag{A.2}$$

It is worth mentioning that the mass flux $(\rho\underline{u})^n$ on the left hand side is taken explicitly in order to uncouple the 3 components of the velocity. In the FVM framework the domain Ω is split into control volumes Ω_i. Let S_{ij} be defined as $S_{ij} = \partial\Omega_i \bigcap \partial\Omega_j$ the common face to Ω_i and Ω_j , and $S_{b_{ik}}$ the k^{th} boundary face of $\partial\Omega_i \bigcap \partial\Omega$ as represented in Fig. A.1. $\underline{S_{ij}}$ is the vector $S_{ij}\underline{n}$ with $\underline{n}$ being the outward unitary face-normal direction. I and J are the centres of cell i and j and I' and J' are the projections of I and J onto the line (F,$\underline{\text{n}}$) (F being the face center).

A.1.1 The convection term

The volume integral $\int_{\Omega_i} \underline{div}(\underline{u}^{n+\frac{1}{2}} \otimes (\rho\underline{u})^{n})$ is transformed, using the Gauss' theorem, into $\int_{\partial\Omega_i} (\underline{u}^{n+\frac{1}{2}} \otimes (\rho\underline{u})^{n}).\underline{dS}$. The discretisation over the faces of Ω_i reads:

$$\sum_{j \in Neigh(i)} [(\rho\underline{u}_{ij}^{n}).\underline{S}_{ij}]\underline{u}_{f,ij}^{n+\frac{1}{2}} + \sum_{k \in \gamma_b(i)} [(\rho\underline{u}_{b_{ik}}^{n}).\underline{S}_{b_{ik}}]\underline{u}_{f,b_{ik}}^{n+\frac{1}{2}} \tag{A.3}$$

[2]In this section u and P respectively denote the velocity and the pressure solved by the code.

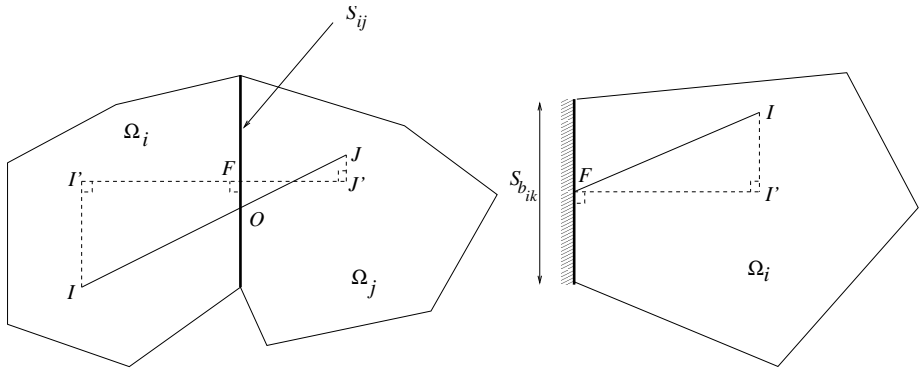

Figure A.1: Representation of a cell and a boundary face

The terms $(\rho \underline{u}_{ij}^n).\underline{S}_{ij}$ and $(\rho \underline{u}_{b_{ik}}^n).\underline{S}_{b_{ik}}$ stand for the mass fluxes expressed on inner faces and boundary faces respectively. $Neigh(i)$ is the set of neighbouring cells of cell i and $\gamma_b(i)$ the set of boundary faces of cell i. The unknown terms $\underline{u}_{f,ij}^{n+\frac{1}{2}}$ and $\underline{u}_{f,b_{ik}}^{n+\frac{1}{2}}$ are expressed at the face centre and have to be related to the values of the variables expressed at the cell centre. *Code_Saturne* uses three schemes to compute these unknowns:

- The UPWIND scheme (first order) :
  $\underline{u}_{f,ij}^{n+\frac{1}{2}} = \underline{u}_I^{n+\frac{1}{2}}$ if $(\rho \underline{u}_{ij}^n).\underline{S}_{ij} \geqslant 0$
  $\underline{u}_{f,ij}^{n+\frac{1}{2}} = \underline{u}_J^{n+\frac{1}{2}}$ if $(\rho \underline{u}_{ij}^n).\underline{S}_{ij} < 0$

- The second-order centred scheme :
  $\underline{u}_{f,ij}^{n+\frac{1}{2}} = \alpha_{ij} \underline{u}_I^{n+\frac{1}{2}} + (1-\alpha_{ij}) \underline{u}_J^{n+\frac{1}{2}} + \frac{1}{2}(\underline{\underline{grad}}(\underline{u}^{n+\frac{1}{2}})_I + \underline{\underline{grad}}(\underline{u}^{n+\frac{1}{2}})_J).\underline{OF}$, using $\alpha_{ij} = \frac{\overline{FJ'}}{\overline{I'J'}}$ (see Fig. A.1)

- The Second Order Linear Upwind scheme :
  $\underline{u}_{f,ij}^{n+\frac{1}{2}} = \underline{u}_I^{n+\frac{1}{2}} + \underline{IF}.\underline{\underline{grad}}(\underline{u}^{n+\frac{1}{2}})_I$ if $(\rho \underline{u}_{ij}^n).\underline{S}_{ij} \geqslant 0$
  $\underline{u}_{f,ij}^{n+\frac{1}{2}} = \underline{u}_J^{n+\frac{1}{2}} + \underline{JF}.\underline{\underline{grad}}(\underline{u}^{n+\frac{1}{2}})_J$ if $(\rho \underline{u}_{ij}^n).\underline{S}_{ij} < 0$

When the mesh features non-orthogonality ($I \neq I'$) the computation of gradients uses a reconstruction technique. It is an iterative process. At the boundaries, the value of the predicted velocity is always given by : $\underline{u}_{f,b_{ik}}^{n+\frac{1}{2}} = \underline{u}_I^{n+\frac{1}{2}}$ if $(\rho \underline{u}_{b_{ik}}^n).\underline{S}_{b_{ik}} \geqslant 0$ and $\underline{u}_{f,b_{ik}}^{n+\frac{1}{2}} = \underline{u}_{b_{ij}}^{n+\frac{1}{2}}$ if $(\rho \underline{u}_{b_{ik}}^n).\underline{S}_{b_{ik}} < 0$.

The default scheme used by the code is a blending between the second-order scheme and the UPWIND scheme. To enhance stability, a slope test enables to locally switch from second-order to first-order scheme without blending.

A.1.2 The diffusion term

In the FVM the discretisation of the diffusion term $\int_{\partial\Omega_i} \underline{div}(\mu_{eff}\underline{\underline{grad}}(\underline{u}^{n+\frac{1}{2}}))$ reads:

$$\sum_{j\in Neigh(i)} \mu_{eff}\frac{\underline{u}_{J'}^{n+\frac{1}{2}} - \underline{u}_{I'}^{n+\frac{1}{2}}}{\underline{I'J'}}S_{ij} + \sum_{k\in\gamma_b(i)} \mu_{eff}\frac{\underline{u}_{b_{ik}}^{n+\frac{1}{2}} - \underline{u}_{I'}^{n+\frac{1}{2}}}{\underline{I'F'}}S_{b_{ik}} \tag{A.4}$$

This way of discretising the diffusion term does not cause any problem on orthogonal meshes (if $I = I'$) . Otherwise, as done for the convection term, reconstruction techniques are used.

The value of the velocity at the boundaries $\underline{u}_{fb_{ik}}^{n+\frac{1}{2}}$ is a function of the velocity in the adjacent cell I and the boundary conditions given by the user.

This discretisation leads to a system to be solved for each component of the velocity, which is not linear in general (firstly because of the non orthogonalities of the mesh, secondly in case of slope tests for the convection term). An iterative process is then used.

A.2 The correction step

The correction step consists in solving a Poisson equation to compute the pressure in order to produce a corrected velocity field $\underline{u}^{n+1}$ which is divergence free. The pressure P^n is updated by adding an increment δP^{n+1}:

$$P^{n+1} = P^n + \delta P^{n+1} \tag{A.5}$$

($\delta P^{n+1} = P^{n+1} - P^n$). The following problem has to be solved (the convection and diffusion of the velocity difference are neglected):

$$\begin{cases} \dfrac{(\rho\underline{u})^{n+1} - (\rho\underline{u})^{n+\frac{1}{2}}}{\Delta t} = -\underline{grad}\delta P^{n+1} \\ \underline{div}(\rho\underline{u})^{n+1} = 0 \end{cases} \tag{A.6}$$

The divergence operator is applied to the first line of Eq. A.6 which yields the equation to be solved:

$$\underline{div}(\Delta t \underline{grad} \delta P^{n+1}) = \underline{div}(\rho \underline{u})^{n+\frac{1}{2}} \tag{A.7}$$

With the usual discretisation of the Laplacien operator, odd and even nodes are uncoupled, leading to the well known chessboard-like pressure field. In order to alleviate this problem, the Rhie & Chow filter (Rhie and Chow, 1982) is used. Once δP^{n+1} is obtained the velocity at time step $n+1$ is then updated.

A.3 The turbulence variables

For the resolution of the turbulent variables equations, the discretisation of the convective and diffusive fluxes is the same as those for the velocity. In RANS mode, a first-order Euler implicit time scheme is used for all the variables.

A.4 The steady state algorithm

In *Code_Saturne* RANS calculations can be performed using the steady state algorithm when a steady solution is expected. When this algorithm is used, the user can define relaxation coefficient α_v for each variable v. The main differences with the unsteady algorithm are:

- The unsteady term $\partial/\partial t$ is removed for all variables.
- For the resolution of each variable v, in the discretisation of the convective (Eq. A.3) and diffusive (Eq. A.4) fluxes, the value of v_I^{n+1} is replaced by $\alpha_v v_I^{n+1} + (1-\alpha^v) v_I^n$ [3] and the diagonal of the matrix M_{ij} of the resulting linear system is relaxed (*i.e.* the terms M_{ii} are replaced by M_{ii}/α_v)
- At the end of the correction step, the pressure update Eq. A.5 now becomes $P^{n+1} = P^n + \alpha_P \delta P^{n+1}$

[3] the term v_J^{n+1} appearing in the discretisation of the convective flux (for an upwind scheme when $(\rho \underline{u}_{ij}^n)\underline{S}_{ij} < 0$) and of the diffusive flux is not relaxed however.

Appendix B

The $k-\omega$ SST model

The version of the model presented here is the one which is implemented in *Code_Saturne* and whose results are presented in this work.

$$\frac{Dk}{Dt} = min(P, 10C_\mu k\omega) - C_\mu k\omega + \frac{\partial}{\partial x_j}\left[\left(\nu + \frac{\nu_t}{\sigma_k}\right)\frac{\partial k}{\partial x_j}\right] \tag{B.1}$$

$$\frac{D\omega}{Dt} = \alpha\frac{P}{\nu_t} - \beta\omega^2 + \frac{\partial}{\partial x_j}\left[\left(\nu + \frac{\nu_t}{\sigma_\omega}\right)\frac{\partial \omega}{\partial x_j}\right] + 2\frac{1-F_1}{\sigma_{\omega 2}}\frac{1}{\omega}\frac{\partial k}{\partial x_j}\frac{\partial \omega}{\partial x_j} \tag{B.2}$$

where :

$$\alpha = F_1\alpha_1 + (1-F_1)\alpha_2 \tag{B.3}$$

$$\beta = F_1\beta_1 + (1-F_1)\beta_2 \tag{B.4}$$

$$\sigma_k = F_1\sigma_{k1} + (1-F_1)\sigma_{k2} \tag{B.5}$$

$$\sigma_\omega = F_1\sigma_{\omega 1} + (1-F_1)\sigma_{\omega 2} \tag{B.6}$$

The blending function F_1 is given by the formula:

$$F_1 = tanh(arg_1^4) \tag{B.7}$$

$$arg_1 = min\left[max\left(\frac{\sqrt{k}}{C_\mu \omega y}, \frac{500\nu}{y^2\omega}\right), \frac{4\rho k}{\sigma_{\omega 2} CD_{k\omega} y^2}\right] \tag{B.8}$$

$$CD_{k\omega} = max\left(2\rho \frac{1}{\sigma_{\omega 2}\omega}\frac{\partial k}{\partial x_j}\frac{\partial \omega}{\partial x_j}, 10^{-20}\right) \tag{B.9}$$

$$\nu_t = \frac{a_1 k}{max(a_1\omega, SF2)} \tag{B.10}$$

$$F_2 = tanh(arg_2^2) \tag{B.11}$$

$$arg_2 = max\left(\frac{2\sqrt{k}}{C_\mu \omega y}, \frac{500\nu}{y^2\omega}\right) \tag{B.12}$$

$$S = \sqrt{2S_{ij}S_{ij}} \tag{B.13}$$

α_1	α_2	β_1	β_2	σ_{k1}	σ_{k2}	$\sigma_{\omega 1}$	$\sigma_{\omega 2}$
$\frac{\beta_1}{C_\mu} - \frac{\kappa^2}{\sigma_{\omega 1}\sqrt{C_\mu}}$	$\frac{\beta_2}{C_\mu} - \frac{\kappa^2}{\sigma_{\omega 2}\sqrt{C_\mu}}$	0.075	0.0828	1.176	2	2	1.1682

a_1	C_μ	κ
0.31	0.09	0.41

Appendix C

The Kolmogorov time-scale lower bound

In the $\overline{v^2} - f$ modelling framework, the time-scale is involved in the ε equation, Eq. 4.13, as well as in the expression for the turbulent viscosity ν_t, Eq. 3.37, and in the return-to-isotropy model for the slow part of the pressure-strain rate term of $\overline{v^2}$,Tab. 4.2. Here a different notation is adopted for each use of the time-scale and the equations read as follows:

$$\begin{cases} \dfrac{D\varepsilon}{Dt} = C_{\varepsilon 1}\dfrac{P}{T_1} - C_{\varepsilon 2}\dfrac{\varepsilon}{T_2} + \dfrac{\partial}{\partial x_j}\left[\left(\nu + \dfrac{\nu_t}{\sigma_\varepsilon}\right)\dfrac{\partial \varepsilon}{\partial x_j}\right] \\ \nu_t = C_\mu \overline{v^2} T_\mu \\ \phi_{22}^s = -C_1 \dfrac{1}{T_{\overline{v^2}}}\left(\overline{v^2} - \dfrac{2}{3}k\right) \end{cases} \tag{C.1}$$

To avoid a singularity at the wall the following choice is made in most $\overline{v^2} - f$ models:

$$T_2 = \max\left(\frac{k}{\varepsilon}, C_T\sqrt{\frac{\nu}{\varepsilon}}\right) \tag{C.2}$$

whereas in the BL-$\overline{v^2}/k$ model Eq. 4.15 is used instead. In all models this modified time-scale is bounded by its Kolmogorov counterpart, $C_T\sqrt{\dfrac{\nu}{\varepsilon}}$, which is used in the near-wall region where $k/\varepsilon \to 0$. However in all models this Kolmogorov time-scale limiter is also used in T_1, T_μ and $T_{\overline{v^2}}$ for the sake of consistency. As seen in a channel flow, the time-scale equals the Kolmogorov expression only in a small region very near

the wall (for $y^+ < 3$ for most models, as seen in Tab. 4.7), unlike the length-scale, for which the switch between the Kolmogorov and the integral expression may occur in the log layer. This tends to minimise the importance of the Kolmogorov time-scale limiter at least in the channel flow case. In order to understand the implications of including or not the limiter in T_1 and T_μ, the case of homogeneous sheared turbulence is studied, with a focus on the behaviour of the model for very low values of turbulence. In the present analysis we use the expression Eq. 4.14 for T so as to remain in the general framework of $\overline{v^2} - f$ modelling, but it is believed that the same conclusions will hold when the alternative expression for the scales, Eq. 4.15, is chosen, as in the BL-$\overline{v^2}/k$ model.

For simplicity, the variable $\overline{v^2}$ is taken as constant $\overline{v^2} = \varphi_\infty k$ with $\varphi_\infty = 0.4$[1] and the simpler $k - \varepsilon$ system is considered. Evolution equations can be derived for the turbulent Reynolds number defined as $Re_t = \dfrac{k^2}{\nu\varepsilon}$ and the turbulent to mean strain-rate time-scale ratio $\eta = S\dfrac{k}{\varepsilon}$. Rewriting

$$\max\left(\frac{k}{\varepsilon}, C_T\sqrt{\frac{\nu}{\varepsilon}}\right) = \frac{k}{\varepsilon}\max\left(1, C_T Re_t^{-1/2}\right) \tag{C.3}$$

the evolution equations of Re_t and η (with respect to $t^* = St$) read:

$$\begin{cases} \dfrac{dRe_t}{dt^*} = 2Re_t\eta C_\mu F_\mu - 2\dfrac{Re_t}{\eta} - C_{\varepsilon 1}C_\mu\dfrac{F_\mu}{F_1}Re_t\eta + \dfrac{C_{\varepsilon 2}Re_t}{F_2\eta} \\ \dfrac{d\eta}{dt^*} = C_\mu F_\mu\eta^2 - 1 - C_{\varepsilon 1}C_\mu\dfrac{F_\mu}{F_1}\eta^2 + \dfrac{C_{\varepsilon 2}}{F_2} \end{cases} \tag{C.4}$$

The functions F_i can be either 1 or $\max(1, C_T Re_t^{-1/2})$. The system evolution is represented on Fig. C.1, Fig. C.2 and Fig. C.3 which show, for different choices for the F_i functions, the stream-lines of the vector field $(\dfrac{\partial\eta}{\partial t^*}, \dfrac{\partial Re_t}{\partial t^*})$ in the plane $(\eta; Re_t)$. The Re_t (resp. η) nullclines are the set of points $(\eta; Re_t)$ for which $\dfrac{\partial Re_t}{\partial t^*} = 0$ (resp. $\dfrac{\partial\eta}{\partial t^*} = 0$) and are represented by thick straight (resp. dashed) line. Possible finite equilibrium exist if the nullclines intersect and the eigenvalues of the Jacobian at the intersection point are both negatives. 5 of the 8 possible cases are here considered:

[1] this value is of the same order as those taken by models in this type of flows, as given in Tab. 4.9

- Case A: $(F_\mu, F_1, F_2) = (1; 1; 1)$ (configuration of the standard $k - \varepsilon$ system) (Fig. C.1, left)
- Case B: $(F_\mu, F_1, F_2) = (1, 1, \max(1, C_T Re_t^{-1/2}))$ (Fig. C.1, right)
- Case C: $(F_\mu, F_1, F_2) = (1; \max(1, C_T Re_t^{-1/2}); \max(1, C_T Re_t^{-1/2}))$ (Fig. C.2, left)
- Case D: $(F_\mu, F_1, F_2) = (\max(1, C_T Re_t^{-1/2}); 1; \max(1, C_T Re_t^{-1/2}))$(Fig. C.2, right)
- Case E: $(F_\mu, F_1, F_2) = (\max(1, C_T Re_t^{-1/2}); \max(1, C_T Re_t^{-1/2}); \max(1, C_T Re_t^{-1/2}))$ (configuration used by the $\overline{v^2} - f$ model) (Fig. C.3)

As pointed out in Pettersson-Reif et al. (2006) the situation $(Re_t \to 0; \eta \to \infty)$ characterises a proper laminar solution, whereas $(Re_t \to 0; \eta \to 0)$ corresponds to a pseudo-laminar state, recalling that the expected solution in homogeneous sheared turbulence is $(Re_t \to \infty; \eta \to C^{ste})$. It was shown by the same authors that some modifications of the coefficients, such as the sensitivity of $C_{\varepsilon 2}$ to Re_t, could lead to a pseudo laminar stable solution.

At light of the plots it can be seen that with the $\overline{v^2} - f$ model (Fig C.3) there is a region of initial conditions from which there is convergence to the point ($\eta = 0$,$Re_t = 0$) (pseudo laminar state), unlike the standard $k - \varepsilon$. Alternatives choices for the F_i functions which also prevent the ε equation singularity are all configurations for which $F_2 = \max(1, C_T Re_t^{-1/2})$ (Case B, C, D, E) and for all of them there is a region of initial conditions which lead to pseudo laminar state, but respective phase planes are rather different from each other for large values of η and low values of Re_t.

Further investigation on this matter (low Reynolds number limit of the $\overline{v^2} - f$ model) should be worthwhile, particularly if there is an interest in extending the approach to transition modelling.

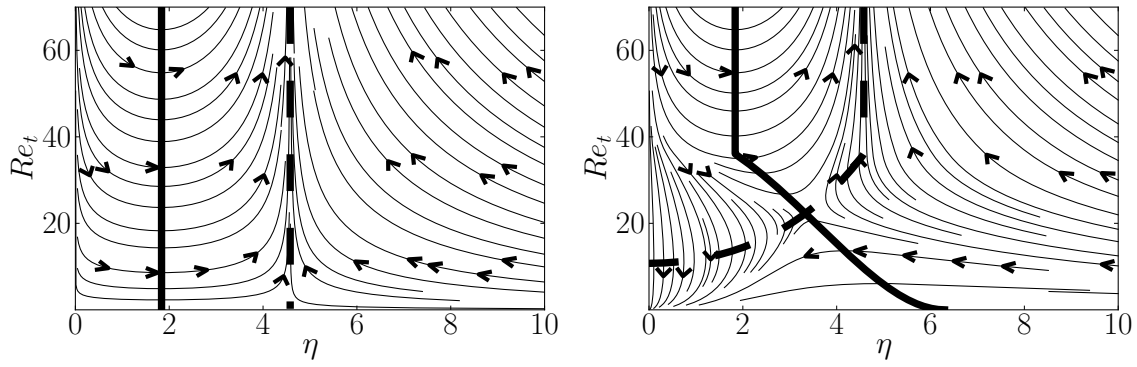

Figure C.1: Nullclines of the system C.4 with Case A ($k-\varepsilon$) (left) and Case B (right)

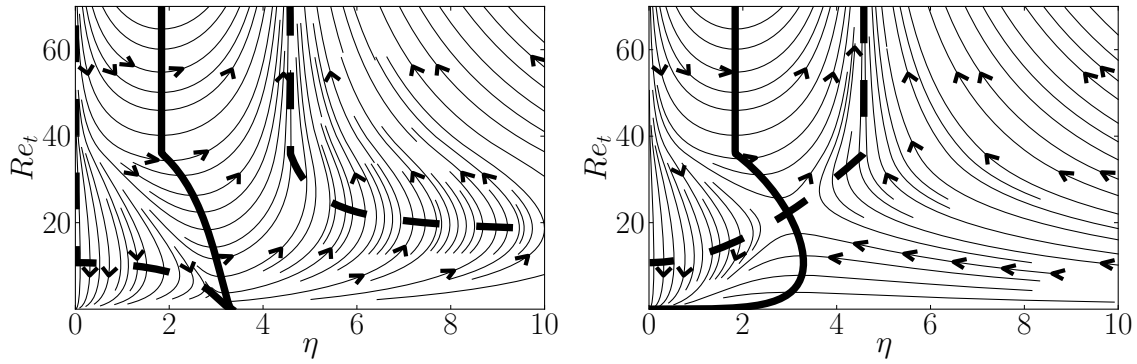

Figure C.2: Nullclines of the system C.4 with Case C (left) and Case D (right)

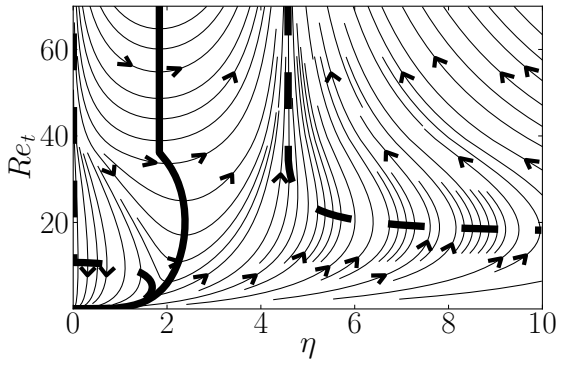

Figure C.3: Nullclines of the system C.4 with Case E ($\overline{v^2} - f$)

Appendix D

Article submitted to: International Journal of Heat and Fluid Flow in 2011

A robust $k-\varepsilon-v^2/k$ elliptic blending turbulence model applied to near-wall, separated and buoyant flows[1]

F. Billard[a,*], D. Laurence[a,b]

[a] *School of Mechanical, Aerospace and Civil Engineering, University of Manchester, George Begg Building, Sackville Street, Manchester, M13 9PL, UK*
[b] *EDF R&D MFEE, 6 quai Watier, 78401 Chatou, France*

Abstract

This paper first reconsiders evolution over 20 years of the k-epsilon-v2-f strand of eddy-viscosity models, developed since P. Durbin's 1991 original proposal for a near-wall eddy viscosity model based on the physics of the full Reynolds stress transport models, but retaining only the wall-normal fluctuating velocity variance, v2, and its source, f, the redistribution by pressure fluctuations. Added to the classical k-epsilon (turbulent kinetic energy and dissipation) model, this resulted in three transport equations for k, epsilon and v2, and one elliptic equation for f, which accurately reproduced the parabolic decay of v2/k down to the solid wall without introducing wall-distance or low-Reynolds number related damping functions in the eddy viscosity and k-epsilon equations. However, most v2-f variants have suffered from numerical stiffness making them unpractical for industrial or unsteady RANS applications, while the one version available in major commercial codes tends to lead to degraded and sometimes unrealistic solutions. After considering the rationale behind a dozen variants and asymptotic behaviour of the variables in a number of zones (balance of terms in the channel flow viscous sublayer, logarithmic layer and wake region, homogenous flows and high Reynolds number limits), a new robust version is proposed, which is applied to a number of cases involving flow separation and heat transfer. This k-epsilon type of model with v2/k anisotropy blends high Reynolds number and near-wall forms using two dimensionless parameters: the wall-normal anisotropy v2/k and a dimensionless parameter alpha resulting from an elliptic equation to blend the homogeneous and near-wall limiting expressions of f. The review of variants and asymptotic cases has also led to modifications of the epsilon equation: the second derivative of mean velocity is reintroduced as an extra sink term to retard turbulence growth in the transition layer (i.e. embracing the E term of the Jones and Launder (1972) k-epsilon model), the homogeneous part of epsilon is now adopted as main transported variable (as it is less sensitive to the Reynolds number effects), and the excessive growth of the turbulent length-scale in the absence of production is corrected (leading to a better distinction between log layer and wake region of a channel flow). For each modification numerical stability implications are carefully considered and, after implementation in an industrial finite-volume code, the final model proved to be significantly more robust than any of the previous variants.

Keywords: RANS, turbulence modelling review, channel flow buffer, logarithmic and defect layer, near-wall effects, heat transfer, unstructured finite volume method

1. Introduction

The refined modelling of wall effects in the Reynolds Averaged Navier Stokes (RANS) framework is a topic currently revitalised as Large Eddy Simulation (LES) and related "hybrid RANS-LES" approaches become increasingly popular and progress from low (quasi-DNS) to high Reynolds wall-bounded flows. Indeed, because resolution of wall structures by LES would require very expensive meshes (of size $\approx Re^{1.8}$, c.f. Chapman (1979)), in practice, wall turbulence is modelled using a RANS approach in the framework of hybrid methodologies (review in Fröhlich and von Terzi (2008)). To this end, many types of near-wall RANS models have been used, from one equation to full Reynolds Stress models (RSM): to name but a few, the $\overline{v^2}-f$ model is chosen in the method of Uribe et al. (2010) whereas the PITM method of Chaouat

[1] For reference update please check here: `http://cfd.mace.manchester.ac.uk/twiki/bin/view/CfdTm/ResPub257`

* Corresponding author. Tel: +44 (0) 161 306 3730; fax: +44 (0) 161 200 3723.
Email address: `flavien.billard@manchester.ac.uk` (F. Billard)

and Schiestel (2009) relies on the RSM of Launder and Shima (1989), the Elliptic Blending RSM (EBRSM) (Manceau and Hanjalić (2002)) is used in the seamless approach of Fadai-Ghotbi et al. (2010) and the (D)DES (Spalart (2009)) or the Scale Adaptive Simulation of Menter and Egorov (2005) are based on the $k-\omega$ SST model (Menter (1994)).

Certainly the high popularity of the two latter hybrid approaches is closely related to the simplicity and robustness of the SST model, which has facilitated full scale industrial applications, *e.g.* complete aircrafts. Still, the latter model carries a certain amount of empiricism, as acknowledged by the author himself (Menter (1994)), and it features several empirical functions following the trend of many near-wall models (Patel et al. (1985)). Over time, and as computing power persistently grows the question as to what is the best trade-off between cost, accuracy and robustness should be revisited. The aim of the present work is to try to devise an equivalently simple and robust approach on somehow sounder physical bases: the $\overline{v^2}-f$ model (Durbin (1991)). Its formulation inherits the minimalism of eddy viscosity models and naturally integrates wall turbulence "damping" by using the wall-normal fluctuations $\overline{v^2}$ as additional scale. However it also models non-local effects of the fluctuating pressure on the turbulent fields and separately represents wall blockage effects and low Reynolds number effects.

While the number of research groups focussing on RANS modelling has dwindled over the past 20 years, a notable part of the work has been carried out in the framework of elliptic relaxation based models, leading to several versions of the $\overline{v^2}-f$ model, which will be compared in the present article. In the first section, the pros and cons of each formulation are weighted, with focus on both stability and accuracy issues. This is followed by the presentation of the new model proposal. Lastly its performances are compared to the $k-\omega$ SST model and the most widely used version of the $\overline{v^2}-f$ model. The cases under consideration are two-dimensional pressure induced separating flows as well as a case of buoyancy impaired turbulence. Some three-dimensional applications are also presented. More test cases have been successfully considered, particularly for heat transfer as this is one of the areas where the original $\overline{v^2}-f$ model has been most successful, but these will be reported elsewhere: the main objective of the present paper is to propose an optimal formulation of the $\overline{v^2}-f$ type of Eddy Viscosity Model (EVM).

2. The $\overline{v^2}-f$ models

2.1. Presentation of the approach:

The model stems from the standard $k-\varepsilon$ system (with some low Reynolds number corrections added to the dissipation rate ε transport equation) and a third transport equation is solved for a scalar $\overline{v^2}$, which can be assimilated near solid walls to the wall-normal fluctuations responsible for turbulent heat and momentum transfer from the wall to the core of the flow. The $\overline{v^2}$ equation follows the classical transport equation of the wall-normal Reynolds stress component. To facilitate presentation of modelling concepts, y, v, ε_{22} and ϕ^*_{22} represent the wall-distance and the wall-normal component of the fluctuating velocity, the dissipation rate and the pressure-strain[2] tensors, but this does not require programming the model in a boundary fitted coordinate system as it remains at EVM level using only scalars as turbulence characterising variables. The difference between ϕ^*_{22} and ε_{22} is modelled as a whole (ν is the kinematic molecular viscosity):

$$\phi^*_{22}-\varepsilon_{22}=-\frac{2}{\rho}\overline{v\frac{\partial p}{\partial y}}-2\nu\overline{\frac{\partial v}{\partial x_k}\frac{\partial v}{\partial x_k}}=\varphi_{22}-\varepsilon\frac{\overline{v^2}}{k} \tag{1}$$

and $\varphi_{22}=kf$ where f is solution of an elliptic equation:

$$f-L^2\partial_j\partial_j f=f_h \tag{2}$$

L is a turbulent length-scale and f_h is derived from "classical" second moment closure modelling in quasi homogeneous regions. In order to ensure the correct asymptotic behaviour $\overline{v^2}=O(y^4)$ the following boundary condition should be used:

$$\lim_{y\to 0} f=\lim_{y\to 0}\frac{-20\nu^2\overline{v^2}}{\varepsilon y^4} \tag{3}$$

[2]including both pressure diffusion and redistribution.

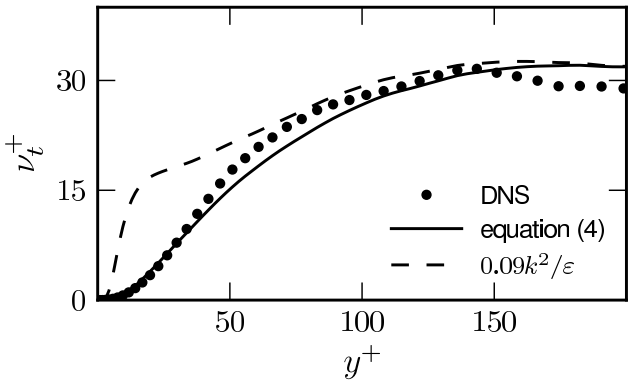

Figure 1: *A priori* evaluation of the EVM relation 4 and of the standard high Reynolds turbulent viscosity expression $C_\mu k^2/\varepsilon$, compared to the exact DNS value $-\overline{uv}/\partial_y U$ for the channel flow case at $Re_\tau = 395$.

Finally the model integrates $\overline{v^2}$ in the definition of the turbulent eddy viscosity:

$$\nu_t = C_\mu \overline{v^2} \max\left(\frac{k}{\varepsilon}, 6\sqrt{\frac{\nu}{\varepsilon}}\right) \tag{4}$$

Durbin (1991) showed that the use of the parameter $\overline{v^2}$ in equation 4 is the main feature allowing a correct reduction of the turbulent mixing efficiency in the buffer and viscous sublayer[3] (as seen in figure 1), circumventing the need of damping functions, *à la* Van Driest (1956) and subsequent models (Patel et al. (1985) review).

2.2. Generic formulation of the terms and constants

The definition of all models studied herein is given in the following. For a simpler comparison a generic description is adopted for the third transport equation ($g = \overline{v^2}$ or $g = \overline{v^2}/k$):

$$\frac{Dk}{Dt} = P - \varepsilon + \partial_j\left[\left(\nu + \frac{\nu_t}{\sigma_k}\right)\partial_j k\right] \tag{5a}$$

$$\frac{D\varepsilon}{Dt} = \frac{C_{\varepsilon 1}P - C_{\varepsilon 2}\varepsilon}{T} + \partial_j\left[\left(\nu + \frac{\nu_t}{\sigma_\varepsilon}\right)\partial_j \varepsilon\right] \tag{5b}$$

$$\frac{Dg}{Dt} = \mathcal{S}_g + \partial_j\left[\left(\nu + \frac{\nu_t}{\sigma_g}\right)\partial_j g\right] \tag{5c}$$

$$f - L^2\partial_j\partial_j f = f_h \tag{5d}$$

The models are referred to by the acronyms given in table 1. The terms and constants of the f, g and ε equations are given in tables 2, 3 and 4 respectively. The definitions of the length and time scales and associated constants are in table 5 and use one of the expressions 6, 7 or 8.

To prevent the turbulence over-prediction at a flow stagnation point, a limiter for the turbulent time scale is proposed in Durbin (1996). The model of LIE01 proposes to use a similar limiter in the length scale for consistency. The version of T and L integrating this limiter are given in expression 8 (S represents the strain rate magnitude and is defined as $S = \sqrt{S_{ij}S_{ij}}$ with $S_{ij} = 1/2\,(\partial_i U_j + \partial_j U_i)$). These limiters are effectively used in LIE01 and HAN04 models.

[3]It may be objected that using Expression 4 yields $\nu_t = O(y^4)$. Therefore the predicted turbulent shear stress modelled as $\overline{uv} = -\nu_t \frac{\partial U}{\partial y}$ is $O(y^4)$ instead of the theoretical behaviour $O(y^3)$. However at walls the momentum equation budget involves the terms $\nu\frac{\partial^2 U}{\partial y^2}$ and $-\frac{1}{\rho}\frac{dP}{dx}$ which are $O(1)$. As explained in Durbin (1991) despite this inaccuracy for the wall behaviour of the predicted turbulent shear stress, whether $\overline{uv}$ is $O(y^3)$ or $O(y^4)$ is insignificant. Indeed in both cases the turbulent diffusion term $-\frac{\partial \overline{uv}}{\partial y}$, modelled as $\frac{\partial}{\partial y}\nu_t\frac{\partial U}{\partial y}$ is at least two orders of magnitude smaller than the leading order terms. Likewise similar arguments can be developed for the turbulent kinetic energy equation.

DUR91	Durbin (1991)
DUR93	Durbin (1993)
DUR95	Durbin (1995)
DUR96	Durbin and Laurence (1996)
LIE96	Lien and Durbin (1996)
PAR97	Parneix and Durbin (1997)
LIE01	Lien and Kalitzin (2001)
MAN02	Manceau, Carpy, and Alfano (2002b)
HAN04	Hanjalić, Popovac, and Hadžiabdić (2004)
URI06	Uribe (2006)

Table 1: Acronyms used for models.

Model	f	f_h	C_1	C_2
DUR91	$\frac{\varphi_{22}}{k}$	$\frac{1}{T}(C_1-1)\left(\frac{2}{3}-\frac{\overline{v^2}}{k}\right)+C_2\frac{P}{k}$	1.2	0.3
DUR93	$\frac{\varphi_{22}}{k}$	$\frac{1}{T}(C_1-1)\left(\frac{2}{3}-\frac{\overline{v^2}}{k}\right)+C_2\frac{P}{k}$	1.3	0.3
DUR95	$\frac{\varphi_{22}}{k}$	$\frac{1}{T}(C_1-1)\left(\frac{2}{3}-\frac{\overline{v^2}}{k}\right)+C_2\frac{P}{k}$	1.4	0.3
DUR96	$L\frac{\varphi_{22}}{k}$	$L\left[\frac{1}{T}(C_1-1)\left(\frac{2}{3}-\frac{\overline{v^2}}{k}\right)+C_2\frac{P}{k}\right]$	1.3	0.35
LIE96	$\frac{\varphi_{22}}{k}+5\varepsilon\frac{\overline{v^2}}{k^2}$	$\frac{1}{T}\left[(C_1-1)\frac{2}{3}-(C_1-6)\frac{\overline{v^2}}{k}\right]+C_2\frac{P}{k}$	1.4	0.3
PAR97	$\frac{\varphi_{22}}{k}$	$\frac{1}{T}(C_1-1)\left(\frac{2}{3}-\frac{\overline{v^2}}{k}\right)+C_2\frac{P}{k}$	1.4	0.3
LIE01	$\frac{\varphi_{22}}{k}+5\varepsilon\frac{\overline{v^2}}{k^2}$	$\frac{1}{T}\left[(C_1-1)\frac{2}{3}-(C_1-6)\frac{\overline{v^2}}{k}\right]+C_2\frac{P}{k}$	1.4	0.3
MAN02	$\frac{\varphi_{22}}{\varepsilon k}$	$\frac{1}{\varepsilon T}(C_1-1)\left(\frac{2}{3}-\frac{\overline{v^2}}{k}\right)+\frac{2}{3}C_2\frac{P}{\varepsilon k}$	1.8	0.4
HAN04	$\frac{\varphi_{22}}{k}$	$\frac{1}{T}\left(C_1-1+C_2\frac{P}{\varepsilon}\right)\left(\frac{2}{3}-\frac{\overline{v^2}}{k}\right)$	1.4	0.65
URI06	$\frac{\varphi_{22}}{k}+\frac{2\nu}{k}\partial_j\frac{\overline{v^2}}{k}\partial_j k+\nu\partial_j\partial_j\frac{\overline{v^2}}{k}$	$\frac{1}{T}(C_1-1)\left(\frac{2}{3}-\frac{\overline{v^2}}{k}\right)+C_2\frac{P}{k}+2\frac{\nu}{\varepsilon T}\partial_j k\partial_j\frac{\overline{v^2}}{k}+\nu\partial_j\partial_j\frac{\overline{v^2}}{k}$	1.4	0.3

Table 2: Terms and coefficients of the f equation.

$$\begin{cases} L = C_L \max\left[\frac{k^{3/2}}{\varepsilon}, C_\eta\left(\frac{\nu^3}{\varepsilon}\right)^{1/4}\right] \\ T = \max\left[\frac{k}{\varepsilon}, C_T\left(\frac{\nu}{\varepsilon}\right)^{1/2}\right] \end{cases} \tag{6}$$

$$\begin{cases} L = \sqrt{C_L^2\left(\frac{k^3}{\varepsilon^2}+C_\eta^2\frac{\nu^{3/2}}{\varepsilon^{1/2}}\right)} \\ T = \sqrt{\frac{k^2}{\varepsilon^2}+C_T^2\frac{\nu}{\varepsilon}} \end{cases} \tag{7}$$

$$\begin{cases} L = C_L \max\left[\min\left[\frac{k^{3/2}}{\varepsilon}, \frac{k^{3/2}}{\sqrt{6}C_\mu\overline{v^2}S}\right], C_\eta\left(\frac{\nu^3}{\varepsilon}\right)^{1/4}\right] \\ T = \max\left[\min\left[\frac{k}{\varepsilon}, \frac{0.6k}{\sqrt{6}C_\mu\overline{v^2}S}\right], C_T\left(\frac{\nu}{\varepsilon}\right)^{1/2}\right] \end{cases} \tag{8}$$

2.3. Evolution in the past 20 years

As seen from the tables, over the last 20 years modifications mainly focussed on the numerical formulation (in search of a bettering robustness) and modelling of the wall effects in the dissipation rate equation.

The original version, DUR91, used an unusually high value of the production coefficient in the ε equation ($C_{\varepsilon 1} = 1.7$ instead of 1.4 as generally adopted in the RANS community). This is first corrected in DUR93, where the coefficients of the ε equation recover more traditional values in the log-layer, where $P/\varepsilon = 1$, together with a functional $C^*_{\varepsilon 1} = f(P/\varepsilon)$ to trigger a surge of dissipation production in the buffer layer, where $P/\varepsilon > 1$, with the rationale that this represents near-wall dissipation anisotropy. In DUR95 P/ε is replaced by the distance to the wall y in the definition of $C^*_{\varepsilon 1}$ to ensure the coefficient returns to its standard

Model	g	$\mathcal{S}_g$
DUR91	$\overline{v^2}$	$kf - \overline{v^2}\frac{\varepsilon}{k}$
DUR93	$\overline{v^2}$	$kf - \overline{v^2}\frac{\varepsilon}{k}$
DUR95	$\overline{v^2}$	$kf - \overline{v^2}\frac{\varepsilon}{k}$
DUR96	$\overline{v^2}$	$\frac{k}{L}f - \overline{v^2}\frac{\varepsilon}{k}$
LIE96	$\overline{v^2}$	$kf - 6\overline{v^2}\frac{\varepsilon}{k}$
PAR97	$\overline{v^2}$	$kf - \overline{v^2}\frac{\varepsilon}{k}$
LIE01	$\overline{v^2}$	$kf - 6\overline{v^2}\frac{\varepsilon}{k}$
MAN02	$\overline{v^2}$	$k\varepsilon f - \overline{v^2}\frac{\varepsilon}{k}$
HAN04	$\frac{\overline{v^2}}{k}$	$f - \frac{\overline{v^2}}{k^2}P$
URI06	$\frac{\overline{v^2}}{k}$	$f - \frac{\overline{v^2}}{k^2}P + \frac{2}{k}\frac{\nu_t}{\sigma_k}\partial_j k \partial_j \frac{\overline{v^2}}{k}$

Table 3: Terms and coefficients of the g equation. Note that $\sigma_g = 1.2$ for HAN04. $\sigma_g = \sigma_k$ for all other models.

Model	$C_{\varepsilon 1}$	$C_{\varepsilon 2}$	σ_k	σ_ε
DUR91	1.7	2.0	1.3	1.6
DUR93	$1.44\left(1 + 0.1\frac{P}{\varepsilon}\right)$	1.9	0.9	1.3
DUR95	$1.3 + 0.25/\left[1 + \left(\frac{C_L y}{2L}\right)^8\right]$	1.9	1	1.3
DUR96	$1.44\left(1 + \frac{1}{30}\sqrt{\frac{k}{v^2}}\right)$	1.85	1	1.5
LIE96	$1.55 + exp\left(-0.00285 R_y^2\right)$	1.92	1	1.5
PAR97	$1.4\left(1 + 0.045\sqrt{\frac{k}{v^2}}\right)$	1.9	1	1.3
LIE01	$1.4\left(1 + 0.05\sqrt{\frac{k}{v^2}}\right)$	1.9	1	1.3
MAN02	$1.44\left(1 + 0.06\sqrt{\frac{k}{v^2}}\right)$	1.91	1	1.3
HAN04	$1.4\left(1 + 0.012\frac{k}{v^2}\right)$	1.9	1	1.3
URI06	$1.4\left(1 + 0.05\sqrt{\frac{k}{v^2}}\right)$	1.85	1	1.3

Table 4: Terms and coefficients of the ε equation. In LIE96 $R_y = y\sqrt{k}/\nu$.

Model	expression for L and T	C_L	C_η	C_T	C_μ
DUR91	eq. 6	0.17	80	6	0.2
DUR93	eq. 6	0.2	90	6	0.23
DUR95	eq. 6	0.3	70	6	0.19
DUR96	eq. 7	0.2	60	4	0.16
LIE96	eq. 6	0.17	70	6	0.19
PAR97	eq. 6	0.25	85	6	0.22
LIE01	eq. 8	0.23	70	6	0.22
MAN02	eq. 8	0.23	100	6	0.22
HAN04	eq. 8	0.36	85	6	0.22
URI06	eq. 6	0.25	110	6	0.22

Table 5: Lengh and time scales.

value in homogeneous cases (where $P/\varepsilon > 1$ and $y \to \infty$). Further validations proved the early proposal for $C^*_{\varepsilon 1}$ to be numerically problematic and besides, the version of DUR95 is in contradiction with the sought-after "wall-distance free" property of the elliptic relaxation concept. Therefore a new parameter, $\sqrt{k/\overline{v^2}}$, is introduced in PAR97. This latter proposal, also more consistent with near-wall dissipation anisotropy rationale, is used in all subsequent versions.

Work was also extensively performed on improving the numerical behaviour of the model. In the original version indeed, the boundary conditions for $\overline{v^2}$ and f are coupled (equation 3) and the elliptic nature of the f equation makes the implementation very unstable in segregated codes. For the latter, the boundary condition, equation 3, requires a ratio of small terms ($O(y^4)$) to be correctly computed. In practice, the time step needed to be drastically reduced.

The model of LIE96 proposes to resolve the elliptic equation for the new variable $\overline{f} = f + 5\varepsilon\overline{v^2}/k^2$. Doing so enables the homogeneous Dirichlet boundary condition to be used for $\overline{f}$ and therefore yields a significantly improved robustness. However LIE96 was an early model, which attempted to pickup by-pass transition by a further sensitivity of $C^*_{\varepsilon 1}$ to the wall distance. The version of LIE01 combines this change of variable with the proposal of PAR97 for $C^*_{\varepsilon 1}$ and LIE01 is the version chosen by major commercial codes (StarCD, StarCCM, Fluent) for its easier convergence.

HAN04 and URI06 (originally in Laurence, Uribe, and Utyuzhnikov (2004)) have simultaneously and independently derived models resolving $\varphi = \overline{v^2}/k$ instead of $\overline{v^2}$. Both teams[4] noticed a shortcoming in the versions of LIE96 and LIE01: the change of variable $f \to \overline{f}$ induces the term $\Delta\left(5\varepsilon\overline{v^2}/k^2\right)$ later neglected in the $\overline{f}$ equation. However Laurence et al. (2004) shows it is of the same order as other $\overline{f}$ source terms in the logarithmic region, and its omission yields a strong over prediction of $\overline{v^2}$. By solving this new variable φ, HAN04 and URI06 attempt to derive a code friendly model which, unlike LIE01, does not deteriorate the predictions of f and $\overline{v^2}$. The derivation of the φ equation (equation 9) from those for $\overline{v^2}$ and k, makes a new term appear, the cross diffusion:

$$\frac{D\varphi}{Dt} = f - P\frac{\varphi}{k} + X + \partial_j\left[\left(\frac{\nu_t}{\sigma_k} + \nu\right)\partial_j\varphi\right] \tag{9}$$

$$X = \underbrace{\frac{2}{k}\nu\partial_j\varphi\partial_j k}_{X_\nu} + \underbrace{\frac{2}{k}\frac{\nu_t}{\sigma_k}\partial_j\varphi\partial_j k}_{X_t} \tag{10}$$

In HAN04 this X term is neglected and the f boundary condition is given as:

$$\lim_{y\to 0} f = \lim_{y\to 0}\frac{-2\nu\varphi}{y^2} \tag{11}$$

This enhances the numerical stability because the stiffness of the boundary condition is now a ratio of $O(y^2)$ terms only. However it still proved insufficiently robust for general use in a segregated industrial purpose code, and a modified version, the $\zeta - f_0$ model was derived in Popovac (2010) in the framework of tests within the FLUENT package. This relies on a change of variable for f to allow a zero boundary condition for this variable, therefore this makes the $\zeta - f_0$ model inherit the same drawbacks as the models of LIE96 and LIE01.

In the URI06 version the cross diffusion X term is kept in the φ equation and the following change of variable is proposed:

$$f = \overline{f} - X_\nu - \nu\partial_j\partial_j\varphi \tag{12}$$

Doing so allows $\lim_{y\to 0}\overline{f} = 0$. Similarly to LIE01 a term is neglected, $\Delta\left(X_\nu + \nu\partial_j\partial_j\varphi\right)$, but Uribe (2006) shows it is of lesser importance. As such the formulation is numerically unstable. Indeed, in the algebraic rearrangement of the equations consecutively to the change of variable, the molecular diffusion of φ is cancelled in the φ equation, which reduces numerical stability in the viscous sub layer. In practice, $\nu\partial_j\partial_j\varphi$ is added to the φ source term, *i.e.* molecular diffusion of φ is effectively doubled. An undesired effect of this numerical workaround is some over-prediction of φ near the wall, compensated by a new tuning of the coefficients.

[4]HAN04 used the letter ζ and URI06 chose φ. The latter notation is kept throughout this work as a matter of consistency.

Model	$Re_\tau = 180$ ($Re_b = 5\ 585$)	$Re_\tau = 395$ ($Re_b = 13\ 763$)	$Re_\tau = 590$ ($Re_b = 21\ 906$)	$Re_\tau = 950$ ($Re_b = 37\ 035$)	$Re_\tau = 2000$ ($Re_b = 87\ 180$)	Error max
DUR91	106	105	106	106	105	+6
DUR93	95	96	97	97	97	−5
DUR95	101	97	97	96	96	−4
DUR96	101	99	100	99	98	−2
LIE96	89	92	95	97	100	−11
PAR97	87	91	94	96	98	−13
LIE01	84	87	90	91	95	−16
MAN02	99	100	101	102	102	+2
HAN04	88	93	97	100	104	−12
URI06	99	102	104	105	106	+6
BL-$\overline{v^2}/k$	100	98	100	100	101	−2

Table 6: Friction coefficient C_f compared to the DNS value for the same friction velocity based Reynolds number Re_τ (given in %).

Stepping outside the scope of numerical stability issues, we now focus on changes to the elliptic operator, equation 5d. Durbin and Laurence (1996) and Wizman et al. (1996) observe that the earlier version of the elliptic operator correctly damps the supply of $\overline{v^2}$ in the viscous and buffer sublayers, but then erroneously augments it in the logarithmic layer, as compared to the homogeneous case, i.e: $f \geq f_h$, whereas $f \leq f_h$ is needed in the logarithmic region[5]. More generally, Manceau et al. (2001) shows that if the variable f behaves as y^n in the log layer, the elliptic equation 5d becomes:

$$f = f_h \times \frac{1}{1 - n(n-1)(C_L\kappa)^2(C_\mu\overline{v^2}/k)^{-3/2}} \tag{13}$$

f defined as $\frac{\varphi_{22}}{k}$ behaves as y^{-1} ($n = -1$) in the log layer, leading to an actual amplification. The strategy adopted by DUR96 and MAN02 is to solve equation 5d for a "rescaled" variable $\tilde{f}$. $\tilde{f} = Lf$ and $\tilde{f} = f/\varepsilon$ are adopted in DUR96 and MAN02[6] respectively. These formulations leave the f variable unchanged (*i.e.* $f = f_h$) in the logarithmic region and are called "neutral".

2.4. Behaviour in fundamental flows

Using well-established DNS databases of channel flow (Kim et al. (1987), Moser et al. (1999), Alamo et al. (2004), Jimenez and Hoyas (2008)) as reference values, the skin-friction predictions of the various versions are shown in table 6 in terms of percentage. The results are mostly lying within the 10% as expected for a case used for constant tuning, but there is a clear upward (sometimes downward) drift, whence the errors are expected to increase for higher Re numbers beyond these DNS cases. In particular LIE96, PAR97, LIE01 and HAN04 models yield a maximum error ranging from −11% to −16%. The neutral formulations of DUR96 and MAN02 are clearly less affected. The properties of the logarithmic layer at infinite Reynolds number ($P = \varepsilon$ and $L = \kappa y$) are classically assumed to reduce the equations to algebraic expressions, following which the Von Kármán constant κ and anisotropy $\overline{v^2}/k = \varphi$ can be evaluated. The values returned by models in this configuration (κ and φ_{log}) are provided in table 7, along with the value taken by the coefficient $C^*_{\varepsilon 1}$, noted $C^*_{\varepsilon 1,log}$. Behaviours of models strongly differ from one another. The Von Kármán constants predicted by LIE96 and LIE01 are excessively high and this is linked to an over prediction of φ_{log} returned by the latter models. Naturally, the larger friction error drifts with Re number observed in table 6 are consistent with the larger errors on the Von Kármán constant prediction.

The asymptotic values of φ_∞ and $C^*_{\varepsilon 1,\infty}$ in the case of homogeneous flow subject to a constant strain rate dU/dy is given, table 7. Large differences amongst models can be observed.

[5] with strict $f < f_h$ for purely homogeneous models or $f = f_h$ for better anisotropy reproducing high Reynolds and wall function based pressure-strain models (LRR-QI of Launder, Reece, and Rodi (1975) or SSG of Speziale, Sarkar, and Gatski (1991)).

[6] MAN02 corresponds to the model presented in Manceau et al. (2002b) but this "rescaled" $\overline{v^2} - f$ version was originally introduced in Manceau et al. (2002a) with different values for some of the constants.

Model	κ	φ_{log}	$C^*_{\varepsilon 1,log}$	φ_∞	$C^*_{\varepsilon 1,\infty}$
DUR91	0.38	0.48	1.7	0.35	1.70
DUR93	0.37	0.49	1.58	0.36	1.58
DUR95	0.41	0.71	1.55	0.34	1.30
DUR96	0.36	0.42	1.51	0.40	1.52
LIE96	0.51	1.13	1.55	0.37	1.55
PAR97	0.45	0.63	1.48	0.37	1.50
LIE01	0.59	1.60	1.46	0.37	1.52
MAN02	0.40	0.44	1.53	0.39	1.53
HAN04	0.49	0.7	1.42	0.31	1.45
URI06	0.41	0.59	1.49	0.37	1.51
BL-$\overline{v^2}/k$	0.42	0.41	1.44	0.37	1.44

Table 7: Predictions of the models in the logarithmic layer (left part) and in homogeneous shear turbulence (right part).

2.5. Limitations of the existing versions

Stability vs accuracy. Among the code-friendly formulations, none is able to effectively suppress the f boundary condition stiffness without impairing the quality of results. In LIE96 and LIE01 the terms rearrangement is done at the expense of an over prediction of $\overline{v^2}$ in the log layer, whereas the modification proposed in URI06 leads to an overshoot of φ near walls. Our experience, after implementing different coding strategies, careful time-stepping and running a number of test cases is that, model version HAN04 still does not reduce the boundary condition stiffness in the f equation sufficiently.

Amplification effect in the log region. All models but DUR96 and MAN02 (thanks to the neutral formulation) show an overshoot of φ in the logarithmic layer. For LIE96 and LIE01 the combination of the two sources of over-prediction is dramatic due to a positive feedback effect: $\overline{v^2}$ is over-estimated due to the change of variable $f \to \overline{f}$ which increases the amplification factor (equation 13) which in turn increases even more $\overline{v^2}$, and so on. Consequently those 2 models, chosen by code vendors for robustness, return values of φ_{log} between 1.13 and 1.60 (table 7), which are not realisable ($\varphi < 2/3$). Similarly DUR95 and HAN04 return excessively high $\overline{v^2}$ values.

The inter-dependance of coefficients. In the $k-\varepsilon$ model, equations 14a and 14b (Jones and Launder (1972)) determine the model behaviour in fundamental flows, where only some of the source terms of k and ε are involved, and constants are tuned accordingly. Table 8 summarises the different modes. D^t_k and D^t_ε are the turbulent diffusion terms for k and ε ($\partial_j\left(\nu_t/\sigma_k\partial_j k\right)$ and $\partial_j\left(\nu_t/\sigma_\varepsilon\partial_j\varepsilon\right)$ respectively).

$$\frac{Dk}{Dt} = P - \varepsilon + D^t_k + \nu\partial_j\partial_j k \tag{14a}$$

$$\frac{D\varepsilon}{Dt} = \frac{1}{T}\left(C_{\varepsilon 1}P - C_{\varepsilon 2}\varepsilon\right) + D^t_\varepsilon + \nu\partial_j\partial_j\varepsilon \tag{14b}$$

Mode	P	ε	D^t_k	D^t_ε	Constants
DIT		✓			$C_{\varepsilon 2}$
HST	✓	✓			$C_{\varepsilon 1}$
Defect Layer		✓	✓	✓	$C_{\varepsilon 2}, \sigma_k, \sigma_\varepsilon$
Log. Layer	✓	✓		✓	$C_{\varepsilon 1}, C_{\varepsilon 2}, \sigma_\varepsilon$
Near Wall	✓	✓	✓	✓	$C_{\varepsilon 1}, C_{\varepsilon 2}, \sigma_k, \sigma_\varepsilon$

Table 8: Active k and ε source terms and constants in the fundamental configurations: decaying isotropic turbulence (DIT), homogeneous shear turbulence (HST), defect layer, logarithmic layer at infinite Reynolds number and near-wall transition region.

In the versions of PAR97, LIE97, LIE01, MAN02, HAN04 and URI06, the fine-tuning of ε near walls is achieved by optimising the proportionality coefficient linking $C^*_{\varepsilon 1}$ and $\overline{v^2}/k$. However this variability subsists in the logarithmic layer and in homogeneous flows where it is undesirable. For those models, the difference in

the $C^*_{\varepsilon 1}$ definition (table 4) leads to strong diversity of prediction of the Von Kármán constant in logarithmic layer and turbulence growth rate P/ε in homogeneous shear turbulence (table 7). This interdependence also leads to a tedious calibration of the other model constants. Noteworthily the defect layer modelling (where $P/\varepsilon \to 0$) is not specifically considered in any of the formulation proposals (besides those neutralising the elliptic relaxation effect in the log-layer, which can also influence the defect layer).

The wall bounded/free shear flows distinction. DUR95 is the only model able to return a substantially lower value of the coefficient $C_{\varepsilon 1}$ in homogeneous shear flows, hence a larger shear layer spreading rate. It is actually the difference between $C_{\varepsilon 1}$ and $C_{\varepsilon 2}$ that is most influential, but $C_{\varepsilon 2}$ remains fixed within each model. All other versions return the same $C_{\varepsilon 1}$ value regardless of the presence of a wall.

3. The present formulation

A new formulation is now developed to address the problems exposed in the previous section, while simultaneously exploring more robust or "code friendly" solutions, which mostly stem from source terms groupings and changes of variables. One such solution was found in an adaptation to the eddy viscosity framework of the elliptic blending RSM approach of Manceau and Hanjalić (2002). It relies on the resolution of an elliptic equation for a non-dimensional coefficient α:

$$\alpha - L^2 \partial_j \partial_j \alpha = 1 \tag{15}$$

This coefficient is given the boundary condition $\alpha = 0$ at solid walls and relaxes towards 1 away from walls. It is used as a blending parameter in the $\overline{v^2}$ source term modelling to feature a smooth transition between near-wall and quasi-homogeneous models: $\varphi_{22} = (1-\alpha^p)\,\varphi^w_{22} + \alpha^p \varphi^h_{22}$. The present choice $p = 3$ (instead of $p = 2$ as in Thielen et al. (2005)) is used throughout the model's derivation following the suggestion of Lecocq (2008) who showed that a value at least equal to 3 is needed for the homogeneous term $\alpha^p \varphi^h_{22}$ to vanish in the near-wall balance of the $\overline{v^2}$ transport equation.

The model principal variable to be solved in a transport equation is the reduced variable $\varphi = \overline{v^2}/k$ and as such it formally can be considered as a follow-up of the work of Laurence et al. (2004).

This formulation enables setting a zero wall boundary condition for the elliptic variable α, therefore solving the numerical problems associated to the wall limit. For the definition of L and T, expression 7 is used as this provides a smoother transition between the Kolmogorov and the integral scale (Durbin and Laurence (1996)). For the coefficient C_T associated to the time scale, Equation 7, the value recommended by the latter authors $C_T = 4$ is adopted. Moreover, the constant C_L is chosen so that the turbulent length-scale (Equation 7) recovers its theoretical behaviour (*i.e.* $L = \kappa y$) in the logarithmic region in the limit $Re_\tau \to \infty$. Indeed in this situation the following holds: $L = C_L \left(C_\mu \overline{v^2}/k\right)^{-3/4} \kappa y$. Hence the value $C_L = \left(C_\mu \overline{v^2}/k\right)^{3/4} = 0.164$ is adopted (we use the numerical value $\overline{v^2}/k = 0.41$ obtained in the logarithmic layer as presented in Table 7). Finally, similarly to HAN04, the quasi-linear SSG model has been used (but with the same simplifications as the ones performed in HAN04). However we keep here the same original values for C_1 and C_2 as recommended in Speziale et al. (1991) [7].

The model uses the realisability constraint but only in the expression of the time scale present in the definition of the turbulent viscosity. This choice finds its justification in the analysis done in Sveningsson and Davidson (2004) which shows that a systematic use of the limiter wherever T is present makes it less efficient and can even lead to numerical instabilities originating from the redistribution term. The same authors also questioned the relevance of the length-scale limiter (as used in expression 8).

This new proposed blended $k-\varepsilon-\overline{v^2}/k$ model will be denoted as BL-$\overline{v^2}/k$ throughout this paper. Equations and constants of the BL-$\overline{v^2}/k$ model are given in full in Appendix A, while the incremental changes are described below:

The modifications brought to the $k-\varepsilon$ system can be formally seen as a double change of variable:

[7] Note that the present C_2 constant is noted C^*_1 in their paper.

$$\varepsilon = \underbrace{\varepsilon_h + \frac{k}{\varepsilon}E}_{\varepsilon'_h} + \frac{1}{2}\nu\partial_j\partial_j k \tag{16}$$

Where the E term is defined in equation 17.

$$E = 2\nu\nu_t \left(\partial_k\partial_j U_i\right)\left(\partial_k\partial_j U_i\right) \tag{17}$$

This E term, originally proposed by Jones and Launder (1972) (JL) to account for viscous wall effects in the ε equation, is a sounder alternative to making the production of dissipation constant $C^*_{\varepsilon 1}$ dependant on anisotropy. The E term removes some of the non-linearities and is clearly an inhomogeneity and low-Reynolds number correction (second derivative of velocity and molecular viscosity contributions respectively) which, in a channel flow makes it active only in the buffer-layer. A term by term modelling of the dissipation equation is highly debatable: ε or ω are in effect substitutes for an integral length-scale (a most essential parameter in the EVM framework, but which does not lend itself easily to modelling at one-point transport equation level). However one may recall that the E term has much similarity with the P^3_ε term of the exact ε equation (Rodi and Mansour (1993)). Moreover the JL E term was shown to be an essential ingredient for the success in bypass transition modelling (Savill (1993), Savill (2002)). Adaptation of the E term in the framework of $\overline{v^2} - f$ modelling was also successfully applied in the case of a skewed channel flow (Howard (1999), Howard and Sandham (2000)).

However its presence introduces numerical difficulties[8]. Therefore, in the present model the E term is reintroduced in the k equation using the change of variable $\varepsilon'_h = \varepsilon_h + k/\varepsilon E$. This allows it to be handled implicitly and causes no numerical instability.

Moreover, the decomposition $\varepsilon = \varepsilon'_h + 1/2\nu\partial_j\partial_j k$ is adopted from Jakirlić and Hanjalić (2002) with an aim to reduce the sink term ε in the k equation when $k \to 0$.

In the present model, a transport equation is finally solved for ε_h , and to satisfy near-wall balances of the source terms in the k, ε_h and φ equations, the viscous diffusion of the three variables is halved. This also explains the presence of a factor $\times 1/2$ in the term f_w of the φ equation. The following boundary condition is used for ε_h :

$$\lim_{y\to 0} \varepsilon_h = \frac{\nu k}{y^2} \tag{18}$$

The variable ε_h is used in place of ε wherever it appears in the k, ε_h and φ equations, as well as in the definition of L and T. The formal change of variable would involve more terms which are deliberately neglected in the present approach, on the bases that they would only play a role in the vicinity of walls.

Besides the numerical gain of using such a decomposition (which facilitates the numerical treatment of the E term), the latter features a decisive advantage for the model accuracy: the Kolmogorov time and length scales are used as lower bound of T and L, equations A.6, and they depend on the near-wall value of ε_h . It may be argued that these Kolmogorov scales should not be influenced by the outer flow; therefore they should be independent of the Reynolds number Re_τ. The variable ε_h resolved by the present model is much less Re_τ dependant compared to the DNS values, as shown figure 2. Indeed the presence of the term $-C_{\varepsilon 3}\left(1-\alpha\right)^3 k/\varepsilon_h E$ in the k equation strongly diminishes the predicted value of the turbulent kinetic energy peak in the buffer layer, the latter being known to be strongly Re_τ dependent.

The k sensitivity to Re_τ number is mainly due to the streamwise fluctuations (and streak structures) whereas the wall-normal component $\overline{v^2}$ is nearly independent of Re_τ, therefore removing the effect of E term, via the Re_τ independent ε_h, on the right hand side of the φ equation A.4 (as well as in L and T, equations A.6) and introducing it directly into the k equation A.1 is justified. Moreover, this allows an easier tuning of the model in channel flow for which case the present formulation shows the best predictions for both low and high Reynolds number, as seen on table 6. The correct theoretical behaviour of the model in the log layer is also recovered (table 7).

Finally the coefficient $C_{\varepsilon 1}$ is kept constant, equal to its conventional value 1.44. The extent of the E term effect is limited by the blending factor $\left(1-\alpha\right)^3$ although the presence of the product $\nu \times \nu_t$ in E already makes it a "buffer layer" term.

[8]It was adopted in the first version of the elliptic blending Reynolds Stress model in Manceau and Hanjalić (2002) but later abandoned (e.g. Thielen et al. (2005)).

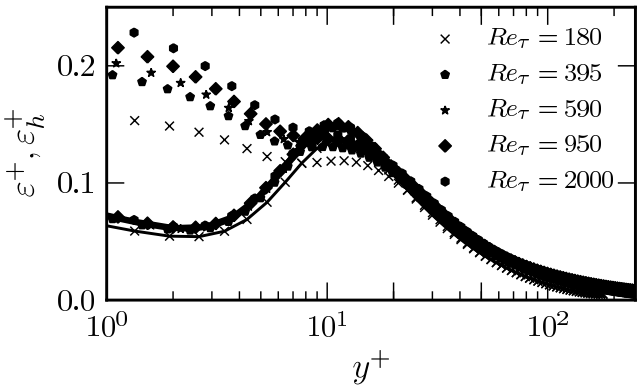

Figure 2: Comparison of the DNS near wall dissipation rate ε (symbols) and the homogeneous dissipation rate ε_h returned by the present model (symbols with solid lines) for friction velocity based Reynolds number $Re_\tau \in \{180; 395; 590; 950; 2000\}$.

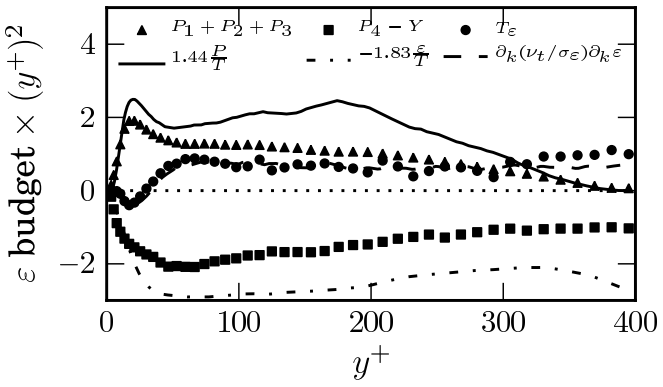

Figure 3: Budget of the ε equation for a channel flow, rescaled by $\times(y^+)^2$, $Re_\tau = 395$. Symbols are DNS values and lines are *a priori* model values. Data of Rodi and Mansour (1993).

We now focus on the defect layer. The local equilibrium hypothesis $P = \varepsilon$ characterising the logarithmic layer no longer holds further outwards. As the velocity gradient decreases turbulence is only sustained by turbulent transport terms, increasingly towards the defect layer. At the centre of the channel in the k equation the equilibrium $P = \varepsilon$ is then replaced by $D_k^T = \varepsilon$, as represented in table 8 and DNS data indicate that $\sigma_k = 1$ is adequate. The standard values of the ε equation coefficients are calibrated to represent the logarithmic layer, homogenous shear and grid turbulence decay only. An analysis of the budget of the ε equation, as performed in Parneix et al. (1996) and also shown on figure 3 using data of Rodi and Mansour (1993), shows that if the exact ε source terms are split between rapid ($P_1 + P_2 + P_3$) and slow terms ($P_4 - Y$) (involving or excluding the mean velocity gradient respectively) the standard values of $C_{\varepsilon 1} = 1.44$ and $C_{\varepsilon 2} = 1.83$ seem overestimated by a factor two.

In the logarithmic layer this overestimation is inconsequential because the excess of production and dissipation cancel each other. But even if the split between rapid and slow terms in the ε equation is highly debatable, $C_{\varepsilon 2}$ needs to be halved in the channel centreline region, so that it can be balanced by the turbulent transport term, which itself compares very well with the DNS data throughout the logarithmic and defect layers with the standard value of $\sigma_\varepsilon = 1.3$, as shown on figure 3.

Neither P/ε, nor anisotropy can be used as a criteria for reducing $C_{\varepsilon 2}$ in the defect layer while not affecting results in grid turbulence decay, since these parameters take the same value in both flow configurations, hence Parneix et al. (1996) suggested a $C_{\varepsilon 2}$ dependency on D_ε^T, but in the RSM context and for the recirculation bubble in a backstep flow. Following the same idea, a functional $C_{\varepsilon 2}$ is proposed here for the present model:

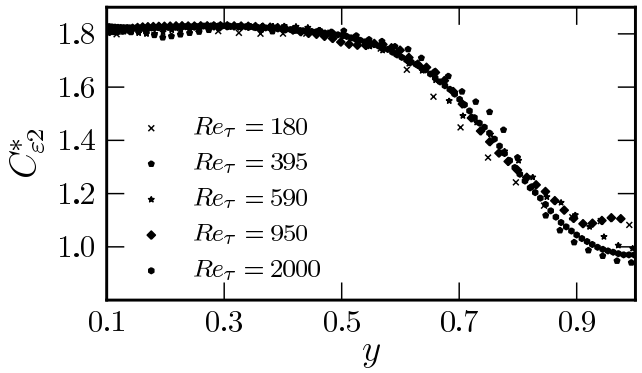

Figure 4: *A priori* evaluation of the proposed $C^*_{\varepsilon 2}$ coefficient sensitive to turbulent transport (equation 19) for a channel flow at $Re_\tau \in \{180; 395; 590; 950; 2000\}$.

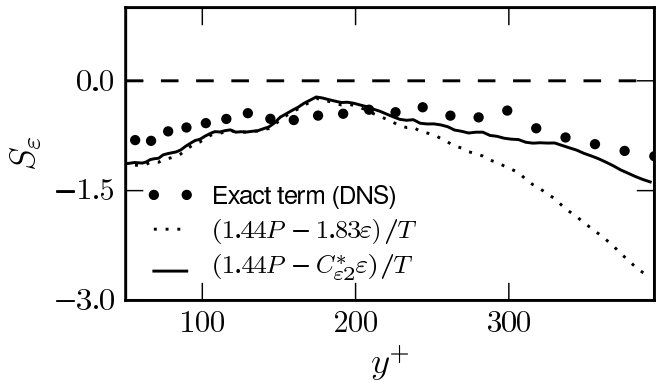

Figure 5: *A priori* evaluation of the main source term of ε, $S_\varepsilon = P_1 + P_2 + P_4 - Y$ in the central region of a channel flow, $Re_\tau = 395$, influence of the use of $C^*_{\varepsilon 2}$ as defined in eq. 19. Comparison with the DNS of Mansour and Rodi (1993).

$$C^*_{\varepsilon 2} = C_{\varepsilon 2} + \alpha^3 \left(C_{\varepsilon 4} - C_{\varepsilon 2}\right) \tanh\left(\left|\frac{D^t_k}{\varepsilon_h}\right|^{3/2}\right) \tag{19}$$

This results in $C^*_{\varepsilon 2}$ going from the standard value $C_{\varepsilon 2}$ in the logarithmic region to a decreased value of $C_{\varepsilon 4}$ in the defect layer. The inclusion of the blending parameter α in relation 19 is very handy as a zonal modelling parameter (rather than *e.g.* a turbulent Reynolds number) and ensures the $C^*_{\varepsilon 2}$ modification is not active near the wall, where turbulent transport is again significant.

The *a priori* evaluation of $C^*_{\varepsilon 2}$ given by relation 19 for different Reynolds numbers in a channel flow is shown in figure 4. This relation yields a fairly Re_τ independent characterisation of the central region of the channel. As achieved in Parneix et al. (1996), the exact source term of the ε equation is better represented using the proposed $C^*_{\varepsilon 2}$, as shown in figure 5, whereas the standard value 1.83 yields a too strongly negative ε sink term. This discrepancy of the standard model returns insufficient level of dissipation in this region resulting in a well-known over-estimation of the turbulent viscosity and turbulent length scale (Laurence et al. (2004)).

The predicted velocity and turbulent viscosity given by the model with and without using the relation 19 for $C^*_{\varepsilon 2}$ are shown in figure 6 for the channel flow case at $Re_\tau = 2000$. When using a constant $C^*_{\varepsilon 2}$ the returned turbulent viscosity is over predicted in the central region, and this discrepancy is common to all $\overline{v^2} - f$ models, and indeed a vast majority of RANS models, which lack information characterising the defect layer. This is to be directly linked to the consistent ε under-prediction.

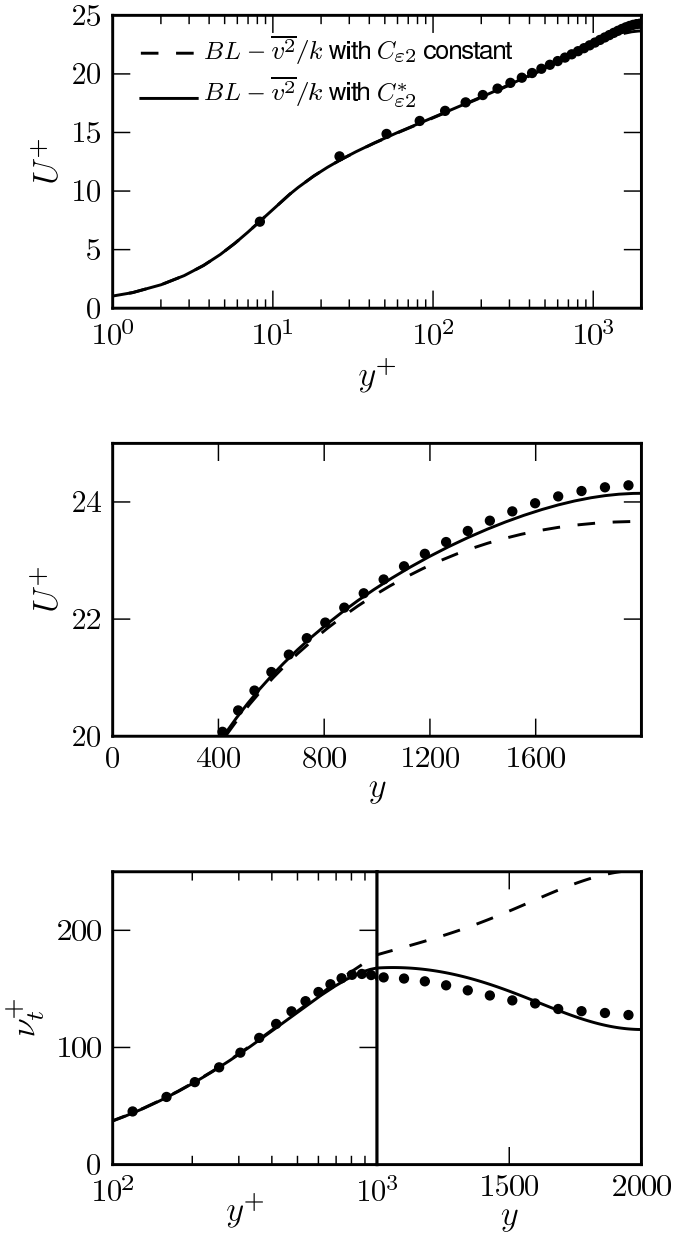

Figure 6: Effect of $C^*_{\varepsilon 2}$ as defined in eq. 19 in a channel flow, $Re_\tau = 2000$: velocity with logarithmic scale (top) close up of the mean velocity profile with linear scale (middle) and turbulent viscosity profile (bottom).

This ν_t over-prediction was shown to be especially severe for models over-predicting $\overline{v^2}$ (for those depicting a strong "amplification" effect, such as the popular "code-friendly" version of LIE96 and LIE01, as shown in Uribe (2006)). The present version yields an improved representation of ν_t in the central region, thus leading to a improved mean velocity prediction. With this modification, the model also returns the correct turbulence growth rate both in wall bounded and free shear flows. The turbulence growth P/ε now takes the different values $(C_{\varepsilon 4}-1)/(C_{\varepsilon 1}-1)$ or $(C_{\varepsilon 2}-1)/(C_{\varepsilon 1}-1)$ at the edge of a boundary layer and in free shear flow respectively.

4. Applications

The model is validated in two classes of flows. The first type of configuration studied is two cases of pressure induced separating flows featuring a recirculation. A good prediction of the flow pattern is directly linked to the correct reproduction of the shear stress evolution, itself, in an eddy viscosity framework, dependent on the length scale determining equation. The second category of problem under consideration is buoyancy induced turbulence generation/impairment, for which the correct near-wall turbulence damping prediction is crucial.

For sake of clarity, the complete present BL-$\overline{v^2}/k$ model equations and constants, consistently benchmarked on a range of test cases (Billard (2011)) is recalled in appendix A. Models are implemented in *Code_Saturne* (Archambeau et al. (2004) and Fournier et al. (2011)) an unstructured, collocated finite volumes, time-dependent yet segregated flow solver, freely available in "open-source" format.

4.1. Pressure induced separating flows

The flow through a periodically constricted channel (Almeida et al. (1993) experiment and reference LES of Temmerman and Leschziner (2001)) and in an asymmetric plane diffuser (Obi et al. (1993), Eaton (2000), reference data of Buice and Eaton (1997)) are two cases often used to validate RANS models. They are named hereafter "periodic hill flow" and "diffuser flow". The computational domains are represented on figure 7.

The length of the periodic hill domain is $L_1 = 9H_1$ with H_1 being the hill height. The Reynolds number based on H_1 and the bulk velocity U_1 is 10 595. The diffuser flow domain consists of an inlet channel of height H_2 subject to a sudden expansion with an angle of 10°. The height of the outlet channel is $4.7 \times H_2$ and the length of the computational domain is $L_2 = 71H_2$. The Reynolds number based on H_2 and the bulk velocity U_2 is 18 000.

The mesh resolution is 172×120 for the periodic hill flow and 292×96 for the diffuser flow. In order to ensure that the present meshes are sufficiently fine, all models were run on finer meshes (with twice as many computational nodes in both directions) with no noticeable changes. Moreover the non-dimensionnal wall distance (in viscous units) of the closest cells to the wall is always smaller than unity, making those meshes suitable for use with low Reynolds number models.

The proposed BL-$\overline{v^2}/k$ version is compared to the most widely used $\overline{v^2}-f$ model of LIE01 as well as the popular $k-\omega$ SST model of Menter (1994). Figure 8 presents the flow pattern returned by all models on the periodic hill flow and the location of the separation and reattachment on both cases are given in table 9. Figures 9 and 11 show the skin friction prediction along the hill surface and the inclined wall of the diffuser respectively and figures 10 and 12 show the profiles of the mean stream-wise velocity and the turbulence shear stress in the two cases.

As it can be seen from the flow streamlines and the skin-friction plots, in both cases the flow pattern prediction is fairly well returned by both $\overline{v^2}-f$ models whereas the $k-\omega$ SST yields excessively long re-circulation in the periodic hill case and predicts a far too early separation point in the diffuser flow, although here the reattachment point is correctly predicted by all models. For the latter case the recovery rate is also noticeably under-predicted by the $k-\omega$ SST model. Some differences between both $\overline{v^2}-f$ based models can be observed on the skin-friction coefficient plots, particularly in the recirculation zone of both cases and the recovery region of the diffuser flow. Minor differences between the two latter models can also be observed in the velocity profiles predictions. In both cases the LIE01 model is somehow superior in the recovery region, although in the periodic hill case this being partly due to the BL-$\overline{v^2}/k$ model reattaching slightly too late. However the reverse flow magnitude in the recirculating part of each flow is very similarly predicted by both $\overline{v^2}-f$ based model. As far as turbulent shear stress predictions are concerned, the main differences between models can be observed in the separation region of the periodic hill flow and the edge

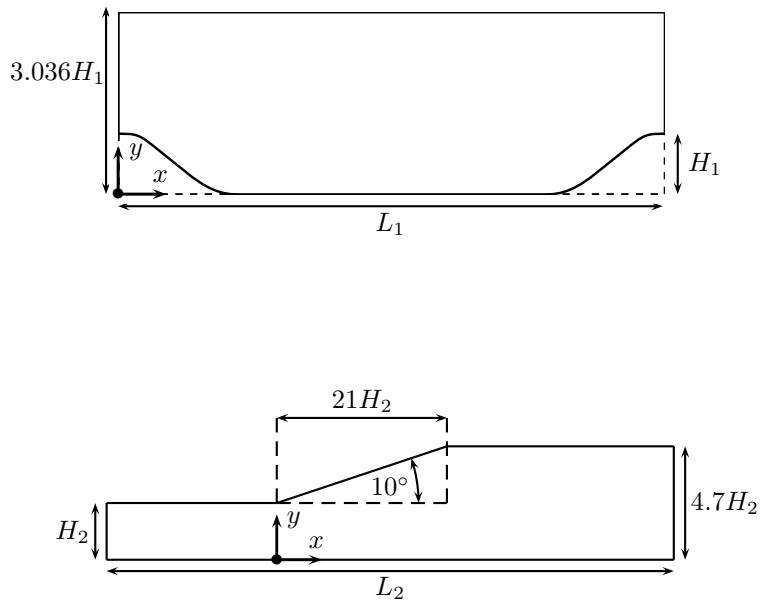

Figure 7: Geometry of the two pressure induced separating flows. Top: Periodic hill flow, Bottom: Diffuser flow.

	Periodic hill		Diffuser	
Model	Sep.	Reatt.	Sep.	Reatt.
Ref.	0.22	4.72	7.34	28.9
BL-$\overline{v^2}/k$	0.33	5.14	8.21	30.3
LIE01	0.39	4.78	5.42	28.9
$k-\omega$ SST	0.24	7.58	1.57	29.1

Table 9: Location of the separation (Sep.) and reattachment (Reatt.) in the periodic hill flow and the diffuser flow. Distances are normalised by H_1 and H_2 respectively.

of the recirculating flow of the diffuser, but all models show a consistent under-prediction of the turbulent shear-stress especially in the periodic hill flow.

The divergence between prediction of the BL-$\overline{v^2}/k$ and LIE01 models in these two configurations is relatively small despite formulations being very different, even regarding the terms and constants of the $k-\varepsilon$ system on which they are based. As seen on figure 13, the $C^*_{\varepsilon 2}$ coefficient returned by the present model gradually departs from its homogeneous turbulence value of 1.83 to reach its minimum in the defect layer of the top boundary layer and most importantly just below the separation shear layer. The conventional values 1.44 and 1.83 for $C_{\varepsilon 1}$ and $C_{\varepsilon 2}$ would yield too high a turbulence growth rate therefore an under predicted recirculation size. All the $\overline{v^2}-f$ models, calibrated to return fair predictions in this type of two dimensional simple flows, use a higher value for the constant $C_{\varepsilon 1}$ (ranging from 1.5 to 1.55). However for all versions but DUR95 the same value is used as in homogeneous cases. On the other hand, the $C^*_{\varepsilon 2}$ modification of the present model is only activated in the presence of inhomogeneities and theoretically derived behaviours in homogeneous configurations of table 8 are properly recovered.

This functional $C^*_{\varepsilon 2}$ proposal limiting the turbulence growth can be somehow compared to the turbulent viscosity limiter of the $k-\omega$ SST model. In the latter model, the limiter is only active when $F_2 = tanh(arg_2^2)$ is close to 1, which is for large magnitude of the argument arg_2 defined as:

$$arg_2^2 = \max\left(\frac{2\sqrt{k}}{0.09\omega y}, \frac{500\nu}{y^2\omega}\right) \tag{20}$$

With y representing the wall distance. Likewise in the present model the constant $C^*_{\varepsilon 2}$ is decreased only in regions where the magnitude of the term $|D^t_k/\varepsilon_h|^{3/2}$ is the largest. Figure 14 compares the fields of

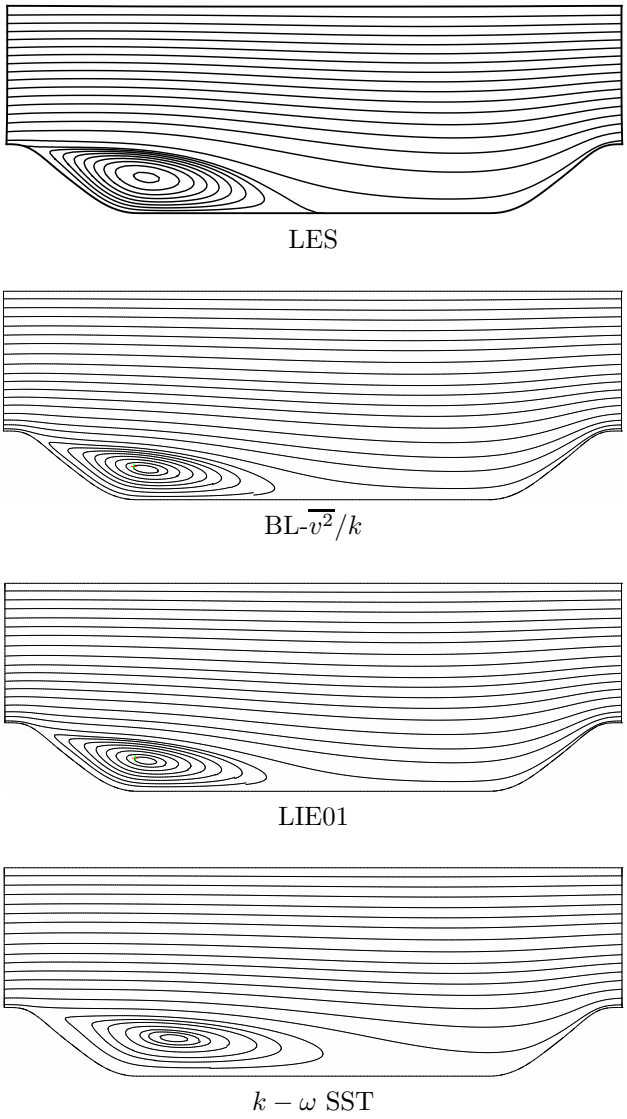

Figure 8: Streamlines prediction in the case of the periodic hill flow compared to the refined LES of Temmerman and Leschziner (2001).

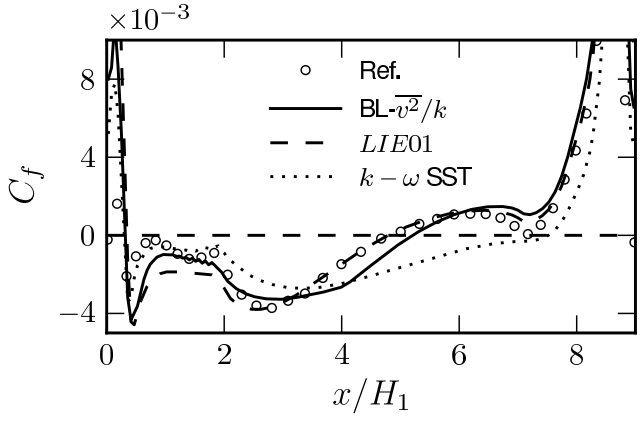

Figure 9: Prediction of the skin friction coefficient C_f in the periodic hill flow.

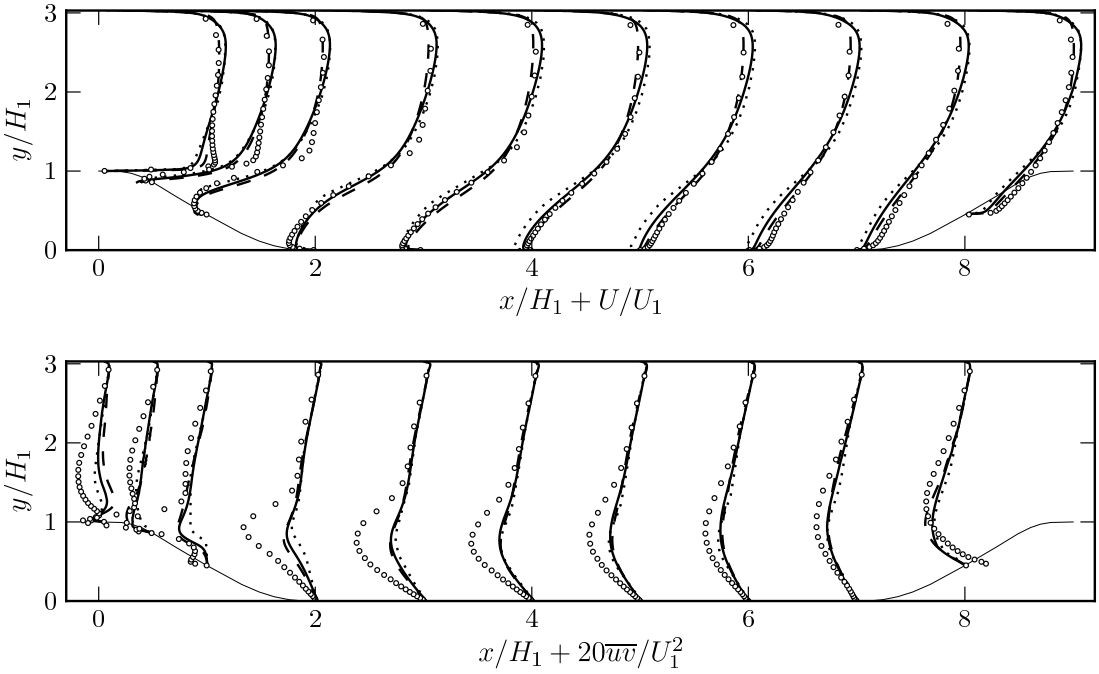

Figure 10: Prediction of the velocity profiles (top) and the turbulence shear stress (bottom) in the periodic hill flow. See Figure 9 for legends.

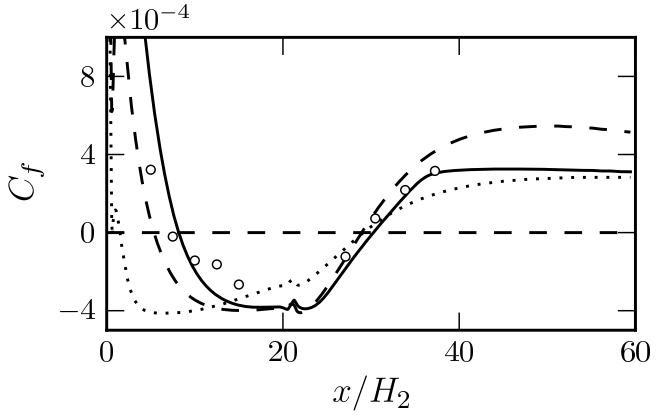

Figure 11: Prediction of the skin friction coefficient C_f in the diffuser hill flow. See Figure 9 for legends.

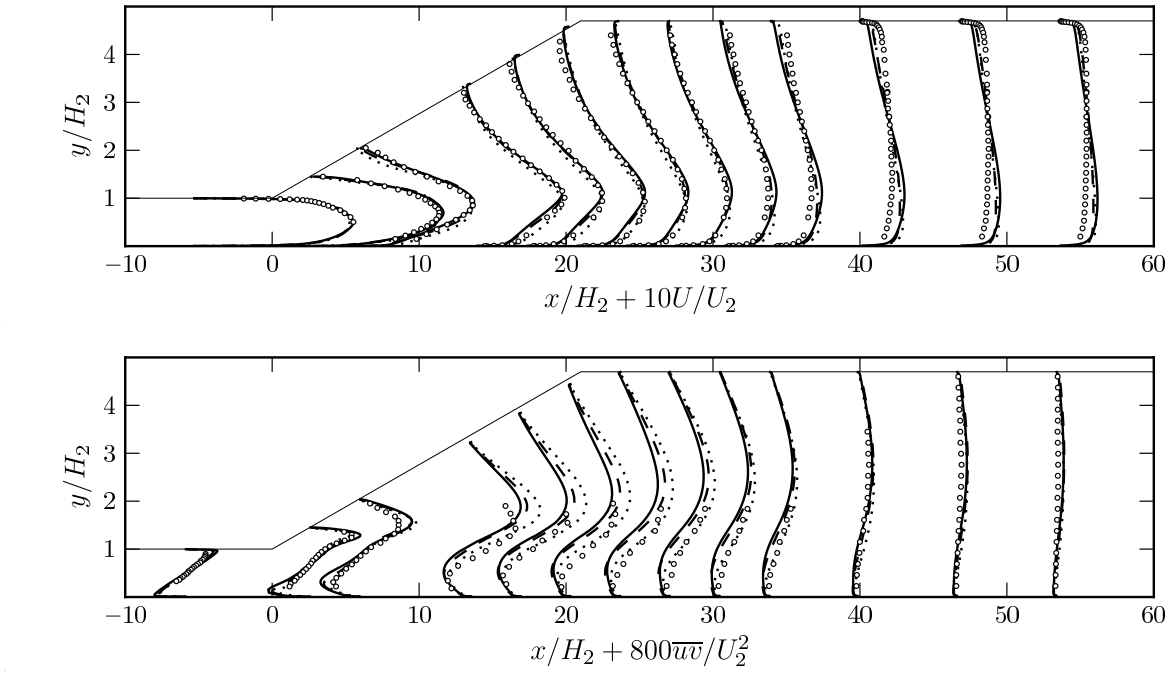

Figure 12: Prediction of the velocity profiles (top) and the turbulence shear stress (bottom) in the diffuser flow. See Figure 9 for legends.

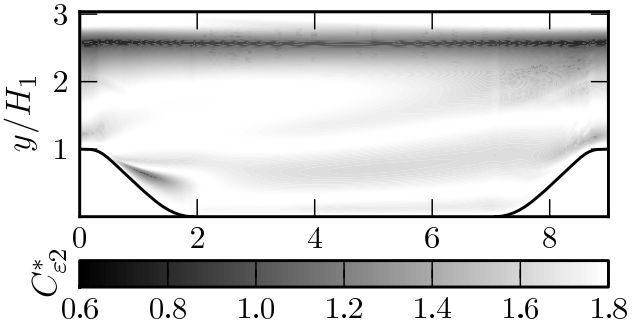

Figure 13: Function $C^*_{\varepsilon 2}$ given by equation 19, returned by the BL-$\overline{v^2}/k$ model in the periodic hill flow.

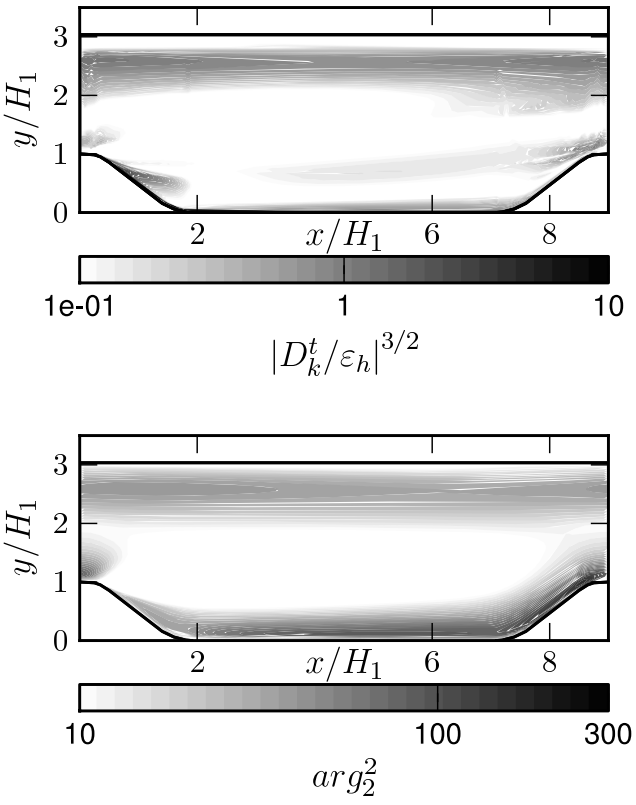

Figure 14: Comparison of the *tanh* arguments in the BL-$\overline{v^2}/k$ definition of $C^*_{\varepsilon 2}$ (*i.e.* $\left|D_k^t/\varepsilon_h\right|^{3/2}$) (top) and in the $k-\omega$ SST definition of the F_2 function (bottom).

$|D_k^t/\varepsilon_h|^{3/2}$ and arg_2^2 of the respective models in the periodic hill flow. It can be seen that both terms take their maximum values in the same regions (edge of top boundary layer and of the recirculation) indicating that the regions where the turbulence is limited by the respective models are reasonably similar[9] near the separation point, although further downstream the $k-\omega$ SST limiter seems more active than that of the present model, and this could explain why the recirculation returned by the SST model is excessively large.

Noteworthily, the realisability constraint limiters present in T (for the present model) and in T and L (for the LIE01 model) do not play meaningful role in these two configurations[10].

4.2. Mixed forced and natural convection in an upward heated channel flow

The added effect of buoyancy on a pressure driven fully turbulent flow was investigated in the DNS of Kasagi and Nishimura (1997) for a flow between two vertical plates kept at different temperatures, T_c and T_h (with $T_c < T_h$), driven upwards by a pressure gradient (the Reynolds number based on the averaged friction velocity on the two walls and the channel half-width δ is $Re_\tau = 150$). The resulting Grashof number is $Gr = 9.6 \times 10^6$, where Gr is defined as $g\beta(T_h - T_c)(2\delta)^3/\nu^2$ (β and ν represent the volumetric expansion and the molecular viscosity respectively).

The pressure gradient drives the flow upwards whereas the buoyant force drives the flow upwards (near the hot wall, aiding flow) and downwards (opposing flow). Owing to the near wall velocity profile modification by buoyancy, the turbulence is decreased in the aiding flow and increased near the opposing flow. The heat flux is modelled using a simple gradient diffusion hypothesis with a turbulent Prandtl number equal to 1. As the gravity is perpendicular to the temperature gradient, the simple model for the heat flux implies the buoyancy production is modelled as 0 in the turbulent equations.

The predictions of mean velocity, mean temperature, turbulent shear stress, turbulent kinetic energy and wall-normal anisotropy are shown in figure 15 for the BL-$\overline{v^2}/k$, the LIE01 version and the $k-\omega$ SST model. In the buoyancy aiding side, the turbulence impairment observed is somehow captured by all models, with returned level for k significantly decreased, whereas in the opposing side only the present model returns a correct level of turbulent kinetic energy, and the LIE01 model yields over prediction. The $k-\omega$ SST consistently under predicts levels of k on both sides. The near-wall anisotropy $\overline{v^2}/k$ is fairly well predicted by both $\overline{v^2}-f$ based models.

The present model gives the best predictions for the turbulent shear stress therefore yielding the best velocity and temperature profiles.

The relaminarisation and 50% drop of Nusselt number in the heated pipe with upward flow (buoyancy aided), You et al. (2003), is another case that the $\overline{v^2}-f$ model including the present version successfully reproduces, in opposition to an even more dramatic failure of the $k-\omega$ SST model. Results on this case for a selection of RANS models including an early version of the BL-$\overline{v^2}/k$ model are reported in Keshmiri et al. (2008).

Other heat transfer cases (not shown here), including natural convection in a cavity (Betts and Bokhari (2000)), flow in a ribbed channel (Rau et al. (1998)) and jet impinging a flat plate (Cooper et al. (1993)) were successfully run with the present model. The BL-$\overline{v^2}/k$ model was also applied to three dimensional flows: the three dimensional diffuser flow reported in Cherry et al. (2008) (the Reynolds number based on bulk velocity and the inlet duct height is 10^4), the flow over a highly swept wing (Zhong and Turner (2009)) (the Reynolds number based on the free stream velocity and the wing chord length is 2.1×10^5) and around the Boeing Rudimentary Landing Gear (the Reynolds number based on the free stream velocity and the wheel diameter is 10^6)(more details on this case can be found in Spalart et al. (2010)). For the three latter cases, the simulations were run on block structured meshes of 1.2, 3.7 and 5.4 million cells respectively using HPC facilities. Noteworthily simulations using other versions of the $\overline{v^2}-f$ model (URI06 and LIE01) failed to converge on the landing gear and were much harder to converge on the swept wing case. Illustrative pictures of the results obtained with the present model are presented Figure 16. Detailed results of the present model on the 3-dimensional diffuser and the swept wing are presented in Billard et al. (2011).

[9]To visually emphasise the similarity between the two turbulence limiter mechanisms, a logarithmic scaling is used.

[10]Switching off this constraint in the BL-$\overline{v^2}/k$ and LIE01 models increases the recirculation by a mere 1.5% and 1% respectively for the periodic hill flow. No difference is noticed in the diffuser flow.

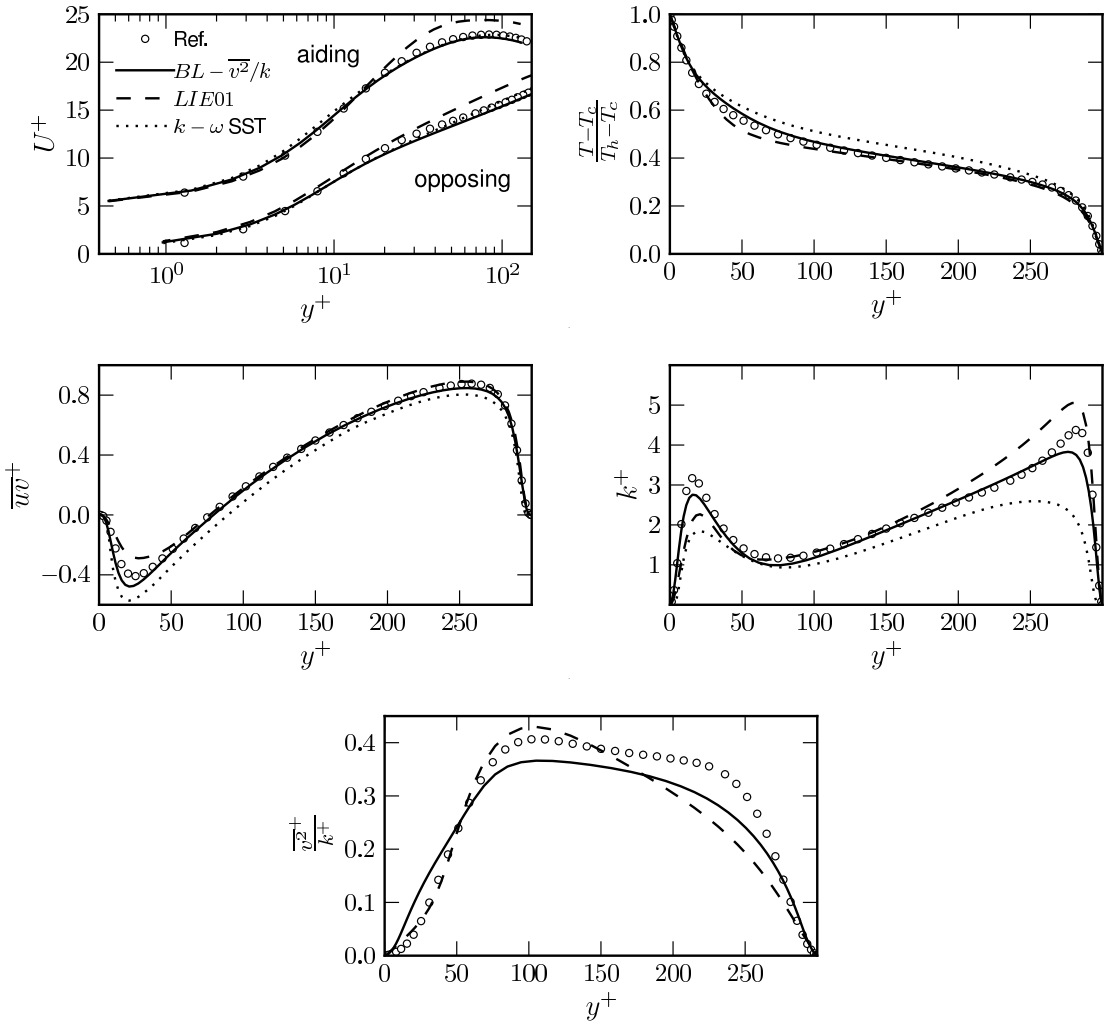

Figure 15: Prediction of the mean upwards velocity U^+, the mean temperature $\frac{T-T_c}{T_h-T_c}$, the turbulent shear-stress $\overline{uv}^+$ as well as the turbulent kinetic energy k^+ and the wall-normal turbulent anisotropy $\overline{v^2}^+/k^+$ in the case of a flow inside a heated channel.

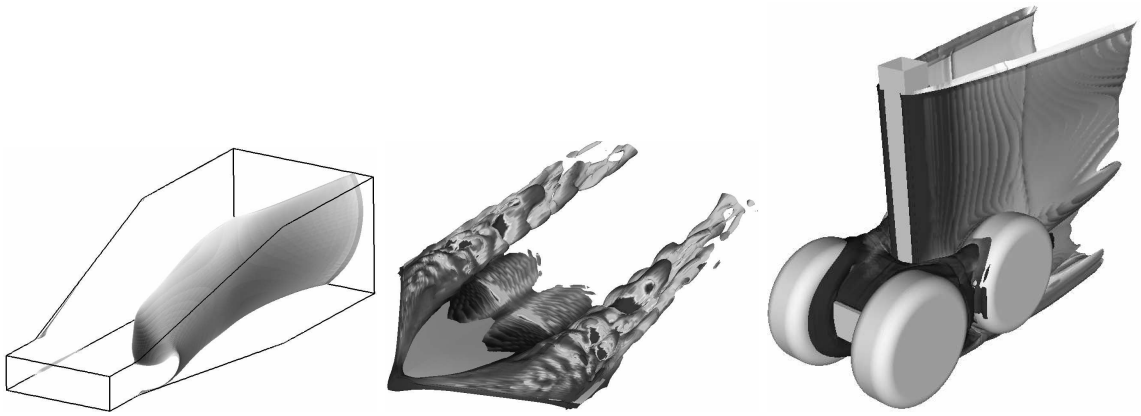

Figure 16: Applications of the BL-$\overline{v^2}/k$ model to three-dimensional flows. Isosurface of zero streamwise velocity for the three dimensional diffuser flow and isosurface of the vorticity coloured by the turbulent kinetic energy on the swept wing flow and the case of the Boeing rudimentary landing gear.

Conclusion

A numerically robust low Reynolds number eddy viscosity model incorporating the principles of the $\overline{v^2} - f$ approach has been derived after a review of 10 variants starting from the model of Durbin (1991). The new model incorporates the near-wall turbulence damping effects through an elliptic equation but relies on the elliptic blending method originally proposed in Manceau and Hanjalić (2002) for an increased robustness. The elliptic blending approach retains the main appealing feature of the original elliptic operator that allows clearer distinction between near-wall kinematic blockage of wall normal fluctuations and low-Reynolds number effects, but now uses the dimensionless variables α and $\varphi = \overline{v^2}/k$ to represent wall proximity and wall-normal velocity fluctuations respectively. This choice of variables yields an improved robustness. Moreover an alternative form of the standard $k - \varepsilon$ system is used and the present model reintroduces the E term originally proposed by Jones and Launder (1972) in order to represent the increased generation of dissipation required near walls. Consecutively to these modifications the predictions of the turbulent variables for the present model in a boundary layer are less dependent on the Reynolds number and this enables a better prediction of the mean flow quantities in a channel flow, at both low and high Reynolds numbers. Noteworthily, the changes introduced in the present version are only active in the regions they are intended for, hence reducing the inter-dependance of the coefficients, and permitting an easier calibration. The expected behaviour in fundamental flows (logarithmic layer at infinite Reynolds number, decaying isotropic turbulence, homogeneous shear turbulence) is now recovered.

Performances of the model, implemented in an industrial CFD code, have then been successfully assessed in the case of pressure induced separating flows as well as buoyancy impairing turbulent flows. Some illustrations of the results of the present model applied to more complex 3 dimensional cases are also presented.

Acknowledgements

This work has benefited from a PhD Scholarship from the School of Mechanical Aerospace and Civil Engineering at the University of Manchester.

Appendix A. Equations of the BL-$\overline{v^2}/k$ model

$$\begin{aligned}\frac{Dk}{Dt} &= P-\varepsilon_h+\partial_j\left[\left(\frac{\nu}{2}+\frac{\nu_t}{\sigma_k}\right)\partial_j k\right] \\ &\quad -C_{\varepsilon 3}(1-\alpha)^3\frac{k}{\varepsilon_h}2\nu\nu_t\left(\partial_k\partial_j U_i\right)\left(\partial_k\partial_j U_i\right)\end{aligned} \tag{A.1}$$

$$\frac{D\varepsilon_h}{Dt}=\frac{C_{\varepsilon 1}P-C^*_{\varepsilon 2}\varepsilon_h}{T}+\partial_j\left[\left(\frac{\nu}{2}+\frac{\nu_t}{\sigma_{\varepsilon_h}}\right)\partial_j\varepsilon_h\right] \tag{A.2}$$

$$C^*_{\varepsilon 2}=C_{\varepsilon 2}+\alpha^3\left(C_{\varepsilon 4}-C_{\varepsilon 2}\right)\tanh\left(\left|\frac{\partial_j\left(\nu_t/\sigma_k\partial_j k\right)}{\varepsilon_h}\right|^{3/2}\right) \tag{A.3}$$

$$\begin{aligned}\frac{D\varphi}{Dt} &= \left(1-\alpha^3\right)f_w+\alpha^3 f_h-P\frac{\varphi}{k}+ \\ &\quad \frac{2}{k}\frac{\nu_t}{\sigma_k}\partial_j\varphi\partial_j k+\partial_j\left[\left(\frac{\nu}{2}+\frac{\nu_t}{\sigma_\varphi}\right)\partial_j\varphi\right]\end{aligned} \tag{A.4}$$

$$f_w=-\frac{\varepsilon_h}{2}\frac{\varphi}{k}\text{ and }f_h=-\frac{1}{T}\left(C_1-1+C_2\frac{P}{\varepsilon_h}\right)\left(\varphi-\frac{2}{3}\right)$$

$$\alpha-L^2\partial_j\partial_j\alpha=1 \tag{A.5}$$

$$\begin{cases}L=\sqrt{C_L^2\left(\dfrac{k^3}{\varepsilon_h^2}+C_\eta^2\dfrac{\nu^{3/2}}{\varepsilon_h^{1/2}}\right)} \\ T=\sqrt{\dfrac{k^2}{\varepsilon_h^2}+C_T^2\dfrac{\nu}{\varepsilon_h}} \\ T_{lim}=\dfrac{0.6}{\sqrt{6}C_\mu\varphi\sqrt{S_{ij}S_{ij}}}\end{cases} \tag{A.6}$$

$$\nu_t=C_\mu\varphi k\ \min(T,T_{lim}) \tag{A.7}$$

$C_{\varepsilon 1}$	$C_{\varepsilon 2}$	$C_{\varepsilon 3}$	$C_{\varepsilon 4}$	σ_k	σ_{ε_h}
1.44	1.83	2.3	0.4	1	1.5

C_μ	C_T	C_L	C_η	C_1	C_2	σ_φ
0.22	4	0.164	75	1.7	0.9	1

Table A.10: Constants of the BL-$\overline{v^2}/k$ model.

References

Alamo, J. C. D., Jimenez, J., Zandonade, P., Moser, R. D., 2004. Scaling of the energy spectra of turbulent channels. Journal of Fluid Mechanics 500, 135–144.

Almeida, G., Durao, D., Heitor, M., 1993. Wake flows behind two-dimensional model hills. Experimental Thermal Fluid Science 7, 87–101.

Archambeau, F., Mechitoua, N., Sakiz, M., 2004. A finite volume method for the computation of turbulent incompressible flows - industrial applications. International Journal on Finite Volumes 1 (1).

Betts, P., Bokhari, I., 2000. Experiments on turbulent natural convection in an enclosed tall cavity. International Journal of Heat and Fluid Flow 21 (6), 675–683.

Billard, F., 2011. A new low reynolds number eddy viscosity model based on elliptic blending. Ph.D. thesis, School of Mechanical Aerospace and Civil Engineering - The University of Manchester, to appear.

Billard, F., Revell, A., Craft, T., 2011. Applications of advanced Reynolds Stress transport models to highly separated flows. In: Proceedings, Seventh Symp. on turbulence and shear flow phenomena, Ottawa, Canada.

Buice, C., Eaton, J., 1997. Experimental investigation of flow through an asymmetric plane diffuser. Report TSD-107, Department of mechanical engineering.

Chaouat, B., Schiestel, R., 2009. Progress in subgrid-scale transport modelling for continuous hybrid non-zonal RANS/LES simulations. International Journal of Heat and Fluid Flow 30 (4), 602–616.

Chapman, D., 1979. Computational aerodynamics development and outlook. AIAA J 17 (12), 1293–1313.

Cherry, E., Elkins, C., Eaton, J., 2008. Geometric sensitivity of three-dimensional separated flows. International Journal of Heat and Fluid Flow 29 (3), 803–811.

Cooper, D., Jackson, D., Launder, B., Liao, G., 1993. Impinging jet studies for turbulence model assessment. I: Flow-field experiments. International Journal of Heat and Mass Transfer 36 (10), 2675–2684.

Durbin, P., 1991. Near-wall turbulence closure modeling without "damping functions". Theoretical and Computational Fluid Dynamics 3 (1), 1–13.

Durbin, P., 1993. Application of a near-wall turbulence model to boundary layers and heat transfer. International Journal of Heat and Fluid Flow 14 (4), 316–323.

Durbin, P., 1995. Separated Flow Computations with the $k-\varepsilon-\overline{v^2}$ Model. AIAA journal 33 (4), 659–664.

Durbin, P., 1996. On the $k-\varepsilon$ stagnation point anomaly. International Journal of Heat and Fluid Flow 17 (1), 89–90.

Durbin, P., Laurence, D., 1996. Nonlocal effects in single point closure. In: 3^{rd} Advances in Turbulence Research Conference. pp. 109–120.

Eaton, J., 2000. Experimental investigation of flow through an asymmetric plane diffuser. Journal of Fluids Engineering 122, 433.

Fadai-Ghotbi, A., Friess, C., Manceau, R., Gatski, T., Borée, J., 2010. Temporal filtering: A consistent formalism for seamless hybrid RANS-LES modeling in inhomogeneous turbulence. International Journal of Heat and Fluid Flow.

Fournier, Y., Bonelle, J., Moulinec, C., Shang, Z., Sunderland, A., Uribe, J., 2011. Optimizing Code_Saturne Computations on Petascale Systems. Computers & Fluids.

Fröhlich, J., von Terzi, D., 2008. Hybrid LES/RANS methods for the simulation of turbulent flows. Progress in Aerospace Sciences 44 (5), 349–377.

Hanjalić, K., Popovac, M., Hadžiabdić, M., 2004. A robust near-wall elliptic-relaxation eddy-viscosity turbulence model for CFD. International Journal of Heat and Fluid Flow 25 (6), 1047–1051.

Howard, R., Sandham, N., 2000. Simulation and modelling of a skewed turbulent channel flow. Flow, Turbulence and Combustion 65 (1), 83–109.

Howard, R. J., 1999. Direct numerical simulation and modelling of turbulent channel flows subjected to complex distortions. Ph.D. thesis, University of London, Queen Mary and Westfield College.

Jakirlić, S., Hanjalić, K., 2002. A new approach to modelling near-wall turbulence energy and stress dissipation. Journal of Fluid Mechanics 459, 139–166.

Jimenez, J., Hoyas, S., 2008. Turbulent fluctuations above the buffer layer of wall-bounded flows. Journal of Fluid Mechanics 611, 215–236.

Jones, W., Launder, B., 1972. The prediction of laminarisation with a two equation turbulence model. International Journal of Heat and Mass Transfer 15 (2), 301–314.

Kasagi, N., Nishimura, M., 1997. Direct numerical simulation of combined forced and natural turbulent convection in a vertical plane channel. International Journal of Heat and Fluid Flow 18 (1), 88–99.

Keshmiri, A., Cotton, M., Addad, Y., Rolfo, S., Billard, F., 2008. Rans and les investigations of vertical flows in the fuel passages of gas-cooled nuclear reactors. In: Paper ICONE16-48372, Proc. 16th ASME Int. Conf. on Nuclear Engineering, ICONE16.

Kim, J., Moin, P., Moser, R., 1987. Turbulence statistics in fully developed channel flow at low reynolds number. Journal of Fluid Mechanics 177, 133–166.

Launder, B., Reece, G. J., Rodi, W., 1975. Progress in the development of a reynolds-stress turbulence closure. Journal of Fluid Mechanics 68 (03), 537–566.

Launder, B., Shima, N., 1989. Second-moment closure for the near-wall sublayer- Development and application. AIAA journal 27 (10), 1319–1325.

Laurence, D., Uribe, J., Utyuzhnikov, S., 2004. A robust formulation of the $\overline{v^2}-f$ model. Flow, Turbulence and Combustion 73 (1), 169–185.

Lecocq, Y., 2008. Contribution à l'analyse et à la modélisation des écoulements turbulents en régime de convection mixte : application à l'entreposage des dechets radioactifs. Ph.D. thesis, Université de Poitiers.

Lien, F., Durbin, P., 1996. Non-linear $k-\varepsilon-\overline{v^2}$ modeling with application to high lift. In: Proceedings of the Summer Program, Center for Turbulence Research. pp. 5–26.

Lien, F., Kalitzin, G., 2001. Computations of transonic flow with the $\overline{v^2}-f$ turbulence model. International Journal of Heat and Fluid Flow 22 (1), 53–61.

Manceau, R., Carlson, J., Gatski, T., 2002a. A rescaled elliptic relaxation approach: Neutralizing the effect on the log layer. Physics of Fluids 14 (11), 3868–3879.

Manceau, R., Carpy, S., Alfano, D., 2002b. A rescaled $\overline{v^2} - f$ model: First application to separated and impinging flows. In: Rodi, W., Fueyo, N. (Eds.), Proceedings of the 5^{th} International Symposium on Engineering Turbulence Modelling and Measurements, Mallorca, Spain, 16-18 September 2002. Elsevier Science, pp. 107–116.

Manceau, R., Hanjalić, K., 2002. Elliptic blending model: A new near-wall Reynolds-stress turbulence closure. Physics of Fluids 14 (2), 744–754.

Manceau, R., Wang, M., Laurence, D., 2001. Inhomogeneity and anisotropy effects on the redistribution term in Reynolds-averaged Navier-Stokes modelling. Journal of Fluid Mechanics 438, 307–338.

Mansour, N., Rodi, W., 1993. Low-Reynolds number $k - \varepsilon$ modelling with the aid of direct simulation data. Journal of Fluid mechanics 250, 509–529.

Menter, F., 1994. Two-equation eddy-viscosity turbulence models for engineering applications. AIAA journal 32 (8), 1598–1605.

Menter, F., Egorov, Y., 2005. A scale-adaptive simulation model using two-equation models. AIAA paper 1095.

Moser, R., Kim, J., Mansour, N., 1999. Direct numerical simulation of turbulent channel flow up to $re = 590$. Physics of Fluids 11, 943–945.

Obi, S., Aoki, K., Masuda, S., 1993. Experimental and computational study of turbulent separating flow in an asymmetric plane diffuser. In: Ninth Symposium on Turbulent Shear Flows, Kyoto, Japan. p. 305.

Parneix, S., Durbin, P., 1997. Numerical simulation of 3D turbulent boundary layer using the $\overline{v^2} - f$ model. Annual Research Briefs, Center for Turbulence Research, NASA Ames/Stanford University, 135–148.

Parneix, S., Laurence, D., Durbin, P., 1996. Second moment closure analysis of the backstep flow database. In: Proceedings of the Summer Program, Center for Turbulence Research. pp. 47–66.

Patel, V., Rodi, W., Scheuerer, G., 1985. Turbulence models for near-wall and low Reynolds number flows- A review. AIAA journal 23 (9), 1308–1319.

Popovac, M., 2010. Conjugate heat transfer simulations using zero wall boundary condition eddy viscosity turbulence model with elliptic relaxation. In: Proceedings of the 8^{th} International Symposium on Engineering Turbulence Modelling and Mesurements. pp. 958–964.

Rau, G., Cakan, M., Moeller, D., Arts, T., 1998. The effect of periodic ribs on the local aerodynamic and heat transfer performance of a straight cooling channel. Journal of turbomachinery 120, 368.

Rodi, W., Mansour, N., 1993. Low-reynolds number $k - \varepsilon$ modelling with the aid of direct simulation data. Journal of Fluid mechanics 250, 509–529.

Savill, A., 1993. Some recent progress in the turbulence modelling of by-pass transition. Near-wall turbulent flows, 829–848.

Savill, A., 2002. By-pass transition using conventional closures. In: Launder, B., Sandham, N. (Eds.), Closures strategies for turbulent and transitional flow. Cambridge Univ Press, pp. 464–491.

Spalart, P., 2009. Detached-eddy simulation. Annual Review of Fluid Mechanics 41, 181–202.

Spalart, P., Shur, M., Strelets, M., Travin, A., 2010. Initial rans and ddes of a rudimentary landing gear. Progress in Hybrid RANS-LES Modelling, 101–110.

Speziale, C. G., Sarkar, S., Gatski, T. B., 1991. Modelling the pressure-strain correlation of turbulence: an invariant dynamical systems approach. Journal of Fluid Mechanics 227, 245–272.

Sveningsson, A., Davidson, L., 2004. Assessment of realizability constraints in $\overline{v^2} - f$ turbulence models. International Journal of Heat and Fluid Flow 25 (5), 785–794.

Temmerman, L., Leschziner, M., 2001. Large eddy simulation of separated flow in a streamwise periodic channel constriction. In: Int. Symp. Turb. Shear Flow Phenomena, Stockholm, Sweden.

Thielen, L., Hanjalić, K., Jonker, H., Manceau, R., 2005. Predictions of flow and heat transfer in multiple impinging jets with an elliptic-blending second-moment closure. International Journal of Heat and Mass Transfer 48 (8), 1583–1598.

Uribe, J., Jarrin, N., Prosser, R., Laurence, D., 2010. Development of a Two-velocities Hybrid RANS-LES Model and its Application to a Trailing Edge Flow. Flow, Turbulence and Combustion 85 (2), 181–197.

Uribe, J. C., September 2006. An industrial approach to near-wall turbulence modelling for unstructured finite volume methods. Ph.D. thesis, School of Mechanical Aerospace and Civil Engineering - The University of Manchester.

Van Driest, E., 1956. On turbulent flow near a wall. J. Aeronaut. Sci 23 (11), 1007–1011.

Wizman, V., Laurence, D., Kanniche, M., Durbin, P., Demuren, A., 1996. Modeling near-wall effects in second-moment closures by elliptic relaxation. International Journal of Heat and Fluid Flow 17 (3), 255–266.

You, J., Yoo, J., Choi, H., 2003. Direct numerical simulation of heated vertical air flows in fully developed turbulent mixed convection. International Journal of Heat and Mass Transfer 46 (9), 1613–1627.

Zhong, S., Turner, J., 2009. MSTTAR project, EPSRC GR/S27443/01.

Appendix E

Conference paper: In Proceedings of the 7^{th} International Symposium on Engineering Turbulence Modelling and Mesurements, 2008

APPLICATION OF ADVANCED REYNOLDS STRESS TRANSPORT MODELS TO HIGHLY SEPARATED FLOWS

F. Billard, T. Craft and A. Revell
School of Mechanical, Aerospace and Civil Engineering,
The University of Manchester, Manchester, M13 9PL, UK
flavien.billard@manchester.ac.uk

ABSTRACT

This paper considers the application of four Reynolds Averaged Navier Stokes (RANS) models to a range of progressively complex test cases, exhibiting both 2-D and 3-D flow separation. Two Eddy Viscosity Models (EVM) and two Reynolds Stress Transport Models (RSM) are employed, of which two (one in each category) are based on elliptic blending formulations. This study attempts to gain more insight into the importance of two modelling features for these flows; the usage of turbulence anisotropy resolving schemes and the near-wall limiting behaviour. As expected, there is no single best model, though some clear trend in performance is observed.

INTRODUCTION

The dramatic increase in available computational power in recent years has tended to draw turbulence research away from advanced Reynolds-Averaged Navier Stokes (RANS) closures, to focus instead on approaches that fully, or partially, resolve the turbulent structures. Since fully resolved approaches (Direct Numerical Simulation) remain impractical for industrially relevant cases, a series of progressively more significant approximations are usually adopted for such applications. While Large Eddy Simulation (LES) has been successfully applied to complex flows for moderately high Reynolds numbers, the formal application of this methodology also remains computationally prohibitive for the majority of industrial flows. In particular, the sufficient resolution of near-wall structures with LES requires extremely fine meshes.

In response to the above limitations, a number of so called hybrid RANS-LES schemes have been developed across the community (see, for example Haase *et al.*, 2009; Fröhlich & von Terzi, 2008) in which the near-wall turbulence is modelled using a RANS approach, and LES employed for the outer flow regions. However, the majority of these hybrid methods retain rather simple (often linear) eddy-viscosity-based RANS closures. These simple modelling schemes are known to perform poorly in flows with, amongst other features, complex separation, reattachment, impingement, and curvature (Haase *et al.*, 2006). As such, it is relevant to question the impact of the RANS model on the hybrid solution, and the potential improvements one might gain by using a more complex scheme within such approaches.

This paper therefore attempts to explore the performance of a number of advanced eddy-viscosity and Reynolds stress transport models in a range of flows involving challenging separation and reattachment features. The focus is on the use of such schemes within a purely RANS solution strategy, to illustrate their performance, although this will also allow some conclusions to be drawn regarding the expected performance if they were applied within the more computationally expensive hybrid approaches. A number of common 2-D flows are first examined, before two flows with 3-D effects are computed.

DESCRIPTION OF THE MODELS

Four models are compared in the present study, namely the k-ω SST of Menter (1994), the *SSG* model of Speziale *et al.* (1991), the blended $k-\varepsilon-\overline{v^2}/k$ (BL-$\overline{v^2}/k$) model of Billard & Laurence (2011) and the Elliptic Blending RSM (EBRSM) of Manceau & Hanjalić (2002). The first two of these are fairly widely used and well validated models, thus serving as a reference against which to judge the performance of the more recent BL-$\overline{v^2}/k$ and EBRSM schemes.

The BL-$\overline{v^2}/k$ and the EBRSM are, respectively, elliptic-blending adaptations of the $\overline{v^2}-f$ and the $R_{ij}-f_{ij}$ models of Durbin (1991) and Durbin (1993). Both models are designed to take at least some account of the correct near-wall asymptotic behaviour of the Reynolds stresses, without using traditional wall-reflection or other geometry-dependent terms, to simplify application to complex geometries. In both models, a non-dimensional parameter α is solved for using an elliptic equation of the form:

$$L^2\partial_{kk}\alpha-\alpha=-1 \tag{1}$$

where L represents some turbulent length-scale. α varies from zero at walls to unity in free-stream regions and is used as a blending parameter in both closures.

The EBRSM formulation: The parameter α is here used in the Reynolds stress transport equations to model the pressure strain term, ϕ_{ij}^{*}[1], and the dissipation rate, ε_{ij}, blending between forms devised for the near-wall (subscript w) and outer flow (subscript h) regions:

[1]The term ϕ_{ij}^{*} in fact represents the sum of the deviatoric pressure-strain, ϕ_{ij}, and the pressure diffusion component.

$$\phi^*_{ij} = (1-\alpha^3)\phi^*_{ij,w} + \alpha^3 \phi^*_{ij,h}$$
$$\varepsilon_{ij} = (1-\alpha^3)\varepsilon_{ij,w} + \alpha^3 \varepsilon_{ij,h} \quad (2)$$

$\varepsilon_{ij,h}$ is simply taken as isotropic, $2/3\varepsilon\delta_{ij}$, while the term $\phi^*_{ij,h}$ is based on the SSG model. In the near-wall region, the model of Rotta (1951) is used for the dissipation rate, $\varepsilon_{ij,w} = \varepsilon\overline{u_i u_j}/k$, whilst $\phi^*_{ij,w}$ is constructed to balance other leading order terms at walls (namely $\varepsilon_{ij,w}$ and molecular diffusion), and is taken as

$$\phi^*_{ij,w} = -5\frac{\varepsilon}{k}(\overline{u_i u_k}n_j n_k + \overline{u_j u_k}n_i n_k - \frac{1}{2}\overline{u_k u_l}n_k n_l(n_i n_j + \delta_{ij})) \quad (3)$$

where $\underline{n} = \nabla\alpha$ is used to identify the direction normal to the wall (See Manceau & Hanjalić, 2002, for details).

The BL-$\overline{v^2}/k$ model: The aim of the more simple elliptic blending eddy viscosity model is to embed in a robust formulation some features of more complex approaches. It uses the blending formulations of equation (2) in a modelled transport equation for the variable $\varphi = \overline{v^2}/k$, in addition to a modified k-ε system:

$$\frac{Dk}{Dt} = P - \varepsilon - C_{\varepsilon 3}(1-\alpha)^3\frac{k}{\varepsilon}E + \partial_j\left(\frac{\nu}{2} + \frac{\nu_t}{\sigma_k}\right)\partial_j k \quad (4)$$

$$\frac{D\varepsilon}{Dt} = \frac{C_{\varepsilon 1}P - C^*_{\varepsilon 2}\varepsilon}{T} + \partial_j\left(\frac{\nu}{2} + \frac{\nu_t}{\sigma_\varepsilon}\right)\partial_j\varepsilon \quad (5)$$

In the k equation, the inclusion of the term $E = 2\nu\nu_t(\partial_{kj}U_i)(\partial_{kj}U_i)$ (introduced by Jones & Launder (1972) to the ε equation), and the factor of two in the denominator of the molecular diffusion, implies that the quantity ε has a different definition to that conventionally employed in k-ε schemes (*i.e.* a change of variable $\varepsilon \to \varepsilon + (1-\alpha)^3\frac{k}{\varepsilon}E + \frac{1}{2}\nu\partial_{jj}k$). The coefficient $C^*_{\varepsilon_2}$ is taken as a function of the turbulent transport of k to ε ratio, $C^*_{\varepsilon_2} = C_{\varepsilon 2} + \alpha^3(C_{\varepsilon_4} - C_{\varepsilon_2})tanh\left(\left|\frac{D'_k}{\varepsilon}\right|\right)$, as proposed by Parneix and Laurence (1997). Full details of the scheme can be found in Billard & Laurence (2011) and Billard (2011).

All the models have been implemented in the open source *Code_Saturne* (Archambeau *et al.*, 2004; Fournier *et al.*, 2011) which is used in the present study. All but the RSM-SSG model are low Reynolds number models which can be integrated all the way to walls. Calculations using the RSM-SSG model use the scalable wall function method of Grotjans & Menter (1998) to handle the near-wall region.

Figure 1 compares the normal Reynolds stresses predicted by the models in the case of plane channel flow for two friction velocity based Reynolds numbers $Re_\tau = 395$ and $Re_\tau = 2000$ (DNS data of Kim *et al.* (1987) and Jimenez & Hoyas (2008) are also shown for comparison). The peak and the near-wall behaviour of the Reynolds stresses are well predicted by the EBRSM model. The same conclusion holds for the BL-$\overline{v^2}/k$ model as far as the wall normal stress is concerned. As expected, the mean velocity predictions of all models are in good agreement with DNS, and are thus not shown here.

TWO DIMENSIONAL SEPARATED FLOWS

We now consider the performances of these models in three 2-D flows. The first case considered is the flow over

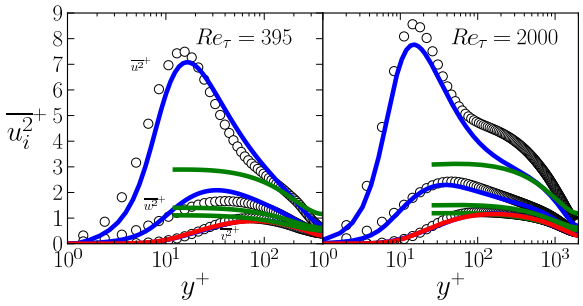

Figure 1. Profiles of the mean Reynolds stresses in a plane channel flow for $Re_\tau = 395$ and $Re_\tau = 2000$, ∘DNS — BL-$\overline{v^2}/k$, — *SSG* , — EBRSM.

periodic 2-D hills, reported by Almeida *et al.* (1992) (reference data taken from the LES of Temmerman and Leschziner (2001)). This is a pressure-induced recirculating flow which has been used quite extensively for comparing the performance of many RANS models (Jang *et al.*, 2002; Temmerman *et al.*, 2003). The geometry is shown in Figure 2 (left): the hill height h_1, domain height H_1 and inter-hill distance L_1 are such that $H_1 = 3.036h_1$ and $L_1 = 9h_1$, and the Reynolds number, based on the bulk velocity and h_1, is 10590. The LES study of Fröhlich *et al.* (2005) suggested that this flow features a strong intermittency in the recirculation zone; the modelling of which is out of the reach of RANS models on 2-D grids. Despite this, several simple models are known to return fairly good predictions of the recirculation length, by virtue perhaps of the consideration of such flows during model development.

In the present results, the skin friction coefficient along the bottom wall (Figure 3, left) indicates an over-prediction of the recirculation length by the EBRSM and the k-ω SST model, unlike the BL-$\overline{v^2}/k$ model which appears to predict a flow pattern closer to that observed in the LES data. This is reflected by the mean stream-wise velocity profiles, shown in figure 4 (top), where it is also seen that the two stress transport models are the most capable of predicting the flow acceleration and resulting near-wall peak of the velocity at the location $x/h_1 = 0$.

The turbulent shear-stress predicted across the recirculation bubble at $x/h_1 = 2$ (Figure 4 (bottom)) is excessively low for all models. This results in a lower level of turbulent mixing between bulk and recirculating flow regions, which explains the over-prediction of recirculation length by the SST and EBRSM schemes. The BL-$\overline{v^2}/k$ model performs well in this case, with an accurate prediction of recirculation length, though examination of skin friction coefficient indicates a slight over-prediction of the velocity gradient.

The second case considered is the flow over a wall-mounted hump, reported by Greenblatt *et al.* (2004). The geometry is shown in Figure 2 (centre). The hump chord length c, its height h_2 and domain height H_2 are related by $H_2 = 0.91c$ and $h_2 = 0.128c$, and the Reynolds number based on c is 9.36×10^5. In this case the flow separation is induced by the geometry. As an illustration of results, the predicted skin friction coefficient is presented in Figure 3 (centre). All models provide a fair representation of the acceleration over the hump, although the SST scheme underpredicts C_f here.

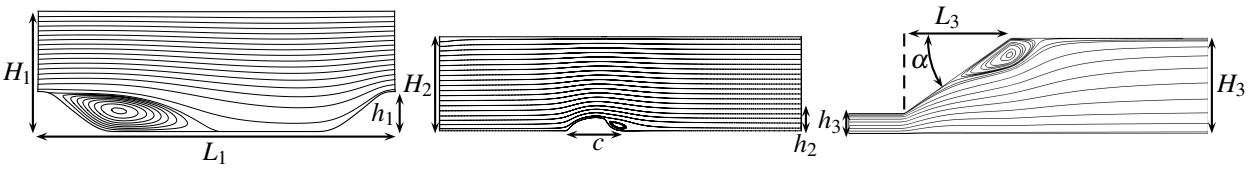

Figure 2. Geometries of the periodic hill (left), the hump (centre) and the diffuser (right) with flow streamlines.

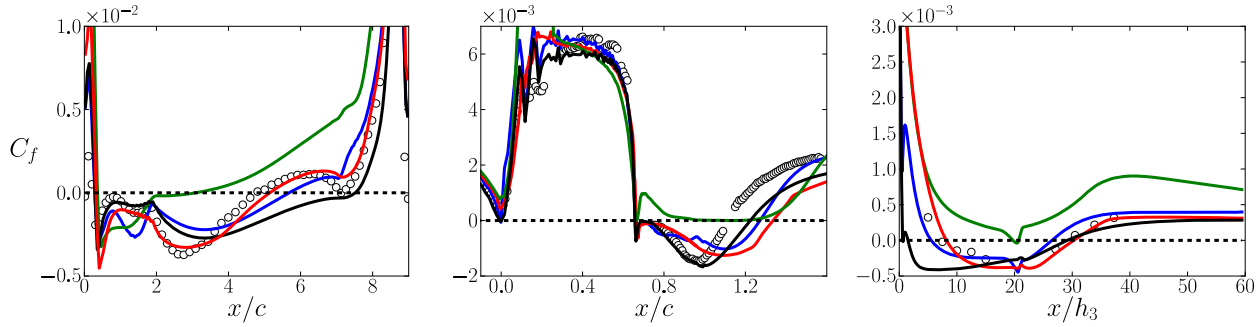

Figure 3. Skin friction coefficient for: the periodic hill (left), the hump (centre) and the 2 dimensional diffuser (right), ∘Ref. — BL-$\overline{v^2}/k$, — k-ω SST , — *SSG* , — EBRSM.

Conversely, the SST appears to provide a good prediction of the magnitude of the recirculating flow and the closest estimate of the reattachment location, although the recirculation length is overpredicted by all models. The two elliptic-blending based models give good results over the hump, but then over-predict the recirculation length.

The third flow considered is the asymmetric plane diffuser, reported by Buice & Eaton (1997) and Obi *et al.* (1993) (reference data of Obi *et al.* (1993)), pictured in Figure 2 (right). The inlet height h_3, outlet height H_3 and length of the expending section L_3 are related by $H_3 = 4.7h_3$ and $L_3 = 21h_3$. The slant angle is $\alpha = 10°$, and the Reynolds number based on bulk velocity and h_3 is 18000. The skin friction coefficient along the inclined wall is shown in Figure 3 (right). In this flow, the two elliptic blending based models correctly predict the separation location, compared to a very early separation from the SST and almost no flow reversal when using the SSG (with scalable wall functions). The flow reattachment is better predicted with all schemes, although the EBRSM indicates a somewhat early reattachment.

The rather ambiguous picture provided by these results will perhaps seem familiar to some readers (*i.e.* the more physical RSM's being apparently unable to consistently provide a gain in accuracy). This is quite likely to be linked to the fact that many EVM based schemes are calibrated to 2-D flows such as those considered here, in which a single shear dominates the flow, while the more complex RSM's may perform more consistently over a wider range of complex 2- and 3-D flows.

In view of commonly held opinion that a single "omnipotent" turbulence model is unlikely to emerge, it is useful to re-iterate the importance of model selection. In the following section, we explore the application of the same models to two 3-D separated flows.

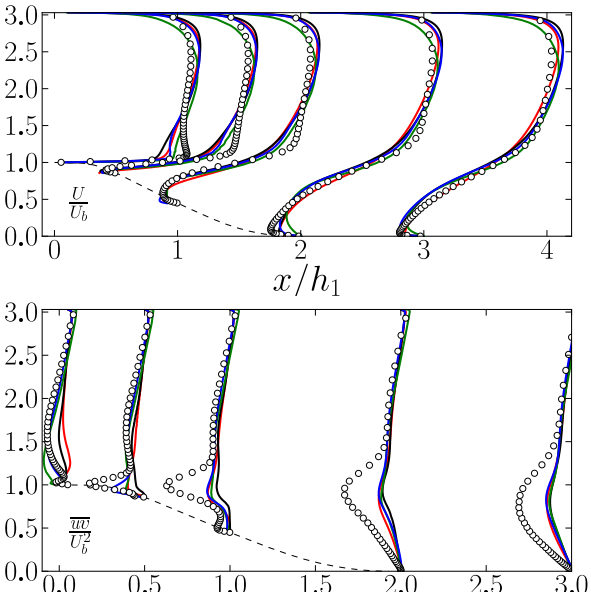

Figure 4. Profiles of mean velocity (top) and turbulent shear stress (bottom) on down-side of periodic hill, ∘LES — BL-$\overline{v^2}/k$, — k-ω SST , — *SSG* , — EBRSM.

THREE DIMENSIONAL FLOWS

The case provided in Cherry *et al.* (2008) consists of flow through a three dimensional diffuser (a duct with two contiguous diverging walls), represented in figure 5, with Reynolds number based on bulk velocity and inlet duct height of 10^4. The authors took measurements using Magnetic Resonance Velocimetry, and reported a separation starting at the upper right diverging corner which extended further downstream along the top wall. Only those models capable of resolving anisotropy are able to capture the secondary vortices present

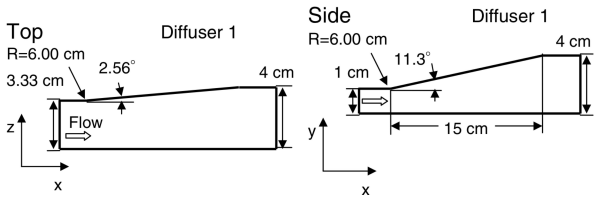

Figure 5. Geometry of the 3D diffuser case.

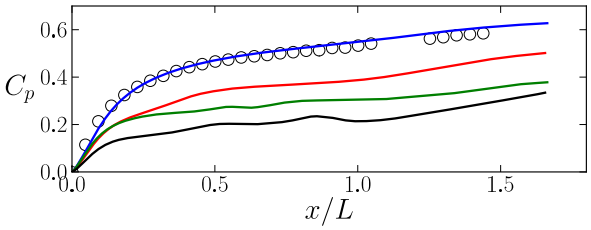

Figure 6. Pressure coefficient along a mid-span line of the lower wall in the 3D diffuser case, ○Exp. — BL-$\overline{v^2}/k$, — k-ω SST , — *SSG* , — EBRSM.

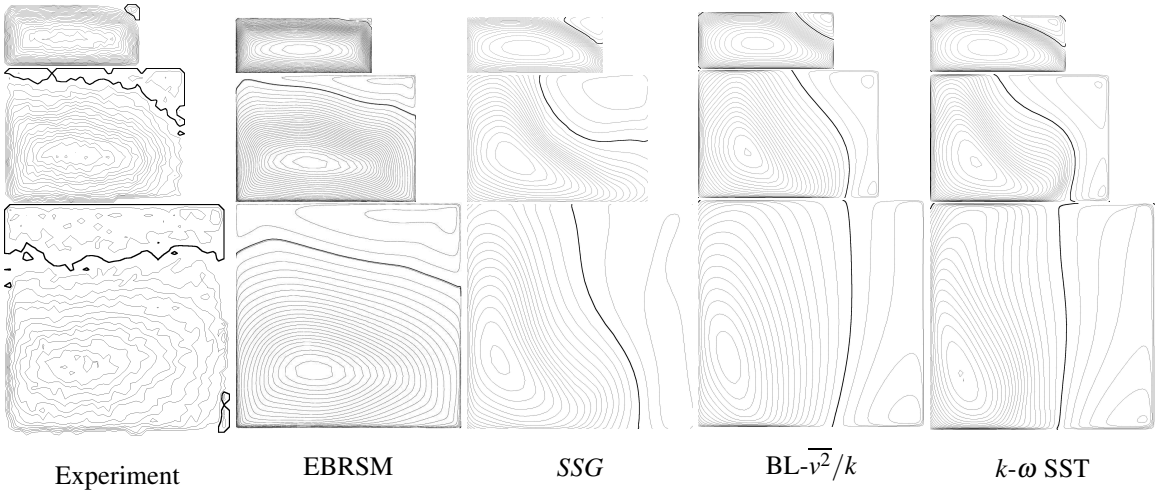

Figure 7. Contours of mean streamwise velocity at three different YZ planes (top-bottom, $x = 2cm$, $x = 8cm$ and $x = 15cm$).

in the inlet and outlet ducts, though at a recent turbulence modelling workshop (Brenn *et al.*, 2008) it was concluded that many RSM's (and most EVMs) predicted the flow recirculation to appear erroneously on the side wall rather than on the top wall.

The simulations were performed on grids of up to $212 \times 60 \times 180$ points, to obtain grid-independent results, with suitable near-wall refinement to ensure that the nondimensional wall-distance of the near-wall nodes was less than unity. Inflow conditions were taken from precursor periodic duct simulations at the same Reynolds number. Figure 6 presents the evolution of the pressure coefficient, C_p, along the bottom wall (at midspan), whilst Figure 7 compares the present results with the experimental data in the form of contours of the mean streamwise velocity at four different cross sections (distance x is defined from the start of the expansion, and the thick line represents the isovalue $U = 0$). As seen from the contours, the EBRSM results are very similar to the experimental data, with the correct location and extent of the recirculation bubble, as confirmed by the C_p prediction. The *SSG* returns a corner recirculation which is larger than the experiment at $x = 2cm$ and which then develops further downstream along the side wall at the end of the diverging section. Its under-prediction of C_p also reveals a larger flow recirculation than in the experiment. The same erroneous trend is observed for the two EVM's, but the development of the recirculation along the side wall starts earlier ($x \leq 8cm$). Both models also over-predict the recirculation, with particularly poor behaviour returned by the k-ω SST model.

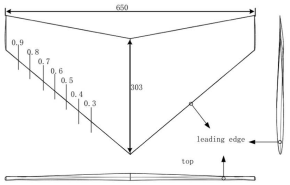

Figure 8. Geometry of the swept wing case.

The difference between EBRSM and *SSG* results reveals the importance of an accurate near-wall turbulence representation, as this is the major difference between these two models. As linear EVM's, both BL-$\overline{v^2}/k$ and k-ω SST do not capture the secondary flow in the inlet duct. However, this is not the origin of the subsequent discrepancies, since simulations (not shown here) with both models using an inlet field as predicted by the EBRSM scheme also failed to capture the correct separation pattern.

The final case reported here is that of flow separation from a highly swept wing. The 3-D geometry, shown in Figure 8, is a 40^o swept wing, at 9^o angle of incidence, representing the onset of stall. The Reynolds number based on freestream velocity and root chord length is 210000, and detailed measurement data have been obtained by Zhong & Turner (2007), highlighting a complex flow pattern over the wing. The case was also the object of an Implicit LES reported in Hahn & Drikakis (2009) and a Hybrid RANS/LES simulation of Li & Leschziner (2007).

The computational domain represents half of the wing

Figure 9. Visualisation of instantaneous vorticity (left) and time averaged streamlines (right) of the Implicit LES simulation of Hahn & Drikakis (2009).

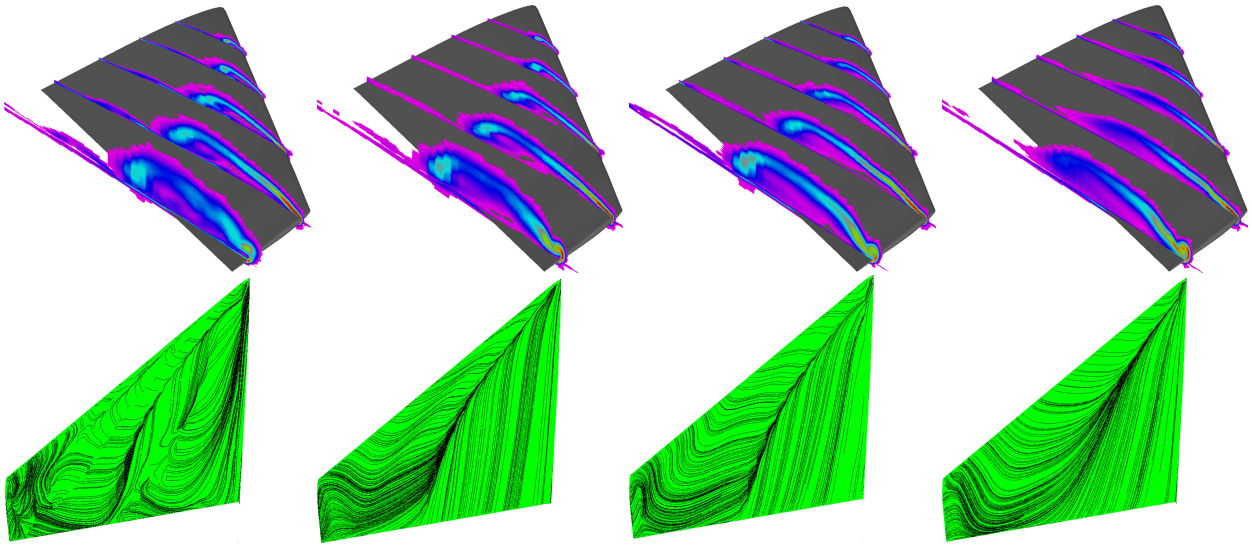

EBRSM *SSG* BL-$\overline{v^2}/k$ k-ω SST

Figure 10. Vorticity contours at different streamwise locations (top) and streamlines (btm) over the wing.

geometry and was meshed with $256 \times 134 \times 112$ cells (total $3.8M$), using an hyperbolic tangent based refinement in the near-wall region to ensure the presence of enough points within the viscous sublayer; the largest non-dimensional wall-distance of the near-wall nodes was found to be of order 0.5 near the wing tip. Symmetry conditions are prescribed for all variables at the symmetry plane, and freestream inlet turbulence is prescribed so that the associated turbulent lengthscale $k^{3/2}/\varepsilon$ represents 20% of the chord length. As a consequence of this fully turbulent approach flow, a by-pass transition occurs on the wing.

Figure 10 shows the predicted vorticity on plane cuts over the wing and the streamlines just over the wing. Figure 9 provides equivalent flow visualisations of the implicit LES as presented in Hahn & Drikakis (2009). The leading edge vortex (LEV) captured by all models is comparable to that reported by the LES and experimental data, and is characterized by strong vorticity (as seen in Figure 10) and delimited by the re-attachment line clearly shown by the streamlines. Both the LES and experimental data also report the presence of a secondary vortical region, represented by additional saddles on the surface streamlines within the LEV (as seen on Figure 9, right). This feature is only captured clearly by the EBRSM in the present study, and is also visible in the vorticity plots, where the EBRSM is the only model whose results exhibit a second smaller region of high vorticity beneath the main one. Towards the wing tip the interaction between the LEV and the opposing outer flow is characterized by another saddle point (see Figure 9, right). Although this is picked up qualitatively by all models, as seen in the streamlines, it is best represented by the two elliptic blending based models.

Hahn & Drikakis (2009) also reported a further flow feature inboard of the main vortex, where their simulation predicted a portion of fluid revolving around a focal point and a separation zone near the trailing edge. In contrast, the experimental data only showed streamlines aligned with the freestream direction here. It is interesting to note that the EBRSM results indicate a similar feature, whereas the *SSG* and both EVM's show trends similar to that of the experiment.

Mean stream-wise velocity predictions are compared to Laser Doppler Anemometry (LDA) experimental profiles in Figure 11 at 50% span (as indicted on Figure 8), for 5 different chord-wise locations. At this location the secondary vorticity is captured by the EBRSM from the first station (10% chord) where the profiles are marked by a wiggle visible at 10%, 30% and 50% chord. It can also be seen in the experiment at the same locations but with a smaller amplitude (though a change in the profile concavity is still clearly visible). This secondary vortical region also appears on the SSG profiles, but somewhat displaced (at 30% chord). Although this feature is totally missed by the k-ω SST model (which predicts monotonic profiles until the peak) the BL-$\overline{v^2}/k$ model also captures a near-wall velocity kink but at considerably greater chord lo-

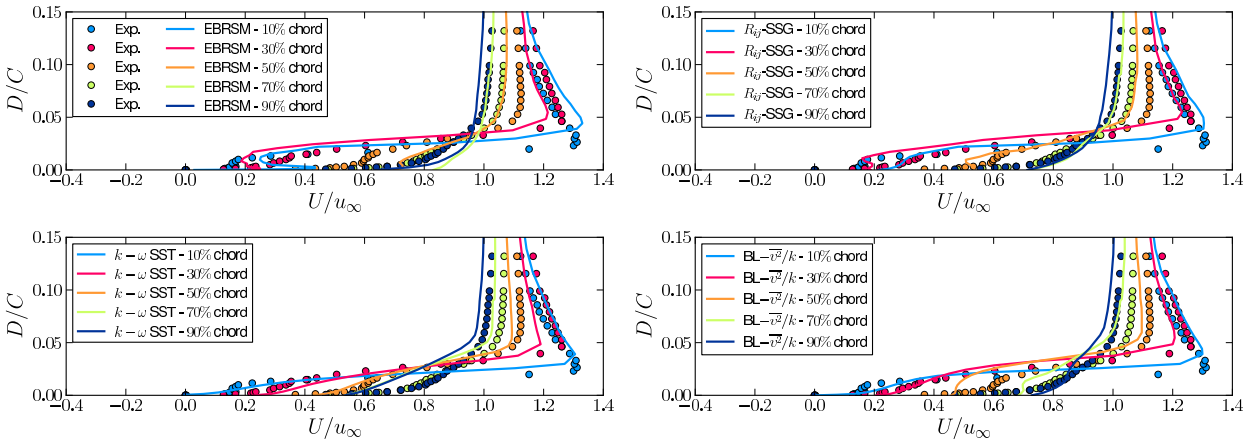

Figure 11. Velocity profiles at different chord location at 50% span over the wing.

cation (50% chord). The location of the velocity peak for all four models is displaced away from the wall at 10% and 30% chord locations, suggesting an excessive size of the LEV.

Approaching the wing tip (80% span), velocity profiles (not shown here) reveal that the experimental data exhibits a near-wall region of negative stream-wise velocity over all the chord length, which is only partially captured by the models (both elliptic relaxation based models only predict a negative velocity for the two first chord locations). All models except the k-ω SST under-predict the magnitude of the velocity peak, but conversely the latter model under-predicts the boundary layer thickness across the wing chord.

CONCLUSION

Differences between eddy viscosity modelling and second moment closure, as well as the effects of the near-wall turbulence representation, are illustrated by the variability of results obtained in the five cases considered. While no clear conclusions are drawn from the 2-D cases alone, some of the flow features (such as the marked acceleration on the uphill side of the periodic hill, or the secondary vorticity appearing on the swept wing) are captured only with the most advanced model considered, the EBRSM. This is also the only model able to predict the correct development of the recirculation in the 3-D diffuser flow. These observations support the principle that flows with strong 3-D effects, involving multiple-shears as opposed to a single shear, necessitate stress anisotropy resolution. The importance of near wall modelling is also highlighted by observing the results of the SSG model in high Reynolds form. These results justify the careful selection of the underlying RANS model in a hybrid RANS-LES approach, as some of the modelling improvements considered here (in particular in the near-wall region) would be active where such approaches are in RANS mode.

Acknowledgements: The authors gratefully acknowledge computational support from EPSRC for UKs National HPC Facility, HEC-ToR, via Direct Access Class 1b. This work was supported in part by the EC project ATAAC, 7th Framework Prog. (No. ACP8-GA-2009-233710-ATAAC). The authors are also grateful to N. Li and M. Leschziner for providing the mesh for the Swept Wing case.

REFERENCES

Almeida, G.P., Durao, D.F.G. & Heitor, M.V. 1992 *Exp. Thermal and Fluid Science* p. 87.

Archambeau, F., Mechitoua, N. & Sakiz, M. 2004 *International Journal on Finite Volumes* **1** (1).

Billard, F. 2011 PhD thesis, School of Mechanical Aerospace and Civil Engineering - The University of Manchester, to appear.

Billard, F & Laurence, D 2011 *Submitted to International Journal of Heat and Fluid Flow* .

Brenn, G., Jakirlić, S. & Steiner, H. editors. 2008 13^{th} *SIG15 ERCOFTAC Workshop on Refined Turbulence Modelling, Graz, Austria*

Buice, CU & Eaton, JK 1997 Report TSD-107, Department of mechanical engineering.

Cherry, E.M., Elkins, C.J. & Eaton, J.K. 2008 *International Journal of Heat and Fluid Flow* **29** (3), 803–811.

Durbin, P.A. 1991 *Theoretical and Computational Fluid Dynamics* **3** (1), 1–13.

Durbin, P.A. 1993 *Journal of Fluid Mechanics* **249**, 465–498.

Fournier, Y., Bonelle, J., Moulinec, C., Shang, Z., Sunderland, AG & Uribe, JC 2011 *Computers & Fluids* **45** (1), 103–108.

Fröhlich, J., Mellen, C.P., Rodi, W., Temmerman, L. & Leschziner, M.A. 2005 *Journal of Fluid Mechanics* **526**, 19–66.

Fröhlich, J. & von Terzi, D. 2008 *Progress in Aerospace Sciences* **44** (5), 349–377.

Greenblatt, D., Paschal, K.B., Yao, C.S., Harris, J., Schaeffler, N.W. & Washburn, A.E. 2004 *AIAA Paper* **2220**, 2004.

Grotjans, H. & Menter, F. 1998. In *Proceedings of the 4th European Computational Fluid Dynamics Conference, John Wiley & Sons*, pp. 1112–1117.

Haase, W., Aupoix, B., Bunge, U. & Schwamborn, D., 2006. Notes on Numerical Fluid Mechanics and Multidisciplinary Design. Vol. 94. Springer, Heidelberg.

Haase, W., Braza, M. & Revell, A. 2009 Notes on Numerical Fluid Mechanics and Multidisciplinary Design, Vol. 103.

Hahn, M. & Drikakis, D. 2009 *AIAA journal* **47** (3), 618–630.

Jang, YJ, Leschziner, MA, Abe, K. & Temmerman, L. 2002 *Flow, Turbulence and Combustion* **69** (2), 161–203.

Jimenez, Javier & Hoyas, S. 2008 *Journal of Fluid Mechanics* **611**, 215–236.

Jones, WP & Launder, B. 1972 *International Journal of Heat and Mass Transfer* **15** (2), 301–314.

Kim, J., Moin, P. & Moser, R. 1987 *Journal of Fluid Mechanics* **177**, 133–166.

Li, N. & Leschziner, MA 2007 *Aeronautical Journal* **111** (1125), 689–698.

Manceau, R. & Hanjalić, K. 2002 *Physics of Fluids* **14** (2), 744–754.

Menter, F.R. 1994 *AIAA journal* **32** (8), 1598–1605.

Obi, S., Aoki, K. & Masuda, S. 1993 *Proceedings 9th Symp. of Turbulent Shear Flow, Kyoto, Japan*.

Rotta, J. 1951 *Zeitschrift für Physik A Hadrons and Nuclei* **129** (6), 547–572.

Speziale, C.G., Sarkar, S. & Gatski, T.B. 1991 *Journal of Fluid Mechanics* **227** (-1), 245–272.

Sveningsson, A., Pettersson-Reif, B.A. & Davidson, L. 2005 In *Proceedings of the* 4^{th} *International Symposium on Turbulence and Shear Flow Phenomena, Williamsburg, VA, USA*.

Temmerman, L., Leschziner, M., 2001 *In: Int. Symp. Turb. Shear Flow Phenomena, Stockholm, Sweden.*

Temmerman, L., Leschziner, M.A., Mellen, C.P. & Fröhlich, J. 2003 *International Journal of Heat and Fluid Flow* **24** (2), 157–180.

Zhong, S. & Turner, J, MSTTAR Project, EPSRC GR/S27443/01.